

## MMC-based conversion for MVDC applications

Présentée le 28 avril 2020

à la Faculté des sciences et techniques de l'ingénieur  
Laboratoire d'électronique de puissance  
Programme doctoral en énergie

pour l'obtention du grade de Docteur ès Sciences

par

**Stefan MILOVANOVIC**

Acceptée sur proposition du jury

Prof. F. Maréchal, président du jury  
Prof. D. Dujic, directeur de thèse  
Prof. A. Mertens, rapporteur  
Dr M. Vasiladiotis, rapporteur  
Prof. J. Kolar, rapporteur

École Polytechnique Fédérale de Lausanne  
Power Electronics Laboratory  
Station 11  
1015 Lausanne, Switzerland

<http://pel.epfl.ch>

© 2020 by Stefan Milovanović



*Dedicated to my family*



# Abstract

In recent years, DC grids have gained momentum due to the advantages they display over their AC counterparts. For instance, high voltage DC grids have been established as the most prominent solution in the underwater power transmission or interconnection of asynchronous systems. Consequently, the success of high voltage DC grids is expected to be replicated in the medium voltage domain. However, medium voltage DC grids have not been standardized yet, leaving the space for various research topics.

To realize a flexible and resilient DC grid, dependable connections among its parts operating under different voltage levels must be ensured. To put it differently, the DC-DC converter represents a keystone of any DC grid, operating at an arbitrary voltage level. Owing to the outstanding flexibility, scalability, and availability, the modular multilevel converter established itself in a vast variety of applications. Hence, the possibilities it offers in the high/medium voltage domain deserve to be further inspected.

This thesis is divided into two parts. The first part concerns the modular multilevel converter operating as the DC-AC converter. The presented modeling approach, implying the averaging of the converter equations on the branch level, provided the grounds for the control-related discussions. The control of terminal currents was elaborated in detail and supported by a thorough analysis and comparison of the methods employed to maintain the proper converter energy distribution. Despite the theoretically unlimited voltage scalability, the modular multilevel converter power extension through the current capacity boost represents a significant technical challenge being comprehensively addressed throughout this thesis. It was shown that by paralleling the converter branches, the current, and implicitly the power, capacity of the converter can be increased while requiring no hardware adaptations of the existing parts. Moreover, branch paralleling offers the possibility to improve the spectral content of voltage at either of the converter terminals.

The second part of this thesis refers to the employment of the modular multilevel converter in the domain of the DC-DC conversion. A novel, high power, bidirectional, DC-DC converter, utilizing the Scott transformer connection to provide galvanic separation between two of its ports, was proposed. It features the possibility of interconnecting a bipolar DC grid of high, or medium, voltage level with another DC grid of an arbitrary voltage level. As the Scott transformer connection comprises two separate transformer units, the proposed topology ensures that the operation can be maintained even in case either of the bipolar grid DC feeders is lost. A set of minor modifications to the above-mentioned topology leads to the structure providing the means for unidirectional energy flow. Nevertheless, control principles for both of the proposed solutions were derived and confirmed through the set of detailed simulations. Additionally, the unprecedented shift of the Scott transformer connection operating frequency towards the medium frequency range was proposed.

A comprehensive analysis of the so-called quasi two-level converter leg was provided in the last part of this thesis. Quasi two-level operating principles imply the sequential and smooth transition of the converter leg AC voltage from one polarity to another. However, the transition occurs in the discrete time steps, being referred to as the dwell time, which makes the analysis of the converter branch currents rather non-trivial. Two, essentially different, analysis methods were presented. It was demonstrated that very precise sizing of the converter parts can be performed in case branch currents, during the leg voltage transition process, are known.

**Keywords:** *medium voltage, high power conversion, modular multilevel converter, quasi two-level converter, Scott transformer connection, solid state transformer*



# Résumé

Ces dernières années, les réseaux d'électricité à courant continu ont pris de l'ampleur grâce aux avantages qu'ils offrent face à leur homologue à courant alternatif. Par exemple, les réseaux haute-tension continu se sont établis comme la solution prédominante dans la transmission de puissance sous-marine ou les interconnexions de systèmes asynchrones. Par conséquent, le succès des réseaux continus haute-tension est censé être traduit dans le domaine de la moyenne-tension. Cependant, les réseaux moyenne-tension ne sont pas encore standardisés, ce qui laisse de la liberté pour des sujets de recherche.

Pour réaliser un réseau continu flexible et robuste, des connections fiables entre les différents partis de niveaux de tension différents en présence doivent être assurées. En d'autres termes, les convertisseurs DC-DC sont la clé de voute de tout réseau continu, quel que soit le niveau de tension. En raison de sa flexibilité, de son évolutivité et de sa disponibilité exceptionnelle, le convertisseur modulaire multi-niveaux s'est imposé dans une vaste gamme d'applications. C'est pourquoi les possibilités qu'il offre dans le domaine de la haute/moyenne tension méritent d'être approfondies en détails.

Cette thèse se divise en deux parties. La première concerne le convertisseur modulaire multi-niveaux fonctionnant comme un convertisseur DC-AC. L'approche de modélisation présentée, impliquant les équations du convertisseur moyennées sur une branche, a servi de base aux discussions sur leur contrôle. Le contrôle des courants aux bornes du convertisseur est élaboré en détails et soutenu par une analyse et une comparaison approfondie des méthodes employées pour maintenir la distribution correcte de l'énergie au sein du convertisseur. Malgré l'extensibilité de la tension théoriquement illimitée, l'augmentation de la puissance des convertisseurs multi-niveaux par le renforcement de ses capacités en courant représente un défi technique important qui est examiné minutieusement tout au long de cette thèse. Il est démontré qu'en mettant en parallèle les branches du convertisseur, le courant, et donc implicitement la puissance, la capacité du convertisseur peut être augmentée en ne nécessitant aucune adaptation matérielle des composants existants. En outre, la mise en parallèle des branches offre la possibilité d'améliorer le contenu spectral de la tension à l'une ou l'autre des bornes du convertisseur.

La seconde partie de la thèse aborde l'usage des convertisseurs modulaire multi-niveaux dans le domaine de la conversion DC-DC. Un convertisseur DC-DC innovant, bidirectionnel et de grande puissance utilisant la configuration du transformateur de Scott pour assurer la séparation galvanique entre ses deux ports est proposée. Il offre la possibilité d'interconnecter un réseau bipolaire à courant continu de tension élevée ou moyenne avec un autre réseau de courant continu d'un niveau de tension arbitraire. Comme le transformateur de Scott comprend deux transformateurs séparés, la topologie proposée permet de maintenir l'exploitation même en cas de perte de l'un ou l'autre des départs de courant continu du réseau bipolaire. Une série de modifications mineures de la topologie susmentionnée conduit à la structure fournissant la possibilité d'un flux d'énergie unidirectionnel. Néanmoins, les principes de contrôle sont dérivés et confirmés pour l'ensemble des solutions proposées grâce à des simulations détaillées. Aussi, le déplacement inédit de la fréquence de fonctionnement du transformateur de Scott vers la gamme des moyennes fréquences est proposée.

Une analyse complète de la branche ainsi appelée convertisseur quasi deux niveaux est fournie dans la dernière partie de cette thèse. Les principes de fonctionnement des quasi deux niveaux impliquent la transition séquentielle et en douceur de la tension alternative de la branche du convertisseur d'une polarité à l'autre. Toutefois, la transition se produit dans un système à pas de temps discrets, aussi appelés temps masqué, ce qui rend l'analyse des courant de branche du convertisseur non

triviale. Deux méthodes d'analyse, essentiellement différentes, sont présentées. Il est démontré qu'un dimensionnement très précis des composants du convertisseur peut être effectué dans le cas où les courants de branche sont connus pendant le processus de transition de la tension.

**Mots-clés:** *moyenne tension, conversion forte puissance, convertisseur multi-niveaux, convertisseur quasi deux niveaux, transformateurs de Scott, solid state transformer*

# Acknowledgments

*"As I review the events of my past life I realize how subtle are the influences that shape our destinies."*

Nikola Tesla

I would like to express my utmost respect and gratitude to my thesis advisor Prof. Dražen Dujić. Besides providing me with the unconditional support in conducting the research over the last three years, he also had an important role in developing my views on various aspects unrelated to the scientific path we have all undertaken.

It must be emphasized that my PhD journey would not have been possible if it had not been for Dr. Maja Harfman Todorović from GE Global Research. Her unreserved support encouraged me to go along the PhD path and gather this precious international experience. I cannot put into words how lucky I was to make her acquaintance.

Furthermore, I was extremely delighted to have Prof. Johann Kolar from ETH Zürich, Prof. Axel Mertens from Leibniz Universität Hannover and Dr. Michail Vasiladiotis from ABB Switzerland as the jury members. Their effort to read my work and be part of the examining process is highly appreciated. Also, I would like to thank Prof. François Maréchal from EPFL, who gladly accepted the role of the jury president.

Many thanks to my dear colleague and friend Nikolina Đekanović for proofreading this document meticulously.

Throughout the PhD I made a lot of new friends without whom the time spent at Power Electronics Laboratory (PEL) would not have been the same. First and foremost, I need to thank all PEL members for accepting me as a team member, which made the working atmosphere, at least to say, pleasant for me. My social life would not be the same without my Serbian friends, gathered around the group being referred to as "Kafana na Balkanu". Thank you all for your support and uncountable and priceless moments of laugh, joy and happiness!

Lastly, the biggest support came from my parents and my beloved sister. They have always represented an inexhaustible source of inspiration to me and I dedicate this thesis to them.

Lausanne, March 2020  
Stefan Milovanović





# List of Abbreviations

1PH	Single-Phase
2LVL	Two-Level
3PH	Three-Phase
AC	Alternating Current
AD	Available Design
AFE	Active Front End
B2B	Back-to-Back
BC	Balancing Circuit
CFSM	Converter-Fed Synchronous Machine
CHB	Cascaded H-Bridge
CS	Complementary Switching
DAB	Dual Active Bridge
DC	Direct Current
DFIM	Doubly Fed Induction Machine
DR	Diode Rectifier
FB	Full-Bridge
FC	Flying Capacitor
FRT	Fault Ride Through
GCC	Grid Current Control
HB	Half-Bridge
HV	High Voltage
HVAC	High Voltage Alternating Current
HVDC	High Voltage Direct Current
IGBT	Insulated-Gate Bipolar Transistor
ISOP	Input Series Output Parallel

KCL	Kirchhoff Current Law
KVL	Kirchhoff Voltage Law
LCC	Line Commutated Converter
LFM	Low Frequency Mode
LFT	Low Frequency Transformer
LV	Low Voltage
MFT	Medium Frequency Transformer
MMC	Modular Multilevel Converter
MV	Medium Voltage
MVDC	Medium Voltage Direct Current
NPC	Neutral Point Clamped
OP	Operating Point
P	Primary
PHSP	Pumped Hydro Storage Power Plant
PLL	Phase Locked Loop
PM	Power Module
PSC	Phase Shifted Carrier
PWM	Pulse Width Modulation
Q2L	Quasi Two-Level
RES	Renewable Energy Sources
ROW	Rights of Way
S	Secondary
SBR	Sub-Branch
SM	Submodule
SRF	Synchronous Reference Frame

SSC	Six-Step Converter
SSCB	Solid State Circuit Breaker
SST	Solid State Transformer
STC	Scott Transformer Connection
SVD	Singular Value Decomposition
THD	Total Harmonic Distortion
VSC	Voltage Source Converter



# Contents

<b>Abstract</b>	<b>i</b>
<b>Résumé</b>	<b>iii</b>
<b>Acknowledgments</b>	<b>v</b>
<b>List of Abbreviations</b>	<b>vii</b>
<b>1 Introduction</b>	<b>1</b>
1.1 AC versus DC	1
1.2 Evolution of high power converters	4
1.3 Modular Multilevel Converter (MMC) perspectives in the Medium Voltage (MV) domain	6
1.4 Objectives and contributions of the thesis	9
1.5 Outline of the thesis	11
1.6 List of publications	12
<b>2 Dynamic Modeling and Basic Operating Principles of the Modular Multilevel Converter</b>	<b>15</b>
2.1 General considerations	15
2.2 Averaged dynamic model of the MMC	18
2.3 MMC operating principles	20
2.4 Summary	26
<b>3 Modular Multilevel Converter Control</b>	<b>29</b>
3.1 Discussion on the converter control layers	29
3.2 Control of the Alternating Current (AC) terminal currents	32
3.3 Direct Current (DC) terminal current control and circulating current concept	35
3.4 Circulating currents control	37
3.5 MMC total energy control	38
3.6 MMC Internal Energy Control	39
3.6.1 Energy Balancing of a Single MMC Leg	39
3.6.2 Energy Balancing in the Three-Phase (3PH) MMC	44
3.7 Simulation Results	63
3.7.1 General operation of the converter	63
3.7.2 Comparison of different energy balancing methods	70
3.8 Summary	72
<b>4 Extension of the Modular Multilevel Converter Power Capacity Through Branch Parallelism</b>	<b>75</b>
4.1 On the need for extension of the converter current capacity	75
4.2 MMC scalability options	76
4.3 Preliminary Considerations	78
4.4 Balancing of the sub-branch energies	80
4.5 Simulation results	87
	xi

4.5.1	Case with an even number of Submodules (SMs) per Sub-Branch (SBR)	88
4.5.2	Case with an odd number of SMs per SBR	91
4.6	Further considerations	93
<b>5</b>	<b>Modulation Considerations For the MMC Operating With Parallel Branches</b>	<b>95</b>
5.1	Preliminary Considerations	95
5.1.1	Available degrees of freedom	95
5.1.2	Assumptions and adopted simplifications	98
5.2	Analysis of voltage components generated by the converter leg	102
5.2.1	SBR voltage analysis	102
5.2.2	Branch voltage analysis	105
5.2.3	Leg voltage analysis	109
5.3	Summary	118
<b>6</b>	<b>High Power Bidirectional DC-DC Converter Utilizing Scott Transformer Connection</b>	<b>119</b>
6.1	Motivation	119
6.2	Proposed topology	121
6.2.1	Derivation	121
6.2.2	Operating principles	124
6.3	System design	126
6.3.1	Number of MMC submodules	126
6.3.2	Transformers' turns ratios	127
6.3.3	MMC branch inductor design	131
6.3.4	SM capacitance design	131
6.3.5	LV stage capacitor bank design	134
6.4	System control under normal operating conditions	135
6.4.1	Equivalent 3PH-DAB model	135
6.4.2	Output voltage control	138
6.4.3	MMC balancing	139
6.5	Simulation results under normal operating conditions	142
6.6	System control under faulty operating conditions	145
6.6.1	Negative DC pole outage	146
6.6.2	Positive DC pole outage	147
6.7	Simulation results under faulty operating conditions	148
6.7.1	Negative DC pole outage	149
6.7.2	Positive DC pole outage	150
6.8	Closing discussion	152
<b>7</b>	<b>High Power Unidirectional DC-DC Converter Utilizing Scott Transformer Connection</b>	<b>153</b>
7.1	Topology derivation	153
7.2	Preliminary considerations	154
7.3	Operating principles	158
7.3.1	Normal operating conditions	158
7.3.2	Operation under faults	159
7.3.3	Modulation considerations	164

7.4	System design	166
7.4.1	Number of MMC SMs	166
7.4.2	Transformers' turns ratios	166
7.4.3	MMC branch inductor design	167
7.4.4	SM capacitance design	171
7.4.5	Output filter design	173
7.5	System control	175
7.6	Simulation results under normal operating conditions	177
7.7	Simulation results under faulty operating conditions	180
7.7.1	Negative DC pole outage	181
7.7.2	Positive DC pole outage	182
7.8	Concluding remarks	184
<b>8</b>	<b>Comprehensive Analysis and Design of a Quasi Two-Level Converter leg</b>	<b>187</b>
8.1	Motivation	187
8.2	Leg transient analysis	190
8.2.1	Problem statement	190
8.2.2	Piecewise analysis	193
8.2.3	Analytic analysis	197
8.3	Submodule capacitor sizing	207
8.4	Simulation results	209
8.5	Summary	212
<b>9</b>	<b>Summary and Future Works</b>	<b>213</b>
9.1	Summary and contributions	213
9.2	Future works	215
9.2.1	General control of the MMC-based converters	215
9.2.2	Further considerations regarding the MMC operating with parallel branches	215
9.2.3	Improvements on the topologies employing the Scott Transformer Connection (STC)	216
	<b>Appendices</b>	<b>219</b>
<b>A</b>	<b>Notes on the Singular Value Decomposition</b>	<b>221</b>
A.1	Square matrix diagonalization	221
A.2	Symmetric matrices	222
A.3	Derivation of the Singular Value Decomposition (SVD)	226
A.4	SVD and its subspaces	229
A.5	Application of the SVD to a 3PH MMC	231
<b>B</b>	<b>Expansion of the SM switching function obtained in the manner characterizing the MMC closed-loop control</b>	<b>235</b>





# 1

## Introduction

### 1.1 AC versus DC

Notwithstanding the possibility of extending the production capacity, more efficient use and transmission of energy currently available within the power system is also to be considered. In the Battle of currents, which took place during the late 1880s and early 1890s, the Alternating Current (AC) prevailed over the Direct Current (DC) mainly due to the effortless voltage stepping-up, explained by Faraday's law, through the use of transformers. Also, the invention of the induction motor had significant impact upon the shaping of the power system back then. Nevertheless, the presence of reactive power, the phenomenon being closely tied to the AC systems, introduces a whole set of drawbacks:

- The distance the energy can be transferred across an AC power line is limited by the system stability constraints [1].
- Although inconvertible into the useful work, inevitable presence of reactive power, caused by the inductive voltage drops, increases the amount of energy being lost in the transmission lines.
- Effects caused by the power line capacitance come to the fore under two typical scenarios. If a long line (normally, over 400km) is operated under a light load, or even no load at all, voltage at the receiving end of the line goes beyond the transmitting end voltage. This phenomena, known as Ferranti effect [2], can be explained by the fact that only capacitive charging currents flow through the line on the above defined terms. Unless properly treated, Ferranti effect imposes serious threat to the power system equipment which is normally sized for a strictly defined operating voltage range. Similar reasoning can be applied to a set of applications, such as the underwater bulk power transmission systems, requiring cable connection. Cable capacitance, significantly exceeding the one of a power line having the same transmission rating, results in the substantial reactive power consumption, thus providing unsatisfactory energy transmission performance.
- Skin and proximity effects [3], also being observed only in the AC systems, increase the resistance of the transmission lines, thus having a negative impact upon the system efficiency.

Therefore, removing the reactive power from the energy transfer equation can be considered the remedy for a set of shortcomings listed above. None of these limitations can be observed in the DC systems, where various advantages can be observed from both technical and economic viewpoints. It is worthy to note, however, that historic events that shaped the today's power system took place long before power electronics was invented. Consequently, the AC systems have dominated the area of energy transfer for the past 150 years despite all of the listed deficiencies.

As the transmission distance increases, so does the transmission voltage with the aim of reducing the energy losses. Since the limitations of the High Voltage Alternating Current (HVAC) transmission were observed in case long distances were to be bridged, it was in this field where the ideas of High Voltage Direct Current (HVDC) systems commercialization emerged during the early 1940s [4]. However, it must be emphasized that it was not until the advent of power electronics that reemergence of the DC systems was feasible. Inability of stepping-up the DC voltage can be overcome by stepping-up the AC voltage followed by the power electronics-based rectification, which can be considered a milestone in the wide adoption of the DC systems. From the technical aspect, HVDC systems offer several advantages when compared to their AC counterparts [5]:

- As there is no reactive power, all stability related problems observed in the AC systems disappear. Once charged, power line/cable capacitance does not have an impact on the power transmission in case the energy is transmitted using the DC voltage. Additionally, line/cable inductance does not contribute to the steady state line voltage drop. Hence, no technical limits in the length of the HVDC cable exist. For instance, 700MW,  $\pm 450$ kV connection link between the power systems of Norway and the Netherlands was successfully realized using 580km long subsea High Voltage (HV) cables [6], [7].
- To improve the resilience and reliability of what the AC system represents nowadays, inter-connections were established on different levels including countries and even the continents. Nevertheless, direct connection of two (or multitude of) AC systems implies that they have to operate at the same frequency, phase and voltage level. In other words, the systems must be synchronized. Given that quantities such as frequency and phase do not exist in case DC transmission is considered, effortless interconnection of asynchronous systems is possible [8].
- Despite increasing the initial costs of a DC system, the need for power electronics converter brings several beneficial aspects into the spotlight. First and foremost, power flow control gets significantly alleviated compared to the AC systems. Thereafter, depending on the converter topology, additional services (independent control of active and reactive power [9], frequency control [10], black-start capability [11], damping of power swings [12], etc.) can be provided to the AC grid the converter is connected to. Owing to the inherent controllability, HVDC links do not increase the short circuit currents in the AC networks. On the contrary, owing to the above mentioned independent control of active and reactive power flows, HVDC links can provide a certain level of support to the AC grid during faults [13].

Further, an important set of features favoring the DC systems can be observed from the economic as well as environmental points of view:

- Due to the need for a rectification stage, an HVDC system requires higher initial investments when compared to an HVAC system [14], as presented in **Fig. 1.1(a)**. However, HVDC transmission lines, along with the land acquisition, were reported to be cheaper compared to ones operating at HVAC for the same power transfer capabilities [15]–[17]. Consequently, investment costs of an HVAC system exceed the HVDC system costs once the transmission distance higher than the so-called break even distance is bridged. Break even distance varies case by case, however, if overhead lines are considered, it falls in the range of 400 – 800km. If subsea installations are in the focus of a study, break even distance gets reduced to around 50km [14]. Hence, HVDC is nowadays seen as the most prominent solution in the high power, water crossing, transmission.

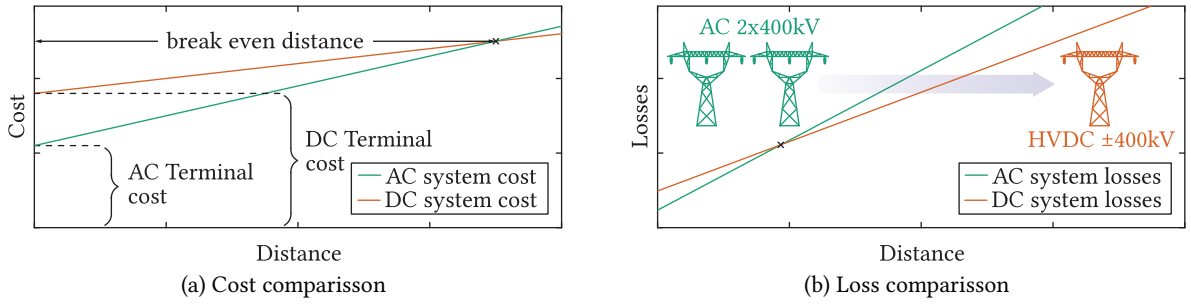


**Fig. 1.1** Comparison of HVDC and HVAC systems

- Apart from conducting the techno-economic analysis concerning the new power lines, the possibility to increase the transmission capacity of the existing AC lines by converting them into DC can also be exploited. Namely, using the existing power AC system infrastructure, without changing the conductors and performing a slight modifications of the towers and isolators, allows for an increase of the line rated power in case it is operated under DC voltage [15]–[19]. As depicted in **Fig. 1.1(b)**, two single circuit AC lines can be compared to one HVDC line [14], [18], indicating that significant Rights of Way (ROW) reduction can be achieved. In other words, significant savings can be made by reutilizing the existing structure instead of commissioning the new lines.

Although superior from the energy transmission viewpoint, wider adoption of the DC systems, in general, was constrained by the lack of standardized DC circuit breaker technology [20]. In contrast to the AC systems, where current zero-crossing occurs naturally, an artificial crossing of current in the DC circuit must be induced, otherwise an electric arc occurs between the contacts of a breaker. To ensure the outstanding performance in terms of the DC current extinguishing, modern DC breakers rely on the use of semiconductor devices, hence the name Solid State Circuit Breakers (SSCBs) [21]–[23]. Another set of applications where the economic savings, as well as the lack of need for generators' synchronization, promoted the DC systems relates to energy distribution within the electric ships [20], [24]. Voltages considered for this purpose fall in the Low Voltage (LV) or Medium Voltage (MV) range. Nevertheless, to ensure a secure and robust DC distribution system, capability of breaking the DC side fault currents must be ensured. So far, only LV solutions have been commercialized, with possible MV realizations being widely discussed in the literature. It is to be emphasized, however, that converters providing the possibility to cope with the DC side faults exist. Consequently, when realizing the DC breaker imposes significant technical challenge (as in the HV systems for example), an important protection feature can be obtained by means of the suitable rectification stage control. One can conclude that the power electronics converter represents the essential part of any system operating under DC voltage within any of its stages.

## 1.2 Evolution of high power converters

In the power transmission domain, inability of the DC voltage stepping-up is normally dealt with in two steps. Initially, AC voltage is stepped-up by means of the Low Frequency Transformer (LFT). This transformation is subsequently followed by the power electronics based rectification. Thereafter connection with the stage ensuring the energy transfer towards the other AC grid can be established to form the so-called point-to-point configuration, as presented in **Fig. 1.2**. Different configurations were mentioned in [25], [26], however, conversion principles remain the same irrespective of the analyzed structure. It is clear though that performance of any DC system strongly depends on the employed converter topology, therefore this topic deserves further attention.

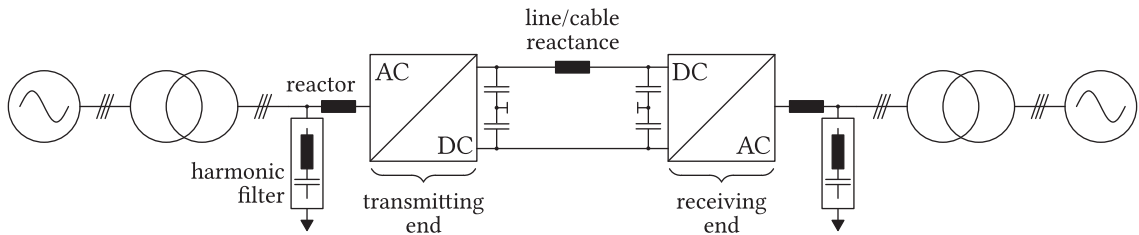


**Fig. 1.2** Typical HVDC system in symmetrical monopole configuration [25]

It was in 1941 that the first commercial HVDC system transmissioning 60MW at  $\pm 200\text{kV}$  was ordered in Germany. It was based on mercury arc valves which have dominated the HVDC market until the early 1970s, when they were pushed out by the thyristors. **Fig. 1.3(a)** presents Three-Phase (3PH) thyristor rectifier, which represents a Line Commutated Converter (LCC). In other words, changing the voltage across the converter's DC terminals can be done in time instants dictated by the AC line voltages. Owing to simplicity, low losses, and outstanding robustness of the thyristors, a set of LCC-based solutions is in the industrial use even nowadays under the name HVDC Classic [8], [27]. Successful commissioning of the first Voltage Source Converter (VSC)-based experimental HVDC plant [28] was another step forward in the technology making the HVDC transmission feasible.

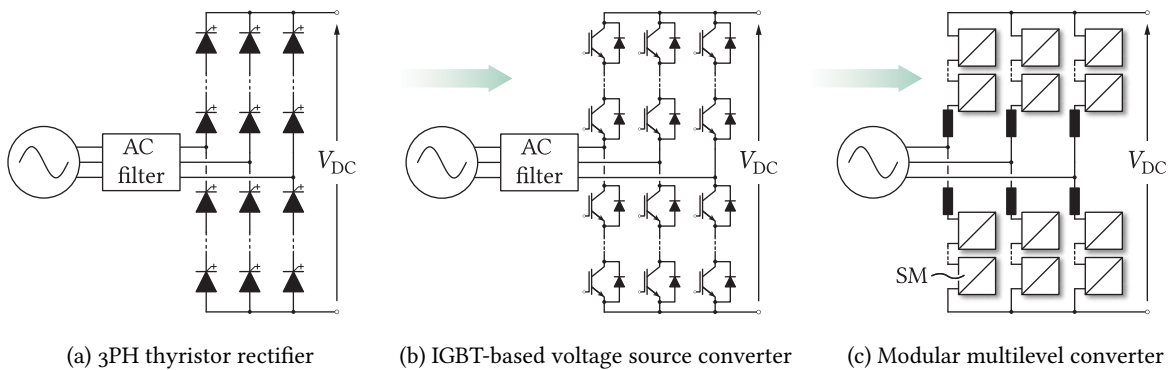


**Fig. 1.3** Converter topologies used for the high power AC-DC conversion purposes

The VSC-based solution, presented in **Fig. 1.3(b)**, uses series connection of Insulated-Gate Bipolar Transistors (IGBTs) to realize the switch of desired voltage ratings owing to the limited blocking capabilities of commercially available semiconductor devices, which nowadays reach as high as 6.5kV. Its main advantages can be outlined as independent control of the AC grid active and reactive power flows, while providing smaller footprint with less electric equipment compared to the LCC-based solutions of the same power range [28], ability of supplying weak networks [9], black-start capability [11], [29], etc. Nonetheless, series connection of semiconductor devices [30]–[33] introduces several disadvantages which require further consideration. To ensure static voltage balancing among the semiconductor devices, passive circuits need to be connected in parallel with every individual device. Furthermore, to ensure dynamic voltage balancing, simultaneous switching (or at least in the microsecond range [9]) is needed, which demands complex driver circuits. Also, voltages generated across the converter's AC terminals contain only two levels (0 or  $V_{DC}$ ) and to synthesize voltage references, demanded by the converter control, Two-Level (2LVL) Pulse Width Modulation (PWM) is normally used. Quality of such a waveform increases with the converter switching frequency [34], [35], however, at the price of generating higher converter losses which further increase the converter cooling requirements. As the converter efficiency should not be compromised, switching frequency of such a structure gets restricted to less than 1kHz leading to high filtering requirements of the AC side quantities. Last but not least, special IGBT design considerations have to be taken into account. Namely, widely used and cheap plastic module IGBTs can not be considered a proper choice for the converter operating in this configuration due to the failure mode shortcomings. Alternatively stated, failure of a single component within an IGBT string causes the isolation of the whole string from the rest of the circuit. Therefore, components such as Press-Pack IGBTs, guaranteeing the short-circuit failure mode, must be used if any level of redundancy is going to be ensured [36].

Introduction of the Modular Multilevel Converter (MMC) [37], [38], presented in **Fig. 1.3(c)**, was a game changer in the area of HVDC converters. While retaining the versatility offered by the 2LVL VSCs, the MMC provides additional assets to overcome the restrictions of its 2LVL counterparts. The basic building block of the MMC is referred to as the Submodule (SM). To a certain extent, it represents an independent structure, which, if properly controlled, operates at the voltage being a fraction of voltage demanded by an application the MMC is serving. Therefore, by stacking the SMs in series, an application voltage requirements can be effortlessly met, therefore no limitations in the converter voltage scalability are observed. It is noteworthy that scalability feature can easily be linked with the flexibility provided by the MMC. Namely, in case an increase in the application voltage requirements occurs, new SMs can be added to the existing structure providing the existence of space and control resources. Furthermore, the process of synthesizing the AC voltages is not constrained to the use of only two voltage levels. Conversely, high quality multilevel AC voltages can be naturally produced resulting in the very little or almost no filtering requirements of the AC side currents. At the end, one of the major amenities offered by the MMC refers to the likely exploited redundancy principles [39]. If any of the SMs happens to fail, the converter operation can be maintained without the need for any stoppage. On these terms, a faulty SM gets bypassed, with the remaining ones continuing the operation with slight voltage reference modifications. Consequently, outstanding availability of the converter is provided. The first commercial MMC-based project was realized in 2010 by Siemens [40]. Ever since then, the MMC has been present in all the fields regarding the high power HV conversion. Nevertheless, the potential of the MMC, and its derivatives, has also been recognized in the MV applications including DC-AC, AC-AC as well as DC-DC conversion. Hence, its perspectives in this voltage range should be discussed more extensively.

### 1.3 MMC perspectives in the MV domain

In the electrical drives area, power converters are quite often referred to as the frequency converters. In other words, variable speed operation becomes viable through the use of power electronics stage. In the power range of approximately 2 – 30MVA, the market of MV drives is dominated by the Neutral Point Clamped (NPC) converter [41] and its derivatives [42], [43]. In cases where the NPC converters failed to fulfill the application voltage requirements, an improvement was found in the Cascaded H-Bridge (CHB) converter [44] depicted in **Fig. 1.4(a)**. It consists of series connection of cells, each one comprising the 3PH Diode Rectifier (DR) with a Full-Bridge (FB) switching stage attached to it. Owing to the series connection of FB stages, high quality AC voltage waveform can easily be synthesized allowing for the removal of the filters on the machine side [45]. On the other side though, as the voltage across the DC terminals of a DR depends exclusively upon its AC terminal line voltages, stable DC link is obtained within all the cells. With the aim of improving the current spectrum on the multi-winding transformer primary side, its secondaries need to alter the phases of DRs' AC currents (in other words, multi-pulse rectifier is to be obtained). Consequently, rather complex structure of the transformer is needed. It is important, however, that the main role of the multi-winding transformer is not primary voltage scaling, but to ensure independent energy supply to every individual cell. Moreover, such a transformer operates connected to an AC grid, implying that it represents an LFT, which is, in its essence, quite bulky. Lastly, incorporating additional cells into such a structure, with the aim of improving the AC voltage quality even further, requires a new design of the multi-winding transformer. Thus, this topology can not be considered modular.

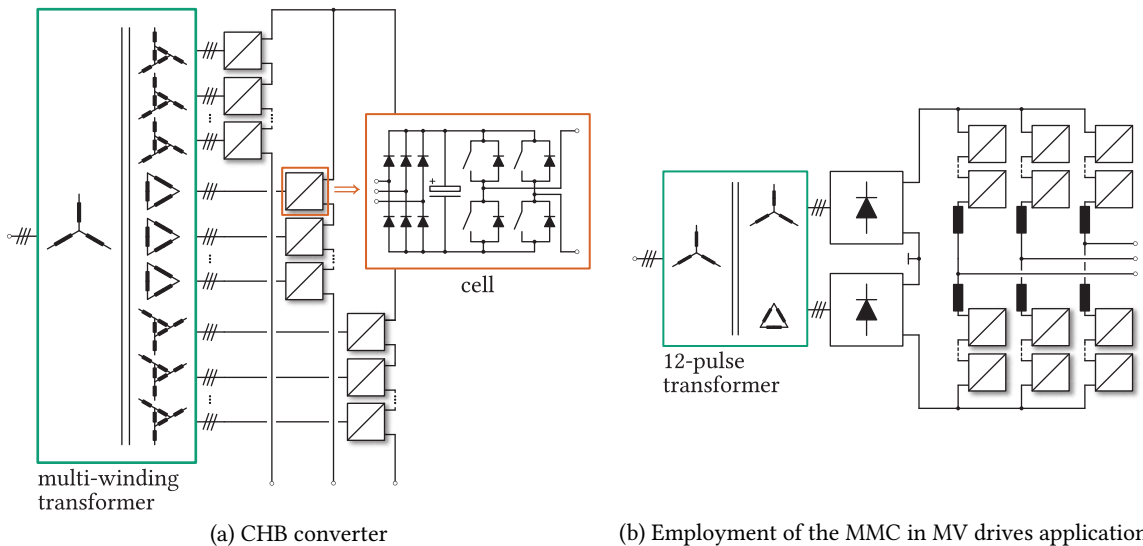


**Fig. 1.4** Possible choices of multilevel topologies for high power MV drives. Please notice that the main difference between the presented topologies refers to the modularity feature. Namely, multi-winding LFT, included on the left, determines the maximum number of switching stages attached to it. On the contrary, MMC allows for addition of the SM into its branches as long as space and control resource requirements are met. Hence, in contrast to the CHB converter, along with the derivatives of the NPC belonging to a set of monolithic converters, the MMC represents a highly modular structure.

When compared to the NPC-based converters [41]–[43], CHB converter features higher installed capacitance demand [45]. The reason for this lies in the fact that every cell produces Single-Phase (1PH) voltage across its terminals, while conducting a sinusoidal current. Therefore, DC link capacitors have to be sized according to the oscillations at twice the critical operating frequency of the drive. Notwithstanding, avoiding the need for a specialized transformer structure can be considered a major improvement in the use of topologies comprising distributed DC links. If, on the other hand, the MMC were to be considered in the span of electric drives applications, one can understand that its advantages are twofold. Firstly, given that MMC SMs represent floating energy sources, the need for ensuring an independent energy supply to each one of them is omitted. Consequently, a specialized multi-winding transformer can be replaced with a simple 12-pulse (or any other arbitrary structure) transformer [46], [47], as presented in **Fig. 1.4(b)**. It is noteworthy that no energy storage in the DC link is required in this case owing to the already achieved distribution of the DC voltage among the MMC SMs. Secondly, increasing the number of AC voltage levels is facilitated taking into account that new design of the converter does not have to be conducted. On the contrary, additional SMs can simply be added to every phase-leg of the converter in case space requirements, defined by such an expansion, are met.

Yet, all the advantages listed above come along with a set of shortcomings revealed in certain operating modes. For instance, it was shown in [48], [49] that the lower the frequency (operation at low speeds, or even standstill, and machine start-up) of the MMC AC currents, the higher the ripple of voltage across its SMs' capacitors. Such an operating mode is normally referred to as the Low Frequency Mode (LFM) in the literature [50]–[54]. In order to accomplish the spectral shift of the low frequency energy oscillations, and thus reduce the converter energy requirements, the use of high-frequency voltage/current injection was proposed. However, in case the additional control measures are not considered during the start-up process, or low speeds, one can conclude that the loads having the quadratic torque (current) vs. mechanical speed (frequency) characteristics can be considered favorable. Additionally, SMs' capacitors require significant amount of space, making the conventional MMC bulkier compared to its counterparts mentioned so far. Altogether, as any other converter, the MMC does not represent an ideal solution within the whole spectrum of possible applications/operating points, so additional control measures must be taken sometimes.

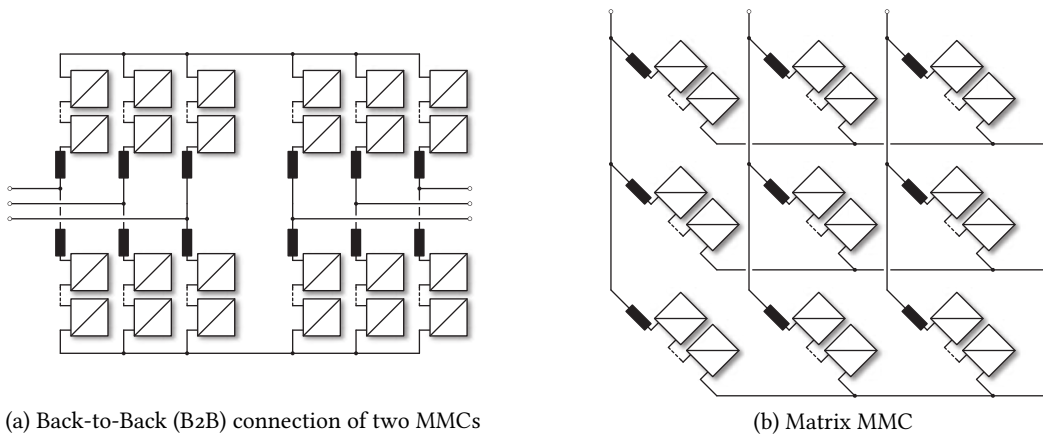


**Fig. 1.5** Two AC-AC MMC-based converters

Further adoption of the MMC-based topologies in the AC-AC conversion domain was evaluated in [55], where the MMC perspectives were analyzed in the Pumped Hydro Storage Power Plants (PHSPs). Two configurations were found suitable for this purpose. One of them, presented in **Fig. 1.5(a)** and referred to as the Indirect MMC, has already enjoyed a lot of success in the HVDC transmission domain. The other one, presented in **Fig. 1.5(b)** essentially represents the structure resembling the matrix converter, hence the name Matrix MMC. Quite often, this topology is also referred to as the Direct MMC since the intermediary rectification is not taking place in the energy conversion process. With respect to the commercial solutions, using either Doubly Fed Induction Machines (DFIMs) or Converter-Fed Synchronous Machines (CFSMs), the MMC-based solutions offer the possibility to operate in the full-speed range, better scalability, the capability of handling DC link short circuits (in case the DC link exists), redundancy, better Fault Ride Through (FRT) performance due to the energy stored in the SMs, etc. However, topologies presented in **Figs. 1.5(a)** and **1.5(b)** suffer from the LFM related drawbacks if used to feed any kind of electrical machine.

To overcome the above mentioned LFM related shortcomings, the use of the Q2L converter was proposed in [56]. In contrast to the conventional MMC, Q2L converter synthesizes its output voltage by relying on the 2LVL PWM principles. However, the existence of series connected SMs, which can also be perceived as a parallel connection of a switch and its active snubber, allows for the voltage generation in the step-wise manner. Consequently, voltage stress imposed upon the machine windings gets significantly reduced. Moreover, a suitable modulation method, as explained in [57], ensures that SMs' voltage oscillations can be compensated over a few PWM periods. As a result, energy storage requirements of the Q2L converter fall significantly below the ones observed in the MMC. As will be explained in the upcoming chapters, MMC utilizes intentionally mounted branch inductors in order to control its internal energy distribution. However, these inductors can be significantly reduced, or even removed, should Q2L converter be employed within a certain span of applications. As branch inductors require a certain volume, their removal can be considered an additional advantage offered by the Q2L converter. It should be emphasized, however, that the Q2L converter was originally proposed with the aim of performing the high-power DC-DC conversion [58], [59] by interfacing two DC grids of different, or the same, voltage levels by means of the Medium Frequency Transformer (MFT). By adjusting the phase-shift between the relevant voltage waveforms, control of the power flow between the stages can be effortlessly achieved. In other words, the configuration described in [58], [59] represents a modified version of the Dual Active Bridge (DAB).

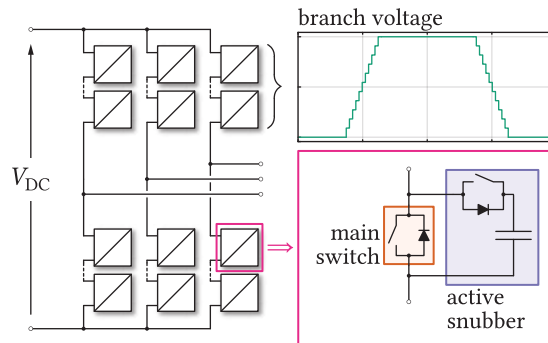


**Fig. 1.6** Quasi Two-Level (Q2L) converter with the typical branch voltage waveform. Please notice that in contrasts to the conventional 2LVL structure presented in **Fig. 1.3(b)**, Q2L converter provides the possibility of step-wise AC voltage generation.



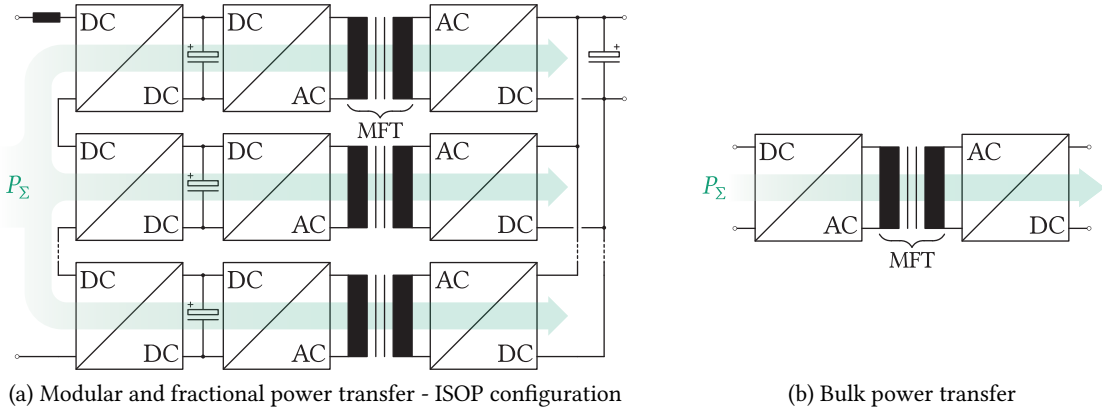


**Fig. 1.7** Two concepts adopted in the high-power MV DC-DC conversion domain

MMC-based 1PH DAB was firstly presented in [60], however, without taking into account the improvements offered by the Q2L converter. Generally, the structures using switching parts, galvanically separated by an isolation stage(s), are also known as the Solid State Transformers (SSTs). Although primarily foreseen in the AC domain [61]–[63], the concept of the SST has also gained a momentum in the DC domain owing to the expectations of the HVDC success being repeated in the MV domain. So far, two concepts, presented in **Fig. 1.7**, have been adopted in the high power MV DC-DC conversion. One possibility of transferring the power between the converter ports assumes the existence of several series/parallel connected isolated stages depending upon the converter's input and output voltage/current specifications [64]–[68]. In other words, connection of stages, each one transferring only a fraction of the total converter power, enables the desired power capability to be achieved in a modular fashion. Input Series Output Parallel (ISOP) configuration, presented in **Fig. 1.7(a)**, can be observed as an example and it is found to be suitable for the connection between a HV/MV and LV networks. With the aim of reducing the converter footprint, each of the isolation stages, being most likely realized as either the 1PH DAB or LLC resonant converter, operates in the medium frequency range. In spite of transferring only a fraction of the total converter power, the isolation of every MFT has to be designed such to withstand full input voltage of the converter. In contrast to fractional power transfer, a concept of bulk power transfer [58]–[60], [69]–[76], presented in **Fig. 1.7(b)**, can be considered. This way, the isolation challenge has to be solved only once, while operation in the medium frequency range can be retained. It is clear that all the configurations utilizing the MMC-based topologies referenced above belong to this group of solutions.

## 1.4 Objectives and contributions of the thesis

The change in the power system structure is anticipated in the near future. From unidirectional, the system is expected to converge towards the so-called omni-directional structure, where local energy production based on the Renewable Energy Sources (RES) represents its inevitable part. Due to alleviated integration and more efficient collection of energy harvested from the RES, wide-spread presence of the system parts operating under DC voltage is highly likely. Since the HVDC grids already exist, and with the Medium Voltage Direct Current (MVDC) grids likely to penetrate into the current system structure, one can conclude that novel converter topologies will be needed to

establish the connections among various parts of the future system. Furthermore, more efficient and flexible utilization of the mainstream RES, for instance hydropower, can be achieved owing to the recent advancements in power electronics.

As already stated, the MMC provides outstanding operational flexibility, scalability, as well as inherent protective features regarding the blocking of the DC link short-circuit currents. Its use has been reported in literally all the conversion schemes (AC-DC, AC-AC, as well as DC-DC). Hence, this thesis focuses on several different topics related to the use of the MMC in the MV domain and its main objectives and contributions can be summarized as:

- Control of the MMC internal energy distribution can be achieved by means of the so-called circulating currents. However, some of the approaches reported in the literature, such as [77], require additional theoretical reinforcements. This thesis fills this gap in a systematical manner.
- What has initially paved the way for the MMC into the field of HVDC conversion was almost unlimited voltage scalability. By stacking the SMs in series, voltage handling, and simultaneously power, capabilities of the converter increase under the constraint of the SM current ratings being unchanged. However, certain applications, such as the above mentioned PHSPs, do not allow an increase in the operating voltage with the aim of extending the power capabilities. As a result, current capacity of the converter supporting an observed application must be increased. Already known solutions to this problem imply the need for various hardware adaptations of the MMC SMs in case current handling requirements of an application are to be met. This thesis, however, provides a thorough explanation on how to extend the MMC power capabilities through paralleling its branches, thus shifting the challenge from the field of hardware to the control domain. In this way, cost-efficient and low engineering effort solutions can be easily obtained. Moreover, paralleling of the MMC branches opens the new set of possibilities regarding the converter design and realization of the AC terminal voltages. These are, for the first time, explained within this thesis.
- It has already been mentioned that one way of extending the power system transmission capacity implies the conversion of the existing AC power lines into DC. However, such a shift is not possible unless suitable converter topologies, providing the necessary interface for realization of a resilient and flexible system, are ready and well mastered. A novel DC-DC converter utilizing the Scott Transformer Connection (STC) is proposed within this thesis as possible means of interfacing a HV/MV bipolar DC grid with another DC grid of different, or the same, voltage level. So far, STC has mostly been employed in the railway applications in order to obtain two sinusoidal voltage supplies out of the symmetrical 3PH voltage source. For that matter, two 1PH transformer units are used. This feature of the STC enables the redundancy concept naturally provided in the bipolar DC grids to be exploited. As no limitation in the STC operating frequency exists in case it is employed as a part of a DC-DC converter, operation in the medium frequency range is possible. Therefore, the unprecedented use of the STC in the domain of high-power DC-DC conversion, along with its use in the medium frequency range, can be outlined as one of the original contributions of this thesis.
- Even though the operating and modulation principles of the Q<sub>2</sub>L converter were thoroughly explained in [58], [59], the fundamentally important current drift between the converter branches, occurring during the voltage transition process, has never been theoretically supported. SM capacitance sizing rules were provided, however, under the very strong assumptions which

were questioned throughout one chapter of this thesis. Here, the equations describing the above mentioned current drift, which provide the means for the correct SM capacitor sizing, were derived in a systematic way. As a result, almost 40% reduction in the converter energy requirements can be achieved when compared to the design guidelines provided in [58], [59].

## 1.5 Outline of the thesis

This thesis is organized in two parts and eight chapters. The first part covers general modeling, control and modulation principles of the MMC, along with its employment in the applications requiring DC-AC conversion. The second part, on the other hand, presents the application of the MMC in the DC-DC conversion area. Therefore,

- **Chapter 2** deals with the basic modeling of the conventional MMC. Through identification of the AC and DC side equivalent circuits, control of the converter's relevant currents is derived.
- **Chapter 3** discusses the need and the methods for energy balancing of the MMC-based circuits. Several common approaches analyzed in the literature so far are presented, with the clear differences among them being outlined.
- **Chapter 4** provides a thorough insight into the possibility of expanding the MMC power capabilities by paralleling its branches. The need and derivation of an additional control layer, ensuring equal energy split among the parallel branches, is explained in detail.
- **Chapter 5** covers the additional degrees of freedom, from the voltage modulation standpoint, offered by the MMC operating with paralleled branches. The analysis was conducted in case Phase Shifted Carrier (PSC) modulation is used. Nevertheless, the other carrier-based modulation schemes can be analyzed in a similar manner.

The second part of the thesis is organized as follows.

- **Chapter 6** presents high-power MMC-based DC-DC converter utilizing the STC. Starting from seemingly logical solution, possibly used to provide the flexible interconnection between a bipolar HVDC/MVDC grid with another DC grid of a random voltage level, the analyzed topology is derived. As the proposed topology provides the possibility to operate in both bidirectional and unidirectional modes, this chapter covers only bidirectional mode of operation.
- **Chapter 7** discusses unidirectional high-power MMC-based DC-DC converter utilizing the STC. As the operating principles are slightly changed with respect to its bidirectional counterpart, this chapter covers it in detail.
- **Chapter 8** provides a comprehensive mathematical approach to analysis of the behavior of the Q2L converter during the step-wise voltage transition periods. Although occurring in the discrete time steps, voltage transitions are described in the continuous domain, thus alleviating the process of sizing the SM capacitance.

## 1.6 List of publications

### Patents:

- P1. Y. Park, S. Ryu, S. Kim, S. Kim, **S. Milovanović**, and D. Dujić, *Power converting apparatus having Scott Transformer*, Korean app. no: KR2018/0050472, Priority date : 2018-05-02.
- P2. Y. Park, S. Ryu, S. Kim, S. Kim, **S. Milovanović**, and D. Dujić, *Power converting apparatus having Scott Transformer*, International app. no: PCT/KR2019/005262, Publication date : 2019-11-07.

### Journal papers:

- J1. **S. Milovanović** and D. Dujić, “High-power DC-DC converter utilising Scott transformer connection,” *IET Electric Power Applications*, 2019
- J2. **S. Milovanović** and D. Dujić, “Comprehensive design and analysis of the quasi two-level converter leg,” *CPSS Transactions on Power Electronics and Applications (CPSS TPEA)*, 2019
- J3. **S. Milovanović** and D. Dujić, “Extending power capacity of modular multilevel converter through branch paralleling (*under review*),” *IEEE Power Electronics Magazine*, 2020
- J4. **S. Milovanović** and D. Dujić, “Comprehensive spectral analysis of pwm waveforms with compensated dc-link oscillations (*under review*),” *IEEE Transactions on Power Electronics*, 2020

### Conference papers:

- C1. **S. Milovanović** and D. Dujić, “Six-step MMC-based high power DC-DC converter,” in *2018 International Power Electronics Conference (IPEC-Niigata 2018-ECCE Asia)*, IEEE, 2018, pp. 1484–1490
- C2. **S. Milovanović** and D. Dujić, “MMC-based high power DC-DC converter employing Scott transformer,” in *PCIM Europe 2018; International Exhibition and Conference for Power Electronics, Intelligent Motion, Renewable Energy and Energy Management*, 2018, pp. 1–7
- C3. **S. Milovanović** and D. Dujić, “Unidirectional high power DC-DC converter utilizing Scott transformer coconnection,” in *10th International Conference on Power Electronics – ECCE Asia (ICPE 2019-ECCE Asia)*, 2019, pp. 1–8
- C4. **S. Milovanović** and D. Dujić, “On facilitating the modular multilevel converter power scalability through branch paralleling,” in *2019 IEEE Energy Conversion Congress and Exposition (ECCE)*, 2019, pp. 1–8
- C5. M. Basić, **S. Milovanović**, and D. Dujić, “Comparison of the two modular multilevel converter internal energy balancing methods,” in *20th International Symposium POWER ELECTRONICS (EE 2019)*, 2019, pp. 1–8
- C6. M. Utvić, **S. Milovanović**, and D. Dujić, “Flexible medium voltage DC source utilizing series connected modular multilevel converters,” in *EPE 2019 - 2019 20th International Scientific Conference on Electric Power Engineering (EPE)*, 2019, pp. 1–8

- C7. **S. Milovanović** and D. Dujić, "Spectral analysis of the modular multilevel converter operated with parallel branches and phase-shifted carriers," in *2020 IEEE 9th International Power Electronics and Motion Control Conference (IPEMC2020-ECCE Asia)*, 2020

Tutorials:

- T1. D. Dujić, A. Christe, and **S. Milovanović**, "MMC-based converters for MVDC applications," 12-th International Symposium on Industrial Electronics - INDEL 2018, Banja Luka, Bosnia and Herzegovina, 2018
- T2. D. Dujić, A. Christe, and **S. Milovanović**, "MMC-based converters for MVDC applications," 21st European Conference on Power Electronics and Applications - EPE, Genova, Italy, 2019
- T3. D. Dujić and **S. Milovanović**, "MMC-based converters for MVDC applications," 20th International Symposium POWER ELECTRONICS (EE 2019), Novi Sad, Serbia, 2019
- T4. D. Dujić and **S. Milovanović**, "MMC-based converters for MVDC applications," *accepted for PCIM Asia 2020*; International Exhibition and Conference for Power Electronics, Intelligent Motion, Renewable Energy and Energy Management, Shanghai, China, 2020



# 2

## Dynamic Modeling and Basic Operating Principles of the Modular Multilevel Converter

*This chapter presents the averaged dynamic modeling of the modular multilevel converter. Starting from the submodule, which represents the converter's basic building block, the need for the chosen modeling approach is explained in detail. Aggregation of the state-space equations describing the converter's branch is presented, allowing for the simple representation being independent on the number of submodules installed within the converter. Basic operating principles of the modular multilevel converter are explained and followed by the discussion on the range of feasible operating voltages depending on the type of submodules used to realize the converter. All the other chapters, addressing specific applications and control of the modular multilevel converter, rely on the modeling framework presented hereunder.*

### 2.1 General considerations

As discussed in the introductory part of this thesis, many different solutions have been proposed in the high-power HV/MV domain. These rely either on series connection of semiconductor devices in the standard 2LVL VSCs, the use of monolithic topologies such as the NPC converter, approaches introduced with the advent of the CHB converter or truly modular principles allowed by the MMC. A set of overviews concerning conventionally employed multilevel topologies can be found in [78]–[80]. Nevertheless, in contrast to the monolithic converters, which operate using the concentrated DC links, the MMC makes use of a different approach assuming distributed voltage among the converter's basic building blocks. Consequently, rather unique modeling and control principles need to be considered.

The MMC provides the possibility for operation in the HV/MV domain by means of stacking the SMs, also quite often referred to as cells, in series, as presented in **Fig. 2.1**. Since the SMs represent floating energy sources, there is no need for ensuring an individual external supply for each one of them. Consequently, limitless voltage scalability can be achieved and considered the main commodity offered by the MMC. In other words, if extension of the converter's operating voltage range were to be necessary at a certain point, additional SMs could be added into the existing structure without the need of undergoing any converter redesign procedures. According to **Fig. 2.1**, a cluster of SMs in series connection with an inductor  $L_{br}$  will henceforth be referred to as branch, whereas two branches comprise the leg.

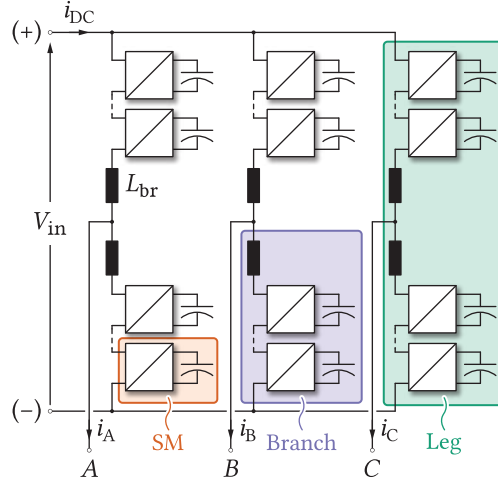


**Fig. 2.1** Modular multilevel converter schematics with its key elements being labeled and highlighted

As a basic building block of the MMC, the SM can be found in various configurations [81]. However, Half-Bridge (HB) and FB SMs, depicted in **Figs. 2.2(a)** and **2.2(b)**, respectively, are the ones being considered basic and therefore used most commonly. Hence, these are the only SMs being considered throughout this thesis. Nevertheless, the choice of the considered SM type will be clearly stated in case an analyzed application requires it.

Semiconductor devices within an HB SM operate in the complementary mode, i.e. when the upper switch ( $S_1$ ) is turned on, the lower switch ( $S_2$ ) must be turned off, and vice versa. **Fig. 2.2(a)** presents all the states an HB SM can be brought into (please notice that a power switch "on" state was denoted by logic '1', whereas "off" state was denoted by logic '0'). When the upper switch of an SM is turned on, the SM is said to be inserted, whereas it is said to be bypassed when the lower switch is turned on. There is the third state, named idle, where both switches are turned off, with the SM voltage  $V_{SM}$  being determined by the direction of an observed branch current  $i_{br}$ . It is noteworthy, however, that state considering both switches being in the "on" state must be avoided, since it results in a short circuit over the SM capacitor, leading to large over-currents with undoubtedly detrimental effect upon the semiconductor devices.

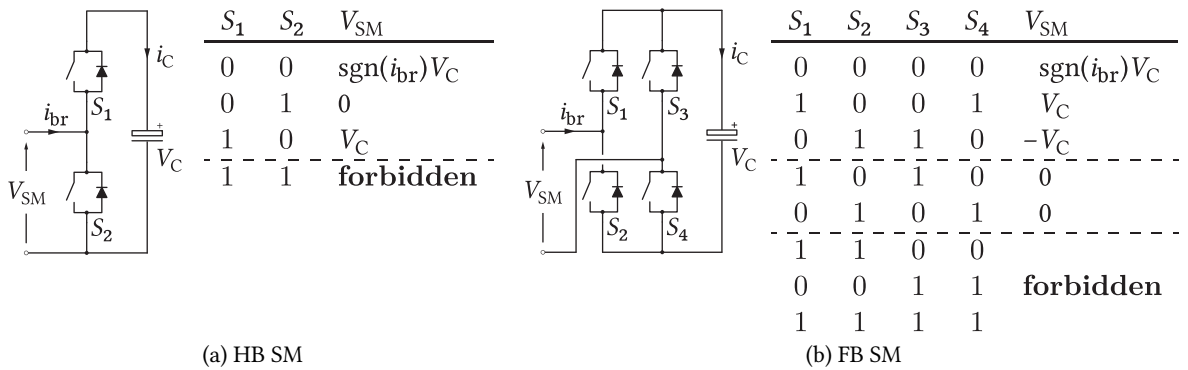


**Fig. 2.2** Basic SM configurations and possible states they can be found in. Please notice that all the SMs belonging to a same branch share the same current at the AC terminals, hence  $i_{SM} = i_{br}$ .



Compared to an HB SM, an FB SM can produce three different voltage levels ( $\pm V_C$  and 0) across its terminals in case suitable switching pattern is employed. It is noteworthy that the possibility of generating negative voltages represents the key difference compared to its HB counterpart. However, the number of switching devices in the conduction path is increased, leading to higher conduction losses compared to an HB SM. **Fig. 2.2(b)** presents all the states an FB SM can be brought into. Since the number of semiconductor devices is four, an FB cell can be found in sixteen different states. However, only the sensible ones were listed in **Fig. 2.2(b)**. Again, one can observe that forbidden states, implying short-circuiting of the SM capacitor, exist. In contrast to an HB SM, there are three forbidden states due to an increased number of the switching devices mounted within the SM.

Generally, the voltage across an SM's terminals can be expressed as

$$V_{SM} = n_{SM} V_C, \quad (2.1)$$

where  $n_{SM}$  denotes the SM's switching function. In other words,  $n_{SM}$  does not take into account the idle states. It is obvious that values of this function correspond to the states listed in **Figs. 2.2(a)** and **2.2(b)**, therefore

$$n_{SM} = \begin{cases} \text{sgn}(V_{SM}), & V_{SM} \neq 0 \\ 0, & V_{SM} = 0 \end{cases} \quad (2.2)$$

Using the similar reasoning, a change in the SM capacitor voltage can be described as

$$C_{SM} \frac{dV_C}{dt} = i_C = n_{SM} i_{br} \quad (2.3)$$

From (2.3), one can conclude that whenever an SM gets inserted, charging of its capacitor depends on the branch current direction. For instance, if an HB SM is inserted, with the branch current being positive, its capacitor voltage slope is positive, meaning that charging process occurs. On the other hand, if the same SM is bypassed, there should be no change in the voltage across its capacitor. It is noteworthy that this represents only a theoretical case given that additional circuits, such as protection and logic circuits, which are normally supplied from the SM capacitor and are not in the focus of this analysis, consume a certain amount of energy even when an SM gets bypassed. Additionally, the SM capacitor leakage current causes a certain amount of losses, regardless of the state the SM is found in.

An important detail in the analysis of the MMC is that each one of its SMs represents an independent structure. Moreover, the capacitor, which is an energy storing element, represents its mandatory part. Strictly speaking, if the MMC analysis was conducted in the state-space, an equation having the form of (2.3) would have to be written for every SM. As the number of SMs mounted within the converter can be quite high, the order of the system describing the MMC would make the analysis extremely tedious, difficult and, above all, not intuitive. Therefore, the need for different analysis and subsequent modeling approach arises.

## 2.2 Averaged dynamic model of the MMC

To reduce the order of the MMC's state-space model, a set of approximations leading to the aggregation of equations on the branch level can be made. Despite the SM representing the basic building block of the analyzed converter, it is actually the cluster of SMs which has the main role in the energy conversion process. Hence,  $N$  series connected SMs can be analyzed instead of observing each of the SMs individually. The voltage across such a string can be expressed as

$$v_{br} = \sum_{i=1}^N n_{SM,i} V_{C,i} \quad (2.4)$$

Firstly, the existence of a control algorithm, maintaining all the SMs' voltages within a predefined band, is assumed. Consequently, one can claim that  $V_{C,i} \approx V_C^*$ . For now,  $V_C^*$  will be assumed to consist exclusively of a DC component. Nonetheless, the next chapter will point out the effects being neglected by this approximation. Further, as there is  $N$  series connected SMs per branch, a total branch voltage defined as  $v_{br\Sigma} = NV_C^*$  can be substituted into (2.4), leading to

$$v_{br} \approx \left( \frac{1}{N} \sum_{i=1}^N n_{SM,i} \right) v_{br\Sigma} \quad (2.5)$$

In the above equation,  $\sum_{i=1}^N n_{SM,i}$  represents a function whose values change in time steps not being necessarily equidistant. Nevertheless, the number of SMs per branch is normally sufficiently high to claim that the term  $\frac{1}{N} \sum_{i=1}^N n_{SM,i}$  can be considered continuous. Henceforth, this quantity, denoted by  $m$ , will be referred to as the insertion index given that it provides a clear image of the fraction of total number of SMs being inserted within an observed branch. Accordingly, (2.5) can be rearranged as

$$v_{br}(t) \approx m(t) v_{br\Sigma} \quad (2.6)$$

Consequently, a branch can be modeled with the series connection of the branch inductor and a voltage source, as presented in **Fig. 2.3**.

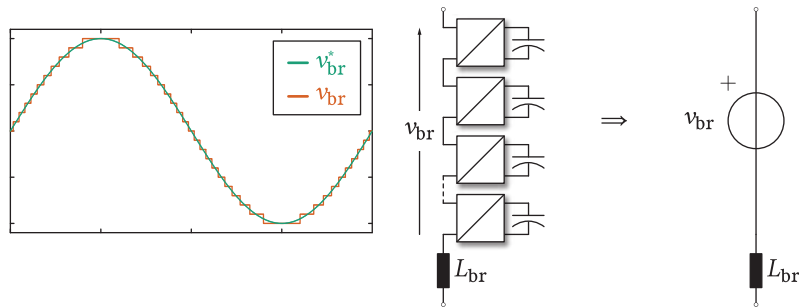


**Fig. 2.3** The process of averaging the voltage across the cluster of SMs

As the voltage source used to model the string of SMs is not ideal but rather controlled by the insertion index, the above analysis can be extended further by inspecting the dynamics of the branch total voltage. Summing the expression (2.3) for all the SMs within the branch gives

$$C_{SM} \sum_{i=1}^N \frac{dV_{C,i}}{dt} = i_{br} \sum_{i=1}^N n_{SM,i} \quad (2.7)$$

Dividing both sides of (2.7) by  $N$ , while keeping in mind that  $\sum_{i=1}^N V_{C,i} = v_{br\Sigma}$ , leads to

$$\begin{aligned} \frac{C_{SM}}{N} \frac{dv_{br\Sigma}}{dt} &= \left( \frac{1}{N} \sum_{i=1}^N n_{SM,i} \right) i_{br} \\ &= m(t) i_{br} \end{aligned} \quad (2.8)$$

According to the above expression, it can be concluded that a branch, as an element having the possibility to store the energy, can also be perceived through a circuit consisting of an equivalent capacitor  $C_{br\Sigma} = C_{SM}/N$  fed by the current source also controlled by the insertion index. Dividing the SM capacitance by  $N$ , in order to obtain the so-called branch equivalent capacitance, symbolizes that the SMs are indeed connected in series. Finally, expressions (2.6) and (2.8) can be combined to form the branch dynamic averaged model presented in **Fig. 2.4**. Unless specified otherwise, the use of the branch model presented bellow will be assumed during all the analysis carried out within this thesis.

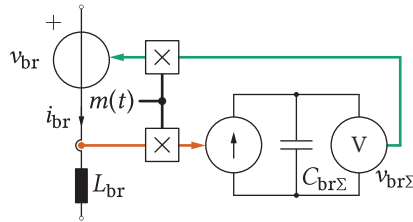


**Fig. 2.4** Averaged model of the MMC branch

To a certain extent, the branch, alike the SM, represents a floating energy source. Unless being taken care of, the branch energy could diverge from its setpoint for various reasons, making the operation of the converter unstable. As will be demonstrated in the upcoming sections, the model presented in **Fig. 2.4** can be successfully used to provide an intuitive insight into the methods used to balance the energy distribution throughout the MMC. It is worth noticing that energy balancing, observed through an averaged branch model, does not take distribution of the total branch energy among the SMs into account. This task belongs to an additional control layer, which will be discussed shortly. Notwithstanding, prior to commencing any energy balancing discussions, the basic operating principles and derivation of the MMC's equivalent circuits should be clarified.

### 2.3 MMC operating principles

A convenient way of commencing the analysis of the MMC operating principles can be found in the observation of a single converter leg, presented in **Fig. 2.5**. As illustrated in the figure below, each leg comprises two DC terminals, (+) and (-), and one AC terminal, labeled with A without the loss of generality. It is assumed that a point of the reference potential, labeled with 0, with respect to which the positive and negative DC terminals of the leg share the input voltage  $V_{in}$  equally, exists. Thereafter, to obtain the results in a general form, coupling of the branch inductors, where  $k$  denotes the coupling factor, is taken into consideration. Please notice that negative values of the coupling factor indicate the dots being positioned in the opposite ends of the inductors.

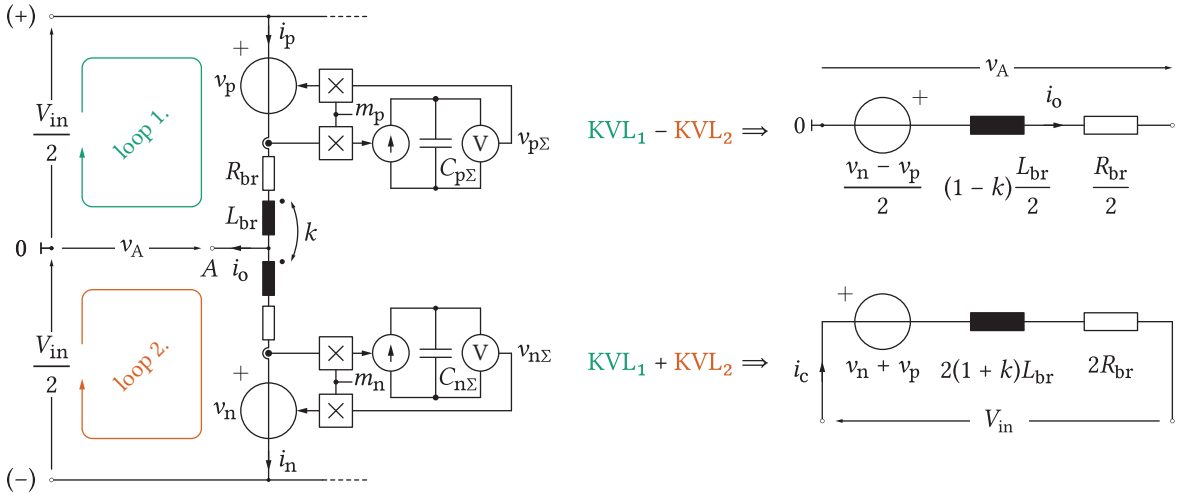


**Fig. 2.5** MMC leg presented by means of the averaged branch model developed in the previous section. Setting up a proper system of equations reveals decoupled control of the leg current components through the equivalent circuits presented on the right-hand side of this figure.

It is straightforward to notice that two equations can be formed within the circuit depicted above according to the Kirchhoff Voltage Law (KVL), giving

$$\frac{V_{in}}{2} = v_p + L_{br} \frac{di_p}{dt} + R_{br} i_p + k L_{br} \frac{di_n}{dt} + v_A \quad (2.9)$$

$$\frac{V_{in}}{2} = v_n + L_{br} \frac{di_n}{dt} + R_{br} i_n + k L_{br} \frac{di_p}{dt} - v_A \quad (2.10)$$

Subtraction and addition of (2.9) and (2.10), respectively, provides (2.11) and (2.12) from which one can notice that two independent control quantities can be established for each leg.

$$(1 - k) \frac{L_{br}}{2} \frac{d}{dt} \left( i_p - i_n \right) + \frac{R_{br}}{2} (i_p - i_n) = \frac{v_n - v_p}{2} - v_A \quad (2.11)$$

$$2(1 + k) L_{br} \frac{d}{dt} \left( \frac{i_p + i_n}{2} \right) + 2 R_{br} \frac{i_p + i_n}{2} = V_{in} - (v_p + v_n) \quad (2.12)$$

Namely, according to the Kirchhoff Current Law (KCL) written for node A, the difference between the upper and the lower branch current corresponds to the leg AC terminal current (2.13). From (2.11), one can conclude that this current can be affected through the adjustment of the difference between the lower and the upper branch voltage. As suggested by (2.12), an average of the currents flowing through the branches comprising an observed leg (2.14) can be controlled by means of the sum of voltages created jointly by them. The leg current component defined by (2.14) has been named differently within the literature so far. Although known to some as the circulating current, throughout this thesis, this current will be referred to as the leg common-mode current given that circulating currents will be given another connotation, as will be explained in the upcoming chapters.

$$i_o = i_p - i_n \quad (2.13)$$

$$i_c = \frac{i_p + i_n}{2} \quad (2.14)$$

Solving the above system enables a different perception of the branch currents. According to (2.15) and (2.16), a branch current can be expressed through a suitable combination of the leg common-mode and AC terminal currents, which is visualized in **Fig. 2.6**.

$$i_p = i_c + \frac{i_o}{2} \quad (2.15)$$

$$i_n = i_c - \frac{i_o}{2} \quad (2.16)$$

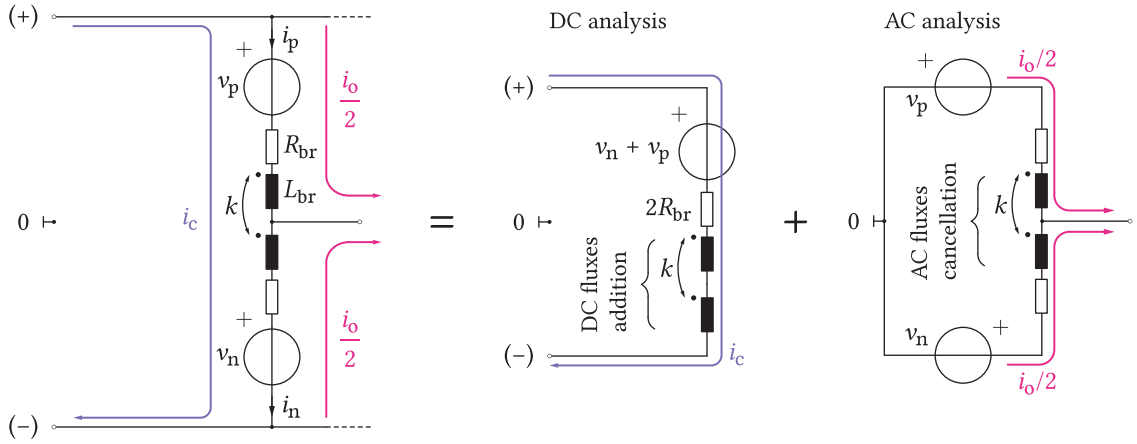


**Fig. 2.6** Illustration of the MMC leg current components

In the multi-phase MMC, AC terminal currents sum up to zero under normal operating conditions. Consequently, it is only the leg common-mode currents that enter the MMC DC link. For this reason the term "circulating" was avoided in the process of naming this current component (common-mode currents leave the converter without circulating inside of it). Similarly, the leg-common mode current can not enter the AC terminal, leading to the conclusion that decoupled analysis of the leg relevant current components can be conducted. A set of remarks, logically aligned with (2.11) and (2.12), can be made through the analysis of **Fig. 2.6**.

Observed from the leg AC terminal, two branches comprising it operate in parallel, which can be anticipated from (2.11), where division of the branch impedance by two is present. Additionally, the direction of the branch inductors coupling, combined with the directions of the leg AC currents, suggests the cancellation of AC fluxes inside the branch inductors' cores. Hence, the equivalent inductance seen from the leg AC terminal must be further reduced by the factor of  $\alpha = 1 - k$ . Similar reasoning can be applied to the analysis of the MMC leg DC circuit. Seen from the DC link, AC components of the branches' currents cancel each other out, therefore, from the leg common-mode current standpoint, the two branches operate in series. Consequently, multiplication of branch impedances by two can be observed in (2.12). Nonetheless, in this case, the fluxes originating from the common-mode current support each other, therefore, equivalent inductance of the leg, seen from the converter's DC terminals, needs to be further increased by the factor of  $\beta = 1 + k$ . Introducing the leg differential and common-mode voltage components as (2.17) and (2.18), respectively, allows (2.11) and (2.12) to be rewritten as (2.19) and (2.20).

$$v_s = \frac{v_n - v_p}{2} \quad (2.17)$$

$$v_c = \frac{v_n + v_p}{2} \quad (2.18)$$

$$\alpha \frac{L_{br}}{2} \frac{di_o}{dt} + \frac{R_{br}}{2} i_o = v_s - v_A \quad (2.19)$$

$$2\beta L_{br} \frac{di_c}{dt} + 2R_{br} i_c = V_{in} - 2v_c \quad (2.20)$$

Please notice that the above analysis was conducted taking into account only a single MMC leg. However, as this chapter focuses on the conventional 3PH MMC, two equivalent circuits concerning the decoupled control of the MMC AC and DC side quantities can be formed, as presented in **Fig. 2.7**. According to **Fig. 2.7(a)**, seen from the AC side, the MMC does not differ from any conventional 3PH VSC, hence already known control principles can be employed. As for the DC side equivalent circuit, a special attention must be devoted to it as its improper treatment gives rise to the operation instabilities. In brief, these two circuits are the heart of all the analyses concerning the 3PH MMC.

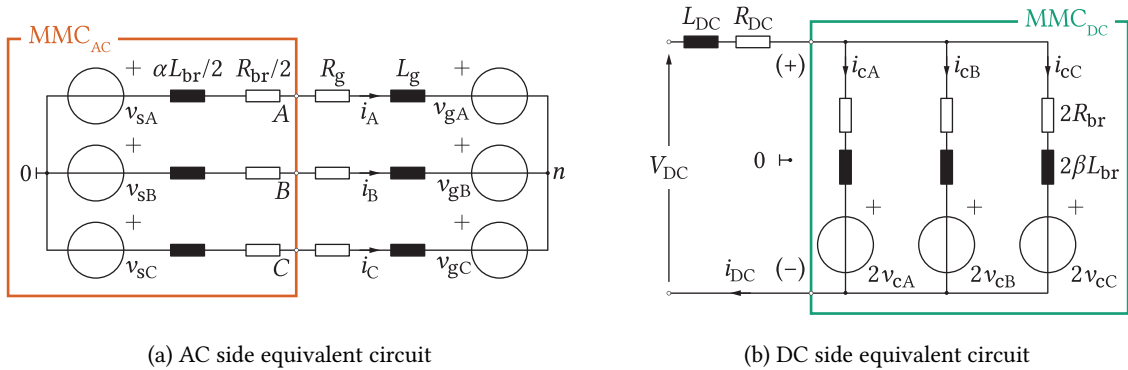


**Fig. 2.7** 3PH MMC equivalent circuits obtained through the analysis of a single MMC leg current components

Once the leg differential and common voltage references ( $v_s^*$  and  $v_c^*$ , respectively) are determined by the appropriate control layers, the voltage reference passed to every branch can be calculated by solving the system comprising the equations (2.17) and (2.18), which provides one with

$$v_p = v_c^* - v_s^* \quad (2.21)$$

$$v_n = v_c^* + v_s^* \quad (2.22)$$

However, to produce branch voltages corresponding to the calculated references, number of inserted SMs per every branch needs to be decided. As already stated, the insertion index provides an image of the number of inserted SMs per branch. Hence, combining (2.6) with (2.21) and (2.22) yields

$$m_p = \frac{v_c^* - v_s^*}{v_{p\Sigma}} \quad (2.23)$$

$$m_n = \frac{v_c^* + v_s^*}{v_{n\Sigma}} \quad (2.24)$$

In case carrier-based modulation schemes are used to synthesize the reference voltages across the SMs terminals, the insertion index can be perceived as the modulation index. The range of  $m_{\{p/n\}}$  can be said to depend on the type of the SM used to build the converter. However, prior to extending on this statement, the analysis regarding the level to which the branches are charged, followed by the discussion on the range of viable operating voltages, must be conducted.

For the moment, the use of HB SMs within the MMC operating as an inverter will be assumed, while adopting the notation from **Fig. 2.7(b)**. It is straightforward to conclude that minimum and maximum voltages that a branch of such a converter can synthesize equal 0 and  $v_{br\Sigma}$ , respectively. For an arbitrary value of a leg common-mode voltage component  $v_c$ , feasible differential-mode voltage amplitude  $\hat{v}_s$  gets constrained by the above mentioned limitations in the branch voltage capacity generation, as can be observed from an example provided in **Fig. 2.8(a)**. In the presented case, voltage components of an observed branch were normalized with respect to its total voltage  $v_{br\Sigma}$ . **Fig. 2.8(a)** can be used to mathematically formulate the constraint analyzed within this paragraph as (2.25)

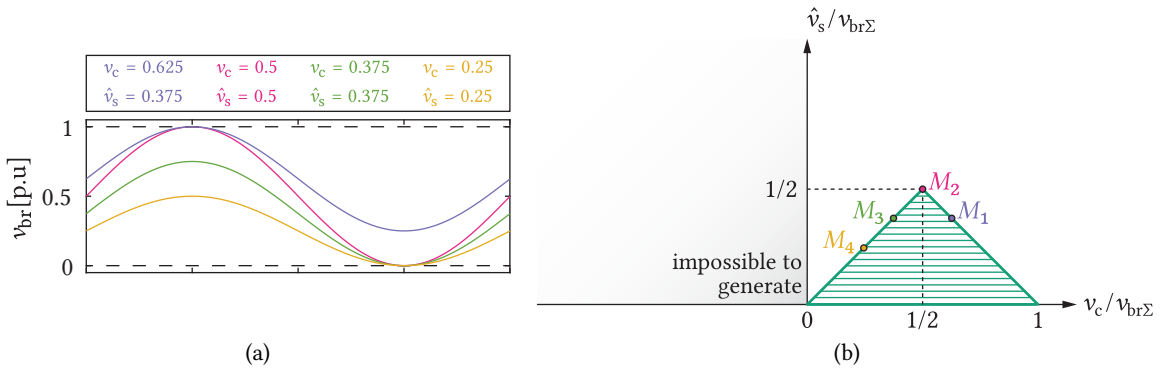


**Fig. 2.8** (a) An example depicting the limitation in the feasible AC voltage generated with a branch utilizing the HB SMs; (b) Graphical representation of the equation describing the analyzed limitation;

$$\hat{v}_s = \frac{v_{br\Sigma}}{2} - \left| v_c - \frac{v_{br\Sigma}}{2} \right|, \quad (2.25)$$

where

$$\left| v_c - \frac{v_{br\Sigma}}{2} \right| = \begin{cases} v_c - \frac{v_{br\Sigma}}{2}, & v_c \geq \frac{v_{br\Sigma}}{2} \\ -v_c + \frac{v_{br\Sigma}}{2}, & v_c < \frac{v_{br\Sigma}}{2} \end{cases} \quad (2.26)$$

Through graphical representation of the above expression, provided in **Fig. 2.8(b)**, several important conclusions can be made. Firstly, one can notice that all the points falling inside the striped area, whose edges actually represent the boundary cases operation-wise (2.25), can be freely synthesized. Notwithstanding, the highest level of flexibility, along with the best utilization of the total branch voltage, can be ensured in case  $v_c = v_{br\Sigma}/2$ . Further, MMC common-mode currents should ideally contain only the DC component. Consequently, observing the **Fig. 2.7(b)**, leads to the logical assumption that  $v_c \approx V_{DC}/2$  once the steady state is reached. This indicates that every branch within the MMC can be charged such that  $v_{br\Sigma} = V_{DC}$ . However, a certain margin is normally adopted in practice in order to provide the means for the converter's DC link current control and balancing of the internal energies. Control of these quantities is left to be addressed in the next chapter.

It is noteworthy that **Fig. 2.8** assumes the permanent operation of the converter at one of the points labeled on its right-hand side. Therefore, if the converter were to operate at the point labeled with  $M_2$ , the maximum amplitude of the line voltage generated across its AC terminals can not exceed the voltage at which its branches are charged. It is important to emphasize that the above mentioned amplitude refers only to the fundamental harmonic of the generated voltage. Similar property characterizes the family of monolithic converters, which can be perceived as buck converters since their line voltage maximum can not reach any value higher than the concentrated DC link voltage. In contrast to the monolithic converters, the MMC utilizing the HB SMs exploits distributed DC links, nevertheless, it can as well be classified as the converter of the buck-type owing to the previously stated reasons.

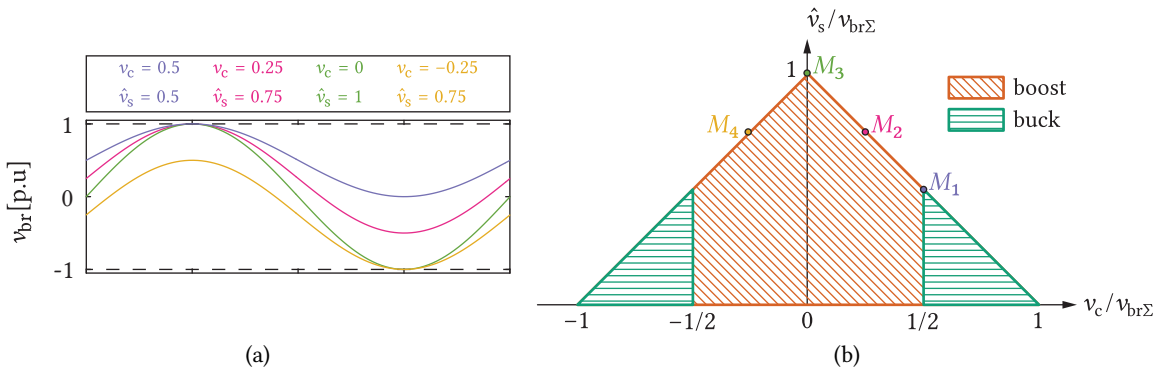


**Fig. 2.9** (a) An example depicting the limitation in the feasible AC voltage generated with a branch utilizing the FB SMs; (b) Graphical representation of the equation describing the analyzed limitation;



A similar analysis can be conducted in case FB SMs are employed to realize the MMC of the desired ratings. **Fig. 2.9(a)** provides an example, which can be used to describe the voltage generation capabilities of a branch using the FB SMs as

$$\hat{v}_s = v_{br\Sigma} - |v_c|, \quad (2.27)$$

where

$$|v_c| = \begin{cases} v_c, & v_c \geq 0 \\ -v_c, & v_c < 0 \end{cases} \quad (2.28)$$

Comparison of **Figs. 2.8(b)** and **2.9(b)** indicates that the MMC utilizing FB SMs features the possibility of generating negative DC voltages across its terminals, making its area of operation wider compared to its counterpart using the HB SMs. However, this comes at cost of increased converter conduction losses (since more devices are introduced into the branch current path), increased silicon area and, most importantly, the converter cost. The highest obtainable AC voltage corresponds to the branch total voltage under the assumption of no DC voltage being generated by the branches. Nevertheless, this case is very unlikely to represent the converter's normal operating mode since no power transfer occurs between its ports.

Hence, the analysis of the range of converter's operating voltages can commence by assuming that  $v_c = v_{br\Sigma}/2$ . On these terms,  $v_{br\Sigma} = V_{DC}$  must be fulfilled if the steady state value of the leg common-mode voltage component is to match half the DC voltage of the grid the MMC is connected to. This operating point was labeled with  $M_1$  in **Fig. 2.9(b)**. Also,  $\hat{v}_s^{(M_1)} = v_{br\Sigma}^{(M_1)}/2$ , which corresponds to the boundary operating point of the MMC utilizing the HB SMs. Steady state operation on the left of this point, with the constraint defined by  $v_c \in (0, v_{br\Sigma}/2]$ , implies the need for charging the MMC branches to the voltage higher than  $V_{DC}$ , as demonstrated in (2.29).

$$\begin{aligned} v_c &= \underbrace{k_1}_{<1} \frac{v_{br\Sigma}}{2} = \frac{V_{DC}}{2} \\ \Rightarrow v_{br\Sigma} &= \underbrace{\frac{V_{DC}}{k_1}}_{>V_{DC}} \end{aligned} \quad (2.29)$$

For example, within the converter permanently operating in the point labeled with  $M_2$  in **Fig. 2.9(b)**, the branches should be charged to the voltage equal to  $2V_{DC}$  (since  $k_1 = 1/2$ ). Substituting  $v_c$  defined in (2.29) into (2.27) indicates that the maximum leg differential-mode voltage amplitude equals

$$\hat{v}_s = \frac{2 - k_1}{2} v_{br\Sigma} \quad (2.30)$$

In this case, the maximum amplitude of the converter's line voltage can be calculated as

$$\begin{aligned}\hat{v}_{s,\text{line}} &= \frac{2 - k_1}{2} \frac{2}{\sqrt{3}} \sqrt{3} v_{\text{br}\Sigma} \\ &= (2 - k_1) v_{\text{br}\Sigma}\end{aligned}\tag{2.31}$$

According to (2.31), the maximum amplitude of the line voltage in case the converter operates in the area defined by  $v_c \in (0, v_{\text{br}\Sigma}/2]$  exceeds the voltage the branches are charged to. Therefore, it is said that the MMC operated with FB SMs achieves the boost of its AC voltage, however, at the price of charging its branches to the voltage higher compared to the voltage of the DC grid it is connected to.

Similar analysis can be conducted using (2.29) and (2.31), however, considering the region defined by  $v_c \in (v_{\text{br}\Sigma}/2, v_{\text{br}\Sigma}]$ . On these terms, the converter branches need to be charged to the voltage lower than  $V_{\text{DC}}$  (since  $k_1 > 1$ ), however, with the line voltage amplitude satisfying  $\hat{v}_{s,\text{line}} < v_{\text{br}\Sigma}$ . In other words, the transition from boost to buck region takes place, as indicated in **Fig. 2.9(b)**. Moreover, due to the symmetry of the function given by (2.27), all the conclusions made in case of the branch common-mode voltage taking positive values can be replicated to the negative part of the  $v_c$  axis. Irrespective of the type of employed SMs, a branch modeled according to **Fig. 2.4** contains an equivalent capacitor whose voltage can be implicitly controlled through its energy adjustments. Consequently, the importance of the total branch voltage determination is revealed.

As stated above, a branch consisting of HB SMs can generate voltages ranging from zero to its total voltage. Thus, insertion indices in this case can take the values falling in the range defined in (2.32). In contrast to such a type of the MMC, its counterpart employing the FB SMs features the extended operating range, taking also the negative voltages into account. Therefore, (2.33) provides a seemingly logical choice of the modulation indices range.

$$m_{\text{p/n}}^{(\text{HB})} \in [0, 1]\tag{2.32}$$

$$m_{\text{p/n}}^{(\text{FB})} \in [-1, 1]\tag{2.33}$$

## 2.4 Summary

The analysis of the conventional 3PH MMC can be conducted in a decoupled manner, as suggested by the previously derived AC and DC equivalent circuits. The leg differential-mode voltage controls the AC terminal current, whereas adjustments of the common-mode voltage result in the control of the leg common-mode current. As the common-mode currents enter the DC link, the role of the legs' common-mode voltage components in the control of power transferred towards the converter DC terminal becomes evident. To synthesize the desired voltage references within all of the converter's branches, proper selection of the modulation indices must be determined.

Nevertheless, correct setting of the branch voltage references has not been discussed so far. Moreover, as branches represent floating energy sources, unless proper control actions are undertaken, there is no guarantee that the amount of energy stored within them will be successfully retained in a predefined band at all times. As the branch energy level provides a direct image of voltage across its SMs, maintaining it as close as possible to the reference can be considered of the utmost importance. The reasons for a possible energy deviation from the setpoints can be various, ranging from the type of control to hardware non-idealities and differences among the converter SMs, which are practically inevitable. Also, any transient occurring during the operation threatens to contribute to the undesired effects in terms of the branches' energies distribution. As one might conclude, being familiar solely with the basic operating principles of the MMC can not be considered sufficient in case safe and reliable operation is demanded. As a result, the analyses presented in this chapter must be extended further by the methods of controlling the MMC terminal currents as well as the internal energies.



# 3

## Modular Multilevel Converter Control

*In order to ensure stable operation of the modular multilevel converter, proper control strategy of its terminal quantities must be employed. Moreover, as converter's branches feature the energy storage nature, equal energy distribution among them must be ensured, otherwise the converter becomes exposed to the risk of failures. This chapter identifies all the variables influencing the energy flow between the converter ports along with the control loops being relevant to this subject. Additionally, the concept of circulating currents is introduced and thoroughly explained, underlying the discussion on converter's internal energy distribution. An extensive description of three different energy balancing approaches is provided giving the grounds for their in-depth comparison.*

### 3.1 Discussion on the converter control layers

In the forthcoming analysis, it will be assumed that a 3PH MMC operates as an inverter. Nevertheless, such an assumption does not affect generality of the results since similar conclusions can effortlessly be derived in case rectifier operating mode is observed. It is noteworthy that control of the MMC has been extensively studied in the literature, however, for the sake of completeness, along with the need to provide a solid foundations for the future analyses, some of the already known principles are brought into the readers attention within the upcoming paragraphs.

Let the analysis of the MMC control layers commence by observing a general power balance equation given by (3.1). As inverter operating mode is considered, identically to any other converter operating in this mode, the MMC is supposed to deliver the AC power matching the reference value  $P_{AC}^*$ . The vast majority of the known converter topologies differing from the MMC, e.g. monolithic converters, store none or almost negligible amounts of energy. Hence, the term  $\Delta P$ , from the below expression, can be said to represent the intrinsic losses of the observed converter. Notwithstanding, it must be emphasized that such a family of converters can not establish an independent control of both terminals' power components. Consequently, an additional stage must be employed in order to ensure the power transfer with the stable DC link voltage [82], [83] (for instance, Active Front End (AFE)).

$$P_{DC} = P_{AC}^* + \Delta P \quad (3.1)$$

On the other hand, it was demonstrated in **Chap. 2** that setting up a suitable system of equations, in case a single MMC leg is observed, provides the framework for decoupled analysis of the converter's AC and DC terminal currents, as depicted in **Fig. 2.7**. As terminal currents are the reflection of power at which the energy flows between the converter ports, it can be claimed that decoupled power

control can easily be established. Since the losses inside the converter can not be avoided, the power taken from the MMC DC terminals needs to match, at least, the sum of the power delivered at the AC side and the total converter losses (3.2).

$$P_{DC,min} = P_{AC}^* + P_{\gamma} \quad (3.2)$$

At this point, it is reasonable to wonder what happens if the MMC DC power is controlled such that  $P_{DC} \neq P_{DC,min}$ . In such a case, the DC terminal power can be expressed as (3.3), where the purpose of the term  $\Sigma P_{br}$  is yet to be investigated.

$$P_{DC} = \underbrace{P_{AC}^* + P_{\gamma}}_{P_{DC,min}} + \Sigma P_{br} \quad (3.3)$$

Averaging of the SM capacitor equations, demonstrated in **Chap. 2**, enables representation of a branch through a pair of controlled sources being associated with an equivalent branch capacitor [84]–[86]. Taking into account the ability of the capacitors to store energy, the MMC can be characterized as an energy storage device to a certain extent, although it is definitely not its primary purpose. Moreover, keeping the branches' voltages within a predefined band suggests that the MMC-based converters indeed store an amount of energy being approximated as (3.4), where  $q$  denotes the number of branches within the converter.

$$W_{MMC\Sigma} \approx q \left( \frac{C}{2N} v_{br\Sigma}^2 \right) \quad (3.4)$$

It is straightforward to conclude that, according to the energy conservation law, any mismatch between the powers denoted by  $P_{DC}$  and  $P_{DC,min}$  contributes to the change of the total amount of energy stored within the MMC branches, as presented in **Fig. 3.1**. Consequently, through the adjustment of DC and AC power components, the total amount of energy stored within the MMC can be controlled. As the inverter operation was assumed at the beginning of this chapter, ensuring the AC power equal to the reference value can be considered the task of the highest priority. Thus, the control of the total energy stored within the converter needs to be established from the DC side.

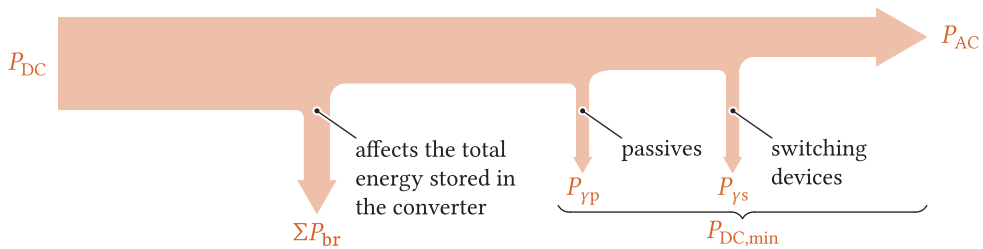


**Fig. 3.1** Power flow chart of the MMC operating as an inverter. Minimum power that needs to be provided from the DC side corresponds to the sum of the AC power reference and the losses inside the MMC itself.

Since decoupled control of the DC and AC side currents can be ensured, two independent control layers get distinctively defined, as presented in **Fig. 3.2**.

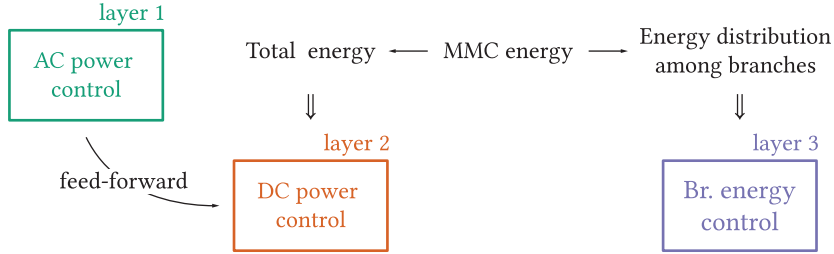


**Fig. 3.2** MMC control layers. As stated above, control of the total energy stored in the converter can be obtained through the DC power adjustment. Nevertheless, an additional control layer, whose structure is to be discussed shortly, must be introduced with the aim of ensuring the equal energy distribution among the MMC branches.

An important detail being neglected during the above discussion refers to the energy distribution among the converter's branches. Namely, in a 3PH MMC one would expect the total energy stored within the converter to be equally distributed among its branches. Nevertheless, this is not necessarily the case, as presented in **Fig. 3.3**, where the sum of the branch energies still corresponds to a desired total energy reference ( $W_{\Sigma, MMC}^* = 6 W_{br}^*$ ). In case any of the branches gets charged to the voltage higher compared to the maximal one foreseen during the converter design phase (e.g. 1 p.u), the semiconductor devices get exposed to the danger of being destroyed either immediately or within a time span falling significantly bellow the predicted operation time of the whole power unit.

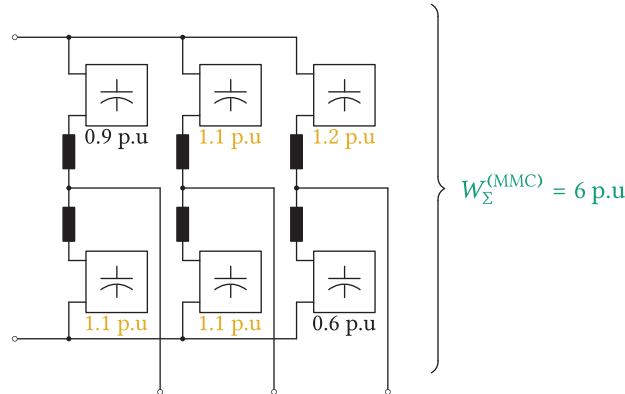


**Fig. 3.3** Example of an inappropriate energy distribution among the branches. Even though the total energy stored within the converter corresponds to the setpoint value, some of the branches store the energy higher compared to the reference being assumed as  $W_{br}^* = 1 \text{ p.u}$ .

To cope with the problems related to the unequal branch energy distribution, an additional control layer must be employed. However, its nature will be revealed once the control of the terminal currents is addressed. Furthermore, it is crucial that all the layers of control must remain decoupled from each other. The methods employed to achieve this goal, in case the controller taking care of the converter energy distribution is observed, will be presented in the subsequent paragraphs.

### 3.2 Control of the AC terminal currents

Since the MMC operating as an inverter has been chosen for the purpose of covering the basic operating principles, a device connected to an AC grid will be considered during the forthcoming analysis. Please notice, however, that any other application, such as control of an AC machine, can also be taken as an example. Control of the power at which the energy is delivered to an AC grid is considered the highest priority task of the MMC analyzed throughout this section. It is clear that such a goal is to be established through the AC Grid Current Control (GCC). For the sake of clarity, the MMC AC equivalent circuit, presented in **Fig. 2.7(a)**, can be redrawn and labeled according to **Fig. 3.4**. It is noteworthy that any grid-connected VSC can be represented in the same manner. As the current control of the grid-connected VSCs has been thoroughly described in the literature [82], [83], this section provides only a short overview of this topic.

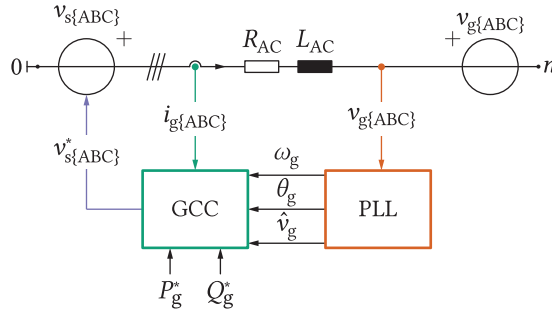


**Fig. 3.4** Simplified control schematics of the grid connected MMC

Unless the information on the AC grid voltage phase and amplitude is obtained, the control of the AC power can not be properly established. For this reason, the Phase Locked Loop (PLL) block, presented in detail in **Fig. 3.5**, is used.

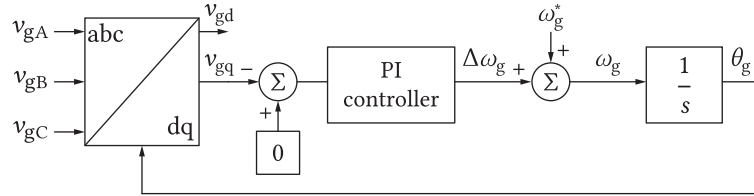


**Fig. 3.5** Basic structure of the PLL block. Nominal angular velocity of the grid the MMC is connected to, denoted by  $\omega_g^*$ , is used as a feed-forward variable. PI controller compensates any mismatch between the nominal and actual grid angular velocity. Setting the grid  $q$ -axis voltage component to zero ensures alignment of the grid voltage vector and the  $dq$  reference frame. Please notice that structure depicted in this figure represents the very basic PLL and more complex versions of it can be used.

Mapping of the measured AC grid voltages  $v_{g\{ABC\}}$  onto the Synchronous Reference Frame (SRF), also being referred to as the  $dq$ -frame, is performed as

$$\begin{bmatrix} v_d \\ v_q \end{bmatrix} = \underbrace{\frac{2}{3} \begin{bmatrix} \cos(\theta_g) & \cos(\theta_g - 2\pi/3) & \cos(\theta_g - 4\pi/3) \\ -\sin(\theta_g) & -\sin(\theta_g - 2\pi/3) & -\sin(\theta_g - 4\pi/3) \end{bmatrix}}_K \begin{bmatrix} v_{gA} \\ v_{gB} \\ v_{gC} \end{bmatrix}, \quad (3.5)$$



where the angular position of the AC grid voltage vector  $\vec{v}_g = v_{gA}(t) + v_{gB}(t)e^{j2\pi/3} + v_{gC}(t)e^{-j2\pi/3}$  in the stationary reference frame was denoted by  $\theta_g$ . Further, setting the reference value of the grid voltage  $q$ -component to zero leads to the SRF being completely aligned with the grid voltage vector.

Consequences of the  $dq$ -transformation introduced in (3.5) are twofold. Firstly, the  $q$  component of the grid voltage vector equals zero, leading to a decoupled control of the active and reactive power delivered to the grid, according to (3.6) and (3.7). Given that (3.5) represents the amplitude and impedance invariant transformation [87], multiplication of both active and reactive powers obtained in the  $dq$  frame by 3/2 must be performed in order to calculate the power in the stationary ( $ABC$ ) reference frame. Secondly, as the reference frame rotates carrying its  $d$  and  $q$  voltages/currents, one can conclude that representation of the rotating voltage vector, or a rotating magnetic field, ensures that  $dq$  quantities are constant. Hence, a simple PI controller can be used to establish the control of grid currents. It is important to emphasize that subsequent calculations assume that the PLL block ensures perfect alignment of the SRF  $d$ -axis and the grid voltage vector  $\vec{v}_g$ . In other words, the information on the grid angular velocity  $\omega_g$ , grid phase angle  $\theta_g$  and grid voltage amplitude  $\hat{v}_{gd}$  is available at all times.

$$P_g = \frac{3}{2} \left( v_{gd} i_{gd} + \underbrace{v_{gq} i_{gq}}_{=0} \right) = \frac{3}{2} v_{gd} i_{gd} \quad (3.6)$$

$$Q_g = \frac{3}{2} \left( \underbrace{v_{gq} i_{gd}}_{=0} - v_{gd} i_{gq} \right) = -\frac{3}{2} v_{gd} i_{gq} \quad (3.7)$$

From the above expressions, one can easily correlate the SRF current references with the AC grid power components. Nevertheless, derivation of the proper current controller structure requires further investigation of the circuit presented in **Fig. 3.4**. Namely, the system of equations describing such a structure can be set as

$$\begin{bmatrix} v_{sA} \\ v_{sB} \\ v_{sC} \end{bmatrix} = \begin{bmatrix} L_{AC} & 0 & 0 \\ 0 & L_{AC} & 0 \\ 0 & 0 & L_{AC} \end{bmatrix} \frac{d}{dt} \begin{bmatrix} i_{gA} \\ i_{gB} \\ i_{gC} \end{bmatrix} + \begin{bmatrix} R_{AC} & 0 & 0 \\ 0 & R_{AC} & 0 \\ 0 & 0 & R_{AC} \end{bmatrix} \begin{bmatrix} i_{gA} \\ i_{gB} \\ i_{gC} \end{bmatrix} + \begin{bmatrix} v_{gA} \\ v_{gB} \\ v_{gC} \end{bmatrix} + v_{n0} \begin{bmatrix} 1 \\ 1 \\ 1 \end{bmatrix}, \quad (3.8)$$

where, in accordance with **Fig. 2.7(a)**,  $L_{AC} = L_g + \alpha L_{br}/2$  and  $R_{AC} = R_g + R_{br}/2$ .

Left multiplication of both sides of (3.8) by the matrix  $K$  from (3.5) yields

$$v_{sd} = L_{AC} \frac{di_{gd}}{dt} + R_{AC} i_{gd} - \underbrace{\omega_g L_{AC} i_{gq}}_{\text{cross-coupling}} + \underbrace{v_{gd}}_{=\hat{v}_g} \quad (3.9)$$

$$v_{sq} = L_{AC} \frac{di_{gq}}{dt} + R_{AC} i_{gq} + \underbrace{\omega_g L_{AC} i_{gd}}_{\text{cross-coupling}} + \underbrace{v_{gq}}_{=0} \quad (3.10)$$

The system of equations (3.9) and (3.10) unveils the cross-coupling between the SRF axes. Namely, the voltage applied in the  $d$ -axis affects the  $q$ -axis current and vice versa.

Hence, removal of the cross-coupling terms from the  $dq$  current control equations must be obtained in case a fully decoupled control is to be performed. In case these are, along with the grid voltage components  $v_{gd}$  and  $v_{gq}$ , fed forward to the GCC according to (3.11) and (3.12), a decoupled control of  $d$  and  $q$  current components can be established, as suggested by (3.13) and (3.14) [83], where  $H_{PI}$  and  $i_{g\{d/q\}}^*$  denote the PI controller transfer function and  $d/q$  reference currents, respectively.

$$v_{sd}^* = \Delta v_{sd} + \underbrace{v_{gd} - \omega_g L_{AC} i_{gq}}_{\text{feed-forward}} \quad (3.11)$$

$$v_{sq}^* = \Delta v_{sq} + \underbrace{v_{gq} + \omega_g L_{AC} i_{gd}}_{\text{feed-forward}} \quad (3.12)$$

$$\Delta v_{sd} = H_{PI}(i_{gd}^* - i_{gd}) = L_{AC} \frac{di_{gd}}{dt} + R_{AC} i_{gd} \quad (3.13)$$

$$\Delta v_{sq} = H_{PI}(i_{gq}^* - i_{gq}) = L_{AC} \frac{di_{gq}}{dt} + R_{AC} i_{gq} \quad (3.14)$$

As both  $i_{gd}^*$  and  $i_{gq}^*$  are constant, with the plant transfer function given in the continuous domain as  $H(s) = 1/(sL_{AC} + R_{AC})$ , the PI controller is employed to generate voltage components  $\Delta v_{sd}$  and  $\Delta v_{sq}$ . **Fig. 3.6** presents the control diagram derived following the above analysis.

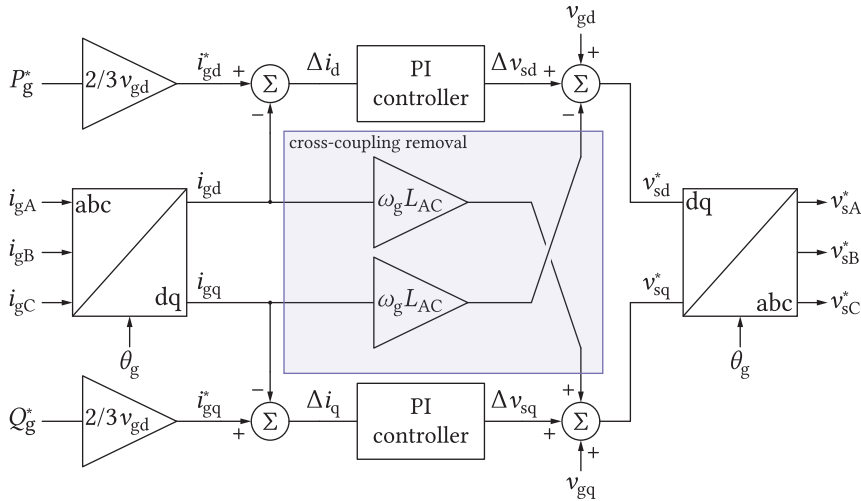


**Fig. 3.6** GCC block diagram. In order to ensure decoupling between  $d$  and  $q$  axes, feed-forward terms in both  $v_{sd}^*$  and  $v_{sq}^*$  are introduced.

It is noteworthy that once the  $dq$  reference frame voltages are obtained, the stationary reference frame voltages can be calculated as

$$\begin{bmatrix} v_{SA}^* \\ v_{SB}^* \\ v_{SC}^* \end{bmatrix} = \begin{bmatrix} \cos(\theta_g) & \sin(\theta_g) \\ \cos(\theta_g - 2\pi/3) & \sin(\theta_g - 2\pi/3) \\ \cos(\theta_g + 2\pi/3) & \sin(\theta_g + 2\pi/3) \end{bmatrix} \begin{bmatrix} v_{sd}^* \\ v_{sq}^* \end{bmatrix} \quad (3.15)$$

If the use of HB SMs is considered, and according to (2.25), the maximum amplitude of the phase voltage seen from the MMC AC terminals equals  $\hat{v}_s = v_{br\Sigma}/2$ . On these terms, the amplitude of the line voltage seen from the AC terminals equals  $\hat{v}_{s,line} = \sqrt{3}v_{br\Sigma}/2$ . Given that the MMC AC equivalent circuit does not differ from the one describing the 2LVL VSC, the same measures for achieving a better DC link utilization can be taken. Namely, the injection of a certain amount of the third harmonic [88], which actually corresponds to the voltage component  $v_{n0}$  from (3.8), results in the possibility to increase the maximal attainable AC voltage by the factor of  $2/\sqrt{3}$ .

### 3.3 DC terminal current control and circulating current concept

The MMC DC equivalent circuit depicted in Fig. 2.7(b) can be rearranged using the Thevenin's theorem, as presented in Fig. 3.7.

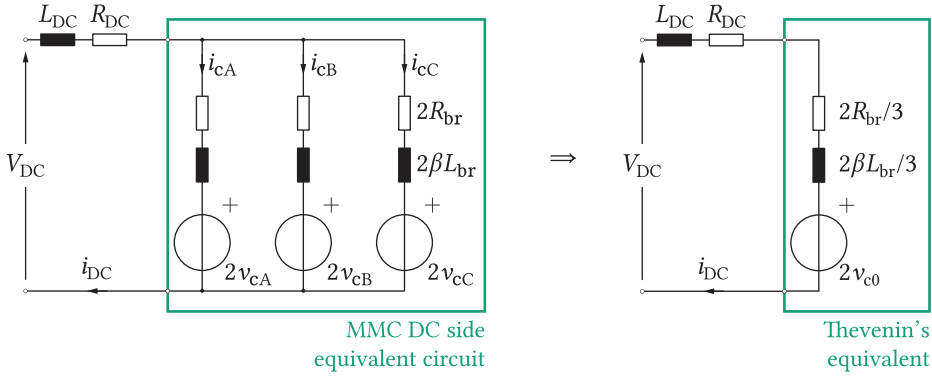


Fig. 3.7 Rearrangement of the MMC DC equivalent circuit

KVL applied to the circuit on the right-hand side of the above figure gives

$$L_{DC}^{\Sigma} \frac{di_{DC}}{dt} + R_{DC}^{\Sigma} i_{DC} = V_{DC} - 2 \underbrace{\frac{v_{cA} + v_{cB} + v_{cC}}{3}}_{v_{c0}}, \quad (3.16)$$

where  $L_{DC}^{\Sigma} = L_{DC} + 2\beta L_{br}/3$  and  $R_{DC}^{\Sigma} = R_{DC} + 2\beta L_{br}/3$ . At this point it is straightforward to conclude that the control of MMC DC current can be established through the adjustment of the legs' common-mode voltage component  $v_{c0}$ . It is noteworthy that the same equivalent circuit can be applied in case B2B connection of two MMCs is considered. Therefore, control logic derived in the upcoming paragraphs can be considered general.

Normally, the mean value of voltage labeled with  $V_{DC}$  might vary in practice, however, in the modest band (e.g.  $\pm 20\%$  of the nominal value  $V_{DC}^*$ ). Therefore, the control variable  $v_{c0}$  can be determined as (3.17), where  $V_{DC}^*$  denotes the nominal voltage of the DC grid.

$$2v_{c0} = V_{DC}^* - \Delta v_{DC} \quad (3.17)$$

For the moment, let one assume that  $V_{DC} = V_{DC}^*$ , which results in

$$L_{DC}^{\Sigma} \frac{di_{DC}}{dt} + R_{DC}^{\Sigma} i_{DC} = \Delta v_{DC} \quad (3.18)$$

According to the above equation, supported by (3.17), it can be concluded that the MMC DC current control can be established in the manner presented in **Fig. 3.8**. Even if  $V_{DC} \neq V_{DC}^*$ , PI controller employed with the aim of synthesizing the component  $\Delta v_{DC}$ , ensures no steady state tracking error  $\Delta i_{DC}(\infty)$  is observed [89].

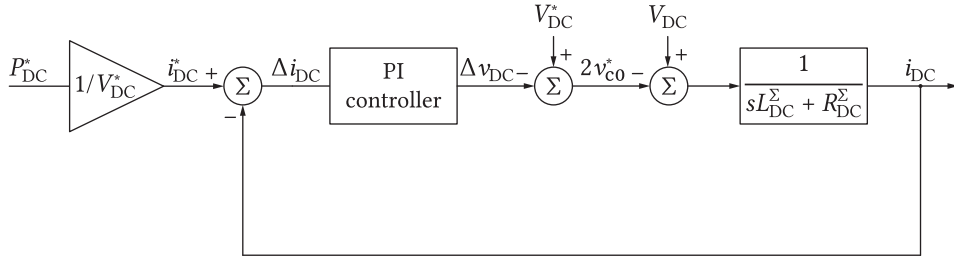


**Fig. 3.8** MMC DC current control block diagram

It is noteworthy that the DC current reference follows directly from the DC power reference as  $i_{DC}^* = P_{DC}^*/V_{DC}^*$ , which is in accordance with the statements made above. Notwithstanding, legs' common-mode voltage component  $v_{c0}$  takes part only in the control of the MMC DC current without concerning its distribution among the legs (keep in mind that  $i_{cA} + i_{cB} + i_{cC} = i_{DC}$ ). Logically, ideal distribution would imply that  $i_{c\{A/B/C\}} = i_{DC}/3$ . However, in case the legs were controlled such that  $v_{c\{A/B/C\}} = v_{c0}^*$  holds, such a requirement is unlikely to be met for various reasons. For instance, absolutely identical leg DC side impedance  $Z_{DC} = 2(R_{br} + j\omega\beta L_{br})$  can not be guaranteed for all the legs comprising the MMC. Therefore, expressing the leg common-mode current as (3.19) comes in handy.

$$i_c = \frac{i_{DC}}{3} + i_{c\Delta} \quad (3.19)$$

Summing the legs' common-mode currents expressed as (3.19), provides

$$\underbrace{i_{cA} + i_{cB} + i_{cC}}_{i_{DC}} = 3 \frac{i_{DC}}{3} + i_{c\Delta A} + i_{c\Delta B} + i_{c\Delta C}, \quad (3.20)$$

which can also be written as

$$i_{c\Delta A} + i_{c\Delta B} + i_{c\Delta C} = 0 \quad (3.21)$$

According to (3.21), the sum of the leg currents mismatches with respect to a third of the DC link current equals zero. As these current components do not enter the DC link, nor are they visible from the converter's AC terminals, it is clear that they "circulate" inside of the MMC. For that reason, these components will henceforth be referred to as the circulating currents. In steady state, circulating currents are normally controlled to zero, however, as will be presented in the next sections, they can be successfully used to achieve the energy balancing among the converter's branches.

### 3.4 Circulating currents control

In the previous section, it was demonstrated that control of the MMC DC current can be established through setting the common-mode voltage of every leg as  $v_c = v_{c0}^*$ . Nevertheless, such a control might cause unequal DC current distribution among the converter's legs. With the aim of mitigating this effect, one can commence the analysis by assuming that an arbitrary leg common-mode voltage can be redefined as

$$v_c = v_{c0} + v_{c\Delta} \quad (3.22)$$

Based on the circuits depicted in **Fig. 3.7**, it is straightforward to notice that

$$2v_{c0} + \frac{2\beta}{3}L_{br}\frac{di_{DC}}{dt} + \frac{2}{3}R_{br}i_{DC} = 2v_c + 2\beta L_{br}\frac{di_c}{dt} + 2R_{br}i_c \quad (3.23)$$

Rearranging the above expression and substituting (3.22) into it, provides one with

$$\begin{aligned} 2\beta L_{br}\frac{d}{dt}\left(\underbrace{i_c - \frac{i_{DC}}{3}}_{i_{c\Delta}}\right) + 2R_{br}\left(i_c - \frac{i_{DC}}{3}\right) &= 2(v_{c0} - v_c) \\ \Rightarrow \beta L_{br}\frac{di_{c\Delta}}{dt} + R_{br}i_{c\Delta} &= -v_{c\Delta} \end{aligned} \quad (3.24)$$

Therefore, the distribution of currents among the converter legs can obviously be achieved by means of the voltage components  $v_{c\Delta}$ . Control block diagram derived from (3.24) can be seen in **Fig. 3.9**. The nature of the circulating current controller  $W_{circ}(s)$  depends on several aspects and it will be discussed more thoroughly in the sections covering the MMC internal energy balancing.

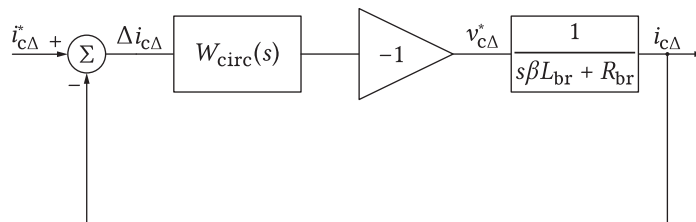


**Fig. 3.9** A leg circulating current control block diagram

Another important remark needs to be made at this point. Equations (3.22) to (3.24) were derived assuming a single MMC leg was observed. However, seen from the DC terminal, all three MMC legs take part in creating an equivalent voltage  $v_{c0}$ , as illustrated in (3.16). Combining (3.16) and (3.22) gives

$$\begin{aligned} v_{c0} &= \frac{1}{3}(v_{cA} + v_{cC} + v_{cC}) \\ &= v_{c0}^* + \frac{1}{3}(v_{c\Delta A}^* + v_{c\Delta B}^* + v_{c\Delta C}^*) \end{aligned} \quad (3.25)$$

From the above equation, it is clear that (3.26) must be fulfilled at all times, otherwise the MMC DC current control gets affected by the control of circulating currents, which is contrasting the goal of achieving the decoupling of MMC control layers.

$$v_{c\Delta A}^* + v_{c\Delta B}^* + v_{c\Delta C}^* = 0 \quad (3.26)$$

Utilizing **Fig. 3.9**, the sum of the above voltage components can be expressed as

$$v_{c\Delta A}^* + v_{c\Delta B}^* + v_{c\Delta C}^* = -W_{\text{circ}}(s) \left\{ (i_{c\Delta A}^* + i_{c\Delta B}^* + i_{c\Delta C}^*) - \underbrace{(i_{c\Delta A} + i_{c\Delta B} + i_{c\Delta C})}_{=0 \text{ according to (3.21)}} \right\}, \quad (3.27)$$

from where it can be seen that decoupled control of DC link and circulating currents can only be achieved if the circulating current references sum up to zero. It is noteworthy that, as long as this condition is met, circulating currents can take any arbitrary form. For example, as will be seen in **Sec. 3.6**, DC components of circulating currents contribute to the energy exchange among the legs (horizontal balancing), whereas their AC components can establish the energy balance between two branches belonging to the same leg (vertical balancing). Several methods of generating the circulating current references have been reported in the literature [77], [84], [90], [91] and it is exactly **Sec. 3.6** addressing this topic in detail.

### 3.5 MMC total energy control

Prior to commencing a discussion on the distribution of MMC internal energies, a short recap on the total energy control should be made. As it was illustrated in **Fig. 3.1**, total energy stored in the MMC is to be controlled from the DC side in case inverter operating mode is considered. In case the operation in rectifier mode is considered, however, the analyzed energy component is to be controlled from the AC port. One can conclude that the total energy control is always to be established from the port representing the source of energy. Nonetheless, this does not affect the generality of the principles demonstrated henceforward.

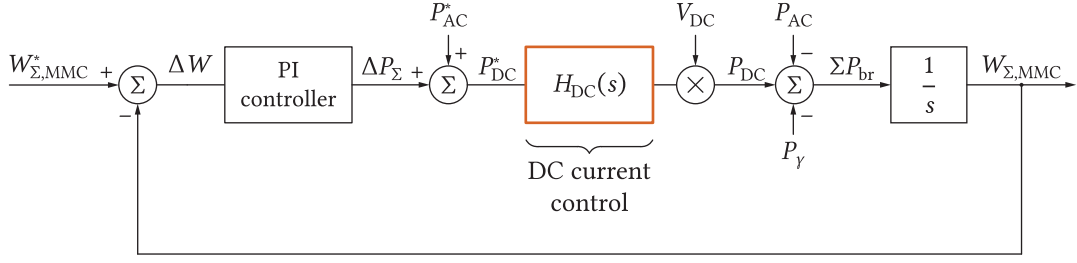


**Fig. 3.10** MMC total energy control block diagram

Generally, control of the total energy stored in the MMC can be established as indicated in **Fig. 3.10**. It is noteworthy that the block diagram from the above can be used irrespective of the number of phase-legs the MMC consists of. In case the conventional 3PH MMC is analyzed, while the use of HB SMs is assumed, the reference of the total energy stored in the converter can be set as (3.28), which is derived through the considerations made in **Chap. 2**.

$$W_{\Sigma,MMC}^* = 6 \times \frac{C_{SM}}{2N} V_{DC}^* \quad (3.28)$$

Although the energy is not directly measurable, converter voltage measurements are normally available. Therefore, the energy of every branch can be obtained through the information on voltage across its SM capacitors. Subsequently, the total energy of the MMC is compared with the reference  $W_{\Sigma,MMC}^*$  and the error, denoted by  $\Delta W$ , is passed to the PI controller. Given that the MMC operating as an inverter must deliver the AC power equal to the reference, feed-forward of the power component  $P_{AC}^*$  can be used to obtain the reference of power drawn from the DC terminal as  $P_{DC}^* = P_{AC}^* + \Delta P_{\Sigma}$ .

The power reference  $P_{DC}^*$  is subsequently passed to the MMC DC current controller  $H_{DC}(s)$ , presented in **Fig. 3.8**, from where legs' common-mode voltage components  $v_{c0}^*$  are obtained. According to **Fig. 3.10**, power component affecting the total energy stored in the MMC is obtained as  $\Sigma P_{br} = P_{DC} - P_{AC} - P_{\gamma}$ . In case both GCC and DC current controller operate with high bandwidth, one can claim that  $P_{AC} \approx P_{AC}^*$  and  $P_{DC} \approx P_{DC}^*$ . Therefore,  $\Sigma P_{br} = \Delta P_{\Sigma} - P_{\gamma}$ , meaning that the task of the PI controller is to provide the power reference covering the internal converter losses along with ensuring the total energy equilibrium. For instance, if  $W_{\Sigma,MMC} = W_{\Sigma,MMC}^*$ , power component  $\Sigma P_{br}$  should match zero, meaning that  $\Delta P_{\Sigma} = P_{\gamma}$ . Similar analysis can be conducted in case  $W_{\Sigma,MMC} \neq W_{\Sigma,MMC}^*$ .

## 3.6 MMC Internal Energy Control

### 3.6.1 Energy Balancing of a Single MMC Leg

The analysis of the MMC internal energy control can commence by observing a single leg presented on the left-hand side of **Fig. 2.5** from where (3.29) and (3.30) can be reestablished.

$$\frac{C}{N} \frac{dv_{p\Sigma}}{dt} = m_p i_p \quad (3.29)$$

$$\frac{C}{N} \frac{dv_{n\Sigma}}{dt} = m_n i_n \quad (3.30)$$

Substitution of (2.21) and (2.22) into (3.29) and (3.30), respectively, leads to

$$\frac{C}{N} \frac{dv_{p\Sigma}}{dt} = \frac{v_c - v_s}{v_{p\Sigma}} \left( i_c + \frac{i_o}{2} \right) \quad (3.31)$$

$$\frac{C}{N} \frac{dv_{n\Sigma}}{dt} = \frac{v_c + v_s}{v_{n\Sigma}} \left( i_c - \frac{i_o}{2} \right) \quad (3.32)$$

Multiplication of (3.31) with  $v_{p\Sigma}$  and (3.32) with  $v_{n\Sigma}$ , along with expressing the leg common-mode current and voltage with (3.19) and (3.22), respectively, yields

$$\frac{d}{dt} \underbrace{\left( \frac{C}{2N} v_{p\Sigma}^2 \right)}_{W_p} = \left( v_{c0} + v_{c\Delta} - v_s \right) \left( \frac{i_{DC}}{3} + i_{c\Delta} + \frac{i_o}{2} \right) \quad (3.33)$$

$$\frac{d}{dt} \underbrace{\left( \frac{C}{2N} v_{n\Sigma}^2 \right)}_{W_n} = \left( v_{c0} + v_{c\Delta} + v_s \right) \left( \frac{i_{DC}}{3} + i_{c\Delta} - \frac{i_o}{2} \right) \quad (3.34)$$

From the above expressions, dynamics of the energy stored within the branches belonging to the same leg is revealed. Nevertheless, to facilitate the forthcoming calculations, the total and differential leg energy components are defined according to (3.35) and (3.36), respectively.

$$W_\Sigma = W_p + W_n \quad (3.35)$$

$$W_\Delta = W_p - W_n \quad (3.36)$$

Differentiation of  $W_\Sigma$  and  $W_\Delta$ , combined with (3.33) and (3.34) results in

$$\frac{dW_\Sigma}{dt} = 2v_{c0}i_{c\Delta} + 2v_{c0}\frac{i_{DC}}{3} - v_s i_o + 2v_{c\Delta}\frac{i_{DC}}{3} + 2v_{c\Delta}i_{c\Delta} \quad (3.37)$$

$$\frac{dW_\Delta}{dt} = -2v_s i_{c\Delta} - 2v_s \frac{i_{DC}}{3} + i_o v_{c0} + i_o v_{c\Delta} \quad (3.38)$$



With the aim of investigating the nature of the leg energy components  $W_\Sigma$  and  $W_\Delta$ , let one assume that steady state operation of the converter is reached with no circulating currents being present within the converter's legs. Consequently, (3.37) and (3.38) can be simplified as (3.39) and (3.40), where  $v_s = \hat{v}_s \cos(\omega_g t - \gamma)$  and  $i_o = \hat{i}_o \cos(\omega_g t - \delta)$ .

In (3.39), the term  $V_{DC} \frac{i_{DC}}{3} - \frac{\hat{v}_s \hat{i}_o}{2} \cos(\gamma - \delta)$  represents the difference between the DC and AC power components of an observed leg. In steady state, this term matches zero, otherwise the leg energy increases/decreases, implying an increase/decrease in voltages across its SMs' capacitors. Apart from the mean value, the MMC leg total energy  $W_\Sigma$  features natural oscillations at twice the frequency of its AC currents. On the other hand, analysis of (3.40) points out that a leg differential energy  $W_\Delta$ , whose mean value is normally controlled to zero, oscillates at frequency of the MMC AC currents.

$$\left. \frac{dW_\Sigma}{dt} \right|_{\text{no circ.}} = 2v_{c0} \frac{i_{DC}}{3} - v_s i_o \approx \underbrace{V_{DC} \frac{i_{DC}}{3} - \frac{\hat{v}_s \hat{i}_o}{2} \cos(\gamma - \delta)}_{=0} - \underbrace{\frac{\hat{v}_s \hat{i}_o}{2} \cos(2\omega_g t - \gamma - \delta)}_{\text{oscillating @ } 2\omega_g} \quad (3.39)$$

$$\left. \frac{dW_\Delta}{dt} \right|_{\text{no circ.}} = \underbrace{-2\hat{v}_s \frac{i_{DC}}{3} \cos(\omega_g t - \gamma) + \hat{i}_o v_{c0} \cos(\omega_g t - \delta)}_{\text{oscillating @ } 1\omega_g} \quad (3.40)$$

Recalling (3.35) and (3.36), the energies of the upper and lower branches can be expressed as (3.41) and (3.42), respectively.

$$W_p = \frac{1}{2} (W_\Sigma + W_\Delta) \quad (3.41)$$

$$W_n = \frac{1}{2} (W_\Sigma - W_\Delta) \quad (3.42)$$

It is straightforward to conclude that energies of both branches within the same leg experience oscillations at identical frequencies. Nonetheless, oscillations at the fundamental frequency (e.g. 50Hz) are in the counter-phase, as illustrated in **Fig. 3.11**.

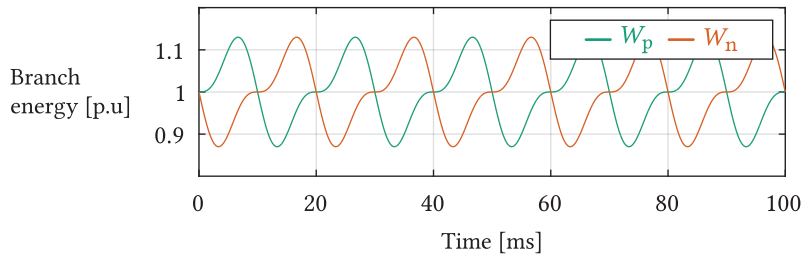


**Fig. 3.11** Steady state appearance of the upper and lower branch energies normalized with respect to the branch mean energy. Even though the branches experience oscillations at identical frequencies, please notice the counter phase orientation of the fundamental frequency components. As will be demonstrated, main task of the MMC energy controllers is to maintain the average energy of both branches at the reference value.

According to (3.33) and (3.34), the total voltage oscillation of an arbitrary branch can be calculated as (3.43), which indicates that limiting of the SMs' voltage ripple gets achieved through a proper selection of the SM capacitance [48], [49].

$$v_{br\Sigma} = \sqrt{\frac{2N}{C}} W_{br\Sigma} \quad (3.43)$$

Since the oscillation of the MMC branch energies occurs naturally, the main task of the internal energy controller can be defined as keeping the average of energy components  $W_{\Sigma}$  and  $W_{\Delta}$  equal to setpoint values  $\overline{W_{\Sigma}^*}$  and 0, respectively. Henceforth, unless specified otherwise, any discussion on the converter energy levels will imply that only the average components are considered. Even though the branch energy oscillation can not be avoided, it can be mitigated/shaped to a certain extent by the optimization of circulating currents, as proposed in [92]–[94], however, such an analysis falls out of this thesis' scope.

To identify the circulating current components taking part in balancing of the leg total and differential energies, its common-mode current can be expressed as

$$i_c = \underbrace{\frac{i_{DC}}{3}}_{\text{circ. DC}} + I_{c\Delta} + \underbrace{\hat{i}_{c\Delta} \cos(\omega_g t - \zeta)}_{\text{circ. AC}}, \quad (3.44)$$

where  $I_{c\Delta}$  and  $\hat{i}_{c\Delta} \cos(\omega t - \zeta)$  denote circulating current DC and AC component, respectively.

Substitution of (3.44) into (3.37) and (3.38), followed by the averaging, results in (3.45) and (3.46).

$$\frac{d\overline{W_{\Sigma}}}{dt} \approx V_{DC} I_{c\Delta} + \underbrace{V_{DC} \frac{i_{DC}}{3} - \frac{\hat{v}_s \hat{i}_0}{2} \cos(\gamma - \delta)}_{=0} + \underbrace{2v_{c\Delta} \frac{i_{DC}}{3} + 2v_{c\Delta} i_{c\Delta}}_{\text{negligible}} \quad (3.45)$$

$$\frac{d\overline{W_{\Delta}}}{dt} \approx -\hat{v}_s \hat{i}_{c\Delta} \cos(\gamma - \zeta) + \underbrace{v_{c\Delta} \hat{i}_0}_{\text{negligible}} \quad (3.46)$$

As balancing currents are not expected to be comparable to the converter nominal currents, it can be claimed that  $v_{c\Delta} \ll V_{DC}$  and  $v_{c\Delta} \ll \hat{v}_s$ . Consequently, the right-most terms in (3.45) and (3.46) are considered negligible, which allows for simplification in the form of (3.47) and (3.48). Please notice from (3.48) that the AC component of the circulating current was chosen to be in phase with the leg voltage component  $v_s$ , meaning that  $\gamma = \zeta$ .

$$\frac{d\overline{W_{\Sigma}}}{dt} \approx V_{DC} I_{c\Delta} \quad (3.47)$$

$$\frac{d\overline{W_{\Delta}}}{dt} \approx -\hat{v}_s \hat{i}_{c\Delta} \quad (3.48)$$

In summary, change of the leg total and differential energies can be achieved by adjusting the circulating current DC and AC components, respectively. As stated in the previous sections, the total energy stored within the MMC gets controlled by the DC link current, whereas the circulating current should not be seen at either of the converter's terminals. Therefore, the DC component of the circulating current allows for the total energy exchange among the MMC legs. In other words, balancing in the horizontal direction is achieved. At the same time, the AC component of the circulating current achieves balancing of the average energies between the branches belonging to the same leg. It is clear, therefore, why this way of balancing is often referred to as vertical balancing.

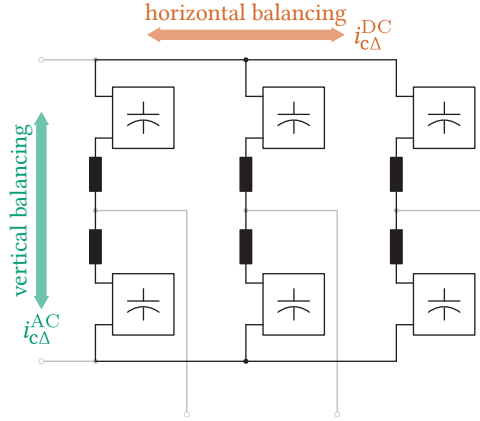


**Fig. 3.12** MMC balancing directions. Legs' circulating currents AC and DC components contribute to the balancing in vertical and horizontal direction, respectively.

With the aim of establishing the proper energy control, average values must be extracted from the measurements of the upper and lower branch energy. As an SM capacitor voltage measurement is normally provided, branch total voltage  $v_{br\Sigma}$  can easily be obtained allowing for the energy calculation introduced in (3.33) and (3.34). Thereafter, in accordance with **Fig. 3.11**, one can conclude that energy oscillations occurring at angular frequencies  $\omega_g$  and  $2\omega_g$  are to be attenuated. To filter out a component at the specific frequency denoted by  $\omega_f$ , a notch filter with the transfer function  $W_{\text{notch}}(s)$  given in (3.49) can be used.

$$W_{\text{notch}}(s) = \frac{s^2 + \omega_f^2}{s^2 + 2\zeta\omega_f s + \omega_f^2} \quad (3.49)$$

Once extracted, branch energies get compared to the reference values, with the errors being subsequently passed to the leg energy controllers, as presented in **Fig. 3.13**. As the controllers' outputs represent the leg total and differential power components defined in (3.47) and (3.48), circulating current components are to be obtained using exactly these expressions.

Given that the leg circulating current reference comprises DC and AC parts, the circulating current controller, depicted in **Fig. 3.9**, apart from the proportional and integral parts which are needed in order to control the DC current component, must also incorporate the resonant part (3.50).

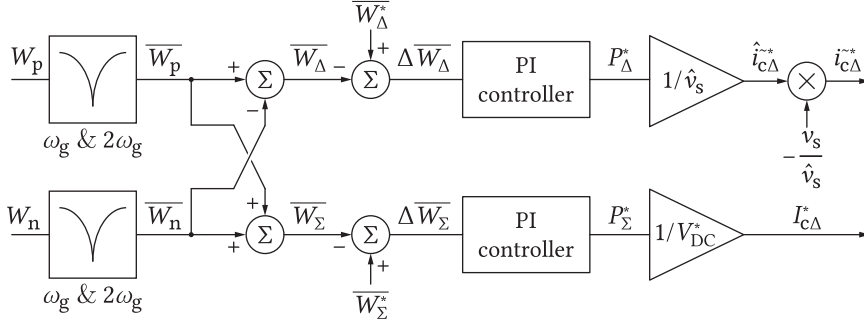


Fig. 3.13 Control block diagram of the MMC leg relevant energies

$$W_{\text{circ}}(s) = \underbrace{k_{p\Delta} + \frac{k_{i\Delta}}{s}}_{\text{PI controller}} + \underbrace{k_{r\Delta} \frac{2\rho\omega_g s}{s^2 + 2\zeta\omega_g s + \omega_g^2}}_{\text{Resonant part}} \quad (3.50)$$

Notwithstanding, the analysis presented within this subsection considers circulating current reference generation taking into account the energy state of a single MMC leg without concerning the existence of the other two phases. Consequently, there is no guarantee that the sum of the circulating current references will be zero ( $i_{c\Delta A}^* + i_{c\Delta B}^* + i_{c\Delta C}^* = 0$ ), which is a constraint set by (3.27) if decoupled control of the MMC energies is to be achieved. As a result, additional measures must be taken in generation of the circulating current references, however, analyzing the MMC as a whole, at least from the energy distribution point of view.

### 3.6.2 Energy Balancing in the 3PH MMC

The leg energy analysis provided in **Sec. 3.6.1** can be utilized as the underlying basis for the energy balancing of the 3PH MMC. Namely, generation of the individual legs' circulating current references commences in accordance with **Fig. 3.13**. In other words, the first step in generating circulating current references corresponds to the procedure defined in case energy balancing is performed in "per-leg" fashion. Nevertheless, additional reference mapping, which ensures that  $i_{c\Delta A}^* + i_{c\Delta B}^* + i_{c\Delta C}^* = 0$  must be considered, as indicated in **Fig. 3.14**.

Even though the control of circulating current DC and AC components can be considered separately, the direction of balancing (vertical or horizontal) will be neglected for now. Therefore, results presented in the upcoming paragraphs can be considered general. Initially, this approach was presented in [77], however, detailed explanation on the logic underlying it was not provided. As circulating currents were defined in the DC equivalent circuit of the MMC, their summation at the DC terminal can be formulated as

$$\underbrace{\begin{bmatrix} 1 & 1 & 1 \end{bmatrix}}_{T_i} \underbrace{\begin{bmatrix} i_{c\Delta A} \\ i_{c\Delta B} \\ i_{c\Delta C} \end{bmatrix}}_{\vec{i}} = 0 \quad (3.51)$$

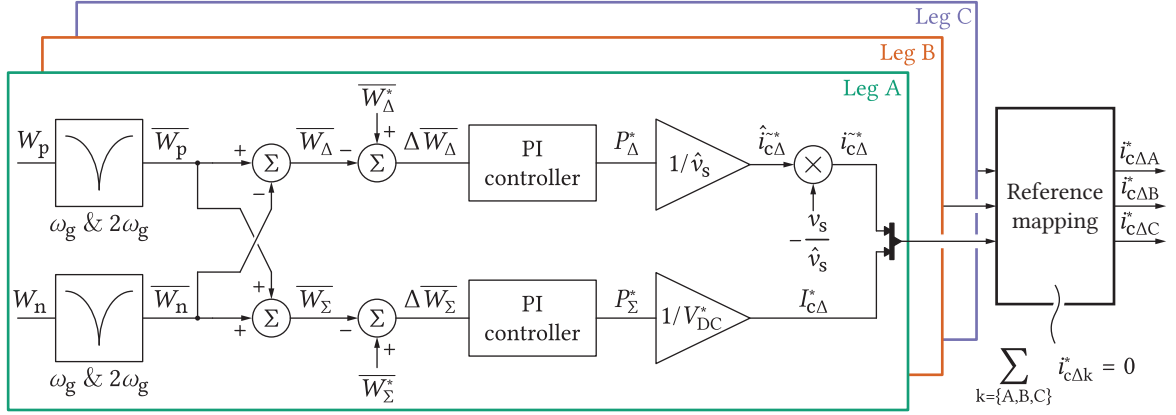


**Fig. 3.14** Concept of generating circulating current references in the 3PH MMC. Mapping of the circulating current references generated in "per-leg" fashion must be performed given that individual control of the leg energies does not guarantee fulfillment of the constraint defined in (3.27).

One can understand that matrix  $T_i$  represents the mapping  $\mathbb{R}^3 \mapsto \mathbb{R}$ , whereas all the vectors  $\vec{I}$  being mapped to zero do not actually corrupt the MMC DC link current. It is exactly this set of vectors that defines the null-space (or kernel, hence the label  $\ker(T)$ ) of matrix  $T_i$ . Nonetheless, energy unbalances among the MMC branches/legs can take any arbitrary values resulting in the control actions violating the constraint of circulating current references summing up to zero (please keep in mind that generation of circulating current references commences by performing the balancing of every leg individually). To overcome this issue, a reference vector  $\vec{I}^*$ , such that  $T_i \vec{I}^* \neq 0$ , can be projected onto the null-space of  $T_i$ , which allows for (3.27) to be satisfied.

Given that the above statements might seem quite abstract at first glance, let one make a digression by observing the simplest possible case - a 1PH MMC, with two relevant circuits presented in **Figs. 3.15(a)** and **3.15(b)**. Additionally, the "per-leg" control logic of the branch energies will be retained, which allows one to assume that an exemplary reference vector of circulating currents  $i_{c\Delta\{A/B\}}$ , presented in **Fig. 3.16(a)**, is demanded by the controllers. In this case, the constraint regarding the mapping of circulating currents to the DC link can be described in the form similar to (3.51) as

$$\begin{bmatrix} 1 & 1 \end{bmatrix} \begin{bmatrix} i_{c\Delta A} & i_{c\Delta B} \end{bmatrix}^T = 0.$$

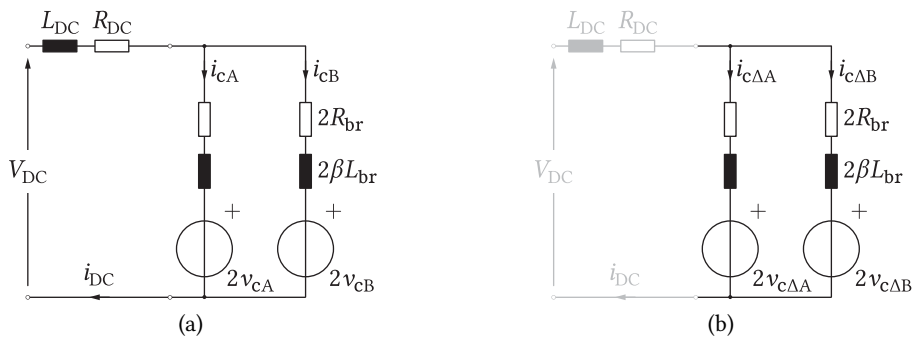


**Fig. 3.15** 1PH MMC equivalent circuits; (a) DC side equivalent circuit; (b) Circuit relevant for the analysis of circulating currents

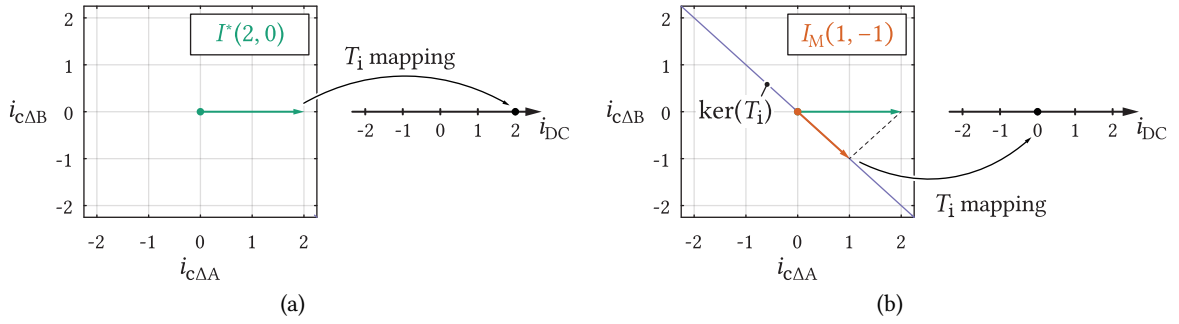


**Fig. 3.16** To avoid corruption of the DC link current, circulating current references must sum up to zero; (a) Mapping of an arbitrary vector of circulating current references to the DC link in case 1PH MMC is observed. Since, in this case, the sum of column elements of  $\vec{I}^*$  differs from zero, projection onto the null-space of the mapping matrix  $T_i$  must be performed. (b) Projection of the reference vector  $\vec{I}^*$  onto the null-space of the mapping matrix  $T_i$ .

It is obvious from **Fig. 3.16(a)** that the vector of circulating current references  $\vec{I}^* = [2, 0]^T$  does not guarantee a decoupled control of MMC quantities since the sum of elements along its column is not equal to zero. Therefore, a new set of references, labeled with  $\vec{I}_M$ , needs to be obtained by mapping the vector  $\vec{I}^*$  to the null-space of matrix  $T_i = \begin{bmatrix} 1 & 1 \end{bmatrix}$ . As a result, the question on identification of  $\ker(T_i)$  arises.

In the observed case,  $\ker(T_i)$  contains all the circulating current pairs fulfilling the requirement given by  $i_{c\Delta A} + i_{c\Delta B} = 0$ . Consequently, null-space is nothing but a line, as presented in **Fig. 3.16(b)**. Minimal discrepancy between the vectors denoted by  $\vec{I}^*$  and  $\vec{I}_M$  implies that the vector  $\vec{I}^*$  needs to be projected onto the line symbolizing  $\ker(T_i)$ . It is well known that the scalar product of two arbitrary vectors  $\vec{x}$  and  $\vec{y}$  can be mathematically formulated as

$$\vec{x} \cdot \vec{y} = |\vec{x}| |\vec{y}| \cos(\theta_{xy}) \quad (3.52)$$

Furthermore, in case  $\vec{y}$  is a unit vector, meaning that  $|\vec{y}| = 1$ , the scalar product  $\vec{x} \cdot \vec{y}$  actually represents the projection of the vector  $\vec{x}$  onto an infinite line passing through the vector  $\vec{y}$ . Graphical representation of such a statement can be found in the figure below.

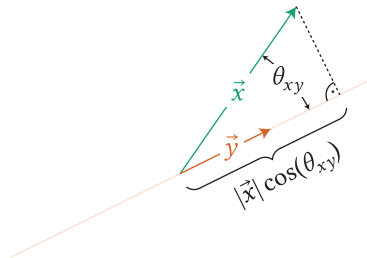


**Fig. 3.17** In case one of the vectors in the scalar product is a unity vector ( $\vec{y}$  in the observed case), then  $\vec{x} \cdot \vec{y}$  represents the projection of the vector  $\vec{x}$  onto an infinite line passing through the vector  $\vec{y}$ .

Based on the example from **Fig. 3.17**, one can conclude that one step towards obtaining a suitable reference vector  $\vec{I}_M$  implies the identification of a unit vector residing on the line representing the null-space of  $T_i$ . This vector will henceforth be referred to as the basis vector of the null-space. As the dimension of the null-space is  $\dim(\ker(T_i)) = 1$ , there exists only one basis vector. In case  $\dim(\ker(T_i)) > 1$ , there is more basis vectors, as will be seen shortly.

In the observed case, as  $\ker(T_i)$  implies  $i_{c\Delta A} = -i_{c\Delta B}$ , the basis vector of the null-space, denoted by  $\vec{v}_N$  can be chosen as

$$\vec{v}_N = \frac{1}{\sqrt{2}} \begin{bmatrix} 1 \\ -1 \end{bmatrix} \quad (3.53)$$

In matrix form, the scalar product of vectors  $\vec{I}^*$  and  $\vec{v}_N$  can be expressed as

$$\vec{v}_N \cdot \vec{I}^* = \frac{1}{\sqrt{2}} \begin{bmatrix} 1 \\ -1 \end{bmatrix}^T \begin{bmatrix} 2 \\ 0 \end{bmatrix} = \sqrt{2} \quad (3.54)$$

Nonetheless, the result of the above multiplication is just a length of the vector  $\vec{I}^*$  projected onto the  $\ker(T_i)$ . To obtain a new set of references, the number obtained by means of (3.54) needs to be multiplied by the vector  $\vec{v}_N$  (keep in mind that this is a unity vector, therefore it gives an orientation to the length obtained by the above expression), yielding

$$\vec{I}_M = \vec{v}_N \vec{v}_N^T \vec{I}^* = \begin{bmatrix} 1 \\ -1 \end{bmatrix} \quad (3.55)$$

What can be concluded from the above discussion is that the identification of the basis vector(s) of  $\ker(T_i)$  represents the heart of the mapping procedure indicated in **Fig. 3.14**. Irrespective of the dimension of the problem (1PH-, 3PH- or  $N$ -phase MMC), the procedure can be broken down into three key steps:

- Identify the basis vector(s) of  $\ker(T_i)$
- Project the circulating current reference vector  $\vec{I}^*$  onto the bases identified in the previous step
- Multiply the obtained projections by the basis vectors to get the new set of references  $\vec{I}_M$

In case  $N$ -phase MMC is observed, the matrix  $T_i$  is the row matrix filled with ones. It can be concluded that  $N - 1$  circulating currents are independent in this case (since  $\sum_{i=1}^N i_{c\Delta i} = 0$ ), therefore, the number of basis vectors in  $\ker(T_i)$  equals  $N - 1$ . A formal proof of this statement will be provided in **Chap. 4**. Nevertheless, **Fig. 3.18** provides an illustration of the above discussion in case 3PH MMC is observed.

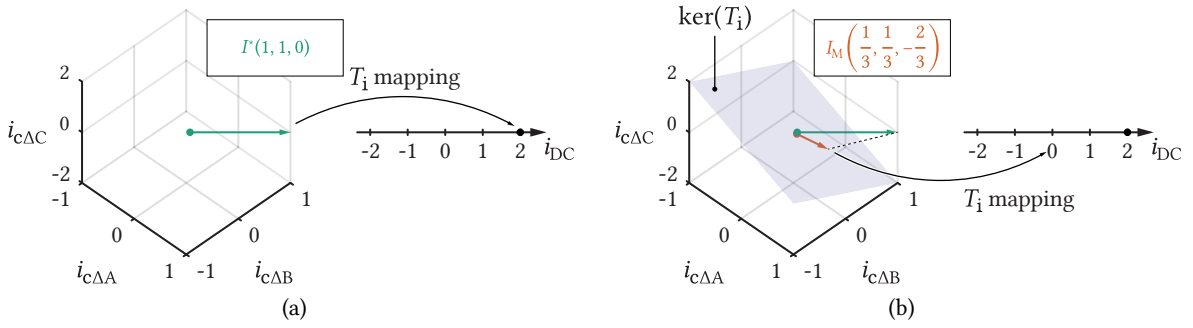


**Fig. 3.18** (a) Mapping of an arbitrary vector of circulating current references to the DC link in case 3PH MMC is observed; (b) Projection of the reference vector  $\vec{I}^*$  which does not satisfy (3.51) onto the null-space of mapping matrix  $T_i$ . As stated above, the number of basis vectors in the null-space of the mapping matrix equals  $N - 1$ , therefore  $\dim(\ker(T_i)) = 2$ , meaning that all the vectors satisfying the condition  $T_i \vec{I} = 0$  reside in a plane.

Basically, the problem of balancing comes down to the identification of a suitable vector  $\vec{I}_M$  which represents the projection of the original reference  $\vec{I}^*$  onto the null-space of  $T_i$ . For this purpose, the Singular Value Decomposition (SVD) can be used, whose detailed explanation can be found in **App. A**.

As explained in **App. A**, if a random matrix  $T_i$  is applied to a set of basis vectors  $\vec{V}_i$ , they are stretched and rotated, as presented in **Fig. A.1**, consequently providing a set of new basis vectors  $\vec{U}_i$ .

$$T_i \underbrace{\begin{bmatrix} \vec{V}_1 & \dots & \vec{V}_n \end{bmatrix}}_V = \underbrace{\begin{bmatrix} \vec{u}_1 & \dots & \vec{u}_m \end{bmatrix}}_U \underbrace{\begin{bmatrix} \sigma_1 & \dots & 0 \\ \vdots & \sigma_r & 0 \\ 0 & \dots & 0 \end{bmatrix}}_\Sigma \quad (3.56)$$

The above equation can be rearranged as

$$T_i = U \Sigma V^* \quad (3.57)$$

In (3.57),  $V^*$  represents the conjugate transpose of  $V$ . If  $V$  is real,  $V^* = V^T$  is true, and (3.57) can be simplified as

$$\underbrace{T_i}_{m \times n} = \underbrace{U}_{m \times m} \underbrace{\Sigma}_{m \times n} \underbrace{V^T}_{n \times n} \quad (3.58)$$

It is noteworthy that projection of the reference vector  $\vec{I}^*$  onto the null-space of  $T_i$  provides the solution satisfying the least squares criteria. In other words, the tip of every vector different from  $\vec{I}_M$ , and being in  $\ker(T_i)$ , falls further from the tip of  $\vec{I}^*$  when compared to  $\vec{I}_M$  itself. However, the null-space of a matrix needs to be firstly defined and the SVD can be used for this purpose.



Since matrices  $U$  and  $V$  from (3.57) are unitary (rotation) matrices (please check **App. A**), it is clear that neither of them can compress a vector to zero (unless the vector itself is a zero vector). Also, (3.58) can be expressed as (3.59), which is the form derived in (A.35).

$$T_i = \underbrace{\begin{bmatrix} U_R & U_N \end{bmatrix}}_{m \times m} \underbrace{\begin{bmatrix} S_{r \times r} & 0 \\ 0 & 0 \end{bmatrix}}_{m \times n} \underbrace{\begin{bmatrix} V_R^* \\ V_N^* \end{bmatrix}}_{n \times n} \quad (3.59)$$

It can be seen from the above equation that matrix  $\Sigma$  contains a square submatrix with elements different than zero and  $n - r$  zero vectors. Number of zero vectors in  $\Sigma$  corresponds to the number of orthogonal vectors comprising an orthonormal basis for  $\ker(T_i)$  (please notice that a set of vectors  $B = \{\vec{v}_1, \dots, \vec{v}_n\}$  is said to be the basis of a space  $\Omega \subset \mathbb{R}^n$  if all the vectors from  $B$  are linearly independent while every vector from  $\Omega$  can be expressed through their linear combination).

Prior to identifying the basis of  $\ker(T_i)$ , (3.59) should be analyzed more thoroughly. By performing a matrix multiplication, this expression can be rewritten as

$$T_i = \underbrace{U_R}_{m \times r} \underbrace{S}_{r \times r} \underbrace{V_R^*}_{r \times n} \quad (3.60)$$

The above equation indicates that any column from  $T_i$  can be obtained through the linear combination of vectors from  $U_R$ . By the definition of SVD, all the vectors from  $U$  are orthogonal, meaning that the number of independent columns of  $T_i$  equals to the number of vectors composing the matrix  $U_R$  (which equals  $r$ ). In other words,  $r$  represents the rank of  $T_i$ . Moreover, as all the vectors from  $U_R$  have magnitude equal to one, this matrix is referred to as the orthonormal basis of the column space of  $T_i$ .

Also, as the number of vectors in  $V_R$  equals  $r$ , the number of vectors in  $V_N$  equals  $n - r$ . Let one define  $V_N = \begin{bmatrix} \vec{v}_{N,1} & \dots & \vec{v}_{N,n-r} \end{bmatrix}$  and look for  $T_i \vec{v}_{N,j}$ , where  $1 \leq j \leq n - r$ .

$$T_i \vec{v}_{N,j} = \begin{bmatrix} U_R & U_N \end{bmatrix} \begin{bmatrix} S_{r \times r} & 0 \\ 0 & 0 \end{bmatrix} \begin{bmatrix} V_R^T \\ V_N^T \end{bmatrix} \vec{v}_{N,j} \quad (3.61)$$

As all the vectors from  $V$  are orthogonal, it can be said that  $V_R^T \vec{v}_{N,j} = 0_{r \times n}$ , from where one can see that  $T_i \vec{v}_{N,j} = 0$ . Therefore, every vector from  $V_N$  is in the null-space of  $T_i$ . Additionally, given that all the vectors from  $V_N$  are orthogonal, they could be called a basis of the  $\ker(T_i)$  providing their number is enough to support this claim.

According to the rank-nullity theorem [95], for any matrix  $T_{m \times n}$ , expression (3.62) holds. Consequently, dimension of the null-space (in other words, number of independent vectors comprising the null-space) corresponds to the number of vectors in  $V_N$ .

$$n = \text{rank}(T_i) + \dim(\ker(T_i)) \quad (3.62)$$

In summary, matrix  $V_N$  can be called the basis of the null-space of  $T_i$  since:

- All the vectors from  $V_N$  are in the null-space of  $T_i$
- All the vectors from  $V_N$  are independent (moreover, they are orthogonal)
- Number of vectors in  $V_N$  corresponds to the dimension of the null-space

Once the orthogonal basis of  $\ker(T_i)$  is identified, the vector demanded by the converter balancing controllers  $\vec{I}^*$  must be mapped into a suitable vector  $\vec{I}_M$ . Henceforth, matrix  $V_N$  will be denoted by  $B$  (in order to suggest its basis nature) and in case basis vectors  $B = [\vec{v}_{N,1}, \dots, \vec{v}_{N,n-r}]$  are at disposal, (3.63) is to be observed at first instance.

$$B^T \vec{I}^* = \begin{bmatrix} \vec{v}_{N,1}^T \\ \vec{v}_{N,2}^T \\ \vdots \\ \vec{v}_{N,n-k}^T \end{bmatrix} \vec{I}^* = \underbrace{\begin{bmatrix} \langle \vec{v}_{N,1}, \vec{I}^* \rangle \\ \langle \vec{v}_{N,2}, \vec{I}^* \rangle \\ \vdots \\ \langle \vec{v}_{N,n-k}, \vec{I}^* \rangle \end{bmatrix}}_{\text{scalar products}} \quad (3.63)$$

The vector on the right hand side of (3.63) contains scalar products of orthogonal basis vectors and a balancing reference vector  $\vec{I}^*$ . Given that  $|\vec{v}_{N,k}| = 1$ , these scalar products actually represent projections of the vector  $\vec{I}^*$  onto the basis vectors from  $B$ . However, these are the coordinates of the vector  $\vec{I}^*$  in a new coordinate system consisting of vectors  $\vec{v}_{N,k}$ . To obtain the coordinates of the new vector in the conventional reference frame (which actually is the vector  $\vec{I}_M$ ), the term  $B^T \vec{I}^*$  needs to be multiplied by  $B$ , which yields (3.64). Please notice that identical, though scaled down, problem was presented in **Figs. 3.16(a)** and **3.16(b)**. Therefore, as stated in one of the previous paragraphs, irrespective of the problem dimension, the required reference mapping procedure remains unchanged.

$$BB^T \vec{I}^* = \begin{bmatrix} \vec{v}_{N,1} & \vec{v}_{N,2} & \dots & \vec{v}_{N,n-k} \end{bmatrix} \begin{bmatrix} \langle \vec{v}_{N,1}, \vec{I}^* \rangle \\ \langle \vec{v}_{N,2}, \vec{I}^* \rangle \\ \vdots \\ \langle \vec{v}_{N,n-k}, \vec{I}^* \rangle \end{bmatrix} = \sum_{j=1}^{n-k} \vec{v}_{N,j} \langle \vec{v}_{N,j}, \vec{I}^* \rangle \quad (3.64)$$

An advantage of the presented principle is that once the balancing current components are identified per each leg, one should only define the converter terminal mapping matrix to apply (3.64).

The null-space of the matrix  $T_i$  from (3.51) can be identified by firstly creating its SVD form (3.65). Please notice that detailed procedure which resulted in (3.65) can be found in **Sec. A.5**.

$$T_i = \begin{bmatrix} 1 \\ 1 \end{bmatrix} \begin{bmatrix} \sqrt{3} & 0 & 0 \\ 0 & 0 & 0 \\ 0 & 0 & 0 \end{bmatrix} \sqrt{\frac{2}{3}} \begin{bmatrix} \frac{1}{\sqrt{2}} & \frac{1}{\sqrt{2}} & \frac{1}{\sqrt{2}} \\ 1 & -\frac{1}{2} & -\frac{1}{2} \\ 0 & \frac{\sqrt{3}}{2} & -\frac{\sqrt{3}}{2} \end{bmatrix} \quad (3.65)$$

From here, matrix  $B$  can be easily identified as

$$B = \sqrt{\frac{2}{3}} \begin{bmatrix} 1 & 0 \\ -\frac{1}{2} & \frac{\sqrt{3}}{2} \\ -\frac{1}{2} & -\frac{\sqrt{3}}{2} \end{bmatrix} \quad (3.66)$$

It is important to notice that the choice of the basis vectors of  $\ker(T_i)$  is not unique. Any other orthogonal pair being a subset of  $\ker(T_i)$  could also be chosen. However, the vectors from (3.66) were selected for the reasons which are to become clear shortly. Following (3.64), the mapping of the circulating current references obtained according to **Fig. 3.14** can be performed as

$$\begin{aligned} \vec{I}_M &= \underbrace{\begin{bmatrix} \sqrt{\frac{2}{3}} & 0 \\ \frac{1}{\sqrt{6}} & \frac{1}{\sqrt{2}} \\ -\frac{1}{\sqrt{6}} & -\frac{1}{\sqrt{2}} \end{bmatrix}}_B \underbrace{\begin{bmatrix} \sqrt{\frac{2}{3}} & -\frac{1}{\sqrt{6}} & -\frac{1}{\sqrt{6}} \\ 0 & \frac{1}{\sqrt{2}} & -\frac{1}{\sqrt{2}} \end{bmatrix}}_{B^T} \vec{I} \\ &= \frac{1}{3} \begin{bmatrix} 2 & -1 & -1 \\ -1 & 2 & -1 \\ -1 & -1 & 2 \end{bmatrix} \vec{I} \end{aligned} \quad (3.67)$$

Now, once the appropriate mapping to the null-space of the DC terminal matrix is obtained, a solid foundation for the discussion on two different balancing directions is established.

### 3.6.2.1 Horizontal balancing

By inspecting **Fig. 3.14**, one can come up with the expression defining the vector of mapped circulating current references as

$$\vec{I}_M = \underbrace{BB^T H_{c\Sigma}(s) \frac{1}{V_{DC}^*}}_{\vec{I}_{cA}} (W_{\Sigma}^* - \vec{W}_{\Sigma}), \quad (3.68)$$

where  $\vec{W}_{\Sigma} = \begin{bmatrix} W_{\Sigma A} & W_{\Sigma B} & W_{\Sigma C} \end{bmatrix}^T$  along with the PI controller transfer function being denoted by  $H_{c\Sigma}(s)$ .

Given that the ultimate goal of the MMC control, in general sense, is to provide references for the upper and lower branch voltages, the output of the circulating current controllers is to be investigated further.

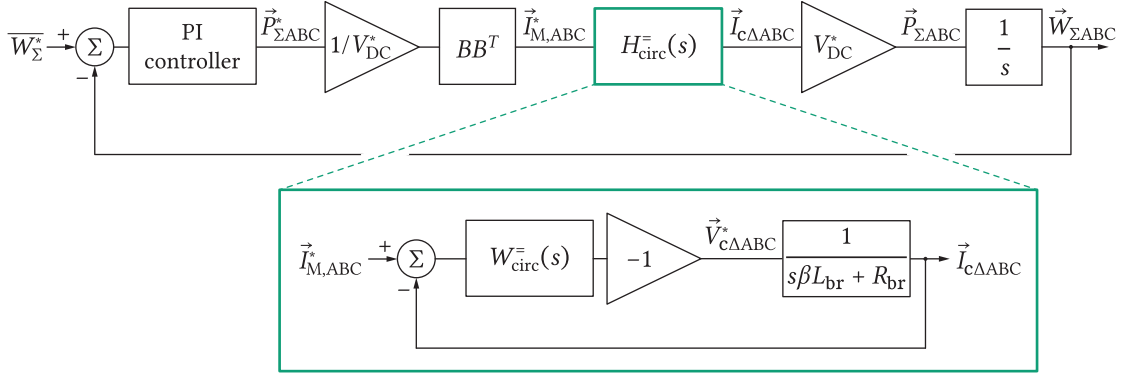


**Fig. 3.19** Control block diagram of circulating current components maintaining the energy balance in horizontal direction (ABC domain)

According to **Fig. 3.9**, the vector of legs' common mode voltages  $\vec{V}_{c\Delta}^* = \begin{bmatrix} V_{c\Delta A}^* & V_{c\Delta B}^* & V_{c\Delta C}^* \end{bmatrix}^T$  can be acquired as

$$\vec{V}_{c\Delta}^* = -W_{\text{circ}}^{\text{=}}(s)(\vec{I}_M - \vec{I}_{c\Delta}) \quad (3.69)$$

Please notice that capital letters denote that DC components of circulating currents are controlled in this case. Such a statement was derived by observing the system of equations (3.47) and (3.48). Accordingly, the control block diagram of circulating currents being in charge of the horizontal balancing can be established as depicted in **Fig. 3.19**.

**Fig. 3.19** suggests that the control of circulating currents can be done for all the legs separately (ABC domain). However, the matrix  $B^T$  represents the well known  $\alpha\beta$  transformation, although with the scaling coefficient equal to  $\sqrt{2/3}$ , hence (3.68) can be rewritten as (3.70) in case  $W_{\Sigma A}^* = W_{\Sigma B}^* = W_{\Sigma C}^*$  is assumed.

$$\vec{I}_M = -BH_{c\Sigma}(s)\frac{1}{V_{DC}^*}\vec{W}_{\Sigma\alpha\beta} \quad (3.70)$$

Substitution of (3.70) into (3.69) results in

$$\vec{V}_{c\Delta}^* = -W_{\text{circ}}^{\text{=}}(s)\left(-BH_{c\Sigma}(s)\frac{1}{V_{DC}^*}\vec{W}_{\Sigma\alpha\beta} - \vec{I}_{c\Delta}\right) \quad (3.71)$$

Left multiplication of both sides of the previous equation with  $B^T$ , yields

$$\vec{V}_{c\Delta\alpha\beta}^* = -W_{\text{circ}}^{\text{=}}(s)\left(-H_{c\Sigma}(s)\frac{1}{V_{DC}^*}\vec{W}_{\Sigma\alpha\beta} - \vec{I}_{c\Delta\alpha\beta}\right) \quad (3.72)$$

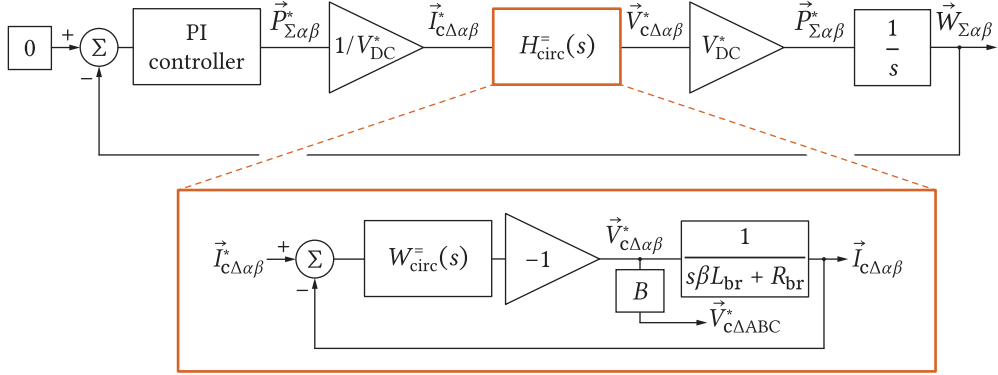


**Fig. 3.20** Control block diagram of circulating current components maintaining the energy balance in horizontal direction ( $\alpha\beta$  domain)

Expression (3.72) indicates that horizontal balancing can be performed in the  $\alpha\beta$  domain, as presented in **Fig. 3.20**. This method of horizontal balancing was proposed in [90], [91]. Nevertheless, previously derived set of equations indicates that irrespective of the reference frame being used for the generation of circulating current references, the obtained results are the same [96], which is also confirmed in **Sec. 3.7**.

### 3.6.2.2 Vertical balancing

It was shown above that the methods proposed in [77], [90], [91] result in identical references concerning horizontal balancing. However, vertical balancing introduces the need for mapping of the current references changing according to the sinusoidal law (3.46), which introduces the non-linearity to the process of analysis. Seemingly different methods were proposed in [77], [90], [91], therefore, the upcoming paragraphs provide a thorough description of these. For the sake of simplicity, three methods proposed in [77], [90], [91] will be referred to as Method 1, 2 and 3, respectively.

#### Method 1

Once again, the analysis on the MMC balancing currents, however, in the vertical direction, commences by observing **Fig. 3.14**. Accordingly, (3.73) can be derived in case  $W_{\Delta A}^* = W_{\Delta B}^* = W_{\Delta C}^* = 0$ , from where one can construct the control block diagram presented in **Fig. 3.21**.

$$\vec{i}_M = BB^T \frac{H_{c\Delta}(s)}{\hat{v}_s} \underbrace{\begin{bmatrix} \cos(\omega_g t - \gamma) & 0 & 0 \\ 0 & \cos(\omega_g t - \gamma - \frac{2\pi}{3}) & 0 \\ 0 & 0 & \cos(\omega_g t - \gamma + \frac{2\pi}{3}) \end{bmatrix}}_{\vec{i}_{c\Delta}} \begin{bmatrix} W_{\Delta A} \\ W_{\Delta B} \\ W_{\Delta C} \end{bmatrix} \quad (3.73)$$

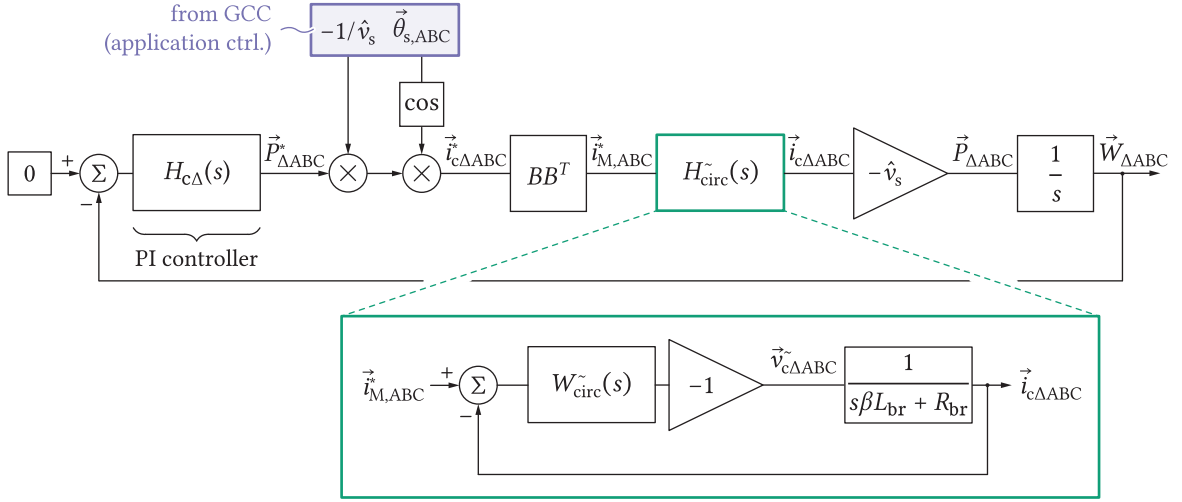


**Fig. 3.21** Control block diagram concerning circulating currents AC component (ABC frame) [77]

Nevertheless, an alternative approach can be adopted in identifying the nature of components generated by the mapping denoted by  $BB^T$  in the above equation. Given that coordinates of the vector  $\tilde{i}_M$  change in time, following the trigonometric law, the phasor representation (underlined quantities) can be adopted, leading to

$$\underline{\tilde{i}_M} = BB^T \frac{H_{c\Delta}(s)}{\hat{v}_s} e^{-j\gamma} \underbrace{\begin{bmatrix} 1 & 0 & 0 \\ 0 & a^2 & 0 \\ 0 & 0 & a \end{bmatrix}}_A \begin{bmatrix} W_{\Delta A} \\ W_{\Delta B} \\ W_{\Delta C} \end{bmatrix}, \quad (3.74)$$

where  $a = e^{j\frac{2\pi}{3}}$ .

Mapping of the reference vector  $\tilde{i}_{c\Delta}$  onto the null-space of matrix  $T_i$  implies that Fortescue transformation (3.75) applied to  $\underline{\tilde{i}_M}$ , must output only positive and negative circulating current sequences. To put in differently, zero sequence vector, which causes the DC link disturbance, equals zero.

$$F_{pno} = \frac{1}{3} \begin{bmatrix} 1 & a & a^2 \\ 1 & a^2 & a \\ 1 & 1 & 1 \end{bmatrix} \quad (3.75)$$

Left multiplication of both sides of (3.74) with  $F_{pno}$ , gives

$$\begin{bmatrix} \tilde{i}_{Mp} \\ \tilde{i}_{Mn} \\ \tilde{i}_{M0} \end{bmatrix} = \frac{H_{c\Delta}(s)}{\hat{v}_s} e^{-j\gamma} \begin{bmatrix} \frac{1}{3} (W_{\Delta A} + W_{\Delta B} + W_{\Delta C}) \\ \frac{1}{3} \left( W_{\Delta A} - \frac{W_{\Delta B}}{2} - \frac{W_{\Delta C}}{2} \right) + j\frac{1}{3} \frac{\sqrt{3}}{2} (W_{\Delta B} - W_{\Delta C}) \\ 0 \end{bmatrix} \quad (3.76)$$

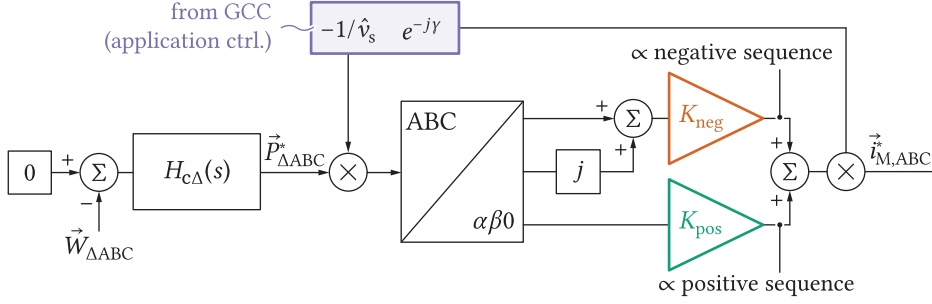


**Fig. 3.22** An alternative way of generating the circulating current references achieving the balancing in vertical direction. Multiplication constants denoted with  $K_{pos}$  and  $K_{neg}$  equal  $1/\sqrt{3}$  and  $1/\sqrt{6}$ , respectively. As will be seen in the upcoming paragraphs, these constants will be useful in the process of comparing different methods of vertical balancing reported in the literature.

From the above equation, it can be verified that zero component of the mapped references indeed corresponds to zero. Nevertheless, positive and negative circulating current sequences resemble the quantities acquired by means of the  $\alpha\beta$  transformation (A.51). Hence, (3.77) and (3.78) can be derived. As the reference of the circulating current component considered in this case can be obtained by summing (3.77) and (3.78), block diagram depicted in **Fig. 3.22** can be created. Its purpose will be revealed shortly after commencing the discussion on another set of possible ways of generating circulating current references ensuring vertical balancing.

$$\tilde{i}_{Mp} = \frac{H_{c\Delta}(s)}{\hat{v}_s} e^{-j\gamma} \times \frac{1}{\sqrt{3}} W_{\Delta 0} \quad (3.77)$$

$$\tilde{i}_{Mn} = \frac{H_{c\Delta}(s)}{\hat{v}_s} e^{-j\gamma} \times \frac{1}{\sqrt{6}} (W_{\Delta\alpha} + j W_{\Delta\beta}) \quad (3.78)$$

## Method 2

According to the previous paragraph, there exists another method for generating circulating current components ensuring vertical balancing. Furthermore, this method does not rely upon the application of SVD nor does it require one to obtain any linear algebra knowledge. Conversely, the idea presented in [90] relies on the injection of orthogonal (reactive) current components in each of the MMC legs with the aim of allowing for the constraint defined in (3.27) to be satisfied.

With the aim of providing a thorough insight into the above mentioned method, the analysis can take the case presented in **Fig. 3.23** into consideration. From the left-most phasor diagram, one can notice that sum of the circulating current references generated in "per-leg" fashion differs from zero. Now, let one observe phasor  $\tilde{i}_{c\Delta A}$  while neglecting the other two legs' balancing references. To perform the cancellation of the current defined by this phasor in the DC link, two currents can be added into the legs B and C, as presented in the middle plot on the figure bellow. What is of crucial importance is that current components  $\tilde{i}_{c\Delta B}^A$  and  $\tilde{i}_{c\Delta C}^A$  do not contribute to any active power transfer in the phases they are injected to. For instance,  $\tilde{i}_{c\Delta B}^A$  denotes the current component injected in the leg labeled with B with the aim of partially canceling the circulating current generated in the leg A. As can be seen, this component is orthogonal to the AC voltage  $v_{sB}$ . Consequently only reactive power is generated. This is an important detail since the reactive power can not contribute to the change of the average energy in any of the converter's branches.

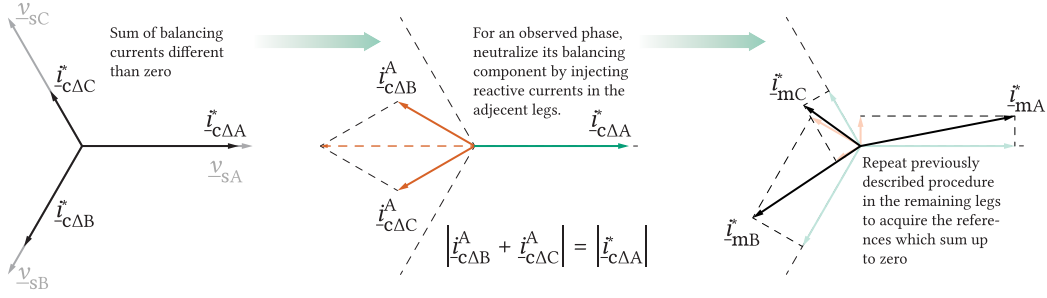


**Fig. 3.23** Vertical balancing procedure based on the injection of orthogonal components into the circulating currents of all the legs [90].

According to the above discussion, the vector of circulating current references satisfying  $\sum_i i_{c\Delta i} = 0$ , can be obtained as

$$\vec{i}_M = M_m \frac{H_{c\Delta}(s)}{\hat{v}_s} \begin{bmatrix} \cos(\omega_g t - \gamma) & 0 & 0 \\ 0 & \cos(\omega_g t - \gamma - \frac{2\pi}{3}) & 0 \\ 0 & 0 & \cos(\omega_g t - \gamma + \frac{2\pi}{3}) \end{bmatrix} \begin{bmatrix} W_{\Delta A} \\ W_{\Delta B} \\ W_{\Delta C} \end{bmatrix} \quad (3.79)$$

Please notice that, compared to (3.73), the mapping matrix  $BB^T$  was replaced by another mapping matrix  $M_m$ , while  $W_{\Delta}^* = 0$  holds for each one of the legs. As the matrix  $M_m$  indicates rotation of phasors (shifting of components in time), observing it through the complex domain is considered more convenient, thus

$$\vec{i}_M = \frac{H_{c\Delta}(s)}{\hat{v}_s} e^{-j\gamma} \underbrace{\begin{bmatrix} 1 & j\frac{a}{\sqrt{3}} & -j\frac{a^2}{\sqrt{3}} \\ -j\frac{a^2}{\sqrt{3}} & 1 & j\frac{a}{\sqrt{3}} \\ j\frac{a}{\sqrt{3}} & -j\frac{a^2}{\sqrt{3}} & 1 \end{bmatrix}}_{M_m} \underbrace{\begin{bmatrix} 1 & 0 & 0 \\ 0 & a^2 & 0 \\ 0 & 0 & a \end{bmatrix}}_A \begin{bmatrix} W_{\Delta A} \\ W_{\Delta B} \\ W_{\Delta C} \end{bmatrix} \quad (3.80)$$

Multiplying both sides of (3.80) with  $F_{pn0}$ , defined in (3.75), from the left, gives

$$\begin{bmatrix} \tilde{i}_{Mp} \\ \tilde{i}_{Mn} \\ \tilde{i}_{M0} \end{bmatrix} = \frac{H_{c\Delta}(s)}{\hat{v}_s} e^{-j\gamma} \begin{bmatrix} \frac{1}{3} (W_{\Delta A} + W_{\Delta B} + W_{\Delta C}) \\ \frac{2}{3} \left( W_{\Delta A} - \frac{W_{\Delta B}}{2} - \frac{W_{\Delta C}}{2} \right) + j\frac{2\sqrt{3}}{3} (W_{\Delta B} - W_{\Delta C}) \\ 0 \end{bmatrix} \quad (3.81)$$

Once again, the  $\alpha\beta$  transformation (A.51) is recalled in order to express the above components in a slightly different fashion, providing one with (3.82) and (3.83).



$$\tilde{i}_{Mp} = \frac{H_{c\Delta}(s)}{\hat{v}_s} e^{-j\gamma} \times \frac{1}{\sqrt{3}} W_{\Delta 0} \quad (3.82)$$

$$\tilde{i}_{Mn} = \frac{H_{c\Delta}(s)}{\hat{v}_s} e^{-j\gamma} \times \frac{2}{\sqrt{6}} (W_{\Delta\alpha} + jW_{\Delta\beta}) \quad (3.83)$$

Now, once the decomposition into symmetrical components is established, a short comparison between the presented methods, ensuring the MMC vertical balancing, can be made. By comparing (3.77) and (3.82) one can not observe the difference in the positive sequence of circulating currents, irrespective of the analyzed method. Notwithstanding, comparison of (3.78) and (3.83) shows that the method based on the injection of orthogonal currents presented in [90] requires a circulating current negative sequence twice as high as the one obtained by the mapping to the null-space of the matrix representing the summation of circulating current references in the converter's DC link [77]. Consequently, the block diagram depicted in **Fig. 3.22** can be reused, however, with the constant labeled with  $K_{neg}$  being doubled and equal to  $2/\sqrt{6}$ .

As demonstrated above, Methods 1 and 2 differ only by the multiplication constant  $K_{neg}$ . Hence, current references synthesized through any of these two methods can also be obtained through the independent control of current components labeled with  $\tilde{i}_{Mp}$  and  $\tilde{i}_{Mn}$ . Actually, this represents the underlying basis of the method described in the following few paragraphs.

### Method 3

Throughout **Sec. 3.6.2**, it was proven that rows of the matrix used to perform the  $\alpha\beta 0$  transformation (A.51) represent the bases of the null-space of matrix  $T_i$  from (3.51). To a certain extent, this is the indication that vertical balancing, similarly to horizontal, can be performed directly in the  $\alpha\beta 0$  domain by means of relevant power components, which can be found bellow.

$$\frac{d}{dt} \begin{bmatrix} W_{\Delta\alpha} \\ W_{\Delta\beta} \\ W_{\Delta 0} \end{bmatrix} = \begin{bmatrix} P_{\Delta\alpha} \\ P_{\Delta\beta} \\ P_{\Delta 0} \end{bmatrix} = \sqrt{\frac{2}{3}} \begin{bmatrix} 1 & -\frac{1}{\sqrt{3}} & -\frac{1}{\sqrt{3}} \\ 0 & \frac{2}{\sqrt{3}} & -\frac{2}{\sqrt{3}} \\ \frac{1}{\sqrt{2}} & \frac{1}{\sqrt{2}} & \frac{1}{\sqrt{2}} \end{bmatrix} \begin{bmatrix} P_{\Delta A} \\ P_{\Delta B} \\ P_{\Delta C} \end{bmatrix} \quad (3.84)$$

As it was shown in **Sec. 3.6**, a proper control of converter's internal energies requires identification of circulating current components fulfilling this task. Given that  $i_{c\Delta 0} = 0$ , the set of power components  $P_{\Delta} = \{P_{\Delta\alpha}, P_{\Delta\beta}, P_{\Delta 0}\}$  needs to be linked with the circulating currents expressed in the  $\alpha\beta$  domain. For that purpose, two  $dq$  systems, rotating in the opposite directions, were introduced in [91] giving

$$\begin{bmatrix} i_{c\Delta\alpha} \\ i_{c\Delta\beta} \end{bmatrix} = \underbrace{\begin{bmatrix} \cos(\theta) & -\sin(\theta) \\ \sin(\theta) & \cos(\theta) \end{bmatrix}}_{\text{counterclockwise rotation}} \begin{bmatrix} i_{c\Delta d}^+ \\ i_{c\Delta q}^+ \end{bmatrix} + \underbrace{\begin{bmatrix} \cos(\theta) & \sin(\theta) \\ -\sin(\theta) & \cos(\theta) \end{bmatrix}}_{\text{clockwise rotation}} \begin{bmatrix} i_{c\Delta d}^- \\ i_{c\Delta q}^- \end{bmatrix}, \quad (3.85)$$

where  $\theta = \omega_g t - \gamma$ , which unveils the alignment between the  $dq$  system rotating in the counterclockwise direction and the vector of AC voltages synthesized by the MMC branches.

A set of tedious mathematical steps, which are omitted here as they can be found in [91], shows that

$$\begin{aligned} P_{\Delta\alpha} &= -\frac{2}{\sqrt{6}} \hat{v}_s i_{c\Delta d}^- \\ P_{\Delta\beta} &= +\frac{2}{\sqrt{6}} \hat{v}_s i_{c\Delta q}^- \\ P_{\Delta 0} &= -\frac{2}{\sqrt{3}} \hat{v}_s i_{c\Delta d}^+ \end{aligned} \quad (3.86)$$

from where one can see that the component  $i_{c\Delta q}^+$  can be controlled to zero as it does not take part in the control of the above power components. On the other hand, a proper control of circulating current components denoted by  $i_{c\Delta d}^+$ ,  $i_{c\Delta d}^-$  and  $i_{c\Delta q}^-$  ensures balancing in the vertical direction. Further, as the matrix from (A.51) is full-rank, circulating currents in the  $ABC$  domain can be obtained as

$$\begin{bmatrix} i_{c\Delta A} \\ i_{c\Delta B} \\ i_{c\Delta C} \end{bmatrix} = \sqrt{\frac{2}{3}} \begin{bmatrix} 1 & 0 \\ -\frac{1}{2} & \frac{\sqrt{3}}{2} \\ \frac{1}{2} & -\frac{\sqrt{3}}{2} \end{bmatrix} \left( \begin{bmatrix} \cos(\theta) & -\sin(\theta) \\ \sin(\theta) & \cos(\theta) \end{bmatrix} \begin{bmatrix} i_{c\Delta d}^+ \\ i_{c\Delta q}^+ \end{bmatrix} + \begin{bmatrix} \cos(\theta) & \sin(\theta) \\ -\sin(\theta) & \cos(\theta) \end{bmatrix} \begin{bmatrix} i_{c\Delta d}^- \\ i_{c\Delta q}^- \end{bmatrix} \right) \quad (3.87)$$

Translating (3.87) into the complex domain, followed by the left multiplication with  $F_{pn0}$ , from (3.75), yields

$$\begin{bmatrix} \tilde{i}_{Mp} \\ \tilde{i}_{Mn} \\ \tilde{i}_{M0} \end{bmatrix} = \sqrt{\frac{2}{3}} e^{-j\gamma} \begin{bmatrix} 1 & j & 0 & 0 \\ 0 & 0 & 1 & -j \\ 0 & 0 & 0 & 0 \end{bmatrix} \begin{bmatrix} i_{c\Delta d}^+ \\ i_{c\Delta q}^+ \\ i_{c\Delta d}^- \\ i_{c\Delta q}^- \end{bmatrix} \quad (3.88)$$

Combining (3.84) and (3.86) with the fact that  $P_{\Delta\{\alpha/\beta/0\}} = -H_{c\Delta} W_{\Delta\{\alpha/\beta/0\}}$  (which is valid according to **Figs. 3.21** and **3.22**, where legs' delta energy references were set as zero) along with  $i_{c\Delta q}^+ = 0$ , leads to

$$\begin{bmatrix} \tilde{i}_{Mp} \\ \tilde{i}_{Mn} \\ \tilde{i}_{M0} \end{bmatrix} = \sqrt{\frac{2}{3}} \frac{H_{c\Delta}(s)}{\hat{v}_s} e^{-j\gamma} \begin{bmatrix} 1 & 0 & 0 \\ 0 & 1 & -j \\ 0 & 0 & 0 \end{bmatrix} \begin{bmatrix} \frac{\sqrt{3}}{2} & 0 & 0 \\ 0 & \frac{\sqrt{6}}{2} & 0 \\ 0 & 0 & -\frac{\sqrt{6}}{2} \end{bmatrix} \begin{bmatrix} W_{\Delta 0} \\ W_{\Delta\alpha} \\ W_{\Delta\beta} \end{bmatrix} \quad (3.89)$$

From (3.89), the positive and negative sequence phasors can be obtained as (3.90) and (3.91), respectively, which corresponds to the form introduced in **Fig. 3.22**.

**Tab. 3.1** Coefficients determining the method used to obtain the balancing in vertical direction

	Method 1	Method 2	Method 3
$K_{\text{pos}}$	$\frac{1}{\sqrt{3}}$	$\frac{1}{\sqrt{3}}$	$\frac{1}{\sqrt{2}}$
$K_{\text{neg}}$	$\frac{1}{\sqrt{6}}$	$\frac{1}{\sqrt{6}}$	$1$

$$\tilde{i}_{\text{Mp}} = \frac{H_{\text{c}\Delta}(s)}{\hat{v}_s} e^{-j\gamma} \times \frac{1}{\sqrt{2}} W_{\Delta 0} \quad (3.90)$$

$$\tilde{i}_{\text{Mn}} = \frac{H_{\text{c}\Delta}(s)}{\hat{v}_s} e^{-j\gamma} \times (W_{\Delta\alpha} + jW_{\Delta\beta}) \quad (3.91)$$

Since the components defining the circulating current positive and negative sequence can be expressed in the form presented in **Fig. 3.22**, the values of coefficients  $K_{\text{pos}}$  and  $K_{\text{neg}}$  for different balancing methods can be summarized as in **Tab. 3.1**. What is straightforward to conclude is that vertical balancing methods analyzed so far differ only in terms of the multiplication constants, whereas the structure of the control block diagram used in **Fig. 3.22** remains legit at all times.

### Methods comparison

Prior to proceeding further with the comparison of vertical balancing methods described so far, it is important to emphasize that (3.86) represents a general equation. In other words, it is valid irrespective of the employed balancing method. Additionally, symmetrical components obtained through the Fortescue transformation of the circulating current references can be expressed in a general form as

$$\tilde{i}_{\text{Mp}} = \frac{H_{\text{c}\Delta}(s)}{\hat{v}_s} e^{-j\gamma} \times K_{\text{pos}} W_{\Delta 0} \quad (3.92)$$

$$\tilde{i}_{\text{Mn}} = \frac{H_{\text{c}\Delta}(s)}{\hat{v}_s} e^{-j\gamma} \times K_{\text{neg}} (W_{\Delta\alpha} + jW_{\Delta\beta}) \quad (3.93)$$

Also, (3.88) can be further expanded to obtain the system of equations (3.94).

$$\begin{aligned} i_{\text{c}\Delta d}^+ &= \Re \left( \sqrt{\frac{3}{2}} e^{j\gamma} \tilde{i}_{\text{Mp}} \right) \\ i_{\text{c}\Delta q}^+ &= \Im \left( \sqrt{\frac{3}{2}} e^{j\gamma} \tilde{i}_{\text{Mp}} \right) \\ i_{\text{c}\Delta d}^- &= \Re \left( \sqrt{\frac{3}{2}} e^{j\gamma} \tilde{i}_{\text{Mn}} \right) \\ i_{\text{c}\Delta q}^- &= -\Im \left( \sqrt{\frac{3}{2}} e^{j\gamma} \tilde{i}_{\text{Mn}} \right) \end{aligned} \quad (3.94)$$

According to (3.92) and (3.94), the circulating current component  $i_{c\Delta q}^+$  equals zero for Methods 1 and 2 since  $e^{j\gamma} \tilde{i}_{Mp}$  is always a real number, whereas it is directly controlled to zero in case Method 3 is considered. Consequently,

$$\begin{aligned} i_{c\Delta d}^+ &= \sqrt{\frac{3}{2}} K_{\text{pos}} \frac{H_{c\Delta}}{\hat{v}_s} W_{\Delta 0} \\ i_{c\Delta d}^- &= \sqrt{\frac{3}{2}} K_{\text{neg}} \frac{H_{c\Delta}}{\hat{v}_s} W_{\Delta \alpha} \\ i_{c\Delta d}^- &= -\sqrt{\frac{3}{2}} K_{\text{neg}} \frac{H_{c\Delta}}{\hat{v}_s} W_{\Delta \beta} \end{aligned} \quad (3.95)$$

Systems of equations (3.86) and (3.95) can be connected in order to establish (3.96).

$$\begin{aligned} P_{\Delta 0} &= -\sqrt{2} K_{\text{pos}} H_{c\Delta} W_{\Delta 0} \\ P_{\Delta \alpha} &= -K_{\text{neg}} H_{c\Delta} W_{\Delta \alpha} \\ P_{\Delta \beta} &= -K_{\text{neg}} H_{c\Delta} W_{\Delta \beta} \end{aligned} \quad (3.96)$$

It is straightforward to see from the above system that the relationship between the relevant power and delta energy components can always be found in the form of  $P_{\Delta\{\alpha/\beta/0\}} = -K_1 H_{c\Delta} W_{\Delta\{\alpha/\beta/0\}}$ . According to (3.86), similar connection can be established between the  $\alpha\beta 0$  power components with their associated  $dq$  pairs as  $P_{\Delta\{\alpha/\beta/0\}} = K_2 \hat{v}_s i_{c\Delta\{d^-/q^-/d^+\}}$ . Consequently, the control block diagram concerning the energy components  $W_{\Delta\{\alpha/\beta/0\}}$  can be provided in a general form, as depicted in the figure bellow.

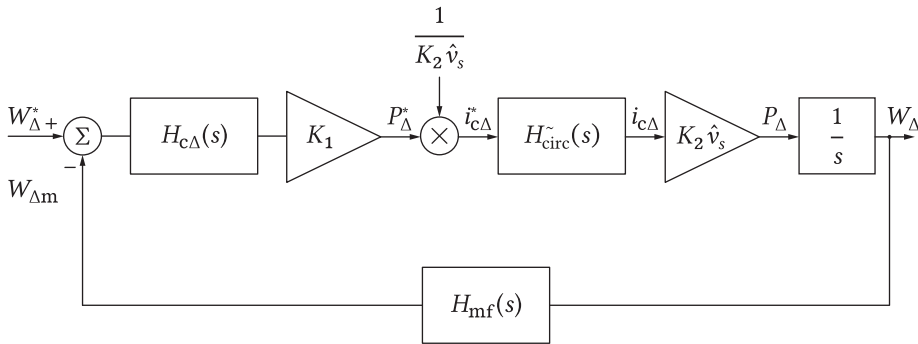


**Fig. 3.24** A general control block diagram concerning vertical balancing of the MMC energies. In case the energy component  $W_{\Delta 0}$  is considered,  $K_1 = \sqrt{2} K_{\text{pos}}$  and  $K_2 = -2/\sqrt{3}$ . In case the component  $W_{\Delta\{\alpha/\beta\}}$  is analyzed,  $K_1 = K_{\text{neg}}$  and  $K_2 = \mp 2/\sqrt{6}$ . The advantage of the presented diagram lies in the fact that dynamic analysis of different balancing methods retains the same analytical form, with the coefficient  $K_1$  being the only variable of interest, as will be seen shortly. The transfer function of the circulating current controller is denoted by  $H_{\text{circ}}(s)$ , whereas filtering and measurement of the analyzed energy component was indicated by the block  $H_{\text{mf}}(s)$ .

It is worthy to note that derivation of the equations, presented throughout this section, assumed that  $W_{\Delta}^* = 0$ . However, a similar analysis could have been conducted in case  $W_{\Delta}^*$  took any arbitrary value, which is also indicated in **Fig. 3.24**.

If the circulating current controller is assumed to be significantly faster when compared to the energy balancing controllers, then  $H_{\text{circ}} \approx 1$ . Furthermore, the transfer function of the block denoting filtering and measurement of the converter's energies differs case to case. However, for the sake of simplicity,  $H_{\text{mf}}(s) = 1$  is adopted in this analysis. Such an assumption does not hinder the generality of the procedure demonstrated herewith. On the contrary, in case  $H_{\text{mf}}(s) \neq 1$ , an identical set of steps can be taken in order to conduct the comparison of different vertical balancing methods.

According to the assumptions adopted above, one can obtain the closed loop transfer function from (3.97).

$$\frac{W_{\Delta}}{W_{\Delta}^*} = \frac{H_{c\Delta} K_1 \frac{1}{s}}{1 + \underbrace{H_{\text{mf}}(s)}_{\approx 1} H_{c\Delta} K_1 \frac{1}{s}} \quad (3.97)$$

If a simple PI controller is used, then  $H_{c\Delta}(s) = (1 + sT_n)/(sT_i)$ , which, when substituted into (3.97), yields

$$\frac{W_{\Delta}}{W_{\Delta}^*} = \frac{K_1(1 + sT_n)}{T_i \left( s^2 + sK_1 \frac{T_n}{T_i} + \frac{K_1}{T_i} \right)} \quad (3.98)$$

Since (3.98) determines the dynamics of a second order system, the damping factor ( $\zeta$ ) along with the natural frequency ( $\omega_n$ ) can be defined as (3.99) and (3.100), respectively.

$$\zeta = \frac{T_n}{2} \sqrt{\frac{K_1}{T_i}} \quad (3.99)$$

$$\omega_n = \sqrt{\frac{K_1}{T_i}} \quad (3.100)$$

As the coefficient  $K_1$  depends on the analyzed energy component, (3.99) and (3.100) can be expanded as

$$\zeta_0 = \frac{T_n}{2} \sqrt{\frac{\sqrt{2}K_{\text{pos}}}{T_i}} \quad \zeta_{\alpha} = \frac{T_n}{2} \sqrt{\frac{K_{\text{neg}}}{T_i}} \quad \zeta_{\beta} = \frac{T_n}{2} \sqrt{\frac{K_{\text{neg}}}{T_i}} \quad (3.101)$$

$$\omega_{n0} = \sqrt{\frac{\sqrt{2}K_{\text{pos}}}{T_i}} \quad \omega_{n\alpha} = \sqrt{\frac{K_{\text{neg}}}{T_i}} \quad \omega_{n\beta} = \sqrt{\frac{K_{\text{neg}}}{T_i}} \quad (3.102)$$

What can be seen from (3.101) and (3.102) is that irrespective of the observed delta energy component, damping, as well as the natural frequency, increases with the coefficients  $K_{\text{pos}}$  and  $K_{\text{neg}}$ . Moreover, the expressions (3.101) and (3.102) provide the means for a qualitative comparison of three balancing methods presented above. It was shown that these methods differ only in terms of the constants  $K_{\text{pos}}$  and  $K_{\text{neg}}$ , which are summarized in **Tab. 3.1**. Furthermore, in **Tab. 3.1** the above mentioned coefficients stand in the ascending order if moving from methods labeled with 1 to 3. This means that, for the identical values of PI controller gains, Method 3 is expected to provide the fastest balancing of energies in vertical direction. Of course, using the identical controller gains is not mandatory, however, the comparison of responses ensured through different balancing methods can still be conducted by means of (3.101) and (3.102).

Last but not least, **Fig. 3.21** shows that vertical balancing, in case Method 1 is observed, commences by generating the circulating current references in "per-leg" fashion. Thereafter, current references are mapped to a suitable vector by means of the matrix denoted by  $BB^T$ . An identical procedure takes place in case Method 2 is chosen, however, with the mapping matrix labeled with  $M_m$  as shown in (3.80). An important detail to notice is that every leg uses an independent energy balancing controller  $H_{c\Delta}$ . Nevertheless, these controllers rely on the use of identical gains since any other choice would not be reasonable engineering-wise. On the other hand, Method 3 relies on the indirect control of legs' delta energies through the actions being taken in the  $\alpha\beta 0$  domain. As  $\alpha$ ,  $\beta$  and 0 axes are decoupled (orthogonal), three separate controllers are used for each of the associated energy components. Even though it is reasonable to use identical gains for all three controllers, owing to the fact that the control block diagram looks identically, which can be confirmed from **Fig. 3.24**, there exists a degree of freedom allowing one to select the gains of controllers  $H_{c\Delta\alpha}$ ,  $H_{c\Delta\beta}$  and  $H_{c\Delta 0}$  differently. For instance, the dynamics guaranteed by Method 1/2 can be obtained through the use of Method 3 in case tuning of the controllers according to (3.103) and (3.104) is performed.

$$H_{c\Delta 0}^{(\text{method 3})} = H_{c\Delta}^{(\text{method 1/2})} \times \frac{K_{\text{pos}}^{(\text{method 1/2})}}{K_{\text{pos}}^{(\text{method 3})}} \quad (3.103)$$

$$H_{c\Delta\{\alpha/\beta\}}^{(\text{method 3})} = H_{c\Delta}^{(\text{method 1/2})} \times \frac{K_{\text{neg}}^{(\text{method 1/2})}}{K_{\text{neg}}^{(\text{method 3})}} \quad (3.104)$$

The next section provides a verification of control methods discussed above. Moreover, a discussion on the differences among the control methods 1, 2 and 3 is conducted through the energy response comparisons under several different scenarios.

**Tab. 3.2** Parameters of the simulated converter

Rated power (S)	Input voltage ( $V_{\text{DC}}$ )	Number of SMs per branch ( $N$ )	Grid voltage ( $V_{\text{SM}}$ )	SM capacitance ( $C_{\text{SM}}$ )	Branch inductance ( $L_{\text{br}}$ )	Branch resistance ( $R_{\text{br}}$ )	PWM carrier frequency ( $f_c$ )
0.5MVar	5.6kV	8	3.3kV	2.25mF	2.5mH	60m $\Omega$	999Hz

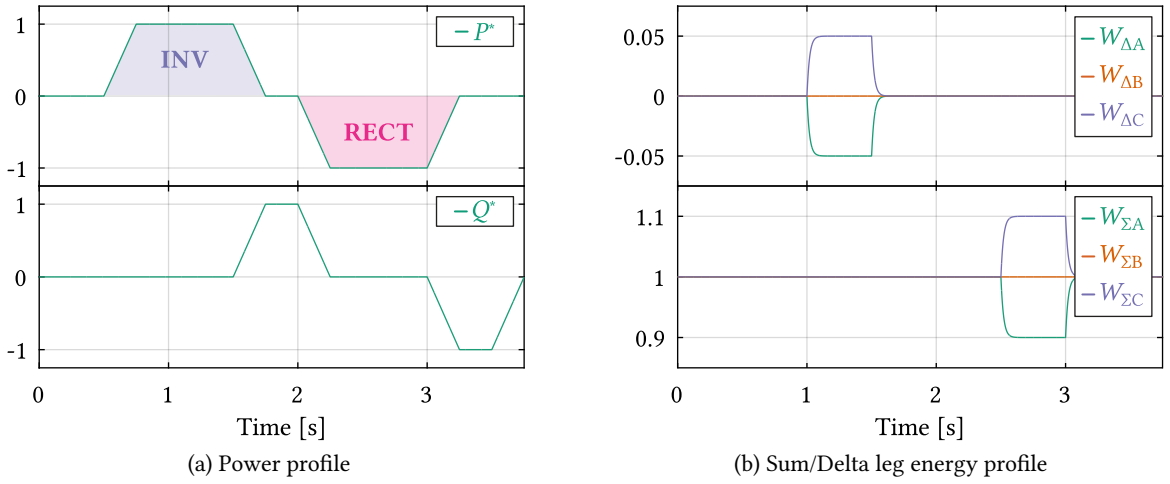


**Fig. 3.25** Profiles of the reference power and energy during the operational interval of  $T_{op} = 3.75s$ . All the values are provided in per-unit fashion. The normalization basis for active/reactive power was adopted as  $S_B = 0.5MVar$ , which corresponds to the rated power of the converter. The base value for the normalization of leg energy components was set as the leg total energy reference  $W_B = C_{SM} V_{DC}^2 / N$ .

## 3.7 Simulation Results

In order to verify the control principles presented so far, the grid connected MMC with parameters provided in **Tab. 3.2** was simulated in PLECS. To test the converter operation in various operating points, the profile of power references provided in **Fig. 3.25(a)** was followed. A change in the direction of energy flow can be observed (reverse of the active power sign), hence the labels "INV" and "RECT", even though a real rectifier operation would assume balancing of the total energy stored in the MMC from the AC side. Further, to verify the correctness of horizontal/vertical balancing principles discussed throughout **Sec. 3.6**, intentional energy unbalances were introduced during two different time intervals, as depicted in **Fig. 3.25(b)**. Realization of the branch voltage references was achieved by means of the  $2N + 1$ -level PSC modulation, which will be discussed in detail in **Chap. 5**.

The first part of this section covers general operation of the MMC relying on the use of energy balancing methods labeled with 1, 2 and 3. As these methods differ from each other only in terms of the leg energy responses, major differences among them should not be observed on the converter's terminals. Therefore, the second part of this section provides an in depth comparison in terms of the dynamics provided from the energy balancing standpoint.

### 3.7.1 General operation of the converter

#### 3.7.1.1 Balancing method 1

Waveforms relevant for the converter operation in case balancing Method 1 is used can be found in **Fig. 3.26**. One can observe the successful tracking of the reference power profiles defined in **Fig. 3.25(a)**.

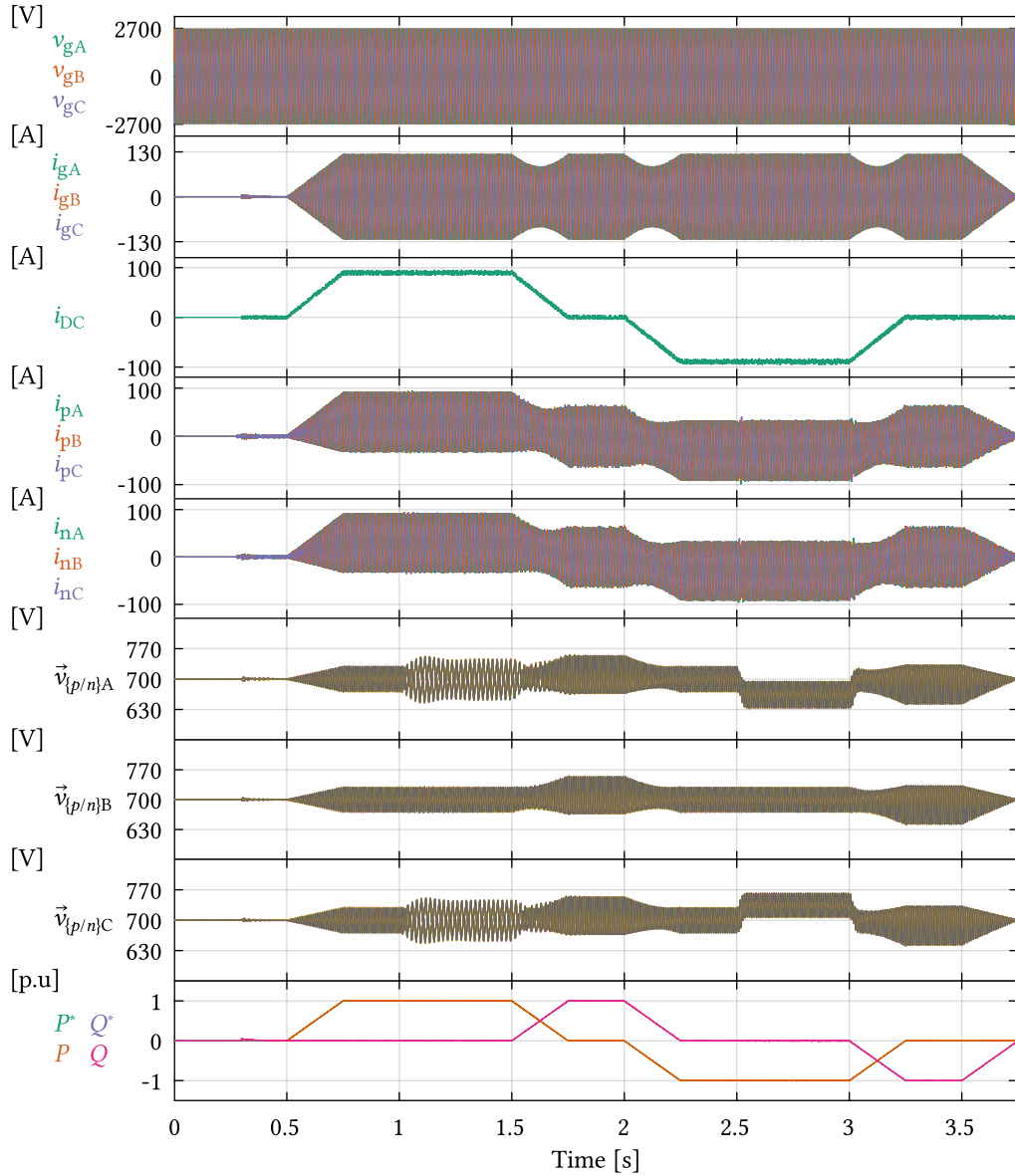


**Fig. 3.26** Operation of the converter during the time period of 3.75s in case balancing method labeled with 1 is employed.

Moreover, branch energies correspond to the energy profiles defined in **Fig. 3.25(b)**, which can be concluded from the upper/lower branch voltages of legs A,B and C, denoted by  $\vec{v}_{\{p/n\}A}$ ,  $\vec{v}_{\{p/n\}B}$  and  $\vec{v}_{\{p/n\}C}$ , respectively.

**Figs. 3.27(a)** and **3.27(b)** provide a closer look into the operating waveforms during the intervals characterized with the disturbances introduced into the legs' energies. In **Fig. 3.27(a)**, a discrepancy between the mean values of the upper and lower branch voltages in phases A and C can be observed, which is in accordance with the converter energy profile defined in **Fig. 3.25(b)**. An important detail to notice is that the input ( $i_{DC}$ ) and output currents ( $i_{g\{A/B/C\}}$ ) of the converter do not become distorted in spite of the introduced energy unbalances.



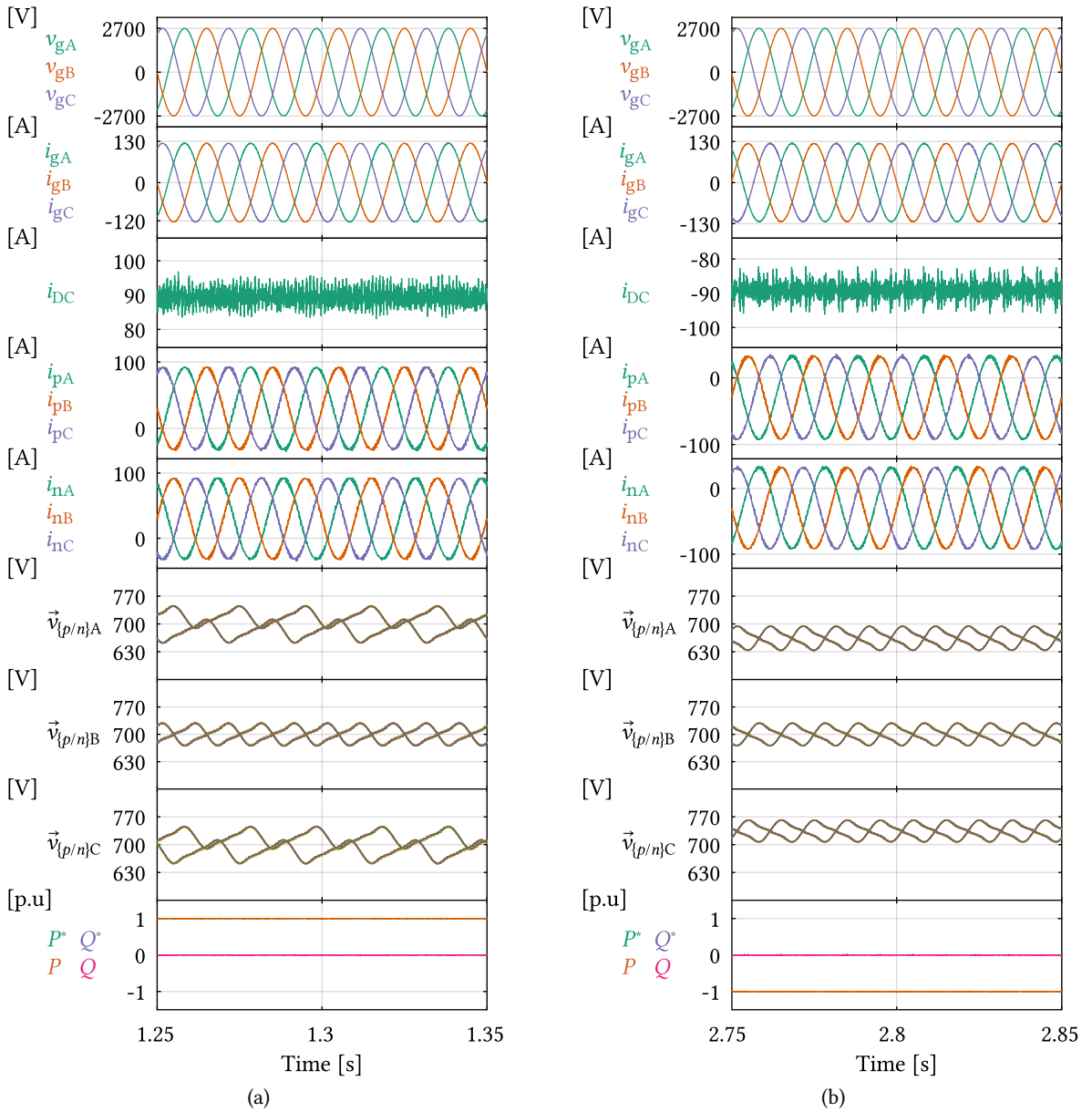


**Fig. 3.27** Relevant operating waveforms during five periods of the grid voltage in case the balancing method labeled with 1 is employed. (a) As can be seen based on the legs A and C voltages, vertical unbalances are intentionally introduced, however, DC and AC terminal currents retain the desired shape; (b) A horizontal unbalance between phases A and C is created. Similarly to the previous case, terminal currents remain undistorted.

A similar situation can be observed in **Fig. 3.27(b)**, where a horizontal energy unbalance between phases A and C was introduced (mean SM voltages in leg A decrease, whereas the opposite occurs in leg C). Once again, preservation of the terminal currents is guaranteed irrespective of the nature of the introduced unbalance. To put it differently, distribution of energies inside the MMC is “an internal” matter and it is never to be seen from the converter’s terminals.

### 3.7.1.2 Balancing method 2

In case balancing method 2 is used, operating waveforms of the converter with parameters matching the ones used in the previous case can be found in **Fig. 3.28**. A simple visual inspection of the provided waveforms leads to the conclusions already derived during the analysis conducted in **Sec. 3.7.1.1**.

Also, **Figs. 3.29(a)** and **3.29(b)** depict operation of the converter during five fundamental periods of the grid the converter is connected to. Similarly to **Figs. 3.27(a)** and **3.27(b)**, introducing a vertical/horizontal unbalance does not hinder the terminal performance of the converter.

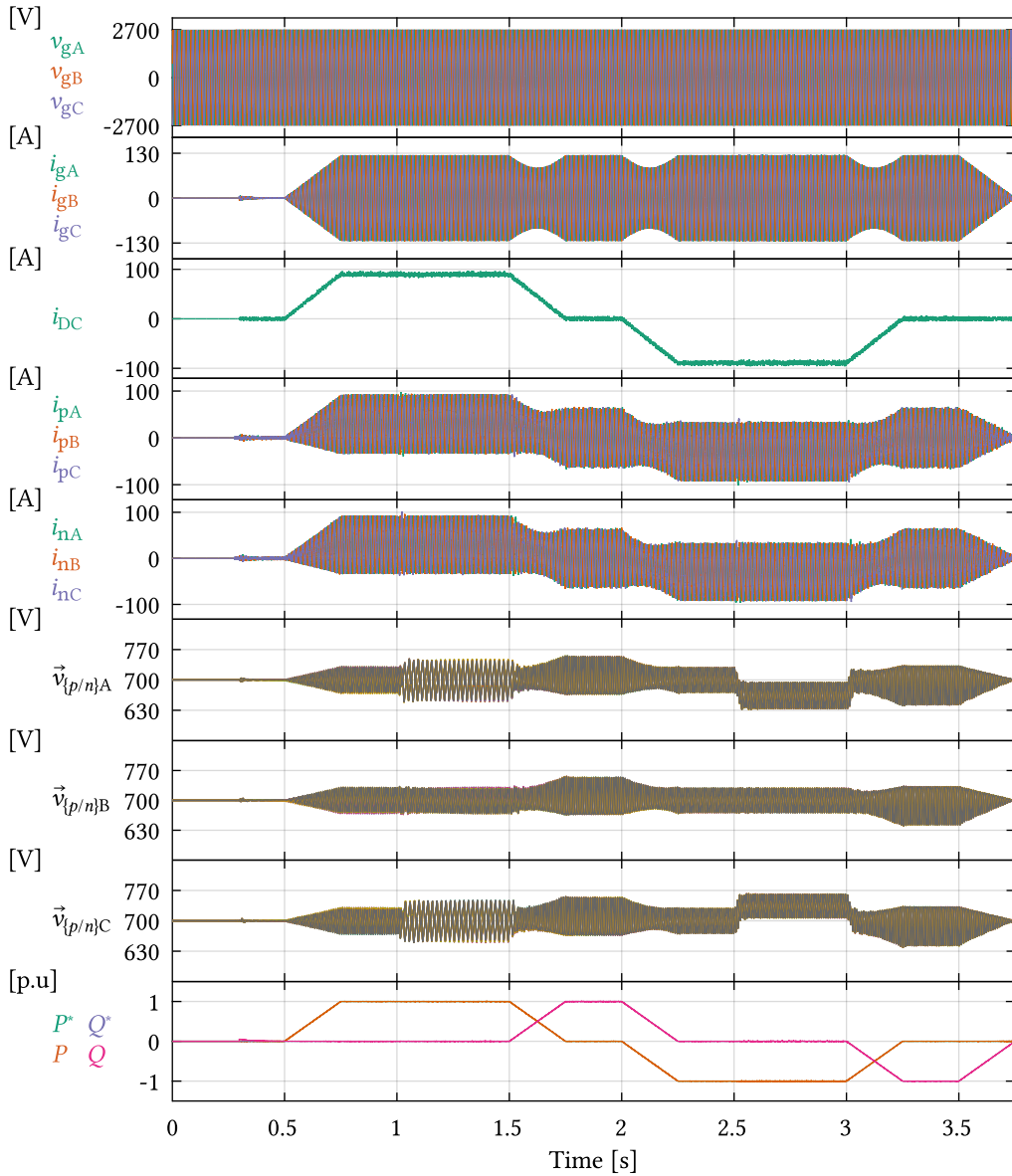


**Fig. 3.28** Operation of the converter during the time period of 3.75s in case the balancing method labeled with 2 is employed.

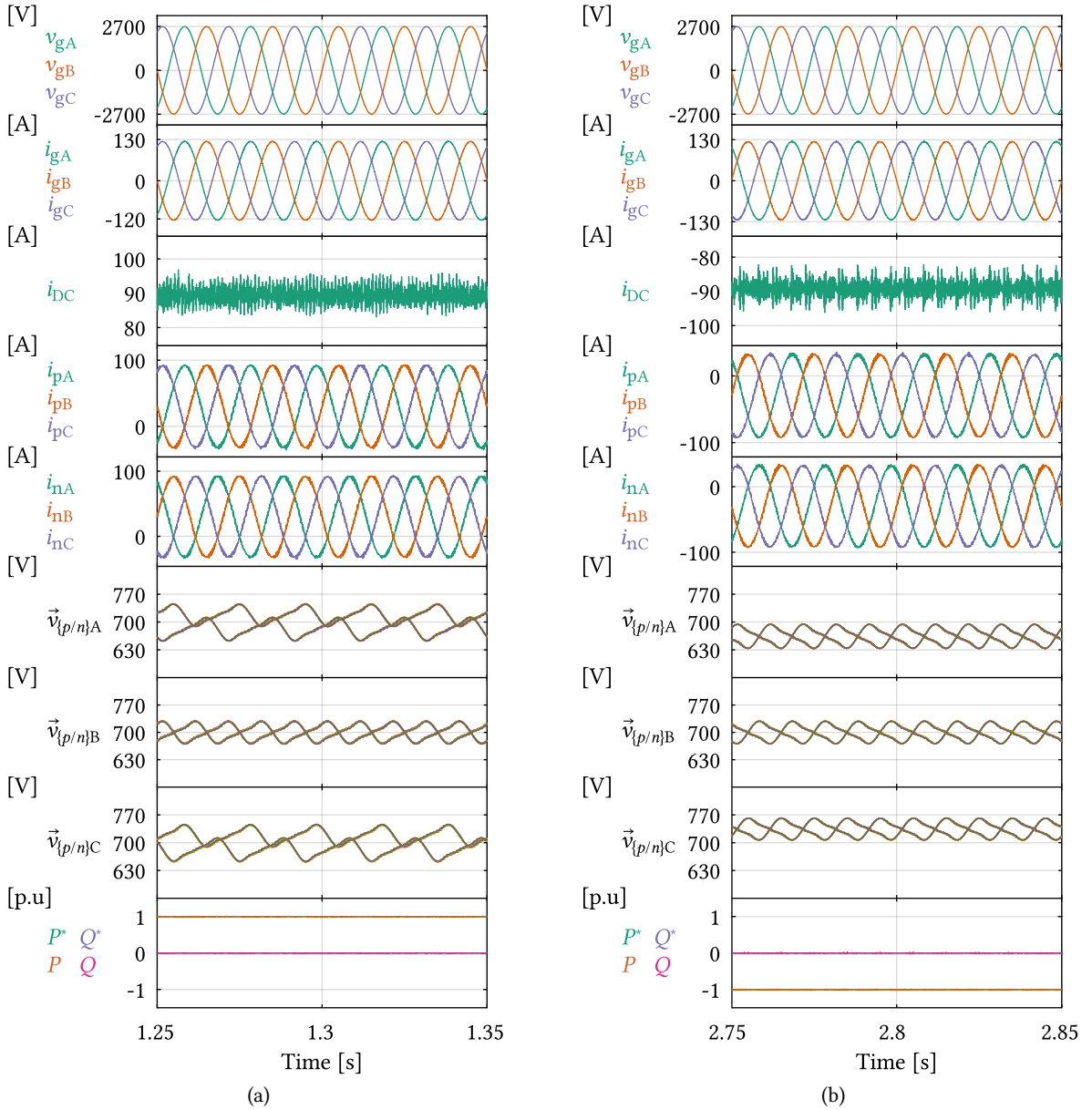


**Fig. 3.29** Relevant operating waveforms during five periods of the grid voltage in case the balancing method labeled with 2 is employed. Conclusions made during the analysis of Figs. 3.27(a) and 3.27(b) hold in this case.

### 3.7.1.3 Balancing method 3

Following the trend from Secs. 3.7.1.1 and 3.7.1.2, operating waveforms of the converter in case the balancing method 3 is employed can be found in Fig. 3.30. Also, Figs. 3.31(a) and 3.31(b) provide an insight into the operation of the analyzed converter during five fundamental cycles of the grid.

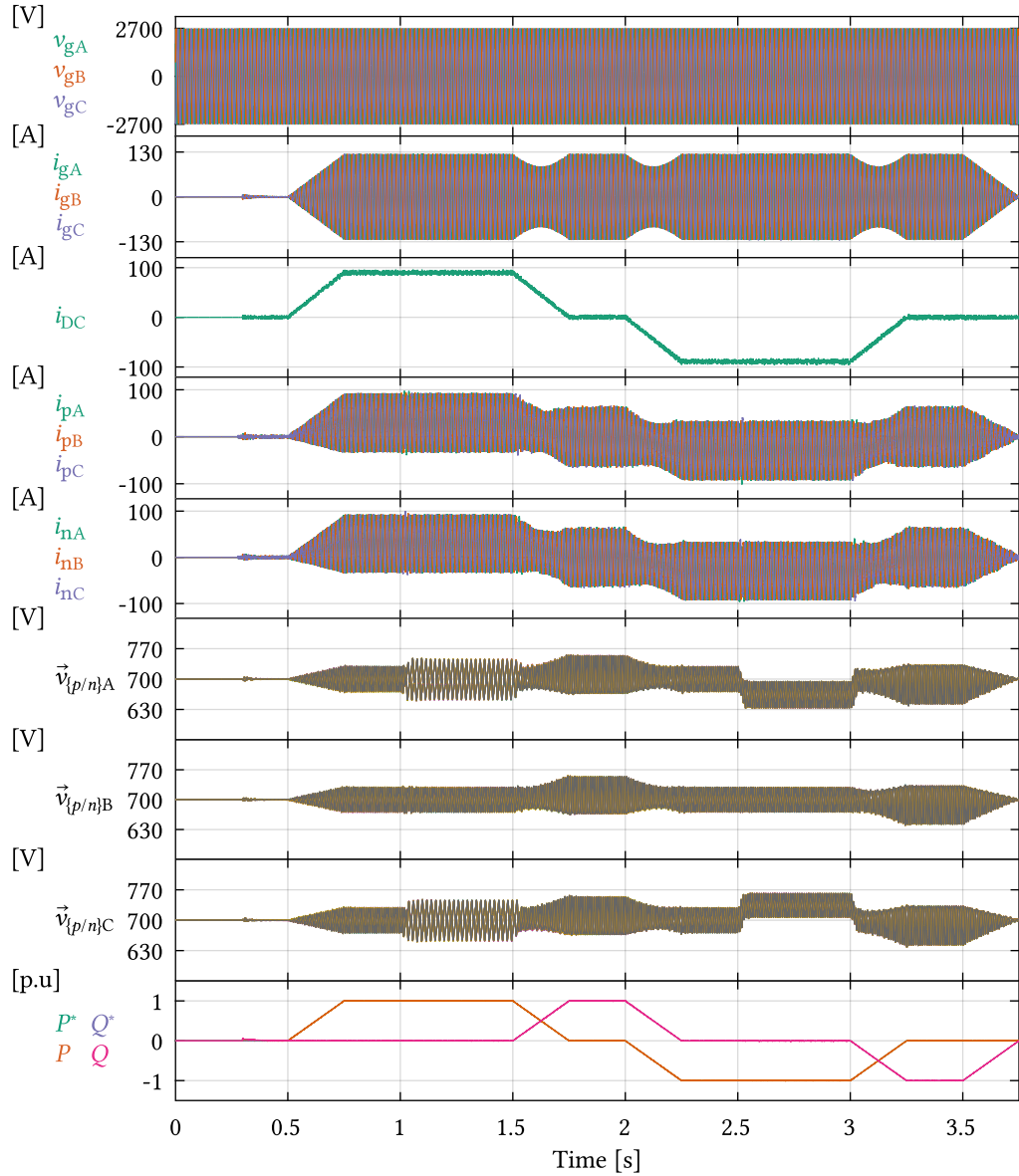


**Fig. 3.30** Operation of the converter during the time period of 3.75s in case the balancing method labeled with 3 is employed.

From the waveforms provided in **Secs. 3.7.1.1 to 3.7.1.3**, one can also notice that SMs' capacitor voltages follow the waveform presented in **Fig. 3.11** owing to the employed modulation type. In case other modulation methods reported in the literature [88], [97]–[105] were used, voltages across the capacitors of individual SMs would feature different shape. However, harmonics in the total branch energy can not be avoided. Another observation relevant for the upcoming analysis refers to the hardly observable differences among the waveforms provided in **Secs. 3.7.1.1 to 3.7.1.3**. Namely, irrespective of the used balancing method, terminal operation of the converter should not be changed, as stated on several occasions so far. Nevertheless, the analysis provided in **Sec. 3.6** indicates that different balancing methods lead to different responses from the leg/branch energy control standpoint.

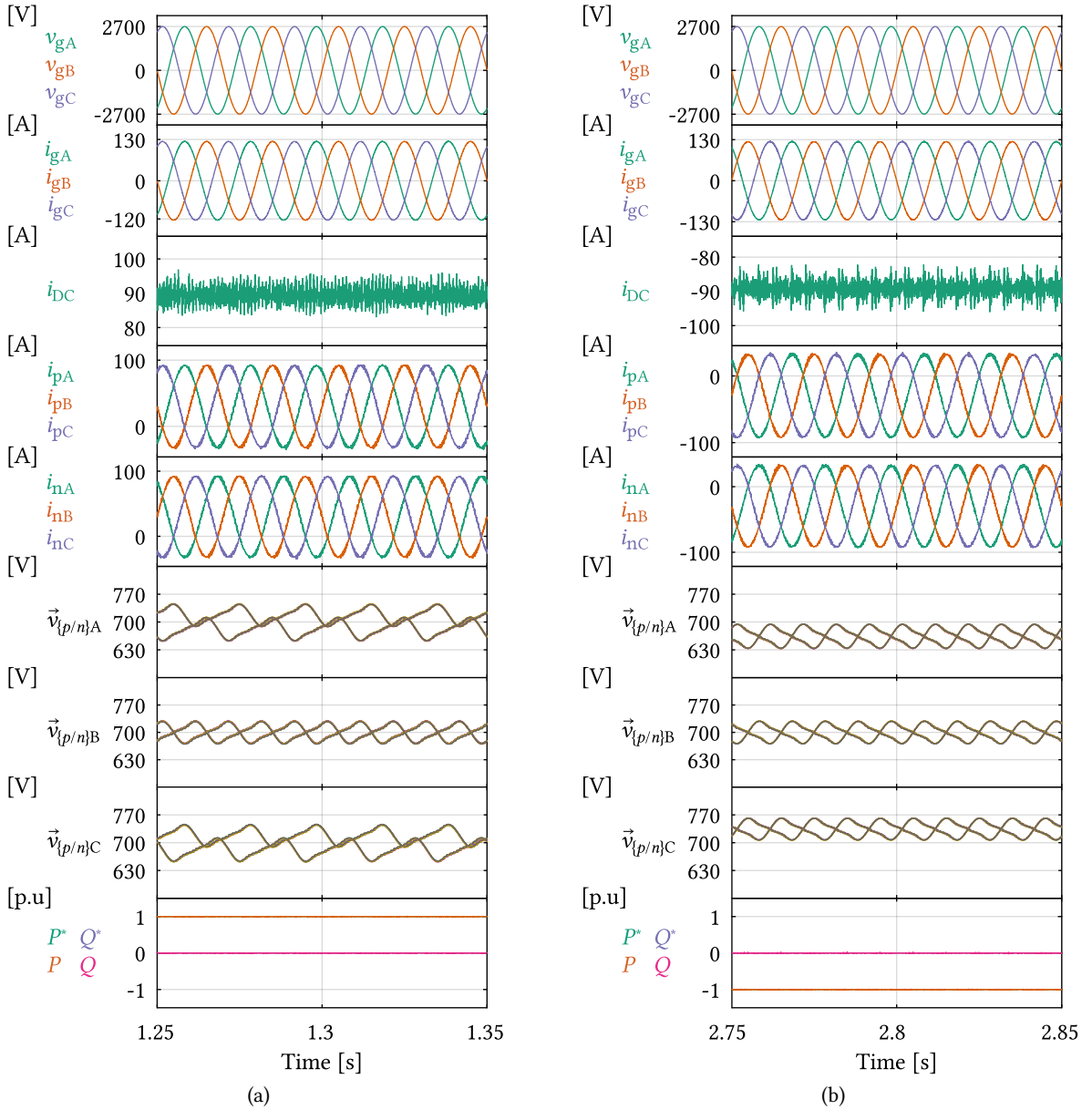


**Fig. 3.31** Relevant operating waveforms during five periods of the grid voltage in case the balancing method labeled with 3 is employed. Conclusions made during the analysis of Figs. 3.27(a), 3.27(b), 3.29(a) and 3.29(b) hold in this case.

Consequently, the leg/branch energy dynamics should be compared instead of observing terminal characteristics of the converter. In case a suitable set of scenarios is defined in advance, verification of the results provided in Sec. 3.6 can be performed, as will be seen shortly.

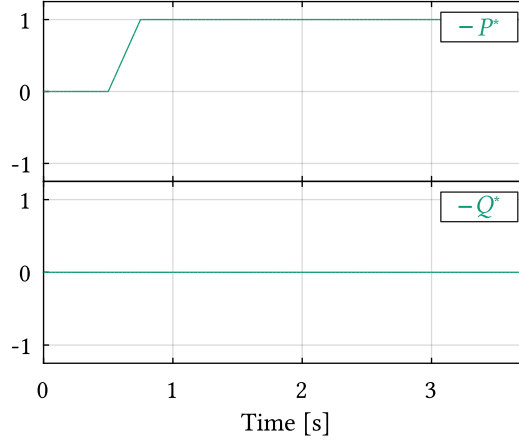


**Fig. 3.32** Reference power profile used for the purpose of comparing different energy balancing methods. Similarly to **Fig. 3.25(a)**, base value of the converter power was adopted as  $S_B = S_{\text{nom}} = 0.5 \text{ MVar}$ .

### 3.7.2 Comparison of different energy balancing methods

With the aim of laying the focus on performance of the leg energy controllers used in case balancing methods 1, 2 and 3 are used, the reference power profile from **Fig. 3.25(a)** got redefined, as presented in **Fig. 3.32**. Moreover, to provide sufficient modulation index reserve, voltage of the grid the converter is connected to was scaled down to  $v_g = 0.9 v_g^{\text{nom}}$ . For all of the inspected balancing methods, energy and circulating current controllers were tuned identically.

It is worthy to note that normal operating conditions of the MMC imply that the sum and delta leg energies are controlled to  $W_\Sigma = 1 \text{ p.u}$  and  $W_\Delta = 0 \text{ p.u}$ . Testing of the energy controller responses would require the MMC to be found in a state with the energies deviating from the above mentioned values. However, equivalent conclusions can be made in case relevant unbalances are intentionally created. Therefore, three different unbalance scenarios were defined, as provided in **Figs. 3.33(a)** to **3.33(c)**.

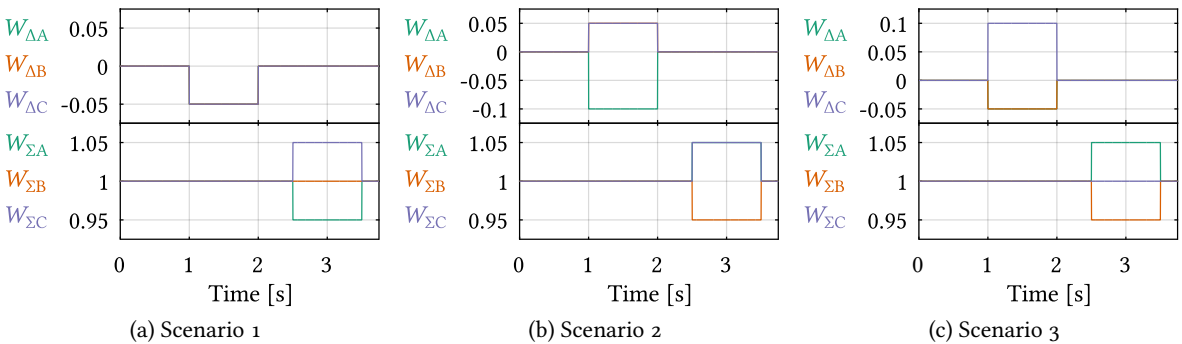


**Fig. 3.33** Three scenarios used for the benchmark of analyzed energy balancing methods. All the energy components are presented in per-unit fashion, with the base energy value adopted in the manner defined in **Fig. 3.25(b)**.

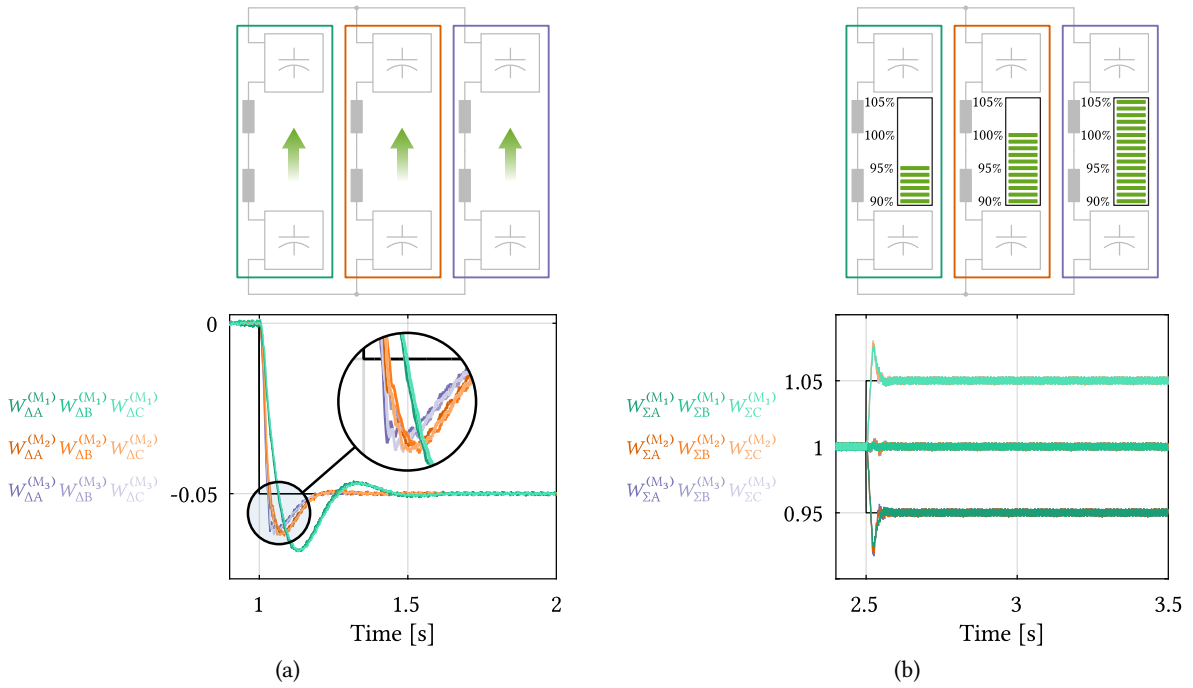


**Fig. 3.34** Step response of the converter leg energies in case the disturbance scenario 1 is considered. (a) Delta energy response; (b) Total energy response;

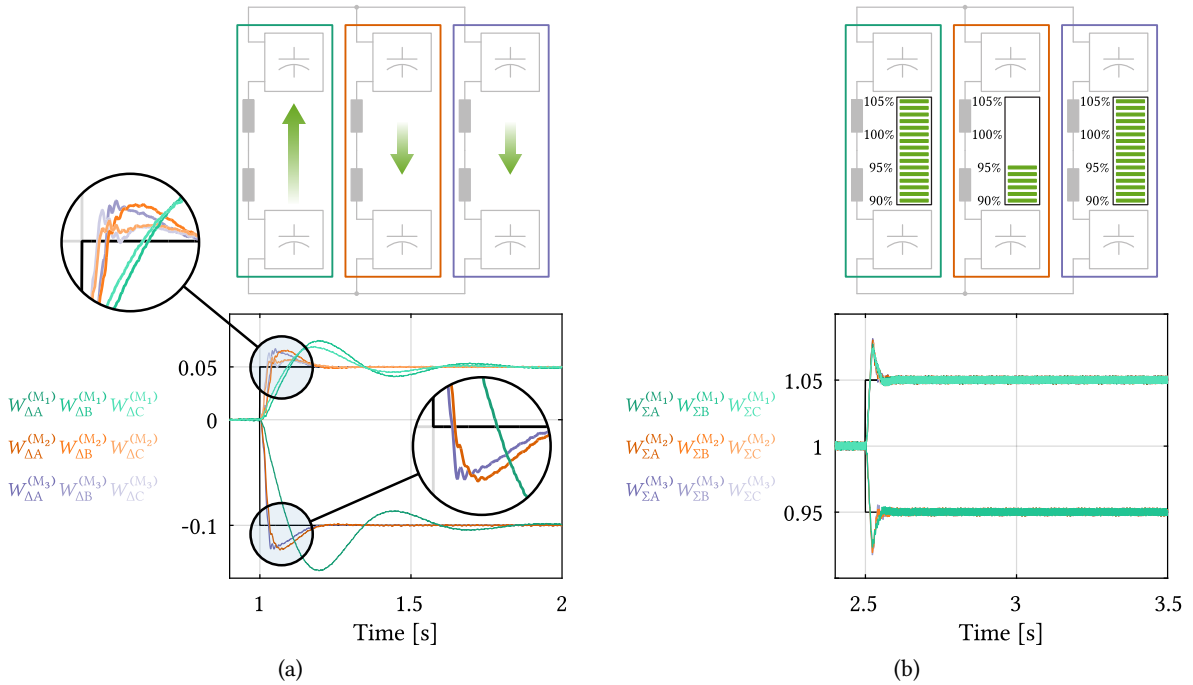


**Fig. 3.35** Step response of the converter leg energies in case the disturbance scenario 2 is considered. (a) Delta energy response; (b) Total energy response;



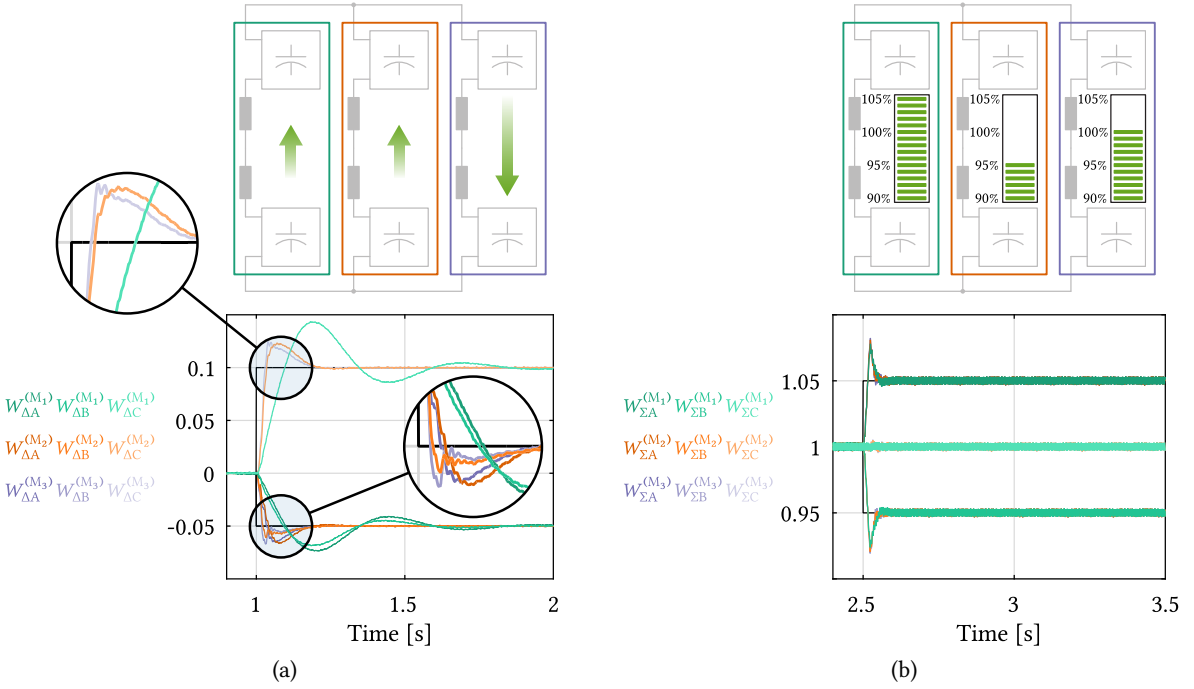


**Fig. 3.36** Step response of the converter leg energies in case the disturbance scenario 3 is considered. (a) Delta energy response; (b) Total energy response;

**Figs. 3.34 to 3.36** present the step response of the converter leg energies under the terms defined by the reference profiles from **Figs. 3.33(a) to 3.33(c)**, respectively.

As can be seen from **Figs. 3.34(a), 3.35(a) and 3.36(a)**, balancing Method 3, provides the fastest tracking of the delta energy reference in all three phase-legs. Method 2 tends to be slightly slower, whereas Method 1 features the slowest step response with the highest overshoot. Such a set of results is in a complete alignment with the reasoning made during the derivation of general vertical energy distribution control diagram from **Fig. 3.24**.

Further, **Figs. 3.34(b), 3.35(b) and 3.36(b)** indicate that horizontal balancing methods covered in **Sec. 3.6** provide identical results irrespective of the observed scenario. According to the analysis conducted in **Sec. 3.6.2.1**, this result is expected.

### 3.8 Summary

In this chapter, a thorough analysis on the control of the conventional 3PH MMC was conducted. Relevant control layers were identified along with the current components being in charge of the converter energy distribution. Three methods, seeming completely different from each other at the first glance, were analyzed in order to demonstrate that they differ only by a set of multiplication constants. However, such a statement becomes obvious only in case of the analysis being conducted in a suitable reference frame. Derived principles were verified through a set of simulations performed in PLECS.



It is worthy to note that the derived control principles remain the same irrespective of the number of SM installed in every branch of an analyzed MMC. This means that the outstanding flexibility in terms of voltage capacity can be easily guaranteed. In other words, the converter rated power can be increased/decreased should one add/remove a certain number of SMs to/from the circuit, under the assumption of the converter's current rating being unchanged. However, there are applications (e.g. hydro applications) where scaling up the voltage in order to meet the application power requirements is not allowed, therefore, the current capacity boost of the MMC must be ensured. As a result, additional challenges, residing in either hardware or control domain, are to be dealt with. It is exactly the following chapter that addresses this subject in a comprehensive manner.



# 4

## Extension of the Modular Multilevel Converter Power Capacity Through Branch Paralleling

Throughout this chapter, different possibilities of extending the current handling capability of the modular multilevel converter are discussed. Inherently, the power capacity of the converter, assuming an unchanged operating voltage, along with the preservation of the submodules' voltage rating, gets increased. Among several different options, paralleling of the branches was recognized as the solution alleviating the challenge of extending the converter power capacity to the highest extent. The adaptations allowing for such a configuration must be performed mostly in the control domain, resulting in minimal hardware interventions. Consequently, time and cost-effective solutions can be effortlessly achieved.

### 4.1 On the need for extension of the converter current capacity

Any MMC design implies clearly defined voltage and current ratings of the SMs. This means that stacking more SMs in series, in order to increase the MMC voltage rating, directly implies the MMC power rating increase, given the fixed current rating of the SMs. **Fig. 4.1** presents the MMC power versus voltage scaling assuming the availability of an SM designed for the rated current and voltage being denoted by  $i^*$  and  $v^*$ , respectively [55]. For an Available Design (AD) of the SMs, changing the number of series connected SMs within a branch causes the converter Operating Point (OP) to slide along the green line. Point  $OP_1$  indicates an increased number of series connected SMs with respect to the converter operating at voltage equal to 1 p.u., yet with the same current rating. However, to meet the requirements of an application with the OP residing above this characteristic, the current handling capabilities of the converter must be increased. If a converter operating at  $OP_2$  is required, reusing the available SMs would not be feasible owing to the current rating insufficiency.

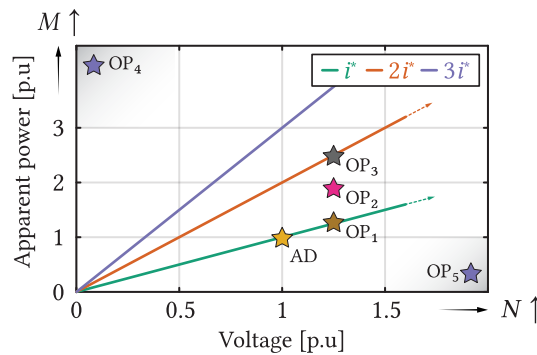


**Fig. 4.1** MMC power scalability depending upon the available SM design

It is straightforward to notice that, for a fixed voltage of an application the MMC is about to serve, power extension implies an increase in its current handling capabilities. On one hand, a new SM design can be carried out to support the application needs, however, this is likely to introduce additional manufacturing costs. On the other hand, the existing SM design can be reused to increase the MMC current rating if paralleling of the Power Modules (PMs) within the SM or paralleling of the SMs themselves had been foreseen in the manufacturing process. This way, the converter operating with twice the rated current of the available SM can be obtained, thus shifting the newly designed system ratings to  $OP_3$ .  $OP_2$  can be served now providing a more expensive MMC, of significantly higher ratings than needed, is acceptable. The same reasoning can be applied to any desired OP residing within an area being delimited by the adjacent MMC power characteristics. It is noteworthy that reaching the power scaling plot corner points (e.g. high power - low voltage and/or low power - high voltage MMC) would not be reasonable economy-wise. Namely, if  $OP_4$  happens to be obtained, the system gets oversized, in terms of voltage, and unreasonably expensive. A similar reasoning can be applied if  $OP_5$  is required. Nonetheless, one can notice that increasing the MMC current rating is not a simple task, and several technical options are available, as briefly explained in the next section.

## 4.2 MMC scalability options

**Figs. 4.2(a) to 4.2(c)** represent several different ways of extending the MMC current capabilities, whereas **Fig. 4.2(d)** presents an arbitrary number of converters operating in parallel, which is a well known and widely used method in case of a single MMC (or any other converter) being incapable of delivering power demanded by an application [106], [107]. In [107] paralleling of the MMC legs, derived based on [108], was discussed, however, from the circuit configuration standpoint, it corresponds to the parallel connected MMCs.

Parallel connection of PMs, as presented in **Fig. 4.2(a)**, introduces the need for special considerations to be included into the SM design due to different static and dynamic characteristics of the employed modules [109], [110]. Furthermore, it is likely that an SM manufacturing process might restrict the choice of PMs to be employed. To provide the flexibility in terms of the SM current rating, without the need for carrying out a new design process for each of the ratings individually, the cooling system as well as the SM frame size are determined for the highest of desired currents. Additionally, paralleling of the PMs implies higher SM capacitance demands. Consequently, during the design phase, a certain amount of space must be allocated within an SM in order to host all the necessary capacitors should PMs paralleling be an option.

**Fig. 4.2(b)** illustrates the extension of the MMC current capacity through paralleling of HB SMs [111], [112]. It is noteworthy that positive terminals of the SMs' capacitors should also be connected, with the aim of equalizing the voltage across all of the SMs. Therefore, even though SMs paralleling might not be needed sometimes, additional terminal (which is not part of a regular MMC SM), allowing for the connection of capacitors' positive terminals, must be foreseen in the SM design phase.

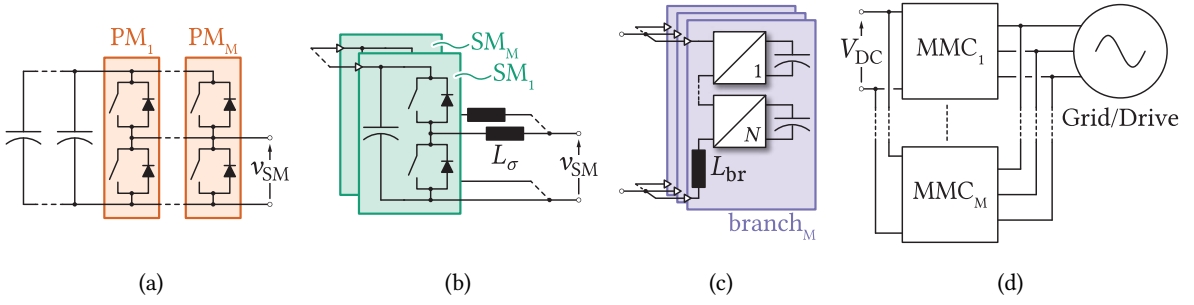


**Fig. 4.2** (a) Parallel connection of PMs within an SM; (b) Parallel connection of SMs; (c) Parallel connection of MMC branches; (d) Parallel operation of an arbitrary number of MMCs;

Furthermore, although small, additional inductance  $L_\sigma$  has to be installed in series with every SM in case of paralleling, owing to the voltage source nature of the SMs as such. One can easily conclude that additional inductance mentioned above represents unnecessary part of the SM should paralleling not be required. Moreover, due to the fact that paralleled SMs are normally switched simultaneously, synchronization among gate signals, or specially designed driver master/slave structure, must also be provided.

None of the above mentioned concerns related to the parallel connection of PMs/SMs comes to the fore if the MMC current capacity increase occurs through paralleling of the branches, which is illustrated in **Fig. 4.2(c)**. Firstly, there is no need to design the SM for maximum of the several current ratings, as in the case presented in **Fig. 4.2(a)**. Consequently, oversizing of the SM cooling system is avoided. Further, drawbacks related to paralleling of the SMs are also mitigated. Small balancing inductors are not needed anymore, and neither is a very precise switching signals synchronization. In contrast to the methods presented in **Figs. 4.2(a)** and **4.2(b)**, where various hardware adaptations are needed, paralleling of the MMC branches significantly simplifies the problem and moves the effort into the control domain. Therefore, the existing SMs can be reused without the need of undergoing any major redesign process. Power scaling of the MMC gets substantially facilitated, yet with the constraints being imposed solely by the employed control platform. To put in another way, cheaper solutions requiring less engineering effort can be obtained.

**Fig. 4.3** presents the MMC operating in this configuration. To retain the naming consistency, what has been referred to as the branch so far, will henceforth be referred to as the Sub-Branch (SBR). The employment of HB SMs will be assumed, although all the principles derived can simply be expanded onto any type of the employed SM. Number of series connected SMs within an SBR is denoted by  $N$ , whereas the number of parallel SBRs within a branch is denoted by  $M$ .

Moreover, **Fig. 4.3** shows that an additional inductor  $L_a$  can be connected in series with the set of parallel SBRs. Consequently, higher level of flexibility is ensured in terms of the converter inductances optimization when compared to a simple paralleling of the MMCs. Notwithstanding, in the analyses concerning the elementary operating principles of the MMC comprising parallel SBRs, the presence of the inductor  $L_a$  will be neglected, however, it does not affect the generality of presented results.

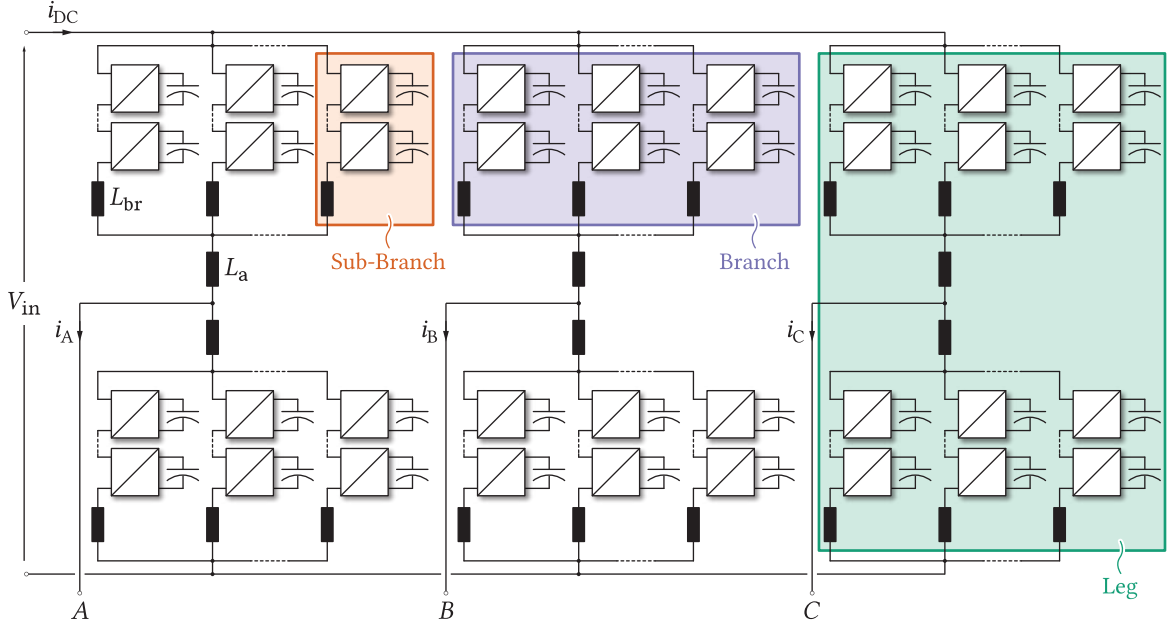


Fig. 4.3 MMC operating with parallel SBRs

### 4.3 Preliminary Considerations

Fig. 4.4 depicts an arbitrary number of parallel connected SBRs assuming that clusters of MMC SMs can be replaced with the ideal voltage sources, as discussed in **Chap. 2**. In accordance with the Thevenin's theorem, a branch can be replaced with the series connection of equivalent voltage source, inductor and resistor. Additionally, parameters of the branch equivalent circuit can be calculated as  $\overline{v_{br\Sigma}} = \sum_{k=1}^M v_{br,k}/M$  and  $\overline{Z_{br}} = Z_{br}^*/M$ , where  $Z_{br}^*$  denotes the nominal SBR impedance. Therefore, equivalent circuit of the analyzed converter does not differ from the conventional MMC [113], as depicted in Fig. 4.5. Consequently, control of the all the relevant quantities can be established by means of two voltages being defined for each leg as (4.1) and (4.2).

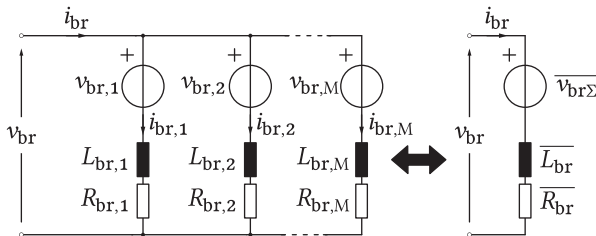


Fig. 4.4 Equivalent circuit of an arbitrary number of parallel connected SBRs

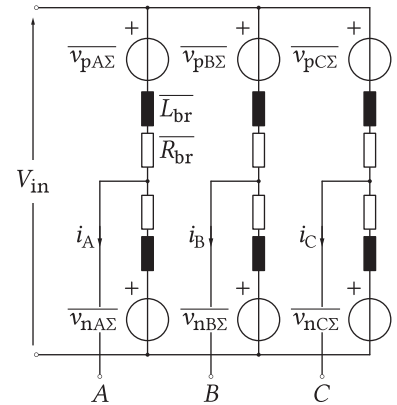


Fig. 4.5 Equivalent circuit of the MMC operating with parallel SBRs

$$v_{si} = \frac{\overline{v_{ni\Sigma}} - \overline{v_{pi\Sigma}}}{2} \quad (4.1)$$

$$v_{ci} = \frac{\overline{v_{ni\Sigma}} + \overline{v_{pi\Sigma}}}{2} \quad (4.2)$$

Likewise, definitions of the leg output current ( $i_o$ ) as well as the common-mode current ( $i_{ci}$ ) are retained from **Chap. 2** and restated bellow for the sake of completeness.

$$i_o = i_{pi} - i_{ni} \quad (4.3)$$

$$i_{ci} = \frac{i_{pi} + i_{ni}}{2} \quad (4.4)$$

Voltages defined by (4.1) and (4.2) control the converter output and common-mode currents, respectively. Since a set of parallel SBRs can be perceived as a floating energy source, similarly to the conventional MMC, all of the control methods presented in **Chap. 3** can be used. However, these control methods aim to control the total amount of energy stored within a branch, without concerning the energy distribution among its SBRs. To track the output current reference, while maintaining the energy balance among the branches, conventional MMC control layers provide every branch with the reference voltage  $\overline{v_{br\Sigma}^*}$  being obtained in the manner corresponding to the regular MMC as (4.5) and (4.6). Henceforth, these control layers will be referred to as the higher control layers.

$$\overline{v_{pi\Sigma}^*} = v_{ci}^* - v_{si}^* \quad (4.5)$$

$$\overline{v_{ni\Sigma}^*} = v_{ci}^* + v_{si}^* \quad (4.6)$$

It is easy to understand that large discrepancies among the SBR energies, which are not taken into account by the higher control layers, lead to inevitable fault or even damage of the converter. Hence, additional control measures must be taken. Perceiving the branch voltage references as the common-mode components of individual SBR voltages, voltage generated by an arbitrary SBR can be expressed as (4.7), where  $\Delta v_{br,i}$  represents the deviation of voltage generated by an individual SBR with respect to the references provided by the higher control layers. Please notice that identical reasoning was introduced in **Sec. 3.4**. As will be seen, the approaches demonstrated in **Chap. 3** will be successfully employed to achieve the balancing of an arbitrary number of SBRs connected in parallel.

$$v_{br,i} = \overline{v_{br\Sigma}^*} + \Delta v_{br,i} \quad (4.7)$$

According to (4.7), there is a certain degree of freedom in the choice of an SBR voltage. However, control of the current components defined by the higher control layers, and the application where the MMC is used, must not be hindered. Consequently, all the deviations  $\Delta v_{br,i}$  must sum up to zero.

$$\sum_{i=1}^M \Delta v_{br,i} = 0 \quad (4.8)$$

#### 4.4 Balancing of the sub-branch energies

Prior to commencing any SBR energy balancing discussions, current sharing among the SBRs belonging to the same branch should be clarified. According to Fig. 4.4, expression (4.9) can be easily derived.

$$L_{br} \frac{d}{dt} \underbrace{\left( i_{br,i} - \frac{i_{br}}{M} \right)}_{\Delta i_{br,i}} + R_{br} \left( i_{br,i} - \frac{i_{br}}{M} \right) = \overline{v_{br\Sigma}} - v_{br,i} \quad (4.9)$$

Replacing  $v_{br,i}$  from (4.9) with (4.7), leads to the conclusion that distribution of currents within a branch can be affected by means of the disturbances labeled with  $\Delta v_{br,i}$  (4.10). As will be demonstrated shortly, if properly generated, these deviations can be effectively used to ensure balancing of the SBR energies.

$$L_{br} \frac{d}{dt} \Delta i_{br,i} + R_{br} \Delta i_{br,i} = -\Delta v_{br,i} \quad (4.10)$$

However, ensuring the equal current sharing (balancing) among the SBRs should not affect the control of other variables within the converter, therefore (4.8) must be respected at all times. This criteria can be met in case the controller presented in Fig. 4.6 is employed. According to (4.11), sum of voltage disturbances generated by the SBR currents balancing equals zero, meaning that the other control layers of the converter are indeed not affected. Further, adopting the nomenclature from the conventional MMC, currents  $\Delta i_{br,i}$  can be perceived as the branch circulating currents. According to the above definition, the branch circulating currents sum up to zero at its terminals, therefore they are not interfering with the currents controlled by the higher control layers.

$$\sum_{i=1}^M \Delta v_{br,i} = H_{\Delta i} \sum_{i=1}^M (\overline{i_{br}} - i_{br,i}) = 0 \quad (4.11)$$

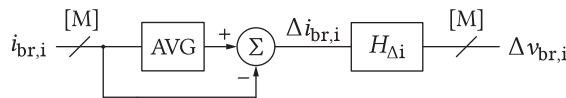
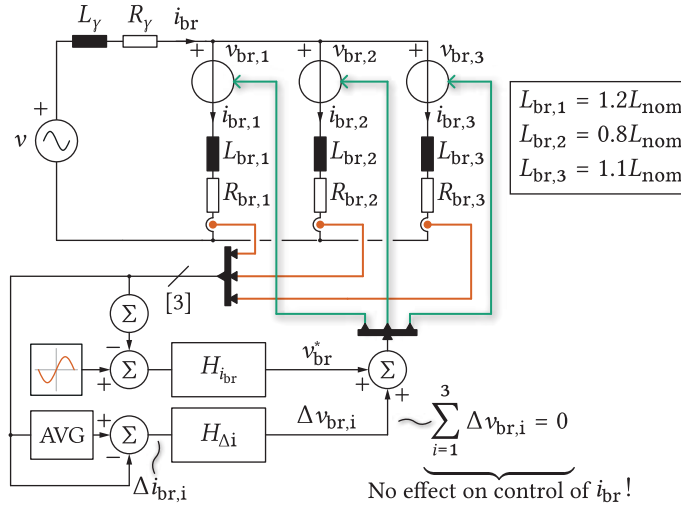


Fig. 4.6 SBR currents balancing controller



In (4.11)  $H_{\Delta i}$  denotes  $\Delta i_{br}$  controller, with the structure being determined by the nature of currents to be controlled. Namely, if DC currents are to be balanced among the SBRs, PI controller can be used. However, in case of an AC component existence, the resonant part must also be included.

To support the upcoming discussions, an exemplary circuit provided in **Fig. 4.7** can be analyzed. It consists of three SBRs, being assigned the task of controlling an AC source ( $v$ ) current. Although desirable, manufacturing the SBRs with any deviations from the rated parameters is practically impossible. For instance, the SBR inductance deviations in the range of  $\pm 20\%$  are unlikely to be completely avoided in practice. Moreover, two adjacent SBRs will hardly have identical impedances. Therefore, if the SBR currents balancing is not performed (SBR voltages are the same), currents flowing through the SBRs differ from each other, as presented in **Fig. 4.8(a)**. Such a mismatch in currents results in the mismatch in powers at which the SBRs receive the energy. Consequently, in the MMC presented in **Fig. 4.3**, the SBR energies diverge. If, however, the SBR currents are balanced, which is desirable given the same current rating of power devices being installed within the converter, voltages generated by the SBRs must be different taking a certain mismatch among the passive components into account, as presented in **Fig. 4.8(b)**. Again, the SBR powers mismatch can be observed.



**Fig. 4.7** An exemplary circuit used to illustrate the need for the SBR energies balancing. Three SBRs are employed with the aim of controlling the AC source current through the actions of the controller denoted by  $H_{br}$ . The SBR currents balancing controller  $H_{\Delta i}$ , presented in **Fig. 4.6**, is also included with the aim of pointing out its importance and limits of effectiveness.

Equal SBR currents distribution is desirable from the installed semiconductor devices current rating standpoint. However, from the energy sharing viewpoint, equal SBR currents sharing is not always desirable, especially if the SBR inductances differ. In case the MMC is considered, ensuring equal energy distribution between its (sub)branches is crucial. Therefore, an additional energy controller must be superimposed to the controller presented in **Fig. 4.6**. Also, the newly introduced SBR energy balancing controller must not hinder the performance of the other control loops, which is mathematically formulated in (4.8).

To determine the correct operation of the SBR energy balancing controller, mean power equation of an arbitrary SBR should be analyzed. Given that SBRs conduct the current consisting of a DC and an AC component, an SBR power equation can be expressed as (4.12).

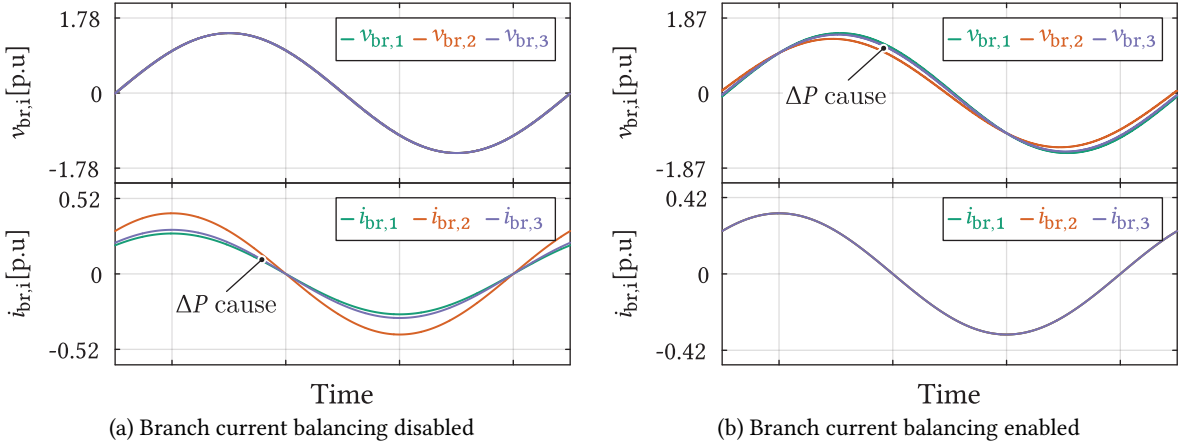


**Fig. 4.8** SBR currents and voltages observed in the circuit provided in **Fig. 4.7**. Regardless of the SBR currents balancing controller state (ON or OFF), the SBRs receive energy at different power levels. Therefore, divergence of the SMs' voltages, in case the MMC is considered, happens to be inevitable unless additional control measures are taken.

$$P_{br} = \overline{v_{br} i_{br}} = \underbrace{\overline{V_{br} I_{br}}}_{\text{DC terms}} + \underbrace{\overline{\tilde{v}_{br} \tilde{i}_{br}}}_{\text{AC terms}} \quad (4.12)$$

If the SBR currents are left uncontrolled, along with the assumption that branch current contains a DC component, steady state distribution of the SBR current offsets does not depend on the SBR inductances. Consequently, if all the SBRs generate the same DC voltage, their DC power components do not significantly differ from each other once the steady state has been reached (since  $I_c(\infty) \approx V_{DC}/R_{br}$ ). In other words, it can be claimed that  $\Delta i_{br,i}^{DC} \approx 0$ , meaning that SBRs share the DC power almost equally. Nevertheless, dynamics of the SBR DC currents differ. Based on the illustrative analysis performed on the circuit depicted in **Fig. 4.7**, one can conclude that the above statement regarding the steady state power sharing does not hold in case of the AC components.

Generally, an SBR power equation can be expanded into the Taylor series having a form of (4.13).

$$P_{br} = P_{br}^{nom} + \underbrace{\Delta P_{br}^{DC}}_{\approx \frac{1}{2} V_{DC}^* \Delta I_{br,i}} + \underbrace{\Delta P_{br}^{AC}}_{\text{depends on } \Delta L_{br}} \quad (4.13)$$

With the current balancing controller from **Fig. 4.6** being enabled, it can be seen that AC components of the SBR powers depend on the SBR inductance mismatches. However, steady state value of DC voltages generated by all the branches can be approximated to half of the converter input voltage  $V_{DC}^*/2$ . Hence, all the mismatches in the SBR powers can be compensated by adjusting the SBR current mismatches  $\Delta I_{br,i}$  (DC components of branch circulating currents), making control problem of the SBR energy balancing linear. The only constraint that must be respected refers to the fact that sum of the branch circulating current references must be zero (similarly to the case presented in **Sec. 3.4**), otherwise interference with the higher control layers occurs.

With the aim of deriving the proper structure of the SBR energy balancing controller, let one describe a branch equivalent circuit depicted in **Fig. 4.4** in the matrix form given bellow.

$$i_{br} = \underbrace{\begin{bmatrix} 1 & 1 & \dots & 1 \end{bmatrix}}_{T_i}_{1 \times M} \begin{bmatrix} i_{br,1} \\ i_{br,2} \\ \vdots \\ i_{br,M} \end{bmatrix} \quad (4.14)$$

It is noteworthy that energy balancing of paralleled SBRs actually represents a generalized case of horizontal balancing of an MMC comprising  $M$  phases. Hence, the approach based on the SVD, similarly to what has been demonstrated in **Chap. 3**, can be reused. Also, an expression similar to (4.14) can be established to formulate the criterion of the SBR energy balancing being invisible to the higher control layers as

$$\underbrace{\begin{bmatrix} 1 & 1 & \dots & 1 \end{bmatrix}}_{T_i}_{1 \times M} \underbrace{\begin{bmatrix} \Delta I_{br,1}^* \\ \Delta I_{br,2}^* \\ \vdots \\ \Delta I_{br,M}^* \end{bmatrix}}_{\Delta \vec{I}_{br}^*} = 0 \quad (4.15)$$

Energy unbalance among the SBRs can take any arbitrary order, therefore (4.15) does not have to be necessarily satisfied at all times in case control of the SBR energies is performed for every SBR individually by following (4.10) and (4.13). Therefore, the vector of the branch circulating current references  $\Delta \vec{I}_{br}^*$  must be mapped onto the null-space of  $T_i$ . Nonetheless, the number of columns in  $T_i$  is not defined, but rather an arbitrary number corresponding to the number of paralleled SBRs per branch.

Initially, SVD of matrix  $T_i = \begin{bmatrix} 1 & 1 & \dots & 1 \end{bmatrix}_{1 \times M}$  is to be considered. According to (3.58),  $U$  is actually  $1 \times 1$  matrix and owing to the fact that it is selected as a unitary matrix, the first step in factorization of  $T_i$  can be presented as

$$T_i = \begin{bmatrix} 1 \end{bmatrix} \Sigma V^T \quad (4.16)$$

Further, the dimension of matrix  $\Sigma$  corresponds to the dimension of the matrix being factorized, however, with the number of elements differing from zero corresponding to  $\text{rank}(T_i)$ . Since the analyzed matrix consists of ones, it is clear that only one column is independent (e.g. the first one). Consequently,  $\text{rank}(T_i) = 1$ , which allows for factorization in the following form.

$$T_i = \begin{bmatrix} 1 \end{bmatrix} \underbrace{\begin{bmatrix} \sigma & 0 & \dots & 0 \end{bmatrix}}_{1 \times M} \begin{bmatrix} \vec{v}_{R,1}^T \\ B^T \end{bmatrix} \quad (4.17)$$

From (4.17), one can see that the number of basis vectors of  $\ker(T_i)$  equals  $M - 1$  (a thorough discussion on this subject can be found in **App. A**). If the vector labeled with  $\vec{v}_{R,1}$  were to be identified, matrix  $B$  would follow up from (4.17). For that purpose, let one look for  $T_i^T T_i$ .

$$T_i^T T_i = V \underbrace{\begin{bmatrix} \sigma^2 & & \\ & \ddots & \\ & & 0 \end{bmatrix}}_{\Lambda} V^T \quad (4.18)$$

It is of crucial importance to notice that  $T_i^T T_i$  is actually a symmetric matrix. Therefore (4.18) represents its eigendecomposition (A.2). According to the eigendecomposition, matrix labeled with  $\Lambda$  in (4.18) is diagonal matrix with eigenvalues of  $T_i^T T_i$ , whereas  $V$  contains its eigenvectors. Also, according to **App. A** all the eigenvectors belonging to the distinct eigenvalues are orthogonal to each other. Moreover, even if the eigenvalues are not distinct (for instance, eigenvalue  $\lambda = 0$  being repeated several times), eigenvectors belonging to them can be chosen to be orthogonal. From the above equation, it is clear that matrix  $T_i^T T_i$  has only one distinct eigenvector belonging to the eigenvalue  $\sigma^2$ , which can be identified by solving  $\det(T_i^T T_i - \lambda I) = 0$ . It can be shown (by induction for example) that the solution of this equation has a general form provided in (4.19).

$$\begin{aligned} \det(\underbrace{T_i^T T_i}_{M \times M} - \lambda I) &= 0 \\ \rightarrow (-1)^M \lambda^{M-1} (\lambda - M) &= 0 \end{aligned} \quad (4.19)$$

As can be seen, (4.19) confirms that there exists only one distinct eigenvalue  $\lambda_1 = M$  and  $M - 1$  repeated eigenvalues equal to zero. What alleviates the identification of eigenvector belonging to the eigenvalue  $\lambda_1 = M$  is the fact that  $\sigma^2 = \lambda_1$ , from where (4.17) can be rewritten as

$$T_i = \sqrt{M} \vec{v}_{R,1}^T \quad (4.20)$$

It is easy to see that (4.21) follows directly from the above expression.

$$\vec{v}_{R,1} = \frac{1}{\sqrt{M}} \begin{bmatrix} 1 \\ \vdots \\ 1 \end{bmatrix}_{M \times 1} \quad (4.21)$$

Once the vector  $\vec{v}_{R,1}$  has been identified, it comes in handy to observe the result of  $V V^T$ .

$$\begin{aligned} V V^T &= \begin{bmatrix} \vec{v}_{R,1} & B \end{bmatrix} \begin{bmatrix} \vec{v}_{R,1}^T \\ B^T \end{bmatrix} \\ &= \vec{v}_{R,1} \vec{v}_{R,1}^T + B B^T \end{aligned} \quad (4.22)$$

According to the definition of the SVD,  $V$  is a unitary matrix, meaning that  $VV^T = I_{M \times M}$ . Further, according to (4.21), product  $\vec{v}_{R,1} \vec{v}_{R,1}^T$  provides (4.23), from where (4.24) finally arises.

$$\vec{v}_{R,1} \vec{v}_{R,1}^T = \frac{1}{M} \begin{bmatrix} 1 & \dots & 1 \\ \vdots & & \vdots \\ 1 & \dots & 1 \end{bmatrix}_{M \times M} \quad (4.23)$$

$$BB^T = I_{M \times M} - \frac{1}{M} \begin{bmatrix} 1 & \dots & 1 \\ \vdots & & \vdots \\ 1 & \dots & 1 \end{bmatrix}_{M \times M} \quad (4.24)$$

Please notice that matrix denoted with  $BB^T$ , which was discussed in **Chap. 3** in detail, actually ensures mapping of the branch circulating current reference vector  $\Delta \vec{I}_{br}^*$  to the null space of matrix  $T_i$  initially defined in (4.14). Also, (4.24) suggest that desired mapping can be obtained solely by subtracting the average of circulating current references from each one of the references individually, according to (4.25).

$$\begin{aligned} \Delta \vec{I}_M &= BB^T \Delta \vec{I}_{br}^* \\ &= \Delta \vec{I}_{br}^* - \underbrace{\left( \frac{1}{M} \sum_{i=1}^M \Delta I_{br,i} \right)}_{\text{refs. avg.}} \begin{bmatrix} 1 \\ 1 \\ \vdots \\ 1 \end{bmatrix}_{M \times 1} \end{aligned} \quad (4.25)$$

To derive the structure of the SBR energy balancing controller, notation presented in (4.26) and (4.27) will be adopted.

$$I_M = \begin{bmatrix} 1 & & \\ & \ddots & \\ & & 1 \end{bmatrix}_{M \times M} \quad (4.26)$$

$$J_M = \begin{bmatrix} 1 & \dots & 1 \\ \vdots & & \vdots \\ 1 & \dots & 1 \end{bmatrix}_{M \times M} \quad (4.27)$$

According to (4.13), an observed SBR power (and therefore the energy) is directly controlled through its circulating current DC component. Energy of every individual SBR is measured and filtered to obtain the vector  $\vec{W}_{\text{SBR}} = \begin{bmatrix} W_{\text{SBR},1} & W_{\text{SBR},2} & \dots & W_{\text{SBR},M} \end{bmatrix}^T$ . For the moment, assume every SBR energy reference to be set as  $W_{\text{SBR}}^*$ . Hence,  $\vec{W}_{\text{SBR}}^* = W_{\text{SBR}}^* \begin{bmatrix} 1 & 1 & \dots & 1 \end{bmatrix}^T$ . As indicated in (4.28), individual control of the SBR energies implies passing the energy errors vector  $\vec{W}_{\text{SBR}}^* - \vec{W}_{\text{SBR}}$  to the controller denoted by  $H_{\Delta W}$  and subsequent division of the obtained results by  $V_{\text{DC}}^*/2$ . This way of reasoning follows directly from (4.13). Thereafter, to obtain a suitable set of circulating current references  $\Delta \vec{I}_M$ , mapping defined in (4.24) must be performed. It is worth restating that all of the analyses conducted within this chapter refer to the SBR energies' average values. Also, as the converter currents contain a certain amount of ripple originating from the switching actions, it is assumed that all of the controlled quantities are filtered in order to extract the frequency components of interest.

$$\Delta \vec{I}_M = \underbrace{\left( I_M - \frac{J_M}{M} \right)}_{\text{mapping to the null-space (4.24)}} \underbrace{\frac{2H_{\Delta W}(s)}{V_{\text{DC}}^*} \left( \vec{W}_{\text{SBR}}^* - \vec{W}_{\text{SBR}} \right)}_{\text{individual energy control}} \quad (4.28)$$

Since all of the SBR energy references are the same, product  $\left( I_M - \frac{J_M}{M} \right) \vec{W}_{\text{SBR}}^*$  gives zero. Therefore, rearrangement in the form presented bellow can be performed.

$$\Delta \vec{I}_M = \frac{2H_{\Delta W}(s)}{V_{\text{DC}}^*} \underbrace{\left( \frac{J_M}{M} \vec{W}_{\text{SBR}} - \vec{W}_{\text{SBR}} \right)}_{\text{SBR energy reference}} \quad (4.29)$$

An important conclusion can be made from (4.29). Namely, setting the energy reference of every SBR to the average energy of a branch as a whole results in the implicit mapping to the null-space of the matrix  $T_i$  defined in (4.15). Energy controller implemented in this form can be superimposed to the branch circulating current controller from **Fig. 4.6**, as depicted in **Fig. 4.9**. As all the derivations presented above did not consider the parity of the number of paralleled SBRs, all of the obtained results are general and can be applied irrespective of  $M$  being odd or even.

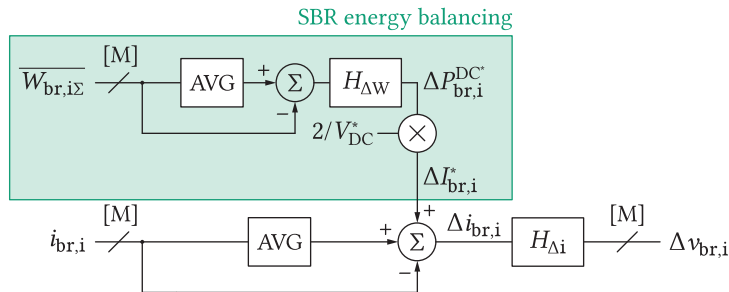


**Fig. 4.9** Structure of the SBR energy balancing controller

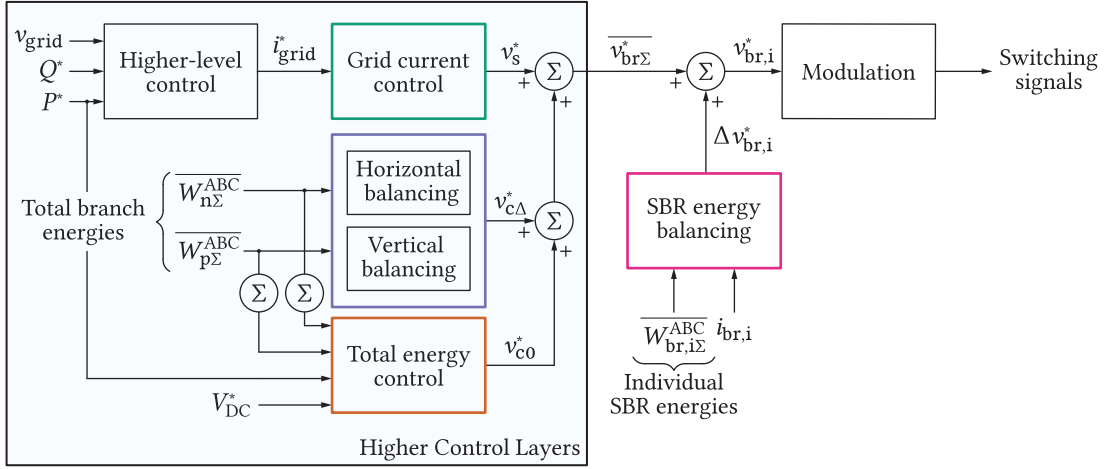


**Fig. 4.10** Control layers of the MMC operating with parallel SBRs. Please notice that conventional MMC control still represent the major part of the schematic.

Given that the analyzed converter operates with the DC voltage ranging from several kV to a few hundred kV, contribution of the SBR energy balancing controller to an SBR current should be very modest. Consequently, despite the differences among the SBR parameters, no current de-rating of the SBRs should be adopted with the aim of providing a certain reserve for the balancing purposes discussed so far. Nevertheless, one should keep in mind that the SBR energy balancing controller does not take care of the total energy stored within a branch. This task is assigned to the controllers belonging to the higher control layers. Similarly to (4.11), and according to **Fig. 4.9**, it can be easily shown that this way of performing the SBR energies balancing does not affect the outer control layers. Once calculated, voltage components  $\Delta v_{br,i}$  are summed with the branch common-mode references  $\overline{v_{br\Sigma}^*}$  obtained from the higher control layers including the GCC, horizontal balancing, vertical balancing and total converter energy control, as presented in **Fig. 4.10**. Effectiveness of the developed control scheme was verified by means of the extensive simulations, as will be demonstrated shortly.

## 4.5 Simulation results

Availability of an SM intended to serve the 0.5MW converter, being connected to the 3kV AC grid on one side and 5kV DC grid on the other side, is assumed. If 1.7kV IGBTs are selected for the observed application, the number of SMs, operating with rated voltage of around 1kV, can be set as  $N = 5$ . SM capacitance, ensuring the voltage ripple of  $\pm 10\%$  around the nominal value, was set as  $C_{SM} = 0.83\text{mF}$  [49]. To demonstrate the possibilities of increasing power capacity of the original converter, cases with two and three SBRs operating in parallel within a branch are simulated in PLECS. Consequently, power rating of the original converter is doubled and tripled, respectively. Simulation parameters can be found in **Tab. 4.1**. Since the SBR inductances can easily be changed depending upon the converter configuration, two different values were chosen to obtain the equivalent branch inductance of  $\overline{L_{br}} = 2.5\text{mH}$ . In order to validate the proposed energy balancing control methods,  $\pm 20\%$  mismatches were randomly included in the SBR inductances, as well as the SM capacitances. PSC modulation was used to generate multilevel voltage waveform across the cluster of SMs.

**Tab. 4.1** Simulated converter parameters

	Simulation 1	Simulation 2
Rated power ( $S^*$ )	1MVar	1.5MVar
Input voltage ( $V_{DC}$ )	5kV	5kV
Number of SMs per SBR ( $N$ )	5	5
SM rated voltage ( $V_{SM}$ )	1kV	1kV
SMs capacitance ( $C_{SM}$ )	0.83mF	0.83mF
Number of parallel SBRs per branch ( $M$ )	2	3
SBR inductance ( $L_{br}$ )	5mH	7.5mH
SBR resistance ( $R_{br}$ )	60m $\Omega$	60m $\Omega$
PWM carrier frequency ( $f_c$ )	999Hz	999Hz

To test the dynamic performance of both converters, reference power profiles, defined in **Fig. 4.11** were followed. Power references provided below were normalized with respect to the maximum power ratings provided in **Tab. 4.1**. Furthermore, to demonstrate the importance of the SBR energy balancing controller, its actions were disabled during the time interval  $T_{wbal}^{OFF} \in [1.5s, 2.5s)$ , as highlighted on the reference power profile from bellow.

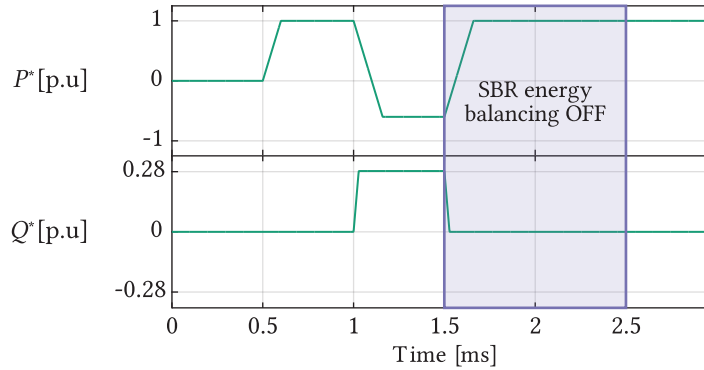


**Fig. 4.11** Power profile used to test dynamic operation of both converters

#### 4.5.1 Case with an even number of SMs per SBR

**Fig. 4.12** presents operation of the converter, utilizing two SBRs per branch, over the time span of  $T_{SIM} = 3s$ . The converter successfully tracks the desired active power profile, which can be concluded based on the presented DC link current  $i_{DC}$ . The lowermost plot presents voltages of the lower SBRs, whereas zoomed parts tend to showcase the contributions of the additional SBR energy balancing controller. It can be observed that, before this controller was disabled, the SBR voltages remained perfectly balanced (the leftmost zoom on the bottom-most plot). However, upon its deactivation at the time instant  $t = 1.5s$ , the SM voltages of all the SBRs start to diverge (middle zoom). Please keep in mind that even though the SBR voltages show the tendency of diverging on these control terms, the total energy of every branch is still maintained at its reference level by the higher control layers. If the SBR energy balancing controller had been kept deactivated for longer, divergence would have become more emphasized, hindering the operation of the higher control layers.



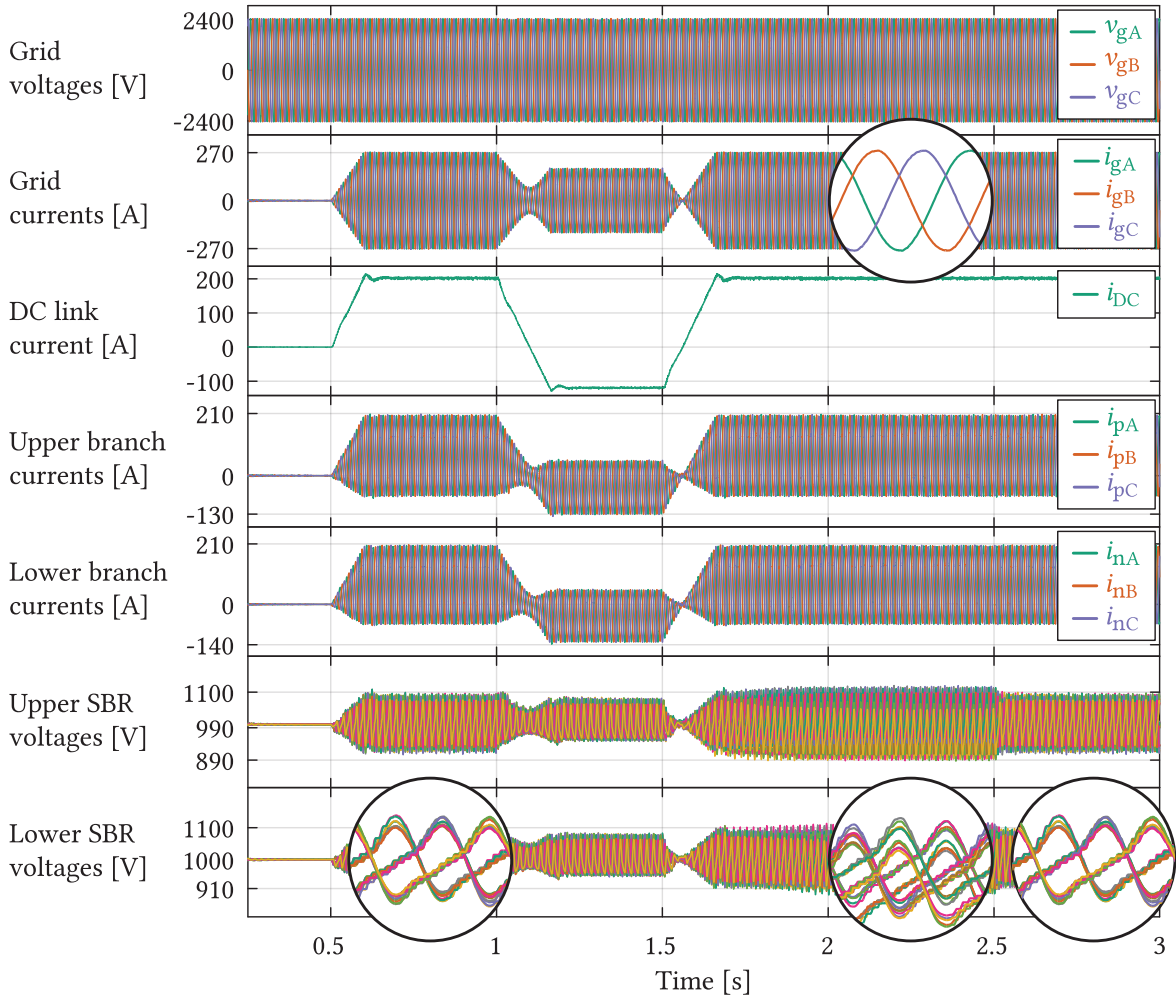


**Fig. 4.12** Operation of the converter utilizing two parallel SBRs within a branch

As it was previously stated, the SBR energy balancing controller does not actually take care of the total amount of energy stored within a branch, but how the energy is distributed inside of it. At the time instant  $t = 2.5\text{s}$ , the SBR energy balancing controller was reactivated, resulting in the balanced SBR voltages (the rightmost zoom). Moreover, due to the closed loop control of the converter as a whole, currents injected into the grid do not get deteriorated even in the case of a slight SBR voltages divergence.

To provide a better illustration of the converter's internal quantities, **Fig. 4.13** presents the leg A lower and upper branch currents, along with the upper branch voltages, during the subintervals being zoomed in **Fig. 4.12**. SBR currents remain balanced, owing to the actions of the SBR currents balancing controller, presented in **Fig. 4.6**. However, notwithstanding the SBR currents balance, SBR voltages divergence can be observed in the middle plot, which corresponds to the period at which the SBR energy balancing controller was still deactivated. It can also be seen from the right hand side plots that voltage ripple across the SM capacitors remains within the predefined boundaries of  $\pm 10\%$  of the rated value if all the necessary controllers are enabled.

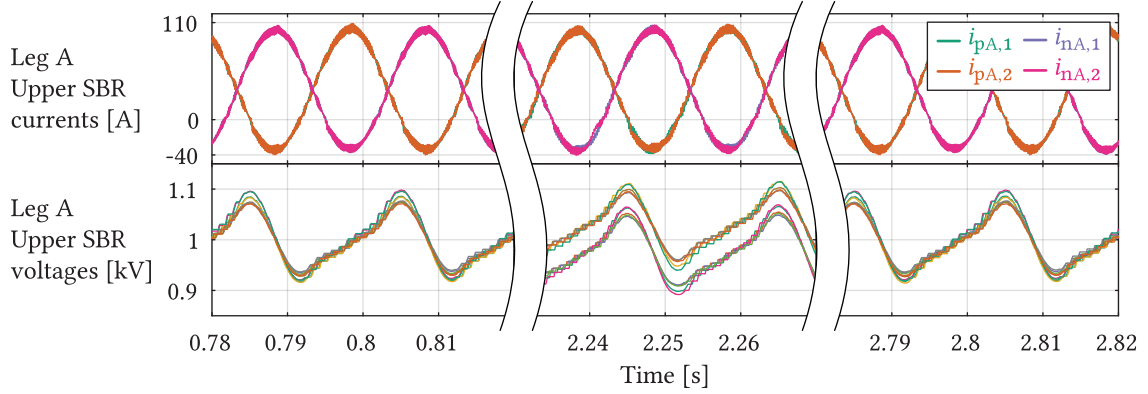


**Fig. 4.13** Leg A upper and lower SBR currents (top); Leg A upper branch voltages (bottom); In spite of the SBR currents being balanced, the SBR voltages tend to diverge in case the SBR energies balancing controller gets deactivated (middle part of the plot). Upon reactivation of this controller, the SBR voltages converge back to the nominal values (the right-most part of the plot). The number of parallel SBRs per branch was set as  $M = 2$ .

Please recall from **Fig. 4.9** that circulating current reference of every SBR is to be obtained by dividing the output of the SBR energy controller  $H_{\Delta W}$  by  $V_{DC}^*/2$ . Owing to the range of voltage denoted by  $V_{DC}^*$ , actions of the SBR balancing controller are expected to be quite modest even in case large energy discrepancies are observed, which is confirmed in **Fig. 4.14**. Namely, as long as the SBR energy balancing controller is activated, the branch circulating current references fall below 1% of the SBR peak currents. On the other hand, reactivation of the analyzed controller (it must be emphasized that this controller should never be deactivated, however, such an action was taken for the demonstration purposes) causes the balancing current references to match roughly 5% of the SBR peak currents. Additionally, symmetry of the branch circulating current references ( $\Delta I_{pA,1}^*$  and  $\Delta I_{pA,2}^*$ ) with respect to the time axis can be observed, meaning that no interference with the higher control layers is ensured.

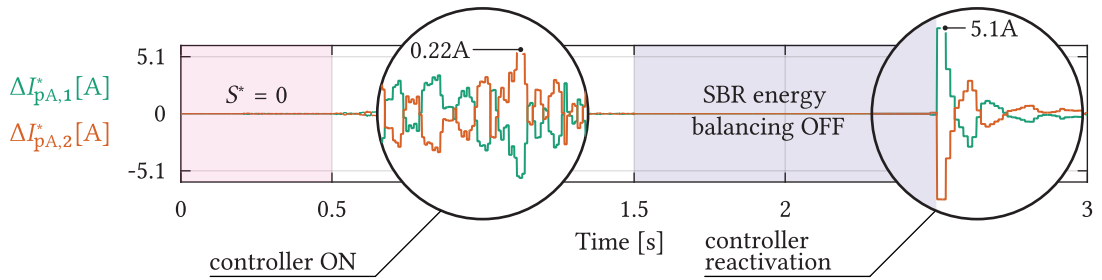


**Fig. 4.14** Branch circulating current references generated by the SBR energy balancing controller.

**Fig. 4.15** presents the SBR energies along with the total branch energies of the converter leg A. It can be seen that the SBR energies diverge from their nominal values, which is a consequence of disabling the SBR energy balancing controller. Nevertheless, higher control layers ensure that total energy stored within either of the branches, calculated as  $W_{br\Sigma} = W_{[p,n],1} + W_{[p,n],2}$ , matches the reference value at all times. Parts of the graph zooming the branch currents around the time instant  $t = 2.5s \pm 10[ms]$  indicate that properly generated, although small, unbalances in the SBR currents successfully bring the SBR energies back into the balance.

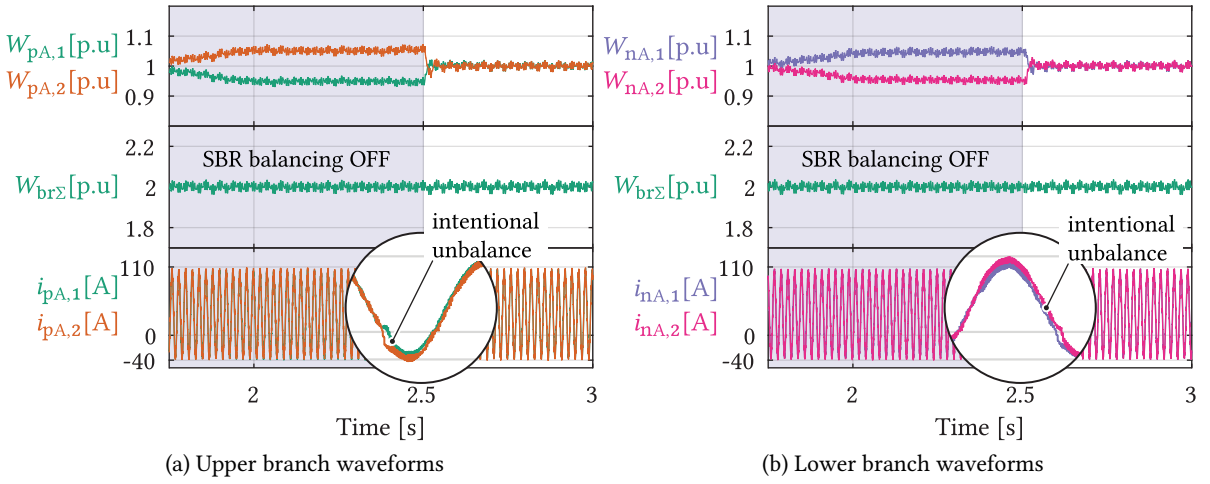


**Fig. 4.15** Energies of the leg A SBRs during the period with the SBR balancing controller being disabled and re-enabled at time instant  $t = 2.5$ s. Please notice, from the zoomed parts of the graph, that intentionally generated SBR currents unbalances (in other words, circulating currents) contribute to reestablishing the SBR energy balance shortly upon reactivation of the controller discussed within this chapter. Normalization of SBR energies was performed with respect the SBR nominal energy  $W_{\text{SBR}} = (C/2N)v_{\text{SBR}}^2$ .

#### 4.5.2 Case with an odd number of SMs per SBR

**Fig. 4.16** repeats the above discussed waveforms, however, in case of the original converter power being tripled. Once again, upon deactivation of the SBR energy balancing controller, the SBR voltages start to diverge, as can be seen from the lowermost graph (middle zoom). Nevertheless, none of the relevant waveforms gets hindered due to the closed loop control of the relevant MMC quantities. Given that identical conclusions can be made in both of the simulated cases, independence of the proposed control method upon the number of parallel SBRs is confirmed. Similarly to **Fig. 4.13**, leg A current distribution along with the upper SBR voltages is presented in **Fig. 4.17**. One can notice that the SBR currents remain balanced at all times, however, deactivation of the SBR energies balancing controller causes the SBR voltages divergence, which diminishes shortly upon reactivation of the controller.

Similarly to **Fig. 4.14**, response of the SBR energies balancing controller, however, in case  $M = 3$  is presented in **Fig. 4.18**. The claim of modest circulating current references can be confirmed once again. Even under significant unbalances in the SBR energies, the highest circulating current reference does not exceed 10% of the branch maximal current. Furthermore, it can be seen that sum of circulating current references matches zero at all times, validating the control strategy derived in (4.29).

Last but not least, **Fig. 4.19** presents leg A SBR energies behavior during the fraction of time corresponding to the SBR energy controller being disabled. It can be seen from both graphs that the SBR energies diverge from the nominal values unless the controller derived in this chapter is employed. Shortly upon its reactivation (at  $t = 2.5$ s), the SBR energies converged back to the reference values. Also, notice that the total energy stored within a branch matches the reference values since it is being taken care of by another control layer.

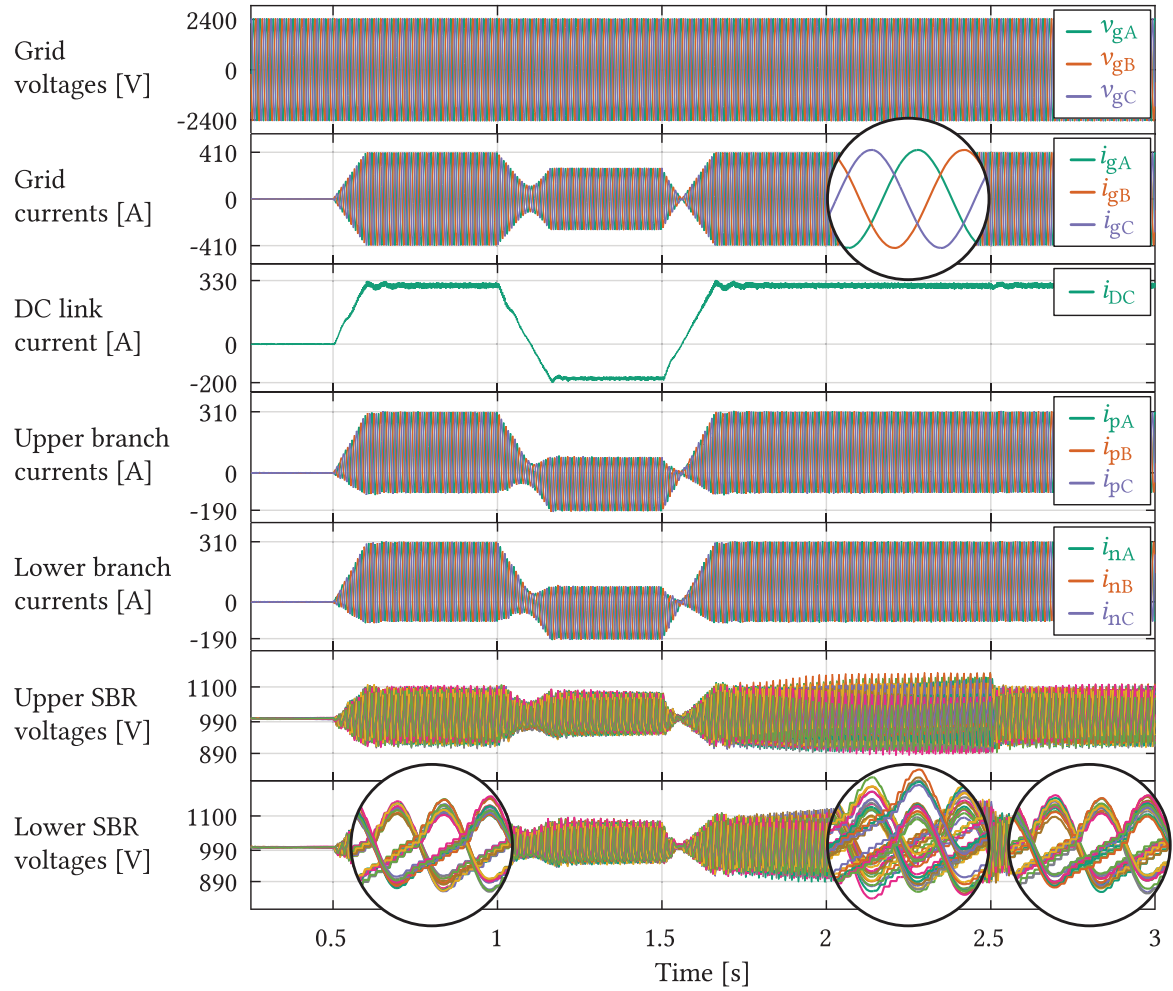


**Fig. 4.16** Operation of the converter utilizing three parallel SBRs within a branch

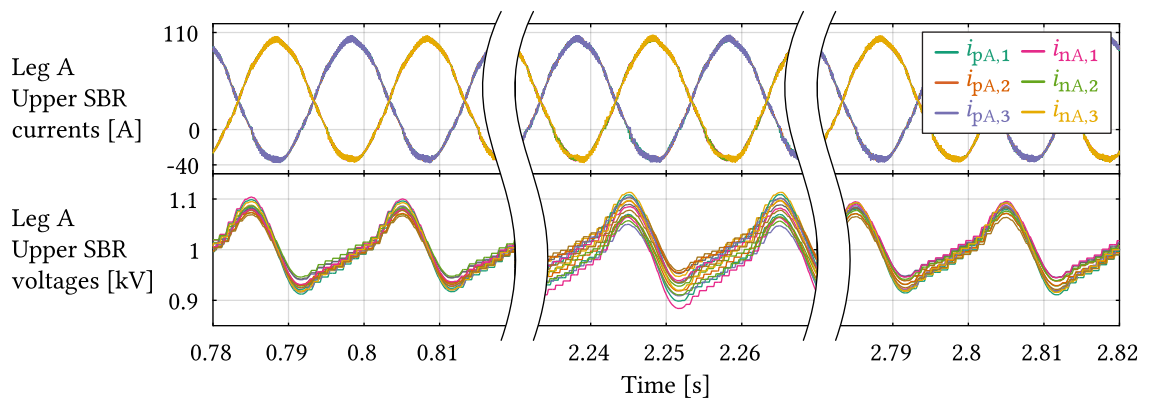


**Fig. 4.17** Leg A upper and lower SBR currents (top); Leg A upper branch voltages (bottom); In spite of the SBR currents being balanced, the SBR voltages tend to diverge in case the SBR energies balancing controller gets deactivated (middle part of the plot). Upon reactivation of this controller, the SBR voltages converge back to the nominal values (the right-most part of the plot). The number of parallel SBRs per branch was set as  $M = 3$ .

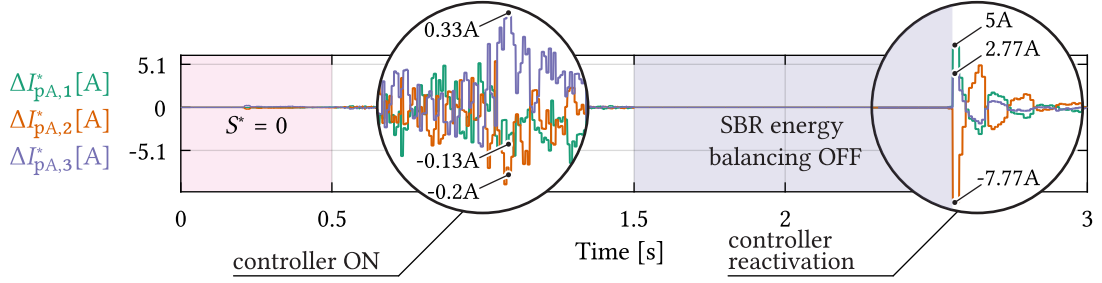


**Fig. 4.18** Branch circulating current references generated by the SBR energy balancing controller.

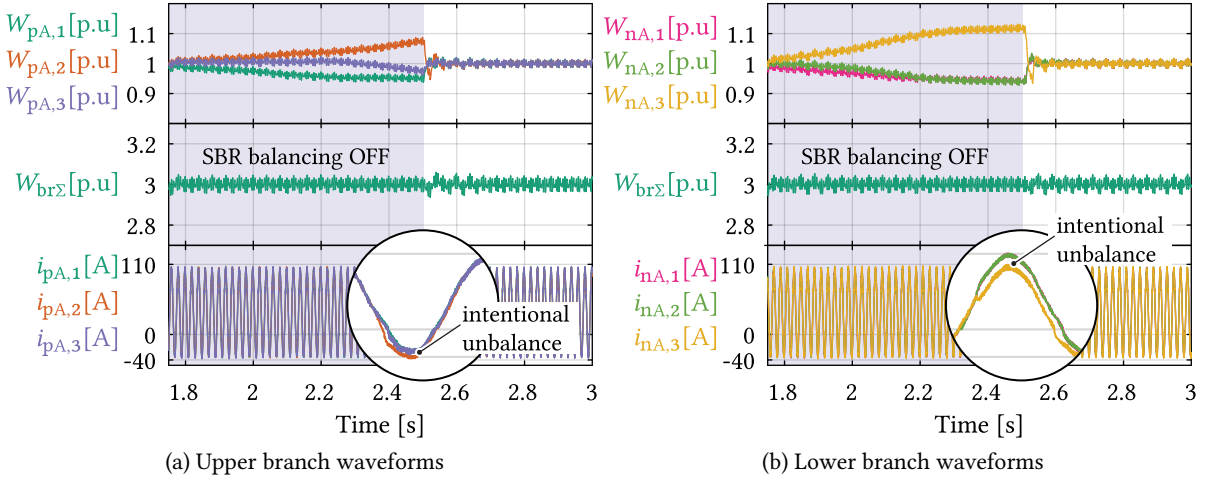


**Fig. 4.19** Energies of the leg A SBRs during the period with the SBR balancing controller being disabled and re-enabled at time instant  $t = 2.5$ s. Please notice, from the zoomed parts of the graph, that intentionally generated SBR currents unbalances (in other words, circulating currents) contribute to reestablishing the SBR energy balance shortly upon reactivation of the controller discussed within this chapter. Normalization of SBR energies was performed with respect the SBR nominal energy  $W_{SBR} = (C/2N)v_{SBR}^2$ .

## 4.6 Further considerations

Another topic relevant to the subject of this chapter refers to the possible improvements in the quality of AC voltage waveforms synthesized by an MMC comprising parallel (sub)branches. Namely, in a conventional MMC, with no parallel SBRs and hosting  $N$  SMs per branch, position of the SM switching instants in time defines whether the so-called  $N + 1$  or  $2N + 1$ -level modulation is going to be obtained [114], [115]. Also, it is obvious that stacking more SMs in series, which can be perceived as an increase in vertical direction, allows for an increase in the number of voltage levels generated by a branch. Paralleling of the SBRs increases the number of installed SMs per branch, however, in horizontal direction. Therefore, various possibilities modulation-wise deserve to be further investigated and it is exactly the next chapter providing a thorough analysis on this matter.



# 5

## Modulation Considerations For the MMC Operating With Parallel Branches

*Taking a conventional modular multilevel converter as a benchmark, it can be shown that paralleling of the converter's branches introduces additional degrees of freedom from the AC voltage modulation standpoint. Namely, the choice of a suitable modulation scheme leads to a reduction in the total harmonic distortion of voltage seen from the converter's AC terminals. The analytic analysis provided in this chapter explores the above mentioned degrees of freedom along with emphasizing the effect of their exploitation on a converter utilizing the phase shifted carrier modulation to synthesize desired voltage references.*

### 5.1 Preliminary Considerations

#### 5.1.1 Available degree of freedom

The first step in conducting the discussion on different modulation possibilities implies the identification of the degrees of freedom provided by paralleling the converter's branches. Henceforth, the term SBRs, adopted in **Chap. 4**), will be used in order to refer to what represents the branch in the conventional MMC. **Fig. 5.1** demonstrates the change in the converter's structure should paralleling of the SBRs be employed with the aim of extending its power capacity. On the left-hand side, two modulation index references ( $m_{pA}^*$  and  $m_{nA}^*$ ) are used in order to synthesize fundamental components of the branch voltages. As stated in **Chap. 4**, control layers providing these references are referred to as the higher control layers. Throughout this chapter, the use of PSC modulation will be considered, although similar reasoning can also be applied to various modulation methods being reported in the literature [101], [104], [116]. As only two branches are used, two sets of carriers, denoted by  $C_p^{(i)}$  and  $C_n^{(i)}$ , where  $i$  denotes the index of an SM within a branch, need to be employed. On the right-hand side, however, one can notice that modulation index references provided by the higher control layers must be adjusted (the terms  $\Delta m_{pA}$  and  $\Delta m_{nA}$ ) in order to achieve balancing of the SBR energies. Given that multiple SBRs are used to fulfill the goal of the converter's power extension, multiple carrier sets are also needed.

Operation of the conventional MMC employing the PSC modulation principles has already been thoroughly analyzed in [114]. Nevertheless, a short recap on this topic will be provided in the next few paragraphs with the aim of providing a framework for the extension in the sense of including additional SBRs into the analysis. According to (5.1), where  $\omega_c = 2\pi f_c$  denotes the carrier angular velocity, two carrier signals modulating two adjacent SMs belonging to the same branch can be displaced by an arbitrary angle  $\gamma_c$ .



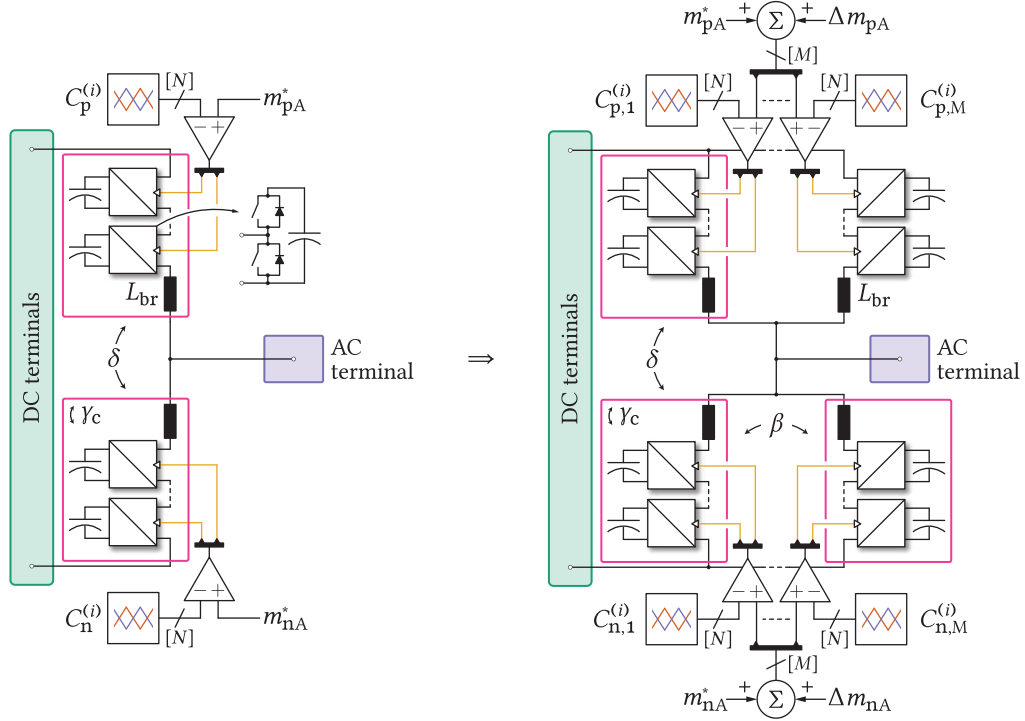


**Fig. 5.1** Migration from the converter leg consisting of two branches (the conventional MMC) towards the configuration comprising multiple paralleled SBRs with the aim of expanding the converter's power capacity.

$$C_p^{(i+1)}(\omega_c t) = C_p^{(i)}(\omega_c t - \gamma_c) \quad (5.1)$$

Owing to the fact that carrier position does not affect the fundamental harmonic of voltage generated by an SM [34], [35], [88], a suitable choice of  $\gamma_c$  can lead to an improvement in the quality of voltage generated by a string of SMs. In other words, harmonic content of the branch voltage can be modified by adjusting the above mentioned carrier displacements.

The forthcoming analyses will assume the use of HB SMs although all of the presented results can be obtained for any type of an SM [81] by employing a slightly modified analytic methods. With no displacement being considered, all the SMs within an observed branch switch at the same time given that the same modulation signal is passed to each one of them. Therefore, irrespective of the number of SMs per branch, the voltage created across its terminals contains only two levels, as presented on the left-most plot of **Fig. 5.2**. Contrary to that, the number of voltage levels can be expanded to  $N + 1$  in case  $\gamma_c = 2\pi/N$  (please keep in mind that annotation introduced in the previous chapter will be retained in the forthcoming paragraphs). According to the middle plot in **Fig. 5.2**, time instants at which different SMs, within the same branch, change their state get shifted with respect to each other. Consequently, multilevel voltage waveforms are generated. Henceforth, it will be assumed that this carrier displacement is naturally chosen without considering it a degree of freedom. This is a rather logical choice taking into account that the purpose of stacking the SMs together is exactly the generation of multilevel voltage waveforms.



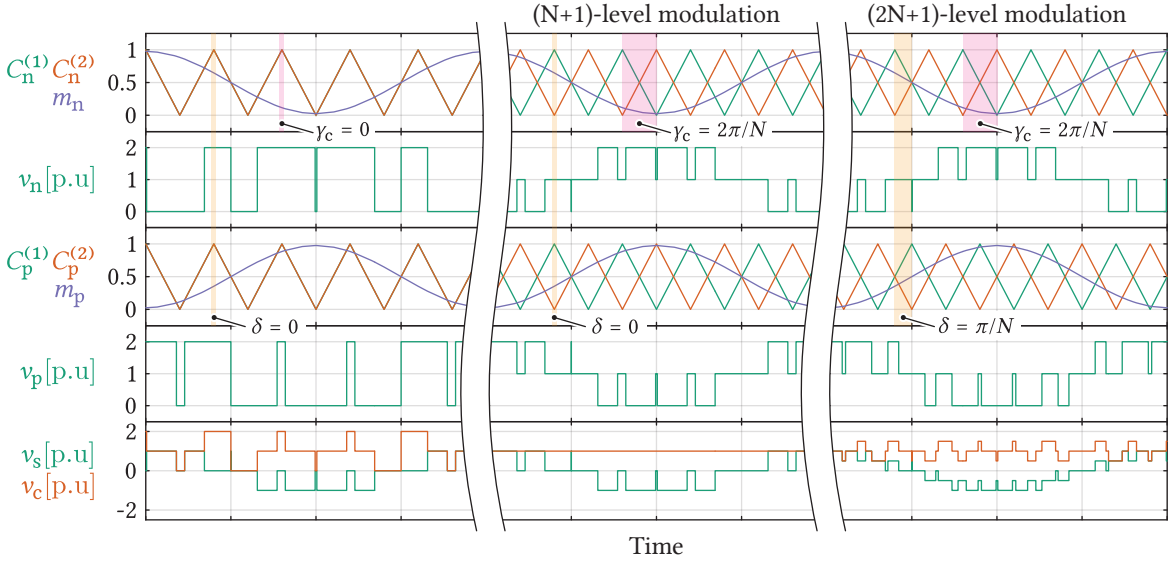


**Fig. 5.2** An example demonstrating the effect that carrier phase shifts have on the voltages synthesized by the conventional MMC leg. According to **Chap. 2**,  $v_s$  and  $v_c$  denote the leg AC and DC voltage components, respectively. For the sake of simplicity, number of SMs per branch was set as  $N = 2$ . Although such a choice might be impractical, it allows for a simple and comprehensible analysis of the leg modulation possibilities.

Further, two carrier signals modulating two identically indexed SMs, however, belonging to different branches ( $C_p^{(i)}$  and  $C_n^{(i)}$ , respectively) can also be displaced according to (5.2). Hence, a degree of freedom is at one's disposal, which, if properly utilized, allows for the leg AC voltage to contain  $2N + 1$  levels [114], as presented on the right-most plot in **Fig. 5.2**. In this case, time instants at which the branches change their state are shifted in time leading to an increase in the number of voltage levels observed from the leg AC terminal.

$$C_p^{(i)}(\omega_c t) = C_n^{(i)}(\omega_c t - \delta) \quad (5.2)$$

According to the above discussion, in the conventional MMC, there is one degree of freedom ( $\delta$ ) regarding the choice of the displacement between two carrier sets modulating two branches belonging to the same leg. Notwithstanding, paralleling of the SBRs increases the number of possibilities from the voltage modulation standpoint. The converter depicted on the right-hand side of **Fig. 5.1** comprises an arbitrary number of paralleled SBRs, whereas carrier signals modulating two identically indexed SMs within two adjacent SBRs can now be misaligned as

$$C_{p,k+1}^{(i)}(\omega_c t) = C_{p,k}^{(i)}(\omega_c t - \beta) \quad (5.3)$$

Additionally, the relationship between two carriers modulating identically indexed SMs within two SBRs belonging to the upper and lower branch can also be established similarly to (5.2), yielding

$$C_{p,k}^{(i)}(\omega_c t) = C_{n,k}^{(i)}(\omega_c t - \delta) \quad (5.4)$$

In contrast to the conventional MMC, an additional degree of freedom referring to the displacement among the SBR carrier sets, denoted by  $\beta$ , provides a new set of possibilities with respect to shaping of the converter's voltage spectral content. Possible carrier displacements within the MMC operating with parallel SBRs can be summarized as follows:

- $\gamma_c$  - misalignment between the carriers modulating two adjacent SMs within the same SBRs. As stated above, its value will be considered fixed and equal to  $2\pi/N$ . Henceforth, it will not be considered a degree of freedom.
- $\beta$  - phase shift between carrier sets modulating two adjacent SBRs within the same branch.
- $\delta$  - phase shift between carrier sets modulating two identically indexed SBRs, however, belonging to the lower and the upper branch of the same leg.

Please notice that **Fig. 5.1** contains a simple illustration of the angles definition provided above. It is noteworthy that, even if only two branches per leg are considered (regular MMC), the effects of various carrier positions depend on parity of the number of SMs per branch [114]. With addition of parallel SBRs into the system, the number of possible combinations increases. Consequently, the effects achieved by utilizing the carrier positioning degrees of freedom should be further investigated with the aim of coming up with a strategy ensuring a reduction in the Total Harmonic Distortion (THD) of voltage seen from the legs' AC terminals.

### 5.1.2 Assumptions and adopted simplifications

In case frequency of the converter AC currents was denoted by  $f_0$ , according to [114], the carrier frequency  $f_c$  must be selected such that  $pf_c = qf_0$ , where  $(q/p) \notin \mathbb{Z}$ . Since all the SMs share the same current, while synthesizing the same fundamental voltage components (please recall that position of the carrier does not affect the fundamental component of voltage synthesized by an SM), power oscillations at their terminals are ideally identical. Therefore, all the SMs should experience the same low frequency voltage oscillations across their capacitors. However, not all the SMs are identical in practice, therefore local SM balancing depicted in **Fig. 5.3** must be used, otherwise individual SM voltages become unbalanced showing the tendency of diverging from their mean values over time.

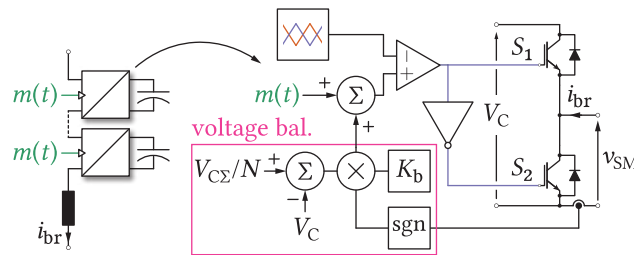


**Fig. 5.3** Modulation index adjustment on the individual level must be performed in case PSC modulation is used. Although all the SMs are expected to experience identical power oscillations across the terminals, not all of them are the same. For instance, SM capacitance deviations in the range of  $\pm 20\%$  around the nominal value are likely to happen in practice. Depending on the branch current direction, along with the measured capacitor voltage, an SM modulation index is corrected. To ensure that these corrections do not corrupt the voltage across the terminals of an observed (sub)branch, every SM receives the voltage reference equal to  $\sum_{i=1}^N V_{Ci}/N$ .

As can be observed, despite receiving identical modulation indices (please recall that in case PSC modulation is used, the modulation index corresponds to the insertion indices defined in **Chap. 2**), every SM performs its local adaptation (the part labeled with **voltage bal.**) in order to achieve voltage balancing on the SBR level.

To avoid the need of analyzing every SM individually, the modifications of modulation indices will be neglected, while keeping in mind their practical importance. Consequently,  $m_i(t) = m^*(t)$ . Phase-shift among the carriers within the same branch, set as  $\gamma = 2\pi/N$ , causes all the SMs to switch at different time instants. Hence, their voltages are not exactly the same, as can be seen in **Figs. 4.13** and **4.17**. Nevertheless, according to the same figures, claiming that  $v_{Ci}(t) \approx v_C(t)$  can be considered a reasonable approximation.

Another observation relevant for the scope of this chapter refers to the oscillations of the SM voltages. Namely, from the higher control layers, every branch receives the reference voltage  $v_{\{n/p\}}^* = V_{br}^* \left( \frac{1}{2} \pm \frac{\hat{m}}{2} \cos(\omega_0 t) \right)$ , where  $V_{br}^*$  denotes the reference of the total branch voltage average value, which is assumed to be properly maintained through the control of branch energies described in **Chaps. 3** and **4**. At this point, one might expect to obtain the modulation (insertion) index as

$$\begin{aligned} m_{\{n/p\}}^* &= \frac{v_{\{n/p\}}^*}{V_{br}^*} \\ &= \frac{1}{2} \pm \frac{\hat{m}}{2} \cos(\omega_0 t) \end{aligned} \quad (5.5)$$

However, as the total branch voltage oscillates according to (3.39) and (3.40), it can be shown that the use of (5.5) causes the voltage produced by the branch to contain all the harmonics present in  $v_{br\Sigma}$ . This method of generating modulation index references is known in the literature as the direct modulation [86]. Even though it features global asymptotic stability, unless additional controllers are employed, poor energy control dynamics is obtained [85], [117], [118]. Therefore, closed-loop control [84], implying modifications of the modulation indices according to the above mentioned branch voltage oscillations is adopted as

$$\begin{aligned} m_{\{n/p\}} &= \frac{v_{\{n/p\}}^*}{v_{br\Sigma}} \\ &= \underbrace{\left\{ \frac{1}{2} \pm \frac{\hat{m}}{2} \cos(\omega_0 t) \right\}}_{m_{n/p}^*} \frac{V_{br}^*}{v_{\{n/p\}\Sigma}} \end{aligned} \quad (5.6)$$

In [34], [35] a systematic approach towards deriving the spectrum of a PWM pulse train was presented. It relies on the use of 1-D functions to obtain the results already presented in [88], however, without the need for utilizing the so-called double Fourier integrals.

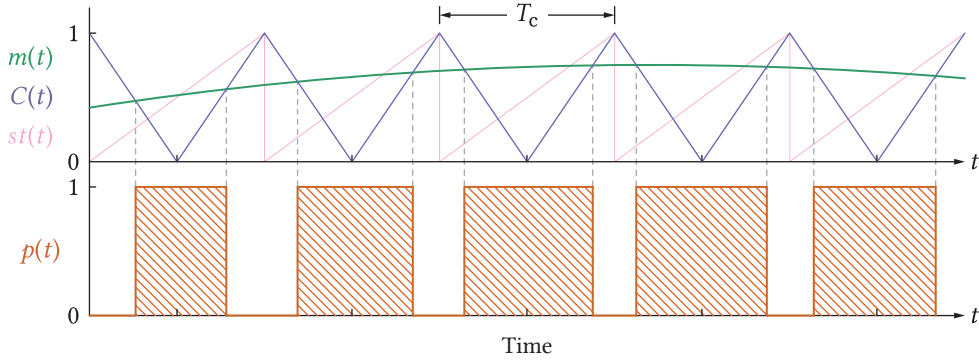


**Fig. 5.4** Pulse train created by the PWM process employing the natural sampling.

Comparison of an arbitrary reference signal  $m(t)$  with a triangular carrier, as depicted in **Fig. 5.4**, results in a pulse train  $p(t)$ , which can be expressed as

$$p(t) = m(t) + \underbrace{st(\theta_1) + st(-\theta_2)}_{\text{higher order harmonics}} \quad (5.7)$$

In (5.7), trailing edge sawtooth carrier function was denoted by  $st(\theta)$ , whereas  $\theta_1 = \omega_c t - \gamma_c - \pi - \pi m(t)$  and  $\theta_2 = \omega_c t - \gamma_c + \pi + \pi m(t)$ . The above equation confirms the statement that carrier position does not affect the fundamental component of the synthesized pulse train, nevertheless, higher order harmonics contained inside the term  $st(\theta_1) + st(-\theta_2)$  heavily depend on it.

By observing a single MMC SM, while adopting the assumptions established so far (identical modulation indices along with equal branch voltage distribution), one can express the voltage across its terminals as

$$v_{SM}(t) = p(t) \frac{v_{br\Sigma}}{N} \quad (5.8)$$

Substitution of (5.6) and (5.7) into the above equation yields

$$v_{SM} = \underbrace{\left\{ \frac{1}{2} \pm \frac{\hat{m}}{2} \cos(\omega_0 t) \right\} \frac{V_{br}^*}{N}}_{\text{corresponds to the idealized case}} + \underbrace{\left\{ st(\theta_1) + st(-\theta_2) \right\} \frac{v_{br\Sigma}}{N}}_{\text{higher order harmonics}} \quad (5.9)$$

It is straightforward to conclude that the first term in (5.9) corresponds to the waveform that would be obtained if a string of SMs with flat capacitor voltages, equal to  $V_{br}^*/N$ , were to be analyzed. On the other hand, precise investigation of the term describing the higher order harmonics requires a certain amount of mathematical manipulations to be performed.

Total branch voltage oscillations introduced in (3.39) and (3.40) can be taken into account in (5.6) by establishing (5.10), where  $\Psi_1$  and  $\Psi_2$  denote the phases of the total branch voltage oscillating components. Nevertheless, their exact values are not considered of importance at this specific moment.

$$\frac{V_{br}^*}{v_{\{n/p\}\Sigma}} = \frac{1}{1 \mp \Delta \hat{v}_1 \cos(\omega_0 t + \Psi_1) + \Delta \hat{v}_2 \cos(2\omega_0 t + \Psi_2)} \quad (5.10)$$

Since both  $m_{\{n/p\}}^*$  and  $V_{br}^*/v_{\{n/p\}\Sigma}$  from (5.6) have the same period, equal to  $2\pi/\omega_0$ , their product also represents a periodic function expandable into the Fourier series. Nevertheless, taking into account an infinite number of harmonics, resulting from the expansion of (5.6), would make the analysis of the right-hand side of (5.7) and (5.9) rather difficult. Therefore, a finite number of terms (harmonics) from the Fourier equivalent of (5.6) should be selected.

To provide an illustration on the sufficient number of harmonics representing (5.6) with the satisfactory precision, the lower branch voltage variations can be calculated in accordance with the averaged model provided in **Chap. 2**. For the converter with parameters provided in **Tab. 5.1**, the nominal SM capacitance  $C_{SM}^*$  was calculated such that variations of voltage in the range of  $\pm 5\%$ , normalized with respect to the branch average voltage, are ensured. As  $\{\hat{v}_1, \hat{v}_2\} \propto 1/C_{SM}$  [48], [49] it is clear from (5.10) that variations in the SM capacitance affect the shape of the modulation index.

**Fig. 5.5** depicts the variations of the converter modulation index in case the SM capacitance is changed in the steps of  $0.25C_{SM}^*$ . Even though the time domain functions presented in **Fig. 5.5(a)** do not significantly differ from each other, one can notice from **Fig. 5.5(b)** that reduction of the SM capacitance contributes to the introduction of an additional spectral components (mostly at  $2\omega_0$  and  $3\omega_0$ ). Cutting the nominal SM capacitance in half leads to the total branch voltage oscillations of  $\pm 10\%$ , which will be considered the boundary point in the sense of oscillations limits. Moreover, it can be seen from **Fig. 5.5(b)** that, on these terms, modulation index can be represented as (5.11). According to **App. B**, such an estimation can be conveniently used in order to obtain the SM switching function in the form of (5.12), where  $J_n(x)$  denotes Bessel function of the first kind.

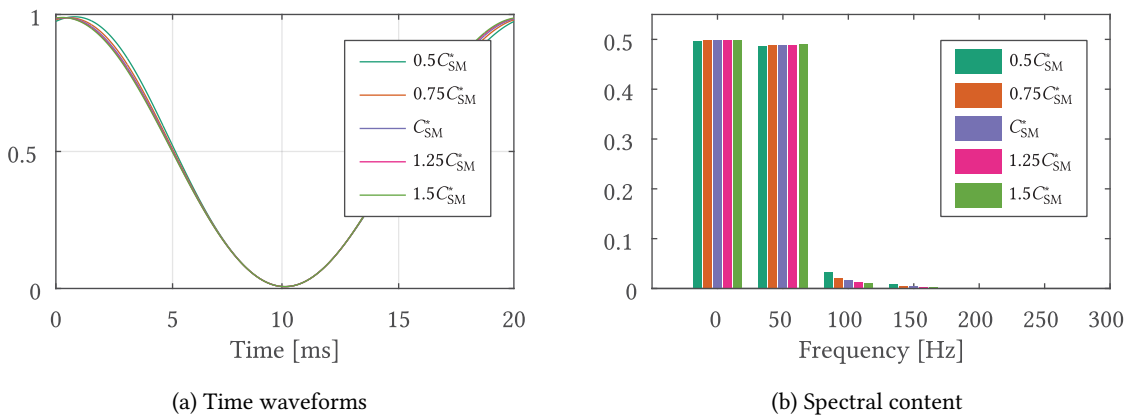


**Fig. 5.5** Variations of the modulation index (both in time and frequency domain) generated in accordance with the MMC closed loop control. Please notice that variations of the SM capacitance affect the generation of modulation index as the total branch voltage oscillations are inversely proportional to it.

$$m(t) \approx m_0 + \hat{m}_1 \cos(\omega_0 t + \zeta_1) + \hat{m}_2 \cos(2\omega_0 t + \zeta_2) + \hat{m}_3 \cos(3\omega_0 t + \zeta_3) \quad (5.11)$$

$$p(t) = m(t) + \frac{2}{\pi} \sum_{k=1}^{\infty} \sum_{z=-\infty}^{\infty} \sum_{q=-\infty}^{\infty} \sum_{n=-\infty}^{\infty} \frac{(-1)^k}{k} J_z(k\pi\hat{m}_3) J_q(k\pi\hat{m}_2) J_n(k\pi\hat{m}_1) \times \\ \times \sin\left(k\pi m_0 + \frac{z+q+n}{2}\pi\right) \cos([k\omega_c + (3z+2q+n)\omega_0]t - k\gamma_c + (z\zeta_3 + q\zeta_2 + n\zeta_1)) \quad (5.12)$$

Last but not least, previously derived expression did not consider the sampling process (for instance, regular symmetric or asymmetric sampling) of modulation indices which is an inherent feature of every digital system. In [34], [35] it was shown that sample and hold block attached to the voltage modulator introduces additional components to the SM voltage spectrum. Notwithstanding, the aim of this chapter is not to provide the exact calculation of the branch voltage harmonics, but to conduct the qualitative analysis of the effects that the use of modulation degrees of freedom has upon the AC voltage seen from the converter's terminals. Hence, the analysis will continue assuming that natural sampling of all the quantities within the system is used. Such an assumption can also be justified by the fact that sampling frequency of currents/voltages in a systems similar to the MMC (which comprises a high number of SMs) significantly exceeds the switching frequency of the semiconductor devices. Moreover, injection of triplen harmonics into the leg AC voltage reference is omitted since it does not affect the reasoning used to derive the forthcoming expressions.

## 5.2 Analysis of voltage components generated by the converter leg

With the aim of providing the reader with a comprehensive analysis of the voltage generated by a converter leg, the bottom-up approach illustrated in the figure bellow will be adopted. Given that the SBR represents a basic structure used for the converter's power extension, this subsection commences with the detailed analysis of the SBR voltage, underlying the upcoming discussions on possible improvements of the converter voltage quality.

### 5.2.1 SBR voltage analysis

As every MMC leg consist of branches, which are further split into the SBRs in the observed case, without the loss of generality, one can start the analysis of the leg voltages by observing a single SBR belonging to the lower branch of leg A.

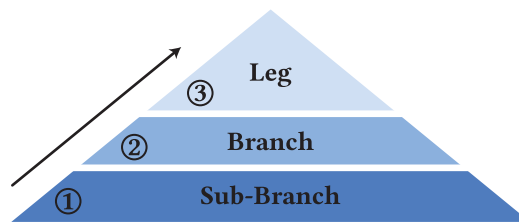


Fig. 5.6 Bottom-up approach adopted in the analysis of the converter leg voltage components

To obtain the SBR voltage, summation of expressions (5.12) written for every individual SM can be performed as

$$v_{\text{SBR}} = \underbrace{\frac{V_{\text{br}}^*}{2} + \hat{m} \frac{V_{\text{br}}^*}{2} \cos(\omega_0 t)}_{v_{\text{br}}^*} + \frac{2v_{\text{br}\Sigma}}{\pi N} \sum_{i=1}^N \sum_{k=1}^{\infty} \sum_{z=-\infty}^{\infty} \sum_{q=-\infty}^{\infty} \sum_{n=-\infty}^{\infty} \frac{(-1)^k}{k} J_z(k\pi\hat{m}_3) J_q(k\pi\hat{m}_2) J_n(k\pi\hat{m}_1) \times \\ \times \sin\left(k\pi m_0 + \frac{z+q+n}{2}\pi\right) \cos([k\omega_c + (3z+2q+n)\omega_0]t - k\gamma_c(i) + z\zeta_3 + q\zeta_2 + n\zeta_1) \quad (5.13)$$

Adopting  $\gamma_c(i) = (i-1)\gamma_c^*$ , while noticing that none of the Bessel functions from the equation above depends on the summation index  $i$ , leads to

$$v_{\text{SBR}} = v_{\text{br}}^* + \frac{2v_{\text{br}\Sigma}}{\pi N} \sum_{k=1}^{\infty} \sum_{z=-\infty}^{\infty} \sum_{q=-\infty}^{\infty} \sum_{n=-\infty}^{\infty} \frac{(-1)^k}{k} J_z(k\pi\hat{m}_3) J_q(k\pi\hat{m}_2) J_n(k\pi\hat{m}_1) \times \\ \times \sin\left(k\pi m_0 + \frac{z+q+n}{2}\pi\right) \sum_{i=1}^N \cos([k\omega_c + (3z+2q+n)\omega_0]t - k(i-1)\gamma_c^* + (z\zeta_3 + q\zeta_2 + n\zeta_1)) \quad (5.14)$$

Choosing the phase shift between two adjacent carriers as  $\gamma_c^* = 2\pi/N$ , leads to the simplification given by (5.15). Namely, the sum of  $N$  cosine functions, chosen such that  $2\pi/N$  corresponds to the phase shift between two adjacent waves, equals zero. On these terms, (5.16) follows directly from (5.14).

$$\sum_{i=1}^N \cos([k\omega_c + (3z+2q+n)\omega_0]t - k(i-1)\gamma_c^* + z\zeta_3 + q\zeta_2 + n\zeta_1) = \\ = \begin{cases} N \cos([rN\omega_c + (3z+2q+n)\omega_0]t + z\zeta_3 + q\zeta_2 + n\zeta_1), & k = rN \ (r \in \mathbb{N}) \\ 0, & \text{otherwise} \end{cases} \quad (5.15)$$

Please notice that the sideband harmonics, which are defined as components for which  $3z+2q+n \neq 0$ , in the SBR voltage spectrum, appear around the multiples of  $\omega_{\text{SBR}} = N\omega_c$ . Consequently, by following the logic introduced with the derivation of a single SM voltage where the first set of sideband harmonics is observed around the SM switching frequency [34], [35],  $\omega_{\text{SBR}}$  is referred to as the SBR apparent switching frequency.

$$v_{\text{SBR}} = v_{\text{br}}^* + \frac{2v_{\text{br}\Sigma}}{\pi N} \sum_{r=1}^{\infty} \sum_{z=-\infty}^{\infty} \sum_{q=-\infty}^{\infty} \sum_{n=-\infty}^{\infty} \frac{1}{r} J_z(rN\pi\hat{m}_3) J_q(rN\pi\hat{m}_2) J_n(rN\pi\hat{m}_1) \dots \\ \dots \sin\left(rN\pi \underbrace{(m_0 - 1)}_{\approx -\frac{1}{2}} + \frac{z+q+n}{2}\pi\right) \sum_{i=1}^N \cos\left([rN\omega_c + (3z+2q+n)\omega_0]t + z\zeta_3 + q\zeta_2 + n\zeta_1\right) \quad (5.16)$$

**Tab. 5.1** Parameters of the converter utilized for verification of the expressions derived above

Rated power	DC link voltage	AC grid voltage	No. of SMs per SBR	No. of SBRs per branch	SM capacitance	SBR inductance	SM switching frequency	Grid inductance
1MW	5.5kV	3.3kV	8	2	2.25mF	5mH	285Hz	6.93mH

At this point, it can be effortlessly examined which carrier harmonics exist depending on the number of SMs per branch. Namely, carrier harmonics are defined as components within the right-hand side summation in (5.14) for which  $3z + 2q + n = 0$ . If  $N$  is odd, then

$$\sin\left(\frac{rN\pi}{2}\right) = \begin{cases} 0, & \text{even } r \\ (-1)^{\frac{rN-1}{2}}, & \text{odd } r \end{cases} \quad (5.17)$$

If, on the other hand,  $N$  is even, then  $\sin\left(\frac{rN\pi}{2}\right) = 0$  meaning that carrier harmonics do not exist. Nevertheless, sideband harmonics do exist.

Calculation of the SBR voltage according to (5.16) introduces the need to represent the SBR total voltage according to (5.18), whereas oscillating components' magnitudes ( $\Delta\hat{v}_1$  and  $\Delta\hat{v}_2$ ) along with their phase angles ( $\Psi_1$  and  $\Psi_2$ ) can be obtained from the branch averaged models presented in **Chap. 2**.

$$v_{br\Sigma} = V_{br}^* - \Delta\hat{v}_1 \cos(\omega_0 + \Psi_1) - \Delta\hat{v}_2 \cos(2\omega_0 + \Psi_2) \quad (5.18)$$

In order to verify the effectiveness of the derived expressions, simulation model of the MMC with parameters provided in **Tab. 5.1** was developed in PLECS. In accordance with the converter averaged model presented in **Chap. 2**, the steady state currents and voltages were calculated under the assumption of the converter delivering the rated power to the grid with the unity power factor. Thereafter, these were used with the aim of calculating the branch energy (voltage) variations. As can be seen from **Fig. 5.7**, excellent matching of the spectral contents of the SBR voltage obtained with (5.16) and PLECS-based simulations can be observed.

THD, defined in (5.19), represents a common practice of expressing the amount of higher order harmonics within a certain waveform. By combining (5.16) and (5.19) in MATLAB, THD of the SBR voltage, under the conditions defined in **Tab. 5.1**, was calculated as  $\text{THD}_{\text{calc}} = 13.48\%$ .

$$\text{THD} = \frac{1}{\hat{v}_1} \sqrt{\sum_{i=2}^N \hat{v}_i^2} \quad (5.19)$$



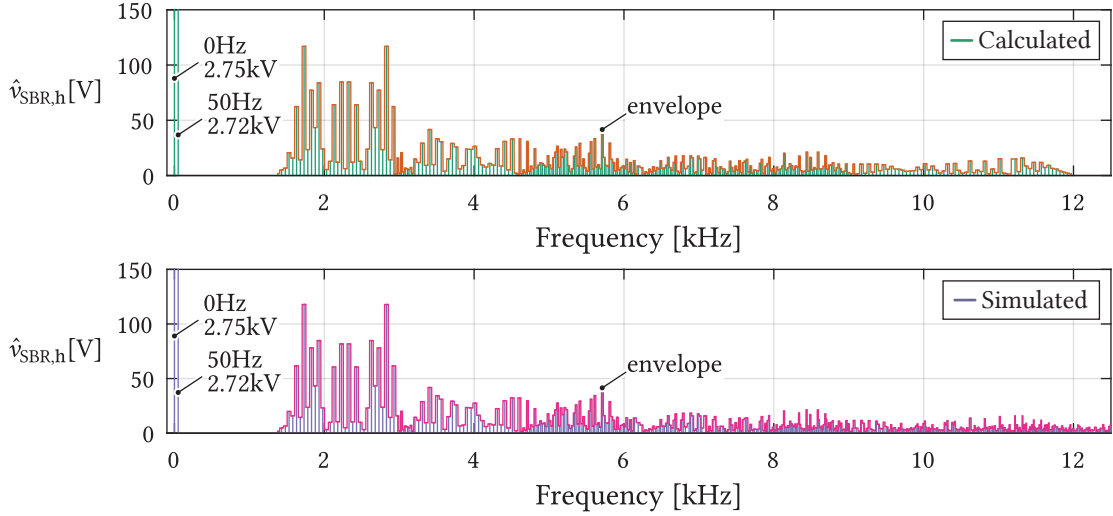


**Fig. 5.7** Comparison between the SBR spectral contents obtained from the analytic analysis (5.14) and the simulations. Since fundamental and DC components of voltage generated by an SBR are not in the focus of this chapter, the scale was adjusted such that higher order harmonics can be presented to the best possible extent.

Also, THD relative error (5.20) provides an illustrative gauge of the mismatch between the simulated and calculated spectra and in the case depicted in **Fig. 5.7** it was calculated as  $\Delta\text{THD}_{\%} = -0.77\%$ . Consequently, the assumptions introduced in **Sec. 5.1.2** do not contribute to the severe errors when considering the possible reductions in the converter's AC voltage components.

$$\Delta\text{THD}_{\%} = \frac{\text{THD}_{\text{calc}} - \text{THD}_{\text{sim}}}{\text{THD}_{\text{sim}}} \cdot 100 \quad (5.20)$$

Additionally, it can be seen from both plots in **Fig. 5.7** that the first set of harmonics indeed appears centered around the SBR apparent switching frequency  $f_{\text{SBR}} = Nf_{\text{sw}}$ , which in the analyzed case equals 2280Hz. As will be demonstrated shortly, introducing a proper time shift in the switching events of paralleled SBRs ensures the cancellation of this harmonics set, leading to the further improvement of the branch voltage THD.

### 5.2.2 Branch voltage analysis

In case  $M$  SBRs are connected in parallel (which is referred to as the branch), and without any SMs being temporarily/permanently bypassed (i.e. no faulty SMs), equivalent voltage seen from the branch terminals can be calculated as (5.21)

$$v_{\text{br}} = \frac{1}{M} \sum_{j=1}^M v_{\text{SBR},j} \quad (5.21)$$

As defined in **Sec. 5.1.1**, the sets of carriers utilized to modulate two adjacent SBR can be shifted by an angle denoted by  $\beta$ . On these terms, substituting (5.13) into (5.21) provides:

$$v_{br} = v_{br}^* + \frac{2v_{br\Sigma}}{\pi NM} \sum_{u=1}^M \sum_{i=1}^N \sum_{k=1}^{\infty} \sum_{z=-\infty}^{\infty} \sum_{q=-\infty}^{\infty} \sum_{n=-\infty}^{\infty} \frac{(-1)^k}{k} J_z(k\pi\hat{m}_3) J_q(k\pi\hat{m}_2) J_n(k\pi\hat{m}_1) \times \\ \times \sin\left(k\pi m_0 + \frac{z+q+n}{2}\pi\right) \cos\left([k\omega_c + (3z+2q+n)\omega_0]t - k\left[(i-1)\frac{2\pi}{N} + (u-1)\beta\right] + z\zeta_3 + q\zeta_2 + n\zeta_1\right) \quad (5.22)$$

Expression (5.22) can be further reduced. By using the logic similar to the one employed to derive (5.16), one can conclude that (5.22) can be rearranged as (5.23).

$$v_{br} = v_{br}^* + \frac{2v_{br\Sigma}}{\pi NM} \sum_{r=1}^{\infty} \sum_{z=-\infty}^{\infty} \sum_{q=-\infty}^{\infty} \sum_{n=-\infty}^{\infty} \frac{(-1)^{rN}}{r} J_z(rN\pi\hat{m}_3) J_q(rN\pi\hat{m}_2) J_n(rN\pi\hat{m}_1) \times \\ \times \sin\left(rN\pi m_0 + \frac{z+q+n}{2}\pi\right) \sum_{u=1}^M \cos([rN\omega_c + (3z+2q+n)\omega_0]t - rN(u-1)\beta + z\zeta_3 + q\zeta_2 + n\zeta_1) \quad (5.23)$$

As the initial step in the analysis being the subject of this subsection, one can set the SBR carrier sets displacement as  $\beta = 0$ . In this case, (5.23) becomes identical to (5.16), meaning that the voltage generated across the terminals of the observed branch corresponds to the voltage generated by any of its SBRs. Such a conclusion is rather logical for two reasons. Firstly, as it has been stated on several occasions so far, all the SBRs receive the same modulation index, therefore all the SBRs change their state at the same time. Secondly, total voltage of all the SBRs is assumed to be the same.

**Fig. 5.8(a)** provides a simple illustration of the above discussion in case two SBRs containing two SMs each are paralleled to form the converter branch. Additionally, voltage across all of the SMs was considered flat and equal to 1 [p.u]. As can be seen, both SBRs change their state at the same time, which is, in general, recognized as the voltage waveform containing  $(N+1)$ -levels. Moreover, the apparent switching frequency of the branch as a whole corresponds to the apparent switching frequency of any of its SBRs.

By carefully analyzing (5.23) one can conclude that if  $\beta = \frac{2\pi}{MN}$ , then

$$\sum_{u=1}^M \cos([rN\omega_c + (3z+2q+n)\omega_0]t - rN(u-1)\beta + z\zeta_3 + q\zeta_2 + n\zeta_1) = \\ \begin{cases} M \cos([pMN\omega_c + (3z+2q+n)\omega_0]t + z\zeta_3 + q\zeta_2 + n\zeta_1), & r = pM \ (p \in \mathbb{N}) \\ 0, & \text{otherwise} \end{cases} \quad (5.24)$$

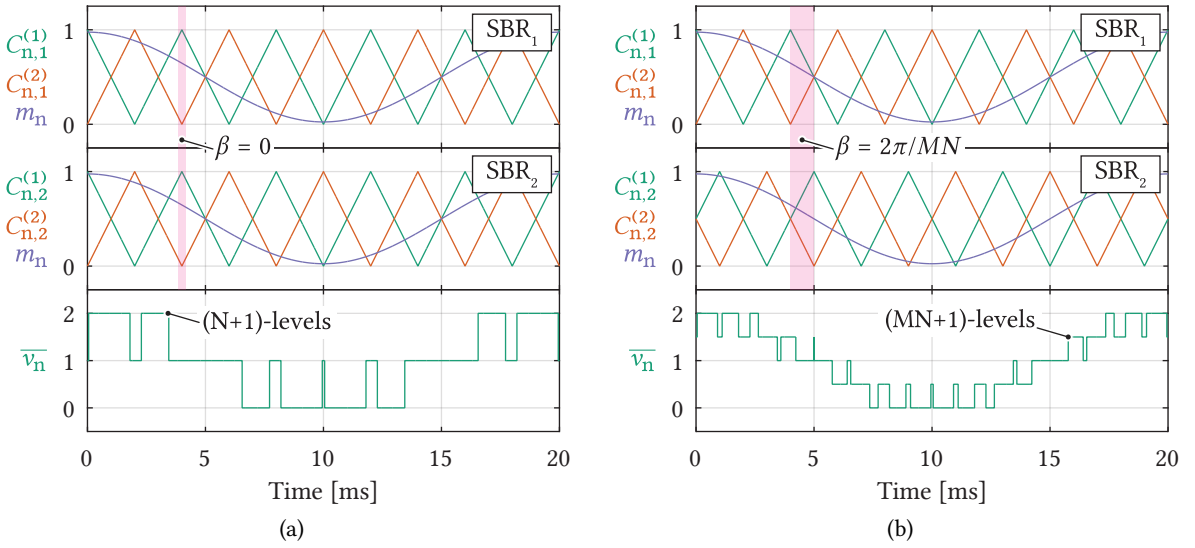


**Fig. 5.8** A simplified example demonstrating the effect of misaligning the carrier sets modulating two adjacent SBRs. In the presented example, two SBRs containing two SMs are used to comprise the converter branch. Also, voltages across the SMs' capacitors was assumed to be flat for the purpose of simplifying the illustrations.

Consequently, (5.25) follows from (5.23). It is noteworthy that such a selection of the angle  $\beta$  causes the apparent switching frequency of the branch to increase  $M$  times when compared to the apparent switching frequency of a single SBRs, which is mathematically formulated as  $\omega_{BR} = MN\omega_c$ .

$$v_{br} = v_{br}^* + \frac{2v_{br\Sigma}}{\pi NM} \sum_{p=1}^{\infty} \sum_{z=-\infty}^{\infty} \sum_{q=-\infty}^{\infty} \sum_{n=-\infty}^{\infty} \frac{1}{p} J_z(pMN\pi\hat{m}_3) J_q(pMN\pi\hat{m}_2) J_n(pMN\pi\hat{m}_1) \sin \left( pMN\pi \underbrace{(m_0 - 1)}_{\approx \frac{1}{2}} + \frac{z + q + n}{2} \pi \right) \cos \left( \underbrace{[pMN\omega_c + (3z + 2q + n)\omega_0]}_{\omega_{br}} t + z\zeta_3 + q\zeta_2 + n\zeta_1 \right) \quad (5.25)$$

**Fig. 5.8(b)** depicts the waveform of a branch equivalent voltage in case SBR carrier sets displacement is set as  $\beta = \frac{2\pi}{MN}$ , while retaining all the assumptions established during the discussion of **Fig. 5.8(a)**. On these terms, two SBRs change their states at time instants being shifted in time. Consequently, the apparent switching frequency of the branch gets doubled (in general, it is increased  $M$  times), whereas the number of levels observed in the branch equivalent voltage gets increased to  $MN + 1$ . Notwithstanding, keep in mind that **Figs. 5.8(a)** and **5.8(b)** depict quite simplified and unrealistic case, therefore to extend the analysis of the branch voltage waveform, comparison of results obtained by using (5.25) with the offline simulations needs to be conducted.

For the purpose of validating the correctness of (5.25), PLECS simulations of the converter with parameters provided in **Tab. 5.1** were reused. **Fig. 5.9** presents the branch voltage spectral components obtained by means of (5.25) (the top-most plot) as well as the simulations (the bottom-most plot). With the aim of emphasizing the effect of shifting the carrier sets modulating two adjacent SBRs, the spectral components of an individual SBR voltage were intentionally included and colored in gray.

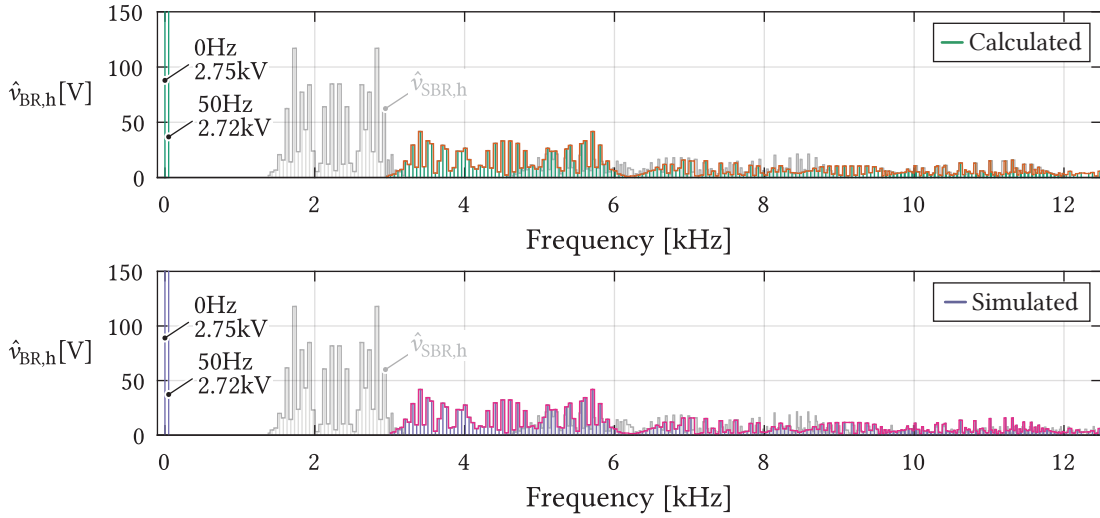


**Fig. 5.9** Comparison between the branch spectral contents obtained from the analytic analysis (5.25) and the simulations. Since fundamental and DC components of voltage generated by a branch are not in the focus of this chapter, the scale was adjusted such that the higher order harmonics can be presented to the best possible extent. Please notice that set of harmonics centered around the SBR apparent switching frequency vanishes. However, to emphasize the change in the branch voltage, an individual SBR voltage spectrum was intentionally included and colored in gray.

In contrast to the SBR voltage, a branch voltage does not contain any spectral components centered around the SBR apparent switching frequency. Conversely, all the sideband harmonics are centered around the branch apparent switching frequency  $\omega_{BR} = MN\omega_c$ , which in the analyzed case equals  $\omega_{BR} = 4560\text{Hz}$ . Since a whole set of harmonics centered around the SBR switching frequency vanished, branch voltage THD, calculated as  $\text{THD}_{\text{calc}} = 6.58\%$ , gets approximately halved when compared to a THD of an individual SBR ( $\text{THD}_{\text{calc}}^{\text{SBR}} = 13.48\%$ ). To estimate the correctness of results obtained by means of (5.25) the relative THD error was calculated, according to (5.20), as  $\Delta\text{THD}_{\%} = 0.64\%$ . Thus, an excellent matching between the calculated and simulated branch voltage spectrum is achieved.

Investigating the carrier harmonics (where, once again, the carrier harmonics will be considered those in (5.25) for which  $3z + 2q + n = 0$ ) shows that different combinations of  $N$  and  $M$  affect the components appearing in the branch voltage spectrum. Analysis of the term  $\sin(pNM\pi/2)$ , which actually determines the existence of carrier harmonics, provides **Tab. 5.2**.

**Tab. 5.2** Effect that parity of the product  $NM$  has upon the existence of the carrier harmonics observed in the branch voltage spectrum. Please keep in mind that, in this specific case, carrier harmonics were defined as the ones occurring at the apparent switching frequency of the branch  $\omega_{BR}$ .

$N$	$M$	$NM$	$p$	$\sin(pNM\pi/2)$
odd	odd	even	odd/even	0
even	even	even	odd/even	0
even	even	even	odd/even	0
odd	odd	odd	even	0
			odd	$(-1)^{\frac{pMN-1}{2}}$

### 5.2.3 Leg voltage analysis

Once the converter branch voltage analysis is conducted, it can be further expanded and carried on the leg level since two voltage components being relevant for each of the legs can be calculated according to (4.1) and (4.2). As it was previously stated, (5.25) represents the lower branch voltage, so it will be rewritten as (5.26), where  $v_n^* = \frac{V_{br}^*}{2} + \hat{m} \frac{V_{br}^*}{2} \cos(\omega_0)$ , for the purposes of the forthcoming analysis.

$$v_n = v_n^* + \frac{2v_{n\Sigma}}{\pi NM} \sum_{p=1}^{\infty} \sum_{z=-\infty}^{\infty} \sum_{q=-\infty}^{\infty} \sum_{n=-\infty}^{\infty} \frac{J_z(pMN\pi\hat{m}_3)J_q(pMN\pi\hat{m}_2)J_n(pMN\pi\hat{m}_1)}{p} \times \sin\left(\underbrace{\frac{z+q+n}{2}\pi}_{\Phi_{zqn}} - \frac{pMN\pi}{2}\right) \cos([pMN\omega_c + (3z+2q+n)\omega_0]t + z\zeta_3 + q\zeta_2 + n\zeta_1) \quad (5.26)$$

Derivation of the upper branch voltage starts with an arbitrary SBR belonging to it, similarly to (5.13). However, there are two differences with respect to (5.13). Firstly, observation of (5.27) and (5.28) shows that all the components oscillating at  $1 \times \omega_0$  in  $m_n$  and  $m_p$  are in the counter phase, whereas the opposite is true for the components oscillating at  $2 \times \omega_0$ . Consequently, it is logical to claim that the same will apply to the spectral components of their Fourier transformations, leading to the establishment of (5.29) and (5.30). Additionally,  $v_p^* = \frac{V_{br}^*}{2} - \hat{m} \frac{V_{br}^*}{2} \cos(\omega_0)$ .

$$m_n = \left\{ \frac{1}{2} + \frac{\hat{m}}{2} \cos(\omega_0 t) \right\} \frac{V_{br}^*}{V_{br}^* - \Delta \hat{v}_1 \cos(\omega_0 + \Psi_1) - \Delta \hat{v}_2 \cos(2\omega_0 + \Psi_2)} \quad (5.27)$$

$$m_p = \left\{ \frac{1}{2} - \frac{\hat{m}}{2} \cos(\omega_0 t) \right\} \frac{V_{br}^*}{V_{br}^* + \Delta \hat{v}_1 \cos(\omega_0 + \Psi_1) - \Delta \hat{v}_2 \cos(2\omega_0 + \Psi_2)} \quad (5.28)$$

$$\{m_{p0}, \hat{m}_{p1}, \hat{m}_{p2}, \hat{m}_{p3}\} = \{m_{n0}, \hat{m}_{n1}, \hat{m}_{n2}, \hat{m}_{n3}\} \quad (5.29)$$

$$\{\zeta_{p1}, \zeta_{p2}, \zeta_{p3}\} = \{\zeta_{n1} - \pi, \zeta_{p2}, \zeta_{p3} - \pi\} \quad (5.30)$$

Secondly, according to (5.4), the upper branch carrier sets can be shifted with respect to their bottom branch counterparts by an angle  $\delta$ , hence

$$v_p = v_p^* + \frac{2v_{p\Sigma}}{\pi MN} \sum_{p=1}^{\infty} \sum_{z=-\infty}^{\infty} \sum_{q=-\infty}^{\infty} \sum_{n=-\infty}^{\infty} \frac{J_z(pMN\pi\hat{m}_3)J_q(pMN\pi\hat{m}_2)J_n(pMN\pi\hat{m}_1)}{p} \times \sin\left(\Phi_{zqn} - \frac{pMN\pi}{2}\right) \cos([pMN\omega_c + (3z+2q+n)\omega_0]t - (pMN\delta + (n+z)\pi) + z\zeta_3 + q\zeta_2 + n\zeta_1) \quad (5.31)$$

AC voltage of an observed leg can be calculated as (5.32), whereas correct derivation of its spectral components, whilst utilizing previously derived results, requires total SBR voltages to be expressed in their complete form (5.33).

$$v_s = \frac{v_n - v_p}{2} \quad (5.32)$$

$$v_{\{n/p\}\Sigma} = V_{br}^* \mp \underbrace{\Delta \hat{v}_1 \cos(\omega_0 t + \Psi_1)}_{\Delta v_1} - \underbrace{\Delta \hat{v}_2 \cos(2\omega_0 t + \Psi_2)}_{\Delta v_2} \quad (5.33)$$

To make the following analyses more lucid, the branch voltages can be written as

$$v_n = v_n^* + g_{h,n}(\omega) v_{n\Sigma} \quad (5.34)$$

$$v_p = v_p^* + g_{h,p}(\omega) v_{p\Sigma} \quad (5.35)$$

Substitution of (5.33) to (5.35) into (5.32) yields

$$\begin{aligned} v_s = & \underbrace{\hat{m} \frac{V_{br}^*}{2} \cos(\omega_0 t)}_{\text{fundamental component}} + \\ & + \underbrace{\frac{V_{br}^*}{2} [g_{h,n}(\omega) - g_{h,p}(\omega)] - \frac{\Delta v_1}{2} [g_{h,n}(\omega) + g_{h,p}(\omega)] - \frac{\Delta v_2}{2} [g_{h,n}(\omega) - g_{h,p}(\omega)]}_{\text{higher order harmonics (AC side)}} \end{aligned} \quad (5.36)$$

Similarly, a leg DC voltage, calculated as (5.37), can be obtained as (5.38).

$$v_c = \frac{v_n + v_p}{2} \quad (5.37)$$

$$v_c = \frac{V_{br}^*}{2} + \underbrace{\frac{V_{br}^*}{2} [g_{h,n}(\omega) + g_{h,p}(\omega)] - \frac{\Delta v_1}{2} [g_{h,n}(\omega) - g_{h,p}(\omega)] - \frac{\Delta v_2}{2} [g_{h,n}(\omega) + g_{h,p}(\omega)]}_{\text{higher order harmonics (DC side)}} \quad (5.38)$$

An interesting fact regarding the terms describing the higher order harmonics can be observed from (5.36) and (5.38). Namely, the terms in the brackets multiplying the same voltage components have the opposite signs. This indicates that cancellation of a certain harmonic group in the AC voltage doubles the same frequency component in the DC voltage of an observed leg and vice versa.

To commence the analysis of the possible use of the branch carrier sets displacement ( $\delta$ ), let one expand  $g_{h,n}(\omega) - g_{h,p}(\omega)$  as (5.39), whereas (5.40) describes the term labeled with  $\Delta_{AC}$ .

$$\begin{aligned} g_{h,n}(\omega) - g_{h,p}(\omega) = \\ \frac{2}{\pi MN} \sum_{p=1}^{\infty} \sum_{z=-\infty}^{\infty} \sum_{q=-\infty}^{\infty} \sum_{n=-\infty}^{\infty} \frac{J_z(pMN\pi\hat{m}_3)J_q(pMN\pi\hat{m}_2)J_n(pMN\pi\hat{m}_1)}{p} \sin\left(\Phi_{zqn} - \frac{pMN\pi}{2}\right) \Delta_{AC} \end{aligned} \quad (5.39)$$

$$\begin{aligned} \Delta_{AC} = \cos\left([pMN\omega_c + (3z + 2q + n)\omega_0]t + z\zeta_3 + q\zeta_2 + n\zeta_1\right) - \\ - \cos\left(\underbrace{[pMN\omega_c + (3z + 2q + n)\omega_0]}_{\omega_{pzqn}} t - (pMN\delta + (n + z)\pi) + \underbrace{z\zeta_3 + q\zeta_2 + n\zeta_1}_{\theta_{zqn}}\right) \end{aligned} \quad (5.40)$$

Prior to proceeding with an investigation of the term denoted by  $\Delta_{AC}$ , one should observe the term  $\sin\left(\Phi_{zqn} - \frac{pNM\pi}{2}\right)$  from (5.39). Unless this term differs from zero, the sideband harmonics around the  $p$ -th carrier harmonic are nullified irrespective of the choice of the angle  $\delta$ . Consequently,  $n + q + z - pNM$  must be odd, meaning that  $z + n + q = \lambda + pNM$ , where  $\lambda$  denotes an arbitrary odd number. Therefore, (5.41) can be derived by adopting  $\delta = \alpha\pi/MN$  ( $\alpha \in \mathbb{R}$ ).

$$\Delta_{AC} = \cos\left(\omega_{pzqn}t + \theta_{zqn}\right) \left(1 + (-1)^{q+p(\alpha+MN)}\right) \quad (5.41)$$

From (5.41), the dependency of parameter  $\Delta_{AC}$  on several indices ( $p, z, q, n$ ), as well as parameter  $\alpha$ , is revealed. Further analysis referring to the minimization of the leg AC voltage spectrum requires one to make a decision on which of these parameters are going to be assigned some discrete values. As can be seen from **Fig. 5.9**, the first group of harmonics observed in the branch voltage spectrum appears around the apparent switching frequency of the branch  $\omega_{br} = MN\omega_c$ . Therefore, cancellation of this harmonics set clearly contributes to the reduction of the leg AC voltage THD. Hence,  $p$  can be replaced with one in (5.41). Determining the value of index  $q$  within the same equation requires the values of harmonics determined by it to be investigated. In other words, with of  $n$  and  $z$  being fixed, the side band harmonics obviously change depending on the value of Bessel function  $J_q(pMN\pi\hat{m}_2)$ .

**Fig. 5.10** provides the values of the function  $J_q(pMN\pi\hat{m}_2)$  with  $\hat{m}_2$  being obtained for the converter operating point related to the information provided in **Tab. 5.1**. It can be noticed that this function reaches its maximum in case  $q = 0$ . Consequently, cancellation of harmonics for which  $p = 1$  and  $q = 0$ , which can be formulated as (5.42) (since it nullifies the term  $\Delta_{AC}|_{\{p,q\}=\{1,0\}}$ ), is expected to lead towards meeting the criteria of the lowest leg AC voltage THD.

$$1 + (-1)^{(\alpha+MN)} = 0 \quad (5.42)$$

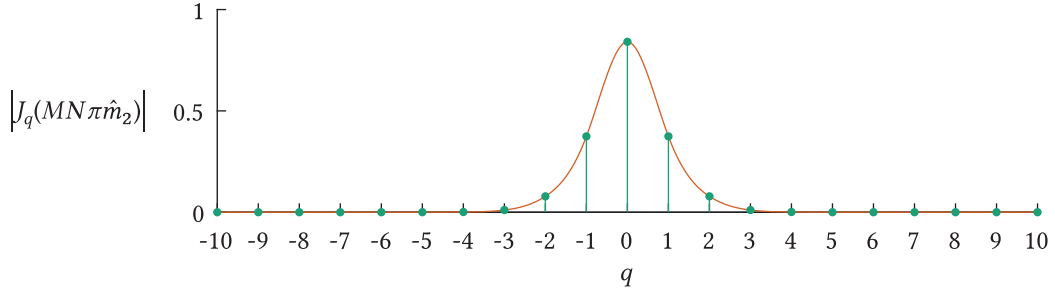


**Fig. 5.10** Values of the Bessel function  $J_q(pMM\pi\hat{m}_2)$  for different values of index  $q$ . Please notice that, as the goal of the presented analysis is reduction of the harmonics concentrated around the branch switching frequency,  $p = 1$ . Also, parameters  $M$  and  $N$  were chosen according to **Tab. 5.1**, whereas  $\hat{m}_2 = 0.016$  was obtained by the Fourier expansion of the modulation index describing the operating point defined by the very same table.

In order to satisfy  $\Delta_{AC}|_{\{p,q\}=\{1,0\}} = 0$ , the term  $\alpha + MN$  must be odd. The values of angle  $\delta$  (please recall that  $\delta = \alpha\pi/MN$ ) allowing for the above stated goal to be obtained are presented in **Tab. 5.3**.

To provide a simplified illustration of the effect achieved by adopting such a displacement of the branch carrier sets, assume, for the moment, that  $\delta = 0$ . The exemplary case presented in **Fig. 5.8(b)** can be extended by the upper branch waveforms, providing one with **Fig. 5.11(a)**. It is inherently assumed that carriers modulating two adjacent SBRs belonging to the same branch are already shifted according to **Sec. 5.2.2**. As can be observed, both branches change their state at the same time causing the voltage seen from the leg AC terminal to contain  $MN + 1$  levels. If, on the other hand,  $\delta$  is selected according to **Tab. 5.3**, time instants at which the branches change their state are shifted in time, resulting in an increase in the number of voltage levels seen from the leg AC terminal to  $2MN + 1$ , hence the name  $(2MN + 1)$ -level modulation.

Notwithstanding, an important conclusion regarding the leg DC voltage can be drawn by observing the bottom-most plots of **Figs. 5.11(a)** and **5.11(b)**. Namely, if the branches are to change their states simultaneously (which can also be referred to as synchronous switching), the voltage seen from the leg DC terminals is supposed to be ideally flat (please note that analysis being currently conducted assumes flat SM voltages). Further improvement of the leg AC voltage spectrum (i.e. increase in the number of voltage levels to  $2MN + 1$ ), implies the asynchronous change of the branches' states, leading to the introduction of high-frequency component in the leg DC voltage. Therefore, there is always a trade-off between an improvements made from the AC voltage point of view and high frequency components introduced from the DC side. It is noteworthy that these high frequency components in the leg DC side voltage contribute to the oscillations of the leg common-mode (and also circulating) currents. Nevertheless, high frequency components in the circulating currents are expected to be successfully filtered from the total branch voltage by an SM capacitances.

**Tab. 5.3** Values of the angle  $\delta$  leading to the achievement of  $(2MN + 1)$ -level modulation

$M \backslash N$			
		odd	even
odd		$\delta = 0$	$\delta = \frac{\pi}{MN}$
even		$\delta = \frac{\pi}{NM}$	$\delta = \frac{\pi}{NM}$



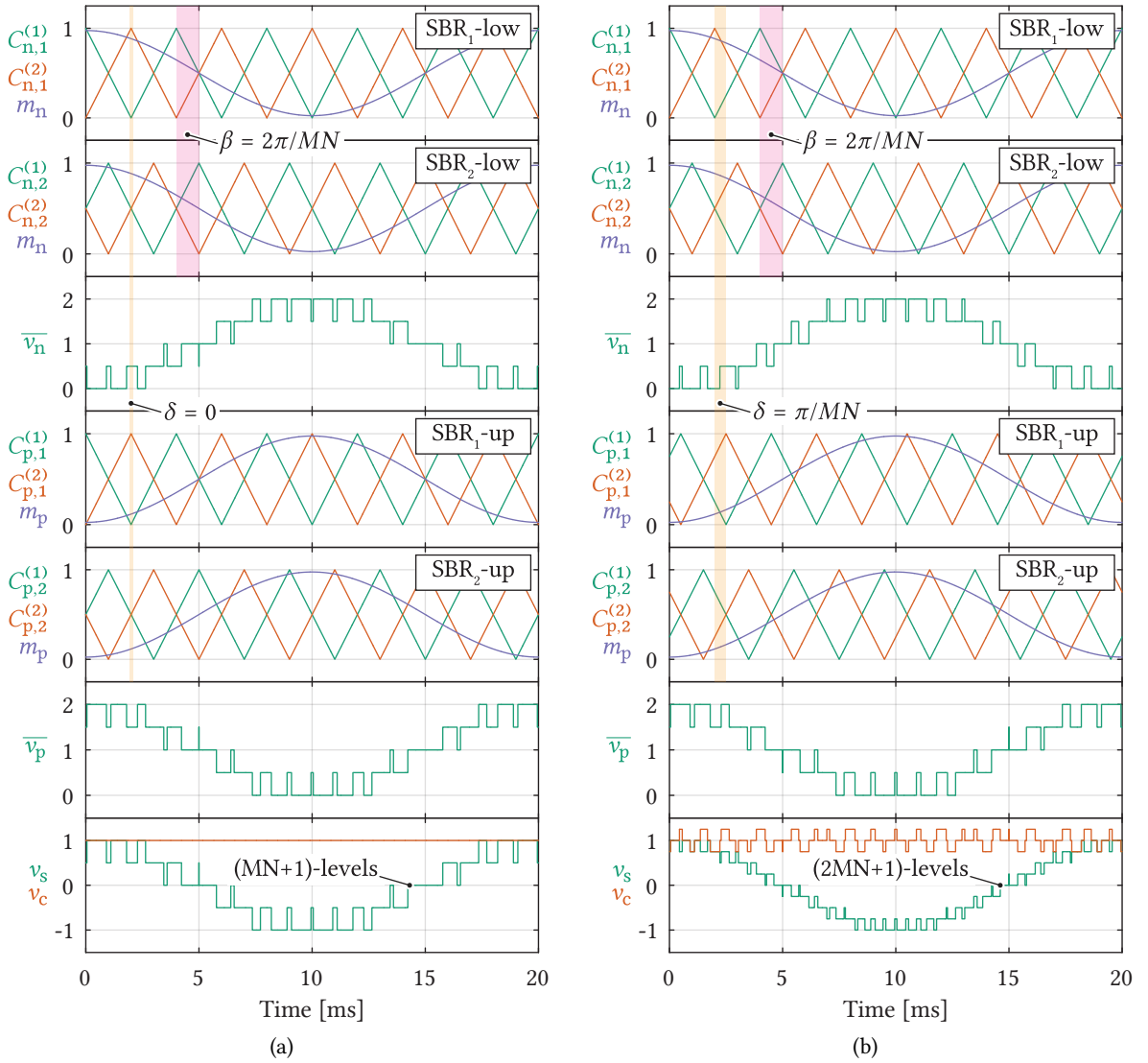


**Fig. 5.11** Extension of the exemplary case analyzed in **Fig. 5.8(a)**. Illustrated are the voltage waveforms of both the upper and the lower branch consisting of two SBRs employing two SMs each. As can be seen, introduction of a properly determined branch carrier sets displacement results in an increase of the number of voltage levels seen from the leg AC terminal. In turn, leg DC voltage quality gets hindered and vice-versa. In this example, voltage across all of the SMs was assumed to be flat and equal to 1 [p.u].

Although convenient for the illustration purposes, the analysis based on the assumption of flat SM voltages does not provide a correct image of the leg voltage component for a few reasons:

- According to (5.36) and (5.38) a proper presentation of the leg voltage spectrum requires the total branch voltage oscillations (labeled with the terms  $\Delta v_1$  and  $\Delta v_2$ ) to be considered. Omitting the analysis of these components causes the spectral components introduced by their multiplication with the functions  $[g_{h,n}(\omega) \pm g_{h,p}(\omega)]$  to remain unrecognized.

- Due to the reversed signs along the terms describing the higher order harmonics in (5.36) and (5.38), cancellation of a certain harmonic set at one of the leg sides causes an increase of the very same set on the other side.

To outline the importance of including the branch voltage oscillation into the analysis of the leg voltage components, expression (5.43) will be observed. Given that  $V_{br}^* \gg \Delta \hat{v}_1 > \Delta \hat{v}_2$ , it is straightforward to conclude that cancellation of the higher order harmonics being multiplied by  $V_{br}^*/2$  contributes to the highest possible reduction in the observed THD. Therefore,  $g_{h,n}(\omega_{BR}) = g_{h,p}(\omega_{BR})$  is obtained as discussed above, which further leads to simplification of (5.43) in the form of (5.44).

$$v_s = \hat{m} \frac{V_{br}^*}{2} \cos(\omega_0 t) + \frac{V_{br}^*}{2} [g_{h,n}(\omega_{BR}) - g_{h,p}(\omega_{BR})] - \frac{\Delta v_1^*}{2} [g_{h,n}(\omega_{BR}) + g_{h,p}(\omega_{BR})] - \frac{\Delta v_2^*}{2} [g_{h,n}(\omega_{BR}) - g_{h,p}(\omega_{BR})] + \text{higher order harmonics } (p \geq 2) \quad (5.43)$$

$$v_s = \hat{m} \frac{V_{br}^*}{2} \cos(\omega_0 t) - \underbrace{\Delta v_1^* \cdot g_{h,n}(\omega_{BR})}_{\text{harmonics centered around } \omega_{BR}} + \text{higher order harmonics } (q \geq 2) \quad (5.44)$$

According to (5.44) despite canceling a certain set of harmonics being centered around the branch apparent switching frequency, there are still components being present in this part of the spectrum owing to the product  $\Delta v_1^* \cdot g_{h,n}(\omega_{BR})$ . It is actually straightforward to see from (5.43) that voltage components of the upper and the lower branch which are in phase (2nd harmonics) get canceled out, whereas the components being in counter-phase (1st harmonics) get doubled in amplitude.

It is noteworthy that in case  $\delta$  is chosen as  $\delta = (2k - 1)\pi \mid (k \in \mathbb{N})$ , which implicitly means that  $\alpha = (2k - 1)MN$ , the expression (5.41) becomes equal to (5.45) irrespective of  $NM$  parity. This indicates that  $(MN + 1)$ -level modulation is obtained.

$$\Delta_{AC} = 2 \cos(\omega_{1z0n}t + \theta_{n0z}) \quad (5.45)$$

It is of interest to check the effects of the AC voltage THD improvement upon the leg DC voltage component calculated as (5.37). It can be shown that such an analysis can be conducted through the investigation of the term  $\Delta_{DC}$ , which is given in (5.46). Please notice that the terms  $\Delta_{DC}$  and  $\Delta_{AC}$  differ from each other only by the sign in the bracket multiplying the cosine function.

$$\Delta_{DC} = \cos(\omega_{pzqn}t + \theta_{zqn}) \left( 1 - (-1)^{q+p(\alpha+MN)} \right) \quad (5.46)$$

Therefore, cancellation of the spectral components centered around the branch apparent switching frequency can be conducted by following the already presented logic, according to (5.47).

$$1 - (-1)^{\alpha+MN} = 0 \quad (5.47)$$

**Tab. 5.4** Values of the angle  $\delta$  leading to the cancelation of carrier harmonics seen from the converter DC terminals

$N \backslash M$		
	odd	even
odd	$\delta = \frac{\pi}{NM}$	$(\delta = 0) \vee (\delta = \pi)$
even	$(\delta = 0) \vee (\delta = \pi)$	$(\delta = 0) \vee (\delta = \pi)$

To satisfy the above equation,  $\alpha + NM$  must be even. This criteria is met in case  $\delta$  is chosen in accordance with **Tab. 5.4**. It is noteworthy that such a choice of  $\delta$  always leads to  $(MN + 1)$ -level modulation since (5.45) is obtained under all the combinations of  $N$  and  $M$ . On the other hand, choosing the angle  $\delta$  according to **Tab. 5.3** results in (5.48), which, once again, points out that there is always a trade-off between the quality of the leg AC and DC side voltages. Namely, improving the quality of the leg AC voltage hinders the quality of its DC voltage component and vice-versa.

$$\Delta_{DC} = 2 \cos(\omega_{pzqn}t + \theta_{zqn}) \quad (5.48)$$

In order to validate the correctness of analytic expressions derived throughout this section, **Figs. 5.12** and **5.13** present the comparison between the spectral contents of the leg voltage components obtained in analytic fashion and simulations conducted in PLECS. Once again, the converter with parameters defined in **Tab. 5.1** was simulated.

**Fig. 5.12** presents the spectrum of both AC and DC voltage components of the observed converter. By comparing the plots from both sides of the figure, one can conclude that an outstanding matching between the harmonic values obtained by calculations and simulations tools is achieved. As functionality of the analytic expressions derived above is confirmed, analysis of the effect obtained by setting the angle  $\delta$  to a non-zero value can be conducted. From **Fig. 5.13(a)** it can be seen that, when compared with **Fig. 5.12(a)**, the density of components centered around the branch apparent switching frequency gets reduced. In turn, these get shifted to the DC side as can be seen through the comparison of **Figs. 5.12(b)** and **5.13(b)**, which is expected according to (5.43).

To provide a quantitative comparison between **Figs. 5.12(a)** and **5.13(a)**, THD was calculated according to (5.19) for both cases and results can be found summarized in the table bellow. As expected, the leg AC voltage THD gets reduced with the introduction of non-zero displacement between the branch carrier sets. The opposite applies to the leg DC voltage THD. Also, relative error of both THD components confirms that excellent matching between the analytic and simulation results is retained.

**Tab. 5.5** THD values for two different values of branch carrier sets shifts

$\delta$	THD <sub>AC</sub> [%]	THD <sub>DC</sub> [%]	$\Delta$ THD <sub>AC</sub> [%]	$\Delta$ THD <sub>DC</sub> [%]
0	5.29	1.92	0.36	0.19
$\pi/16$	3.62	2.70	0.33	0.27

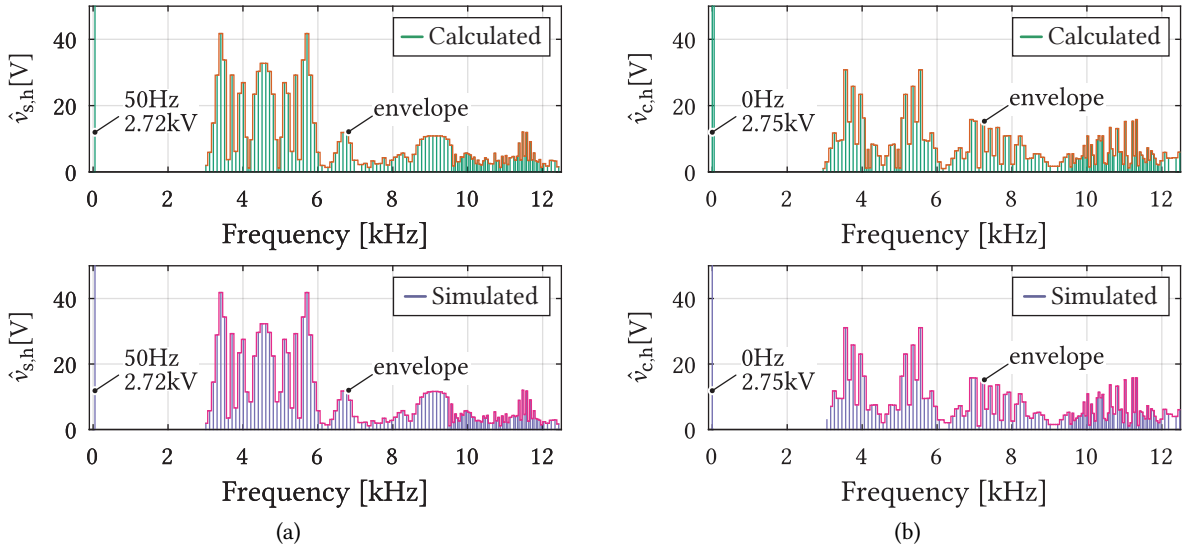


**Fig. 5.12** Comparison of the leg AC (left) and DC (right) voltage spectral contents obtained by means of the analytic expression and the averaged simulation model in case  $\delta = 0$ . According to **Tab. 5.1**,  $N = 8$  and  $M = 2$ .

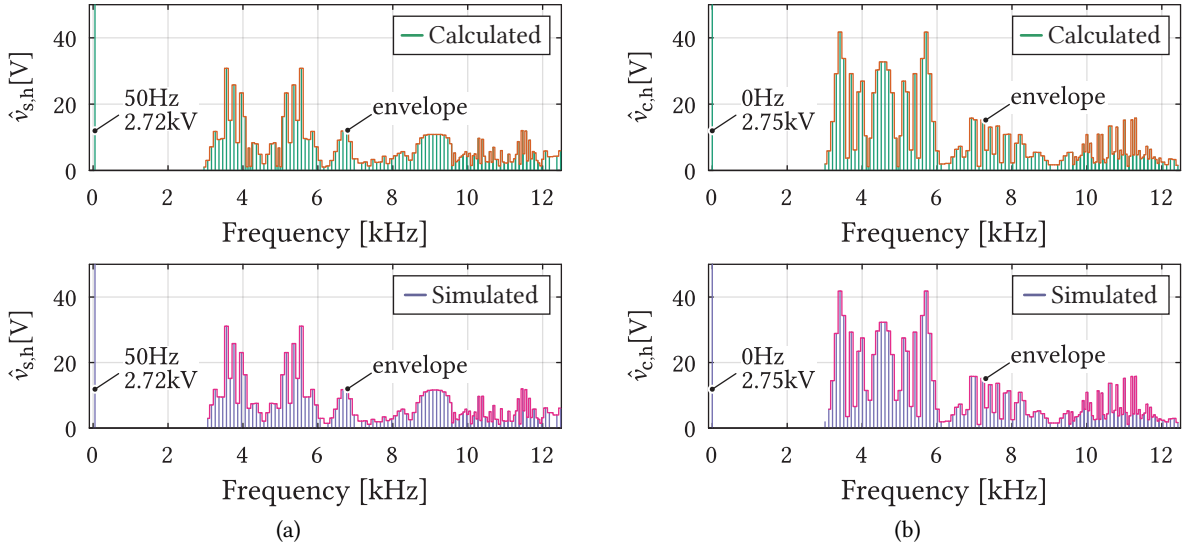


**Fig. 5.13** Comparison of the leg AC (left) and DC (right) voltage spectral contents obtained by means of the analytic expression and the averaged simulation model in case  $\delta = \pi/MN$ . According to **Tab. 5.1**,  $N = 8$  and  $M = 2$ , therefore  $\delta = 11.25^\circ$ .

It is noteworthy that, although uncommon, THD of the leg DC voltage was defined as (5.49) in order to provide the means for comparison of the spectral contents obtained by using different values of  $\delta$ .

$$\text{THD}_{\text{DC}} = \frac{\sqrt{\sum_{i=1}^{\infty} \hat{v}_{c,i}^2}}{V_{\text{br}}^*} \quad (5.49)$$

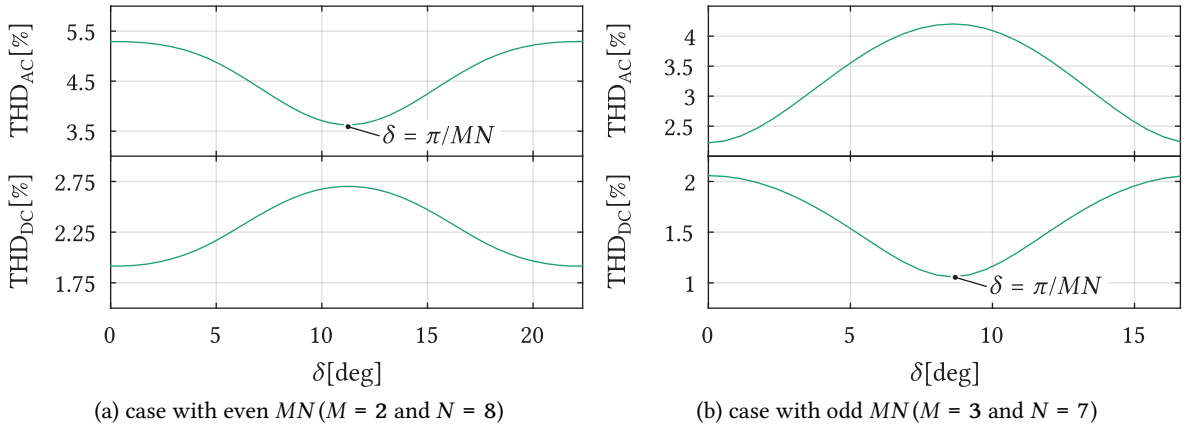


**Fig. 5.14** Variation of the leg voltage components THD depending on the value of branch carrier sets displacement. What can be noticed from both sides of the figure is that AC and DC side THD functions feature the opposite monotonicity. Namely, as long as one of them is increasing with an increase in  $\delta$ , the other one decreases and vice versa.

Last but not least, the question on whether the phase shifts provided in **Tabs. 5.3** and **5.4** are indeed optimal, meaning that they lead to the highest possible minimization of THD at either of the chosen leg sides, remains open. In order to provide the proof regarding the validity of conclusions drawn during the derivation of (5.42), THD was calculated for both AC and DC voltage, with the angle  $\delta$  being swept from 0 to  $2\pi/MN$ . Such a choice of the sweep horizon can be justified through the fact that period of a function  $f(\alpha) = 1 \pm (-1)^{\alpha+MN}$ , which actually unifies (5.42) and (5.48), equals  $\alpha_{per} = 2$ .

**Fig. 5.14(a)** presents the change in the leg voltage components THD in case the converter parameters are unchanged with respect to all the cases analyzed throughout this section. Therefore, as  $M = 2$  and  $N = 8$ , the product  $MN$  is even. It can be noticed that the leg AC voltage THD decreases until  $\delta$  reaches the value corresponding to  $\pi/MN \leftrightarrow 11.25^\circ$ . Please notice the correspondence to **Tab. 5.3**. On the other hand, the lowest value of  $THD_{DC}$  [%] is observed in case  $\delta = 0$ , confirming the correctness of information provided in **Tab. 5.4**.

In contrast to the case considering the product  $MN$  being even, **Fig. 5.14(b)** presents the same THD components in case the converter operates with the same voltages and currents taken into account so far, however, with  $M = 3$  and  $N = 7$ . As the displacement  $\delta$  increases, so does the THD of the leg AC voltage component, which is aligned with the proposal of  $\delta$  from **Tab. 5.3**. Additionally, once  $\delta$  reaches  $\pi/MN$ , leg DC voltage THD reaches its minimum, which is expected should **Tab. 5.4** be observed. Consequently, the logic presented throughout this chapter ensures the highest possible reduction in the THD seen from any of the chosen converter ports.

Previous analysis can also be understood from the energy viewpoint. Namely, high frequency components in branch voltages are inevitable due to the finite switching frequency of their SMs. Hence, there is always a certain energy being present in the upper part of branch voltage spectrum and THD is to a certain extent a measure of it. By looking into **Figs. 5.14(a)** and **5.14(b)** one might reach the conclusion that varying the displacement of the branch carrier sets actually causes the redistribution of spectral energy between the AC and DC sides of an observed converter leg.

### 5.3 Summary

Apart from allowing for an effortless extension of the MMC power capacity, paralleling of its branches offers an outstanding flexibility when it comes to synthesization of its reference voltages. When compared to the conventional MMC, additional degrees of freedom from the modulation standpoint are introduced. Therefore, the MMC utilizing parallel SBRs features the possibility of extending the number of voltage levels created across its terminals even further when compared to its conventional counterpart.

Throughout this chapter, detailed mathematical analysis of the possibilities offered by the use of PSC modulation within the converter operating with an arbitrary number SBRs, comprising an arbitrary number of SMs, was conducted. Moreover, this work incorporates the corrections of modulation index, characterizing the MMC closed loop control, into the analysis making it unique and different compared to the existing references, which focus mainly to the operation implying the so-called direct modulation.

As it was shown, a suitable choice in the angular displacement between the sets of carriers modulating two opposite branches of the same leg, leads to the reduction of THD at either DC or AC port of the converter. Nevertheless, there is always a trade-off which one must be aware of. In other words, reduction of the AC voltage THD implies shifting of a certain part of its spectral energy (more precisely, the one being related to the higher frequencies) to the DC side. The conclusion in the opposite direction, of course, holds as well.

# 6

## High Power Bidirectional DC-DC Converter Utilizing Scott Transformer Connection

*This chapter presents a novel high power, bidirectional, modular multilevel converter based, DC-DC converter intended to connect a bipolar DC network operating at high/medium voltage with a unipolar DC network of an arbitrary voltage level. To ensure the galvanic isolation between the converter stages, the unprecedented use of the Scott transformer connection in the high power DC-DC conversion domain is presented. Consequently, converter operation can be maintained even in case of the converter parts malfunction or loss of either of the DC feeders in the bipolar grid. Moreover, Scott transformer operation in the medium frequency range is proposed, thus following the trend of the solid state transformers, which have drawn the attention of both academia and industry.*

### 6.1 Motivation

The SST concept, primarily foreseen in the AC grids, has also gained momentum within the DC domain due to the proliferation of renewable energy resources along with the growing electrical energy storage and consumption demands. Given that the success of HVDC systems is expected to be replicated within the MV domain, the expansion of the DC grids in the near future is very certain. Flexible and resilient DC grid implies the existence of reliable interfaces among its parts operating under different voltage levels, leading to the conclusion that the DC-DC converter can be thought of as its key element. However, certain requirements have to be met in order to support such a statement, some of which are possibly high step-up/down voltage ratio, high efficiency, isolation due to safety reasons, redundancy, modularity, and so on.

Although a substantial amount of research has been conducted in the field of non-isolated DC-DC converters [119]–[124], this chapter focuses exclusively on galvanically isolated structures. Unlike their counterparts operating in the AC domain, isolation stages within DC-DC converters can be designed to operate at any arbitrary frequency. Therefore, bulky LFT can be replaced by a more compact MFT, which reflects positively upon the reduction of the material requirements.

Considering limited voltage blocking capabilities of commercially available semiconductors, reaching as high as 6.5kV nowadays, dealing with HV/MV at either of a DC-DC converter stage can be quite challenging, thus requiring the series connection of power switches [30]–[33] or converter stages. On the other hand, operational flexibility offered by the MMC, where the challenge of voltage and, as demonstrated in **Chap. 4**, current scalability can be easily addressed, made this topology prominent even in the domain of high power DC-DC conversion. Consequently, the MMC capabilities and limitations deserve to be further investigated in this field of energy conversion.

MMC-based DC-DC converters have been subject to various research projects [58]–[60], [68], [125]. In [60], MMC-based 1PH DAB was thoroughly analyzed, whereas the new control method implying sequential insertion of MMC-alike SMs was proposed in [58], [59]. Additionally, an MMC-based DC-DC converter operating with sinusoidal currents was reported in [68], [125]. However, sinusoidal current generation requires power semiconductor devices to switch at frequency normally higher compared to the MFT operating (fundamental) frequency, consequently increasing the system losses. Hence, this chapter focuses on DAB-alike topologies since fundamental frequency switching of power semiconductors can be provided with low control efforts.

Another topic relevant to the scope of this work refers to the transmission lines capacity increase through the conversion of the existing AC power lines into DC [15]. Although labeled as the least promising in terms of the transmission capacity increase, bipolar DC networks with return (neutral) conductor offer the system redundancy in the case of either of the DC poles outage [16]–[18]. On these terms, the system can continue to operate utilizing the neutral conductor, although with reduced power, providing a suitable DC-DC converter structure is employed. **Figs. 6.1(a)** and **6.1(c)** present generalized structure of a power converter to be used with the aim of interfacing either HV/MV bipolar DC grid or two separate HV/MV DC grids with a LV DC grid, respectively. As suggested by **Figs. 6.1(b)** and **6.1(d)**, system operation, though with reduced power, can be maintained in case either of the DC poles is lost. However, certain system reconfiguration, or operating mode change, might be needed on these terms. Moreover, none of the topologies proposed in [58]–[60], [68] were analyzed operating within a bipolar grid with the neutral conductor, nor the possibility of utilizing its inherent redundancy property was considered.

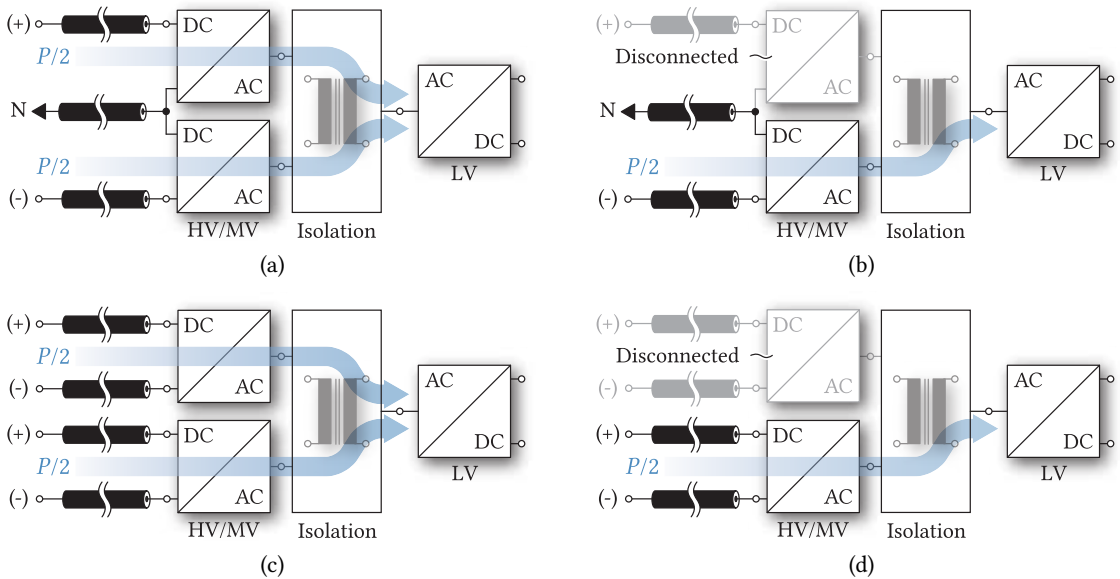


**Fig. 6.1** Generic structure of a DC-DC converter operating within a bipolar HV/MV grid; (a) Structure of a converter used to interface HV/MV bipolar DC grid with a LV DC grid. HV/MV stage consists of two converters, providing the possibility of exploiting the redundancy principle inherently present within bipolar grids with the neutral conductor; (b) Converter operation in case one of the voltage poles is lost. (c) Structure of a converter used to interface two independent HV/MV DC grids of the same voltage level with a LV DC grid. (d) Converter operation in case one of the DC grids is lost.



## 6.2 Proposed topology

### 6.2.1 Derivation

**Fig. 6.2** presents state of the art topology proposed in [126]. In order to ensure galvanic isolation between an HV/MV bipolar DC grid and an LV DC grid, 3PH three-winding transformer was used. VSC used on the LV voltage side operates with the fundamental frequency (square-wave mode), therefore, it was referred to as the Six-Step Converter (SSC). To control the power flow between the HV/MV and LV side, DAB-alike operating principles were employed [127].

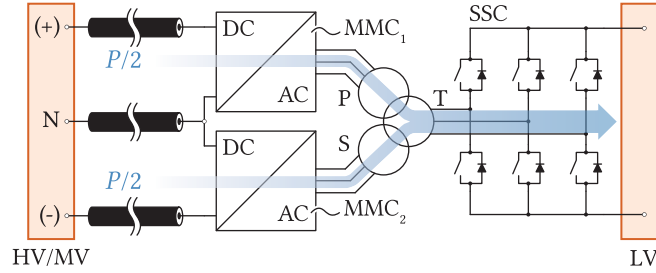


**Fig. 6.2** High power DC-DC converter employing the 3PH three-winding transformer with the aim of interfacing an HV/MV bipolar grid with an LV DC grid [126].

It is noteworthy that the use of 3PH VSC on the LV side can be considered beneficial for several reasons. Firstly, when compared to the two-phase systems, power transfer with three phases ensures a lower current rating of the switching devices, especially in the high power domain (e.g. several MW). Secondly, in the 3PH DAB, the converter input/output current ripple occurs at six times the operating frequency of the converter [127]. Consequently, a reduction in the output filter capacitance, which was not presented in the above figure, can be achieved when compared to the 1PH DAB.

Although seemingly logical, the topology depicted in **Fig. 6.2** suffers from several drawbacks originating from the magnetic coupling of the transformer's windings. In normal operating mode, MMC<sub>1</sub> and MMC<sub>2</sub> supply their associated transformer windings with square-wave voltages having the identical phase shifts with respect to the square voltages created by the SSC. Due to symmetry, which holds in the normal operating mode, the above converter can be analyzed in "per-phase" fashion. As indicated in **Fig. 6.3(a)**, unless the MMCs supply the transformer with identical sets of voltages, circulating current appears between them. It must be emphasized that the generation of identical voltages can not be guaranteed due to different system delays, mismatches between the MMC capacitor voltages, etc. Also, the conclusion regarding previously mentioned circulating current holds only in case Primary (P)- and Secondary (S)- winding impedances are identical, which is very unlikely in practice.

In case a fault, modeled with an impedance  $Z_{\text{fault}}$ , occurs across the DC terminals of either of the MMCs, maintaining the energy exchange between the healthy MMC and the SSC causes the fault to be supplied with energy by the faulty MMC's transformer winding. **Fig. 6.3(b)** illustrates the case where the short circuit occurs across the DC terminal of MMC<sub>2</sub>. As can be seen, despite withdrawing all the switching signals from the faulty MMC (given that DC-DC conversion is considered, the use of HB SMs will be assumed onward), the fault is supplied with the energy from the converter side. Consequently, additional switchgear needs to be used to provide the isolation of the fault from the converter.

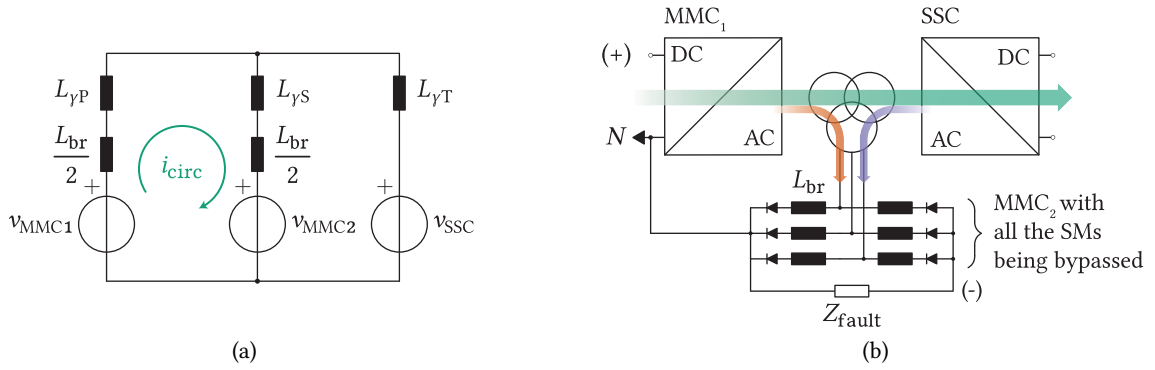


**Fig. 6.3** Drawbacks related to the topology proposed in [126] (a) "Per-phase" equivalent circuit of the analyzed converter. Unless two MMCs supply their associated transformer windings with identical voltages (while the P- and S-winding leakage inductances ( $L_{\gamma\{P/S\}}$ ) are considered identical), the circulating current appears between them. Transformer's magnetizing inductance was neglected; (b) Unless additional switchgear is employed, the energy exchange between the healthy MMC ( $\text{MMC}_1$ ) and the SSC causes the fault to be supplied with energy from the transformer winding belonging to the faulty MMC ( $\text{MMC}_2$ ).

According to the previous discussion, one can conclude that magnetic coupling between the converter stages is to be avoided in case the converter is supposed to interconnect two DC grids of the analyzed types. An additional drawback, which has not been mentioned so far, refers to the use of two 3PH MMC. Namely, such a structure requires a significant number of SMs that need to be supported by appropriate control hardware. Therefore, two modification objectives, followed by the requirement of retaining the 3PH structure of the LV stage, can be set according to the discussions conducted so far:

- Avoiding the magnetic coupling between the converter stages operating at HV/MV
- Minimizing the number of employed SMs

The simultaneous solution to both challenges can be found in the change of the transformer structure. **Fig. 6.4(a)** presents the STC along with its voltage phasor diagram. So far, the STC has mostly been used in the railway applications in the manner illustrated in **Fig. 6.4(b)**. Using the STC, two independent 1PH voltage sources can be obtained out of a symmetrical 3PH voltage source. Actually, the STC performs what is known as the  $\alpha\beta$  transformation of a 3PH system (A.51), although with the scaling coefficient corresponding to its turns ratio. Also, voltage transformation in the opposite direction holds, which can be conveniently used in the application being in the focus of this chapter.

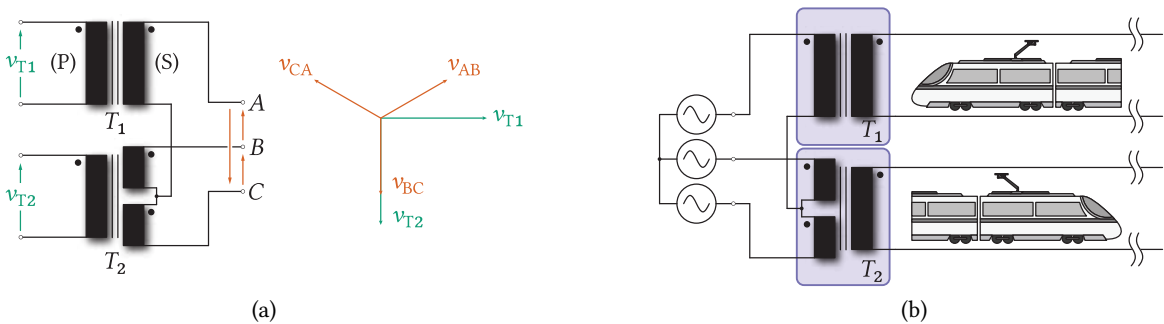


**Fig. 6.4** (a) STC with its voltage phasor diagram; (b) The most common use of the STC.

Given that the STC utilizes two independent transformer units ( $T_1$  and  $T_2$ ), the challenge of magnetic coupling between the converter stages, possibly connected to them, gets addressed. The specific connection of the S-windings, which will be discussed in detail in the next section, provides three terminals (A,B and C) that can be connected to the SSC. On the other hand, P-windings of both transformer units can be interfaced with 1PH MMC employing HB SMs, which results in the converter structure presented below.

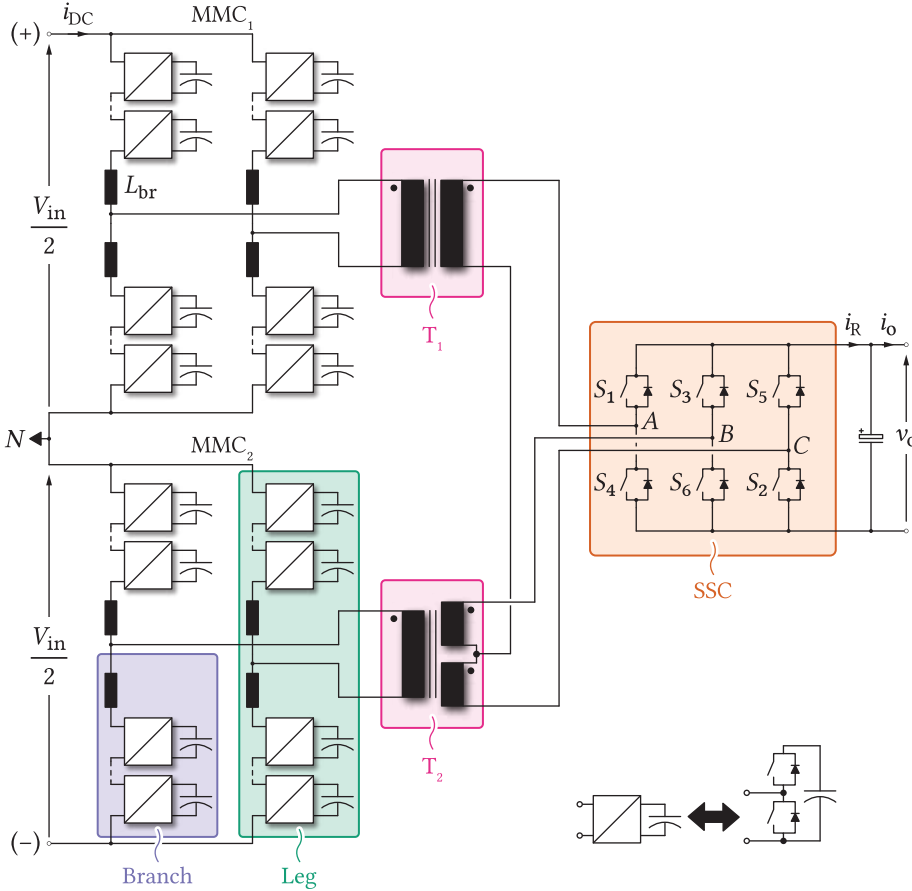


**Fig. 6.5** The proposed topology consisting of two series connected MMCs in the HV/MV stage (since bipolar grid with neutral conductor is available), the STC and the conventional SSC in the LV stage.

Consequently, an interface between a bipolar HV/MV DC grid and an LV DC grid is provided. As two independent transformer units, combined with two MMCs, are used, redundant operation of the converter in case of faults remains possible. Moreover, the operating frequency of the isolation stage can be arbitrarily selected. It must be emphasized, however, that the LV grid can be changed with a grid of an arbitrary voltage level (e.g. 50kV). Consequently, the employed converter structure on the right-hand of **Fig. 6.5** might have to be adjusted. Notwithstanding, the work presented in this chapter concerns only the structure presented above.

As previously stated, the STC is mostly encountered in the railway applications, where the capabilities of the MMC have as well been investigated [128]–[131]. In [128] the possibility of employing the so-called direct MMC in order to provide a single railway line with sinusoidal voltage was presented. On the contrary, the MMC acting as a traction converter was studied in [129]. To obtain a railway

power conditioner, being in charge of the railway grid STC currents balancing, along with harmonics compensation, the authors of [130] combined the STC with two back-to-back 1PH-MMCs. The STC employment has also been reported in [132]–[135] with the aim of obtaining the unity power factor rectifier. Nevertheless, analyzed power, operating frequency and voltage ranges fall significantly below the one being in the focus of this chapter.

None of the references [128]–[135] has considered combining the MMC with the STC in order to perform the DC-DC conversion, which allows for the operating frequency shift towards medium frequency range, nor has it analyzed redundancy principles provided by the existence of two 1PH transformers comprising the STC. Thus, this chapter provides a thorough and systematic analysis of the converter depicted in **Fig. 6.5**. The upcoming sections cover operating principles, control, SMs balancing strategy allowing for the fundamental frequency switching of all power devices, as well as the operation under faulty operating conditions in detail.

### 6.2.2 Operating principles

The STC, presented in **Fig. 6.4(a)** along with its voltage phasor diagram, has already been used for more than a century in the line frequency applications. It is known for providing two 1PH sinusoidal voltage sources out of a single 3PH voltage source (or vice versa), which is widely used in the railway networks even nowadays.  $T_2$  S-winding is divided into two parts, both having the number of turns equal to  $N/2$ . To ensure proper STC operation,  $T_1$  S-winding number of turns has to be set as  $N\sqrt{3}/2$ . Consequently, with an identical number of P-winding turns, turns ratios relation is

$$m_{T1} = \frac{2}{\sqrt{3}} m_{T2} \quad (6.1)$$

Nonetheless, instead of driving the STC with sinusoidal voltages, fundamental switching with square-wave voltages is utilized in this work. With the SSC being connected to  $T_1$  and  $T_2$  S-windings square-wave-alike voltages are created across their P-windings. Further, to interface the voltages created across both transformers' P-windings, 1PH MMCs are used, as presented in **Fig. 6.5**. Both MMCs use HB SMs, whose number depends upon the available HV/MV and voltage class of semiconductors employed within the MMCs. Hence, employment of the STC instead of the 3PH three-winding transformer leads to the reduction of MMC branches number by the factor of 1/3 when compared to the topology presented in [126]. System redundancy can be exploited, though with certain system modifications, that are to be outlined in the upcoming subsections. Furthermore, the STC operation is not constrained to the low operating frequencies (mains frequency) considering the different nature of its employment. Therefore, operating frequency shift towards medium frequency range (e.g. 1kHz) can be achieved resulting in system volume and weight reduction.

The SSC operates with square-wave voltages (fundamental frequency operation) with the aim of minimizing the converter switching losses. It can be shown that instantaneous voltages across  $T_1$  and  $T_2$  P-windings ( $v_{T1}$  and  $v_{T2}$ , respectively) correspond to the combination of the LV side quantities, according to (6.2) and (6.3).

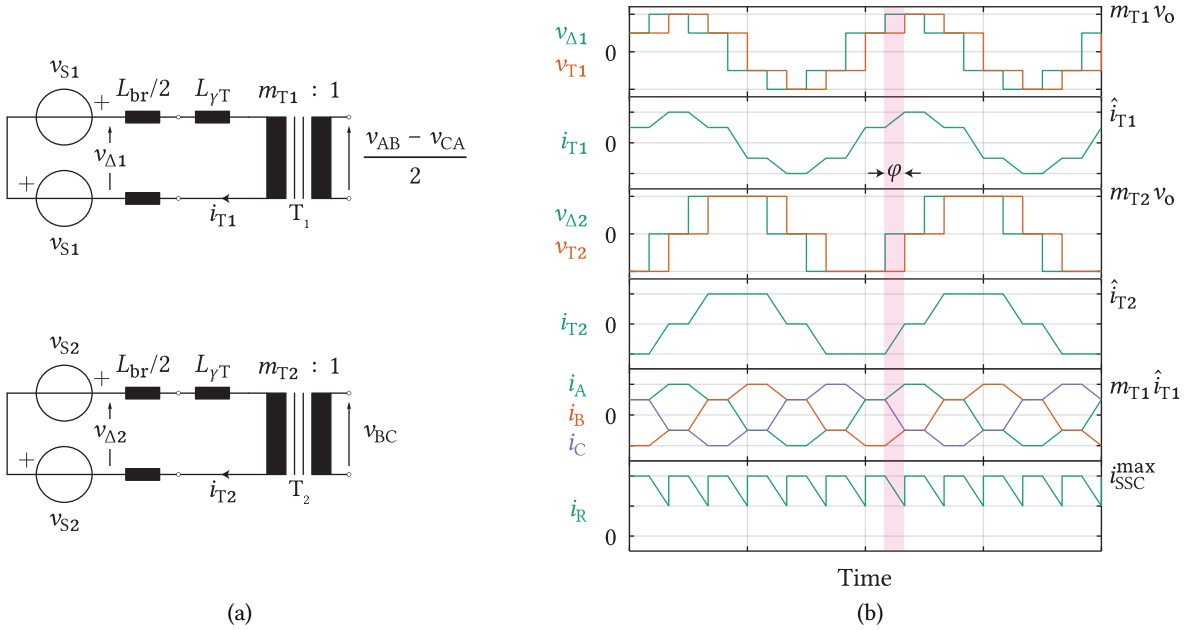


**Fig. 6.6** (a) Equivalent circuits of two MMCs connected to  $T_1$  and  $T_2$ ; (b) Idealized voltage and current waveforms relevant for the converter analysis.

$$v_{T1} = m_{T1} \frac{v_{AB} - v_{CA}}{2} \quad (6.2)$$

$$v_{T2} = m_{T2} v_{BC} \quad (6.3)$$

**Fig. 6.6(a)** depicts equivalent circuits of both MMCs connected to their associated transformers, whereas it can be seen from **Fig. 6.6(b)** that voltages  $v_{T1}$  and  $v_{T2}$  differ in shape. However, MMC provides the possibility of an arbitrary voltage waveform generation, as long as energy balances within the converter are maintained. With the appropriate voltage waveforms generated by the MMCs, energy transfer can be controlled by adjusting the phase shift ( $\varphi$ ) between an observed MMC AC voltage ( $v_{\Delta i}$ ) and its associated transformer EMF ( $v_{Ti}$ ). Consequently, the proposed configuration represents a phase-modulated structure, which relies on the control principles introduced with the appearance of the DAB [127]. It is noteworthy that an MMC AC voltage amplitude should match the amplitude of its associated transformer EMF, therefore  $\hat{v}_{\Delta i} = \hat{v}_{Ti}$ .

**Fig. 6.6(b)** presents idealized voltage waveforms to be generated by the MMCs, as well as the currents flowing through both transformers' P-windings. Based on (6.2) and (6.3), peak voltages  $\hat{v}_{T1}$  and  $\hat{v}_{T2}$  can be calculated. If the output voltage reference value is denoted by  $v_o$ , then

$$\hat{v}_{T1} = m_{T1} v_o \quad (6.4)$$

$$\hat{v}_{T2} = m_{T2} v_o \quad (6.5)$$

By analyzing the waveforms given in **Fig. 6.6(b)**, power at which the energies are flowing through  $T_1$  and  $T_2$  can be derived as (6.6) and (6.7).

**Tab. 6.1** Analyzed system parameters

Input voltage	Output voltage	Rated power	System operating frequency
40kV	1.5kV	10MW	1kHz

$$P_{T1} = \frac{m_{T1}^2 v_o^2}{\omega L_\Sigma} \varphi_1 \left( \frac{1}{2} - \frac{3\varphi_1}{8\pi} \right) \quad (6.6)$$

$$P_{T2} = \frac{m_{T2}^2 v_o^2}{\omega L_\Sigma} \varphi_2 \left( \frac{2}{3} - \frac{\varphi_2}{2\pi} \right) \quad (6.7)$$

It is noteworthy that  $P_{T1} = P_{T2}$  if turns ratios relation from (6.1) holds, while  $\varphi_1 = \varphi_2$ . According to **Fig. 6.6(b)**, adjacent legs within either of the MMCs have to generate two voltages of the same amplitude, however in the counterphase. This means that the observed MMC legs can be controlled in a complementary manner. In other words, a leg AC pole reference voltage  $v_{si}$  will be used with the opposite sign for the adjacent leg within the same MMC, as presented in **Fig. 6.6(a)**. In (6.6) and (6.7)  $L_\Sigma$  accounts for the sum of an MMC branch inductance and its associated transformer leakage inductance. However, throughout the following sections, transformers' leakage inductances are assumed negligible with respect to the MMC branch inductance.

### 6.3 System design

**Tab. 6.1** summarizes the ratings of a system observed for the purpose of providing a thorough insight into the converter design guidelines. In the forthcoming analysis, it will be assumed that proposed converter interfaces either a bipolar HV/MV DC grid or two separate DC grids of the same voltage level with an LV DC grid. Additionally, converter design is conducted assuming the operation without faults, henceforward referred to as the normal operating conditions, which can easily be proven as critical from the system design standpoint.

#### 6.3.1 Number of MMC submodules

It is assumed that both MMCs operate with equal and stiff voltages across their DC terminals. The number of SMs to be employed within an MMC depends on the available HV/MV across its DC terminals along with the voltage class of semiconductor devices to be employed. Considering the voltage level given in **Tab. 6.1** and the desire to have a reasonable number of SMs, the use of 3.3kV IGBT modules can be considered. Hence, according to (6.8), one can calculate that the minimal number of needed SMs equals  $N_{\min} = 12$ . Please keep in mind that a certain number of redundant SMs, denoted by  $N_R$ , can as well be installed. However, throughout this chapter, it is not considered since it is not essential for the upcoming discussions.

$$N = \underbrace{\text{ceil} \left( \frac{V_{\text{DC,mmc}}}{0.55 V_{\text{CE}}} \right)}_{N_{\min}} + N_R \quad (6.8)$$

### 6.3.2 Transformers' turns ratios

Before commencing any further analyzes, it is worth noting that voltage across both transformers' P-windings has to match the voltages impressed into the system by both MMCs with the aim of maintaining the fundamental switching frequency of all semiconductor devices within the converter. Also, (6.1) is expected to be respected.  $T_1$  turns ratio can be determined such that the voltage generated across its P-winding matches the voltage impressed into the system by the MMC<sub>1</sub>. In other words, MMC<sub>1</sub> operates as a "rail-to-rail" converter. Maximal value of the AC voltage generated by a leg of either MMC equals  $\hat{v}_s = V_{in}/4$  (keep in mind that  $V_{in}$  denotes the voltage of a bipolar grid, thus the division by four). As two legs operate in a complementary manner, meaning that  $v_{sB} = -v_{sA}$  for either MMC, expression (6.9) can be derived.

$$m_{T1} = \frac{V_{in}}{2v_o} \quad (6.9)$$

**Fig. 6.7** illustrates the change in the number of inserted SMs within the lower branch of both MMCs' phase A in case  $m_{T1}$  is chosen according to the above expression. In the previous subsection, the number of SMs per branch was set as  $N = 12$  meaning that all of the voltage levels to be generated by MMC<sub>1</sub> can be obtained by inserting a round number of its SMs into the circuit since  $\text{mod}(N, 4) = 0$ .

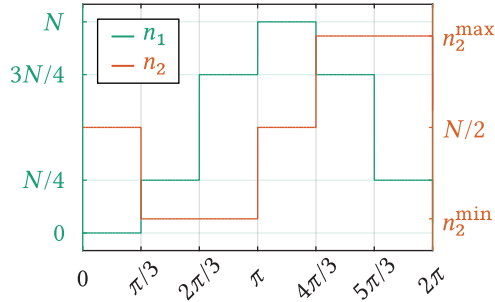


**Fig. 6.7** The number of inserted SMs for both MMCs in case MMC<sub>1</sub> operates as a "rail-to-rail" converter.

To determine the minimal and maximal number of SMs inserted in the branches of MMC<sub>2</sub>, one can assume that every SM voltage level equals  $V_{SM} = V_{in}/(2N)$ . Such an assumption is valid in case a proper controller of SMs' voltages exists. According to **Fig. 6.6(b)**, combined with the fact that

$$v_{s2} = \left( n_2^{\max} - \frac{N}{2} \right) \frac{V_{in}}{2N}, \quad (6.10)$$

one can derive

$$n_2^{\max} = \frac{N}{2} \left( 1 + \frac{m_{T2}}{m_{T1}} \right) \quad (6.11)$$

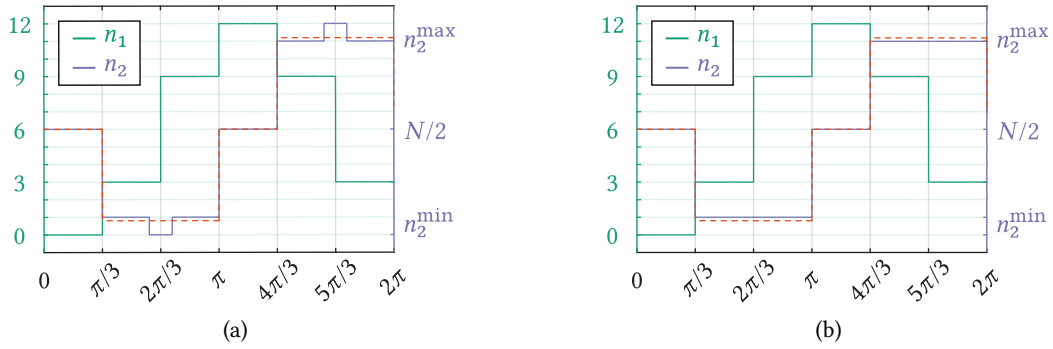


**Fig. 6.8** Possible modifications of the  $\text{MMC}_2$  branch reference in case (6.11) does not result in the number being an integer. In the illustrated case, the number of MMC SMs per branch was set as  $N = 12$ .

In case  $m_{T2}$  is selected according to (6.1),  $n_2^{\max}$  from (6.11) is not an integer. Consequently, special considerations have to be made with respect to the synthesization of  $\text{MMC}_2$  AC voltage. The first option, depicted in **Fig. 6.8(a)**, implies the adjustment of the branch voltage reference signal. Namely, in the areas at which the branch voltage reference does not correspond to the voltage matching an integer number of inserted SMs (e.g. from  $2\pi/3$  to  $\pi$  in **Fig. 6.8(a)**), a voltage pulse is created such that its voltage integral matches the one of the original reference over the observed interval. On the other hand, **Fig. 6.8(b)** presents the branch voltage reference modifications made through the adjustments of  $T_2$  turns ratio. As will be demonstrated shortly, this method is especially suitable in the case  $\text{mod}(N, 4) = 0$ , therefore two separate cases regarding the choice of  $m_{T2}$  will be differentiated henceforth.

### 6.3.2.1 $N$ is divisible by four

As can be seen from **Fig. 6.7**, the number of SM per branch divisible by four allows for a generation of  $\text{MMC}_1$  voltage reference by employing an integer number of SM throughout the whole fundamental period of operation. Consequently, the fundamental switching frequency of all the power switches can easily be maintained.

As for the  $\text{MMC}_2$ , the maximal number of inserted SMs within any of its branches can be calculated according to (6.11). As it has been stated, choosing  $m_{T2}$  according to (6.1) results in a non-integer value of the maximal number of inserted SMs within any of the  $\text{MMC}_2$  branches. Notwithstanding, a whole set of fractions, henceforth denoted by  $\xi$ , being quite close to  $\sqrt{3}/2$ , as listed in **Tab. 6.2**, exists. In case  $n_2^{\max} = \alpha N$ , peak voltage across  $\text{MMC}_2$  AC terminals can be calculated as

$$\hat{v}_2 = (2\alpha - 1) \frac{V_{\text{in}}}{2} \quad (6.12)$$

Given that  $T_2$  P-winding peak voltage equals  $\xi V_{\text{in}}/2$  on these terms, the relationship between a fraction being utilized instead of the original ratio defined by the STC and coefficient  $\alpha$  can be established as (6.13).



**Tab. 6.2** Coefficients possibly used instead of  $\sqrt{3}/2$ 

$\xi$	Float	$\alpha$	No. of employed SMs ( $n \in \mathbb{N}$ )
4/5	0.8	9/10	$4 \times 5n$
5/6	0.833	11/12	$4 \times 3n$
6/7	0.857	13/14	$4 \times 7n$
7/8	0.875	15/16	$4 \times 4n$

$$\xi = 2\alpha - 1 \quad (6.13)$$

Therefore, a fraction of the total SMs number, within the MMC<sub>2</sub>, to be inserted in order to match T<sub>2</sub> peak voltage can be determined as

$$\alpha = \frac{\xi + 1}{2} \quad (6.14)$$

According to the fourth column of **Tab. 6.2**, if the number of MMC SMs is set as  $N = 12$ , T<sub>2</sub> turns ratio is chosen as

$$m_{T2} = \frac{5}{6} m_{T1} \quad (6.15)$$

What comes out as a direct consequence of such a turns ratios choice is uneven split between powers at which the energies are transferred through T<sub>1</sub> and T<sub>2</sub>. However, as shown in the upcoming sections, this issue can easily be addressed by means of a suitable control strategy.

### 6.3.2.2 $N$ is neither divisible by four nor even

In case the number of SMs per branch is neither divisible by four nor even, none of the levels  $N \times \{\frac{1}{4}, \frac{1}{2}, \frac{3}{4}\}$  can be generated without additional considerations. To provide an illustration of such a case, let  $N = 11$ . As depicted in **Figs. 6.9(a)** and **6.9(b)**, synthesization of any of the above mentioned voltage references requires the switching between two of its available neighbouring levels labeled with  $\underline{n}_i = \text{floor}(n_i)$  and  $\overline{n}_i = \text{ceil}(n_i)$ .

For instance, generation of the reference level denoted by  $n_2^{\min}$ , between the instants represented by the angles  $2\pi/3$  and  $\pi$ , requires the switching between the levels defined by (6.16) and (6.17) in case  $\frac{m_{T2}}{m_{T1}} = \frac{\sqrt{3}}{2}$ .

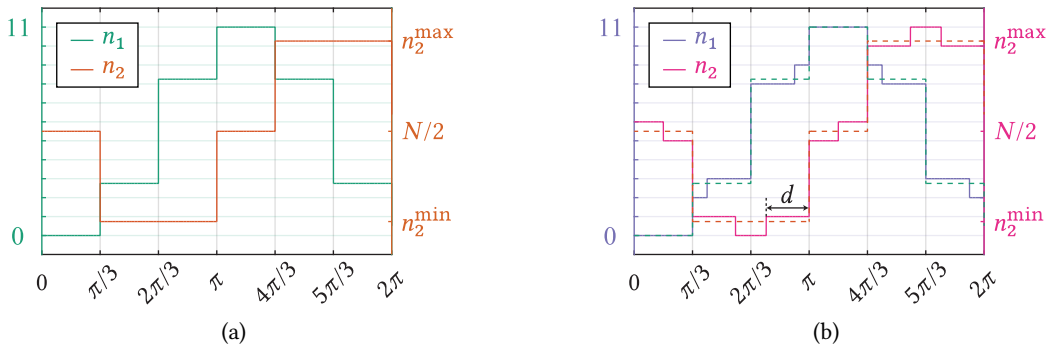


**Fig. 6.9** (a) Both MMCs phase A lower branch voltage references in case  $N$  is neither divisible by four nor even; (b) As can be seen, generation of the presented reference voltages can not be achieved without the additional switching actions. Duration of the voltage pulse (in case switching is needed) can be determined such that its voltage integral over an observed terminal matches the original reference. As explained below, apart from the pulse duration, its position needs to be determined such that fundamental frequency of all the SMs can be achieved.

$$\underline{n_2}|_{2\pi/3}^{\pi} = \text{floor}\left\{\frac{N}{2}\left(1 - \frac{\sqrt{3}}{2}\right)\right\} = 0 \quad (6.16)$$

$$\overline{n_2}|_{2\pi/3}^{\pi} = \text{ceil}\left\{\frac{N}{2}\left(1 - \frac{\sqrt{3}}{2}\right)\right\} = 1, \quad (6.17)$$

Duration of the generated voltage pulse, denoted by  $d$  in **Fig. 6.9(b)** can be calculated as (6.18)

$$d_i = \{n_i - \text{floor}(n_i)\} \frac{\pi}{3} \quad (6.18)$$

As the pulse duration is determined such that its voltage integral over an observed interval matches the original reference, pulse position might seem irrelevant at first glance. However, it is easy to conclude that positioning the voltage pulse in the middle of interval  $\omega t \in [(k-1)\pi/3, k\pi/3]$  requires the converter switching frequency to be higher than the STC operating frequency. Consequently, switching pulses to be generated must always lean against the higher of its adjacent reference levels, as depicted in **Fig. 6.9(b)**. In this way, pulse reference monotonicity is retained on the half-wave level. For instance, as depicted in **Fig. 6.9(b)**,  $n_2$  is constantly increasing its value during the period  $\omega t \in [2\pi/3, 5\pi/3]$ , meaning that fundamental switching frequency can be guaranteed.

It is noteworthy that deviation of the generated branch voltage waveforms from their references become less emphasized with an increase in the number of SMs per branch. Notwithstanding, since the switching between the levels labeled with  $n_i$  and  $\overline{n}_i$  can not be avoided on the terms defined as  $\text{mod}(N, 2) \neq 0$  and  $\text{mod}(N, 4) \neq 0$ , transformers' turns ratios can be chosen according to (6.1) and (6.9), respectively.

### 6.3.3 MMC branch inductor design

Considering the inevitable presence of branch inductors within both MMCs, the double role can be assigned to them. On one hand, branch inductors are used to limit the MMC common-mode current ripple originating from voltage oscillations across the MMC SMs. On the other hand, MMC branch inductors can be used to control the converter power transfer since an MMC equivalent inductance seen from its associated transformer P-winding corresponds to its branch inductance. Of course, such a statement holds providing transformers' leakage inductances can be considered negligible compared to the MMCs branch inductances. Consequently, for a given system rated power  $P_{\text{nom}}$ , operating frequency  $f$  and nominal phase angle  $\varphi_{\text{nom}}$ , branch inductance can be calculated according to (6.6) or (6.7), leading to (6.19).

$$L_{\text{br}} = \frac{2m_{\text{T1}}V_o^2}{\omega P_{\text{nom}}} \varphi_1 \left( \frac{1}{2} - \frac{3\varphi_1}{8\pi} \right) \quad (6.19)$$

Adopting nominal phase angle as  $\varphi_{\text{nom}} = 10^\circ$ , along with the use of parameters provided by **Tab. 6.1** and above derived transformers turns ratios relation, leads to the branch inductance being set as  $L_{\text{br}} = 1\text{mH}$ .

### 6.3.4 SM capacitance design

Given that isolation stages of the DC-DC converters can operate at any arbitrary frequency, the operating frequency increase towards the medium frequency range is widely accepted. Nevertheless, generation of the medium frequency voltages across the transformers' windings can lead to high switching frequencies, and consequently the losses, of the semiconductor devices unless a proper modulation strategy is deployed. Therefore, maintaining the switching frequency equal to the fundamental operating frequency of the isolation stage can be defined as the main goal of an employed modulator.

Sizing of the SM capacitors in the MMC-based DAB converters is tightly bounded with the branch switching patterns. Similarly to the transformers' turns ratios determination, two distinct cases depending on the parity of the number of SMs per branch will be recognized.

#### 6.3.4.1 N is divisible by four

As demonstrated in **Sec. 6.3.2**, the number of SMs per branch being divisible by four allows for all of the branch voltage reference levels to be obtained by inserting an integer number of SMs into the circuit. Such convenience can be taken the advantage of by defining suitable SM groups which, if inserted in right time instants, will guarantee that the instantaneous sum of inserted SMs guarantees that a branch reference voltage is obtained at all times. For example, MMC<sub>1</sub> branch voltage reference comprises six edges (three rising and three falling edges), hence it can easily be synthesized by employing three groups, containing a suitable number of SMs each, as depicted in **Fig. 6.10(a)**. With respect to each other, these groups are shifted by one-sixth of the fundamental period. Consequently, each one of them remains active during one half of the fundamental period.

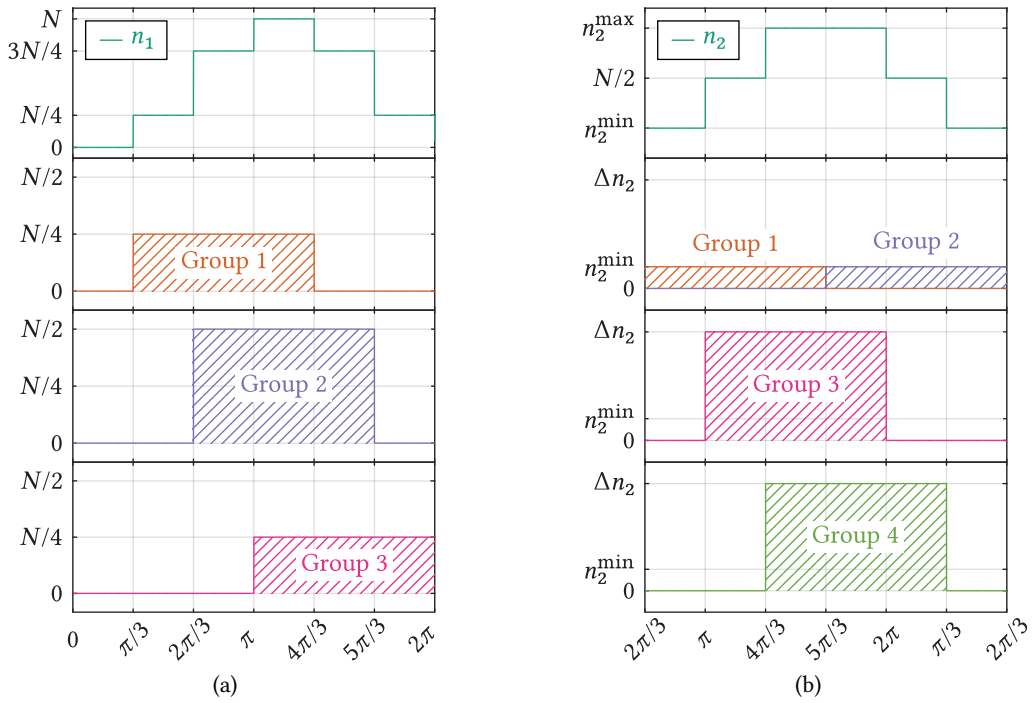


**Fig. 6.10** Possible ways of generating reference voltages for the lower branch of both MMCs phase A. Please notice that the fundamental switching frequency of all the SMs installed within the converter is retained in case desired references are obtained through the combination of suitable SM groups. As a result, branch switching patterns get defined in advance, whereas assignment of an observed SM to a group is the task performed by the SM voltage balancing controller. (a) MMC<sub>1</sub> pulse pattern; (b) MMC<sub>2</sub> pulse pattern.

Similar reasoning can be applied to MMC<sub>2</sub>. Its branch voltage reference can easily be synthesized by employing four SM groups. At first glance, it might look as if groups 1 and 2 could comprise a single entity, however, as will be discussed shortly, such a definition would result in unnecessarily high SM voltage ripple. Consequently, groups 1 and 2 span half of the fundamental period each, as presented in **Fig. 6.10(b)**.

As can be seen from **Figs. 6.10(a)** and **6.10(b)**, the number of inserted SMs varies among the groups. Belonging of a random SM to any of the groups is determined by the SM voltage balancing controller, which will be discussed in **Sec. 6.4.3**. The group an observed SM is being assigned to defines the electric charge the SM accumulates during an analyzed switching period. In accordance with (6.20), the electric charge represents the area bellow an observed SM capacitor current. Hence, **Figs. 6.11(a)** and **6.11(b)** present the charges that the SMs receive depending on what group they are belonging at the present switching cycle.

$$Q_G = \frac{1}{\omega} \int_{\theta_1}^{\theta_2} i_n(\theta) d\theta \quad (6.20)$$

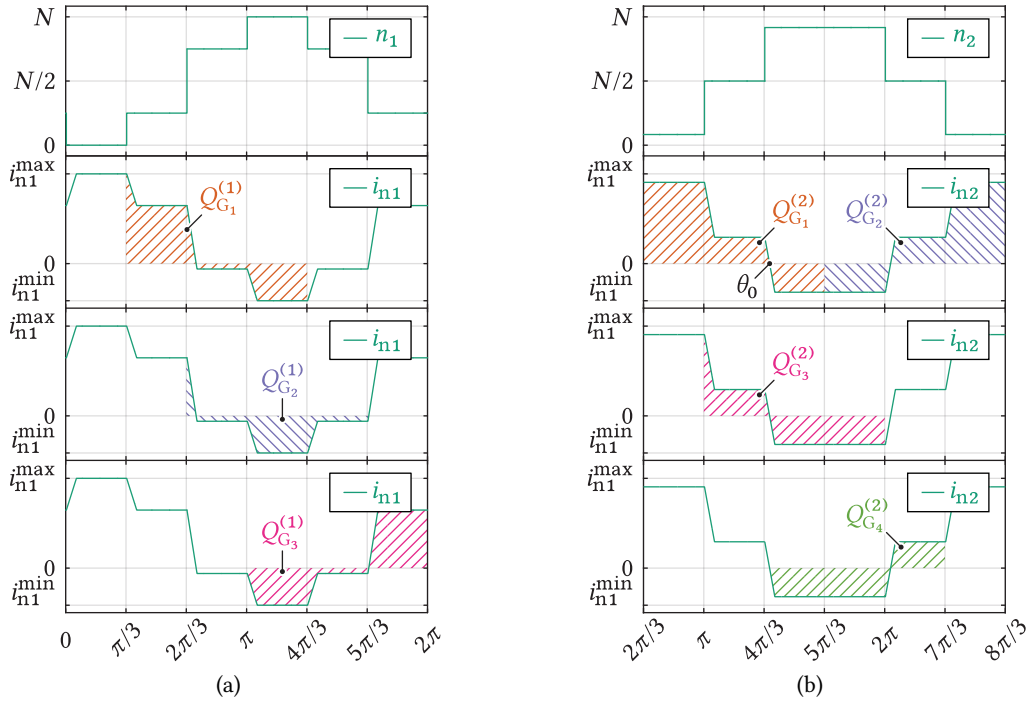


**Fig. 6.11** Electric charges received depending on the group an SM is being assigned to. It is straightforward to conclude that the highest charge of the positive sign causes the SM voltage oscillations which can be referred to as peak-to-peak oscillations. (a) Charges characterizing MMC<sub>1</sub> SM groups; (b) Charges characterizing MMC<sub>2</sub> SM groups.

Total charge acquired during the period a certain group is active can be calculated by setting the angle  $\theta_1$  from (6.20) to the beginning of the period itself, while  $\theta_2 = \theta_1 + \pi$ . However, it can be seen from **Figs. 6.11(a)** and **6.11(b)** that each of the charges calculated as (6.20) can be decomposed as

$$Q_G = \underbrace{Q_G^+}_{\text{positive charge}} + \underbrace{Q_G^-}_{\text{negative charge}} \quad (6.21)$$

It can be concluded that peak-to-peak capacitor voltage rise can be determined according to the positive part of the total accumulated charge  $Q_G$ . A simple visual inspection of **Figs. 6.11(a)** and **6.11(b)** indicates that SMs group 1 of the MMC<sub>2</sub>, labeled with  $Q_{G_1}^{(2)+}$ , carries the highest amount of positive charge, therefore it will be considered critical for the SM capacitance sizing. From the capacitor voltage equation  $C \frac{dv_C}{dt} = i_C$ , (6.22) can be written.

$$C_{SM}^{\min} = \left( \underbrace{\beta \frac{V_{in}}{2N}}_{\Delta V_{SM}} \right)^{-1} \times \underbrace{\frac{1}{\omega} \int_0^{\theta_0} i_{n2}(\theta) d\theta}_{Q_{G_1}^{(2)+}} \quad (6.22)$$

By solving the integral corresponding to the charge  $Q_{G_1}^{(2)+}$ , while keeping in mind that the amplitude of the square waves generated by the observed MMC can be determined according to (6.12), desired sizing equation can be established as

$$C_{SM}^{\min} = \frac{(32N\alpha^2 + 24N\alpha)\varphi_{\text{nom}}\pi^3 + (16N\alpha^3 - 24N\alpha^2 + 36N\alpha)\varphi_{\text{nom}}^2\pi^2 - 24N\alpha^3\varphi_{\text{nom}}^3\pi + 9N\alpha^3\varphi_{\text{nom}}^4}{144L_{\text{br}}\beta\omega^2\pi^2} \quad (6.23)$$

Since practical values of SM capacitances can deviate from the rated values, a certain sizing margin, labeled with  $\gamma$ , can be adopted leading to

$$C_{SM} = \gamma C_{SM}^{\min} \quad (6.24)$$

Adopting the number of SMs per branch as  $N = 12$ , along with  $\beta = 2.5\%$  and  $\gamma = 1.15$  provides the SM capacitance equal to  $C_{SM} \approx 2.65\text{mF}$ .

#### 6.3.4.2 N is neither divisible by four nor even

The identical idea of creating a branch reference voltage by employing the selection of appropriate SM groups can be used in this case. Therefore, the same SM capacitance sizing methodology can be retained. Nevertheless, pulse patterns slightly differ from the ones presented in **Figs. 6.11(a)** and **6.11(b)**.

#### 6.3.5 LV stage capacitor bank design

Capacitor bank in the LV stage can be designed according to the desired output voltage ripple, which originates from the SSC output current ripple ideally occurring at six times the operating frequency of the converter. **Fig. 6.12** presents the idealized waveform of the SSC output current. The current area causing the output capacitor voltage drop can be labeled with  $S^-$ , as depicted in **Fig. 6.12**. Hence, (6.25) can be easily derived.

$$\begin{aligned} |\Delta V_o| &= \frac{1}{\omega C_o} i_{SSC}^{\max} \underbrace{\left| \int_{\theta}^{\frac{\pi}{3}} \left[ 1 - \frac{\omega t - \frac{\pi}{3} + \varphi}{2\varphi} - \left( 1 - \frac{3\varphi}{4\pi} \right) \right] d(\omega t) \right|}_{S^-} \\ &= i_{SSC}^{\max} \left| \frac{4\varphi\pi^2 + 12\varphi^2\pi - 9\varphi^3}{16\omega C_o\pi^2} \right| \end{aligned} \quad (6.25)$$

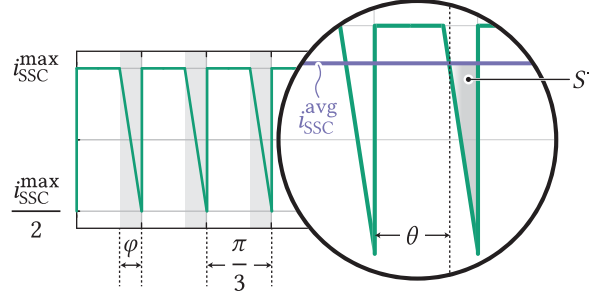


**Fig. 6.12** Idealized SSC output current

According to **Fig. 6.6(b)**, the peak value of the SSC output current can be effortlessly calculated. For the output voltage peak-to-peak ripple being expressed as a percentage of the reference value (mathematically formulated as  $\Delta V_o = \delta \times v_o$ ), the output capacitance can be set according to (6.26), which gives  $C_o \approx 2.65\text{mF}$  should  $\delta = 1.5\%$  be the requirement to meet.

$$C_o \geq \frac{m_{T1}^2 \varphi_{\text{nom}}^2 \left| (4\pi^2 + 12\varphi_{\text{nom}}\pi - 9\varphi_{\text{nom}}^2) \right|}{16\omega^2 L_{\text{br}} \delta \pi^2} \quad (6.26)$$

## 6.4 System control under normal operating conditions

### 6.4.1 Equivalent 3PH-DAB model

Henceforth, the LV stage will be referred to as the output, whereas the HV/MV stage will be referred to as the input stage. To provide a framework for the system control-related discussions, the behavior of the LV side currents should be investigated. Ampere-turns balance equations can be set for both transformers, yielding

$$\begin{bmatrix} i_A \\ i_B \\ i_C \end{bmatrix} = \begin{bmatrix} m_{T1} & 0 \\ -m_{T1}/2 & m_{T2} \\ -m_{T1}/2 & -m_{T2} \end{bmatrix} \begin{bmatrix} i_{T1} \\ i_{T2} \end{bmatrix} \quad (6.27)$$

According to **Fig. 6.6(a)**,  $T_1$  and  $T_2$  P- winding currents can be described with (6.28) and (6.29), respectively.

$$L_{\text{br}} \frac{di_{T1}}{dt} = v_{\Delta 1} - m_{T1} \frac{v_{AB} - v_{CA}}{2} \quad (6.28)$$

$$L_{\text{br}} \frac{di_{T2}}{dt} = v_{\Delta 2} - m_{T2} v_{BC} \quad (6.29)$$

Since the LV stage consists of three phases, its current behavior can be observed in the  $\alpha\beta$  plane, which is achieved through the transformation presented in (6.30).

$$\begin{bmatrix} i_\alpha \\ i_\beta \end{bmatrix} = \frac{2}{3} \begin{bmatrix} 1 & -\frac{1}{2} & -\frac{1}{2} \\ 0 & \frac{\sqrt{3}}{2} & -\frac{\sqrt{3}}{2} \end{bmatrix} \begin{bmatrix} i_A \\ i_B \\ i_C \end{bmatrix} \quad (6.30)$$

It is of interest to observe the SSC currents change during the converter operating period, therefore (6.30) needs to be differentiated, leading to

$$\frac{di_\alpha}{dt} = \frac{2v_{\Delta 1} m_{T1}}{2L_{br}} - m_{T1}^2 \frac{3v_\alpha}{2L_{br}} \quad (6.31)$$

$$\frac{di_\beta}{dt} = \frac{2\sqrt{3}}{3L_{br}} (v_{\Delta 2} m_{T2} - v_\beta \sqrt{3} m_{T2}^2) \quad (6.32)$$

It would be quite convenient if  $\alpha$  and  $\beta$  components of the input stage voltages appeared in (6.31) and (6.32). However, the input stage consists of two 1PH transformers, hence excluding the possibility for  $\alpha\beta$  transformation of its quantities. However, voltages to be generated by both MMCs ( $v_{\Delta 1}$  and  $v_{\Delta 2}$ ) represent a certain combination of the LV quantities, which enables their observation through a virtual voltage system  $\vec{v}'_{ABC}$ . Such a system has the amplitude identical to the LV stage phase voltages while being advanced by the phase angle  $\varphi$ . Mathematically, such a statement can be formulated as

$$\vec{v}'_{ABC} = \vec{v}_{ABC} e^{j\varphi} \quad (6.33)$$

Consequently, voltages  $v_{\Delta 1}$  and  $v_{\Delta 2}$  can be obtained as

$$v_{\Delta 1} = m_{T1} \frac{v'_{AB} - v'_{CA}}{2} \quad (6.34)$$

$$v_{\Delta 2} = m_{T2} v'_{BC} \quad (6.35)$$

Substituting (6.1), (6.34) and (6.35) into (6.31) and (6.32) leads to the simplified system of equations describing the LV stage  $\alpha\beta$  currents as (6.36) and (6.37).

$$\frac{di_\alpha}{dt} = m_{T1}^2 \frac{v'_{AB} - v'_{CA}}{2L_{br}} - m_{T1}^2 \frac{3v_\alpha^{ABC}}{2L_{br}} = \frac{2m_{T2}^2}{L_{br}} (v'_\alpha - v_\alpha) \quad (6.36)$$

$$\frac{di_\beta}{dt} = \frac{2m_{T2}^2}{L_{br}} \frac{v'_{BC} - v_{BC}}{\sqrt{3}} = \frac{2m_{T2}^2}{L_{br}} (v'_\beta - v_\beta) \quad (6.37)$$



Accordingly, the LV stage current vector can be calculated as

$$\frac{d}{dt} \vec{i}_{\alpha\beta} = \frac{2m_{T2}^2}{L_{br}} (\vec{v}'_{\alpha\beta} - \vec{v}_{\alpha\beta}) \quad (6.38)$$

The current vector equation (6.38) indicates that the proposed topology can be observed through its equivalent 3PH-DAB model, presented in **Fig. 6.13**. The circuit consists of an ideal 3PH transformer, with turns ratio equal to one, equivalent inductance  $L_\gamma^* = L_{br}/(2m_{T2}^2)$  and two conventional SSCs being modeled by the ideal 3PH voltage sources. To get the equivalent inductance, the MMC branch inductance has to be divided by the square of  $T_2$  turns ratio, which indicates that the equivalent circuit represents the converter observed from the LV stage. Moreover, seen from the LV stage, two MMCs operate in parallel, which is confirmed by the fact that the branch inductance has to be divided by two in order to acquire the equivalent inductance  $L_\gamma^*$ .

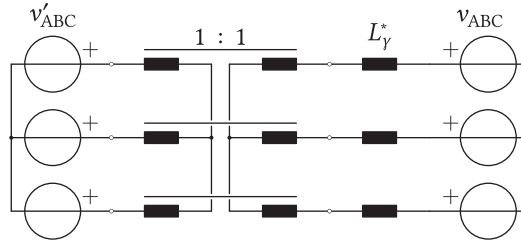


**Fig. 6.13** 3PH DAB equivalence of the proposed converter

To confirm the validity of the circuit presented in **Fig. 6.13**, power at which the energy is transferred from P to the S winding should match the power of the original circuit. It is known that the 3PH-DAB power can be calculated as

$$P_{DAB}^{(3)} = \frac{3\hat{V}^2}{\omega L_\gamma^*} \varphi \left( \frac{1}{2} - \frac{3\varphi}{8\pi} \right), \quad (6.39)$$

where  $\hat{V}$  refers to the amplitude of the equivalent transformer phase voltage, which equals  $\hat{V} = 2\hat{v}_{ABC}/3$ . Considering that voltage sources  $\vec{v}_{ABC}$  have the amplitude equal to the original system output voltage, one can conclude that  $\hat{V} = 2v_o/3$ . Substitution of  $\hat{V}$  into (6.39) yields

$$P_{DAB}^{(3)} = 2 \frac{4v_o^2 m_{T2}^2}{3\omega L_{br}} \varphi \left( \frac{1}{2} - \frac{3\varphi}{8\pi} \right) = 2P_{T1} \quad (6.40)$$

The above expression suggests that the 3PH-DAB equivalent matches the original system in terms of the LV side behavior as well as the power transfer. Therefore, the 3PH-DAB control algorithms already presented in the literature [136]–[138] can be applied to the system being the subject of this chapter. Additionally, even if the transformers' turns ratios relationship, originally defined by the STC, is violated, the precision of the above results should not be severely hindered.

According to **Tab. 6.2**, fractions possibly utilized instead of  $\sqrt{3}/2$  indeed result in a certain transformers' power transfers mismatch, however, it will be shown that this issue can easily be addressed by means of a suitable control strategy.

### 6.4.2 Output voltage control

Output voltage control was performed according to **Fig. 6.14**, with the aim of maintaining the output voltage mean value equal to the reference defined in **Tab. 6.1**. Seen from the LV side, SSC can be perceived as an ideal current source owing to the fact that a DAB-based circuit output current does not depend on its output voltage. Therefore, in order to control the output voltage, the SSC output current mean value ( $i_{SSC}^*$ ) should be adjusted. However, a variable to be affected within the DAB-alike systems is the phase shift between relevant voltage waveforms. Therefore, phase angle information needs to be extracted from the SSC output current reference.

By observing (6.6) and (6.7), one can connect the SSC output current mean value with the HV/MV quantities, however, this results in the need for solving a set of non-linear equations. Linearization of power curves (6.6) and (6.7) around desired operating angles can be performed. It can be shown that this will not significantly hinder the precision of the obtained results. Ultimately, the output voltage controller will compensate for the errors introduced by the aforementioned linearization. If the linearization point is chosen as  $\varphi_{lin} = \pi/6$ , the system power equation (6.6) can be rewritten as

$$P_o = \frac{7\zeta V_{in} v_o m_{T1}}{16\omega L_\Sigma} \varphi \quad (6.41)$$

Given that the output power can be perceived as the product of the SSC output current mean value and the output voltage, the phase angle information can be extracted from the SSC output current reference based on (6.42). Moreover, since the converter can be modeled with an ideal current source seen from the LV side, the load current ( $i_o$ ) can be used as a feed-forward variable in case it is measured. What goes in favor of such a statement is the fact that the SSC output current average matches the load current once the steady state is reached.

$$\varphi^* = \frac{16\omega L_\Sigma}{7\zeta V_{in} m_{T1}} i_{SSC}^* \quad (6.42)$$

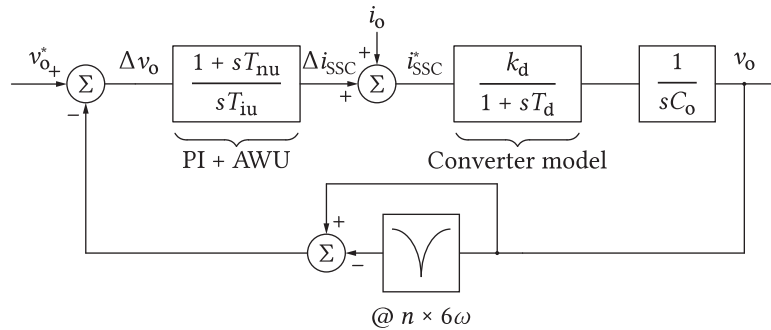


**Fig. 6.14** Output voltage control block diagram

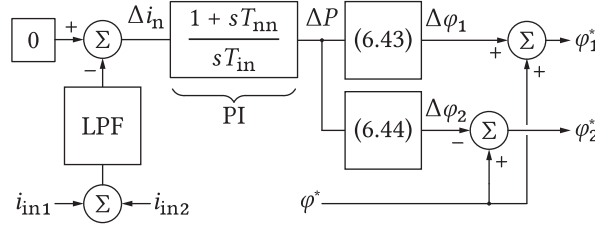


**Fig. 6.15** Transformers' power matching control implementation

Although very convenient, using the same phase angle to control both transformers' power flow can result in the system power distribution inequality. In case  $m_{T1} \neq 2m_{T2}/\sqrt{3}$ , powers defined by (6.6) and (6.7) do not match. Therefore, additional corrective actions have to be performed upon the phase shifts  $\varphi_1$  and  $\varphi_2$ . Assuming stiff HV/MV, mismatch in converters' mean powers results in the neutral conductor current average value being different than zero. Hence, this variable can be used to bringing  $T_1$  and  $T_2$  powers to the same level. According to **Fig. 6.15**, a difference between MMCs' input currents (more precisely, their mean values) gets compared to zero. Thereafter, this value gets passed to the PI controller, whose output can be perceived as a power correction applied to both transformers ( $\Delta P$ ). However, to convert the PI controller output into the phase angle corrections, power equations (6.6) and (6.7) need to be linearized, yielding (6.43) and (6.44). It is noteworthy that the transformer power corrections are expected to be very modest, otherwise, the system design should be reconsidered. Additionally, the controller from **Fig. 6.15** can be slower compared to the output voltage controller.

$$\Delta\varphi_1 = \frac{16\omega L_\Sigma}{7\hat{v}_{T1}^2} \Delta P \quad (6.43)$$

$$\Delta\varphi_2 = \frac{12\omega L_\Sigma}{7\hat{v}_{T2}^2} \Delta P \quad (6.44)$$

### 6.4.3 MMC balancing

In order to keep the SM voltages of both MMCs within a predefined range, the algorithm inspired by the idea presented in [139] was created. In contrast to [139] where the 1PH MMC-based DAB was analyzed, in this work, the SMs need to be assigned to one of the groups illustrated in **Figs. 6.10(a)** and **6.10(b)**. It is exactly the group an SM belongs to that determines its voltage rise over an observed switching period. Consequently, re-assigning the SMs to different pulse groups depending on an observed switching period, with the aim of keeping their voltages balanced, represents the main task of the balancing algorithm being the subject of this subsection.

Since the fundamental switching frequency of the SMs was defined as one of the requirements to be met by an employed modulator, assigning the SMs to an appropriate group occurs only once during the converter's switching period. In other words, once determined, the switching pattern is retained until the next switching period. Also, converter branches belonging to the same leg operate in a complementary manner, therefore, decision making is to be done on the branch level. Moreover, as operating principles of the proposed converter differ from the conventional MMC, balancing of the SMs is ensured in a different fashion, as will be demonstrated in the next paragraphs.

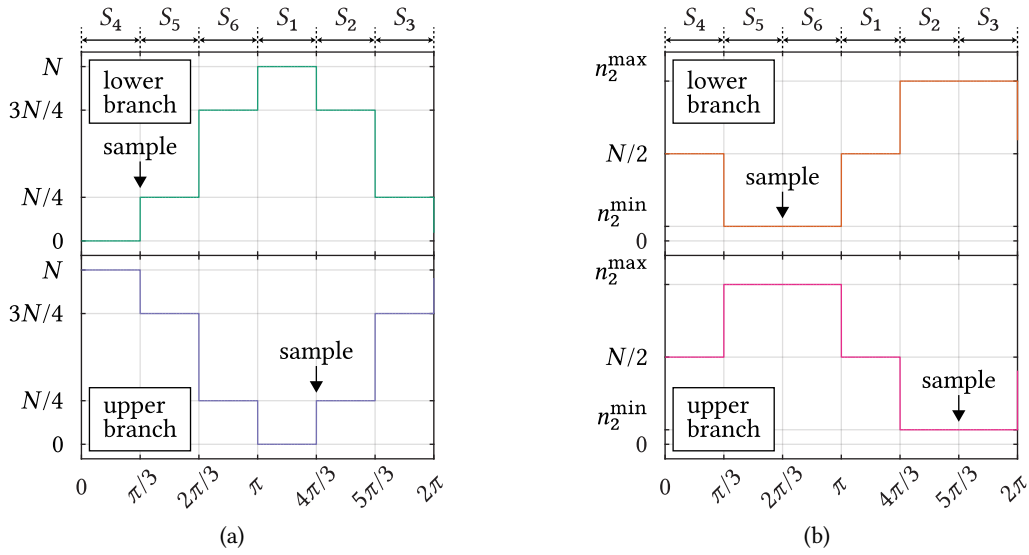


**Fig. 6.16** Division of the fundamental switching period into sectors along with the suitable instants at which the balancing algorithm is activated. (a) MMC<sub>1</sub> phase leg A; (b) MMC<sub>2</sub> phase leg A

Given that the SM voltage balancing algorithm determines the SMs distribution within the switching groups only once during the switching period, a suitable moment for the decision-making process needs to be defined. For that matter, the switching period of both MMCs was divided into sectors. Please notice that these sectors also define the line voltages of the conventional SSC. For instance, sector 1 corresponds to the state 100, where the combination of the SSC line voltages according to (6.2) and (6.3) provides the voltages across the P- windings of  $T_1$  and  $T_2$  having the identical shape as depicted in the figure above (although delayed/advanced by the angle  $\varphi$ ). Further, **Figs. 6.17(a)** and **6.17(b)** present the electric charges acquired by different SM groups for the MMCs with parameters determined following the previous section. It is important to notice that, in both cases, groups' charges always stay in the same order for a chosen phase angle sign. Moreover, in the presented range of phase angles, there is/are always set/sets of positive followed by set/sets of negative charges, which allows for the balancing algorithm to be implemented as presented in **Fig. 6.18**.

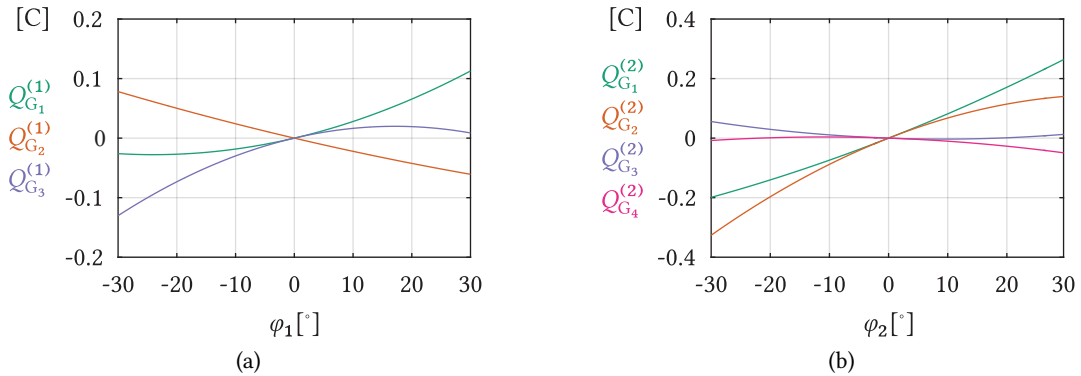


**Fig. 6.17** Electric charges acquired by different SM groups depending on the phase shift between the voltage generated by an observed MMC and its associated transformer P- winding voltage. (a) MMC<sub>1</sub>; (b) MMC<sub>2</sub>

The algorithm starts by defining the appropriate switching groups depending on an observed MMC along with its branch where the algorithm is supposed to ensure the voltage balance. The algorithm consists of five key steps, which are explained bellow.

- **Step # 1**

To ensure that the pulse distribution changes only once per switching cycle, the algorithm makes sure that it takes actions exclusively in the beginning of a sector defined in advance. For instance, beginning of the first group can be adopted as a moment suitable for such a process. Therefore, the arrows in **Figs. 6.16(a)** and **6.16(b)** indicate the time instants at which the balancing algorithms may perform reshuffling of the SMs' gating signals.

- **Step # 2**

SMs' voltages are measured, while the group number to which the SM was assigned in the previous switching period is used to form the pairs  $\{v_{SM}[k], n_G[k - 1]\}$ .

- **Step #3**

SMs' voltage increments  $\Delta v_{SM}$  are calculated.

- **Step #4**

Every pulse gets associated with the voltage increment it caused in order to form the pairs  $\{\Delta v_{SM}[k], n_G[k - 1]\}$ .

- **Step #5**

- SMs' voltages get sorted in the ascending order
- All the pairs  $\{\Delta v_{SM}[k], n_G[k - 1]\}$  get sorted in the descending order depending on the voltage increase  $\Delta v_{SM}[k]$ .
- In the  $k$ -th switching period, a SM with the lowest voltage will be associated with the pulse which caused the highest voltage change and vice versa.

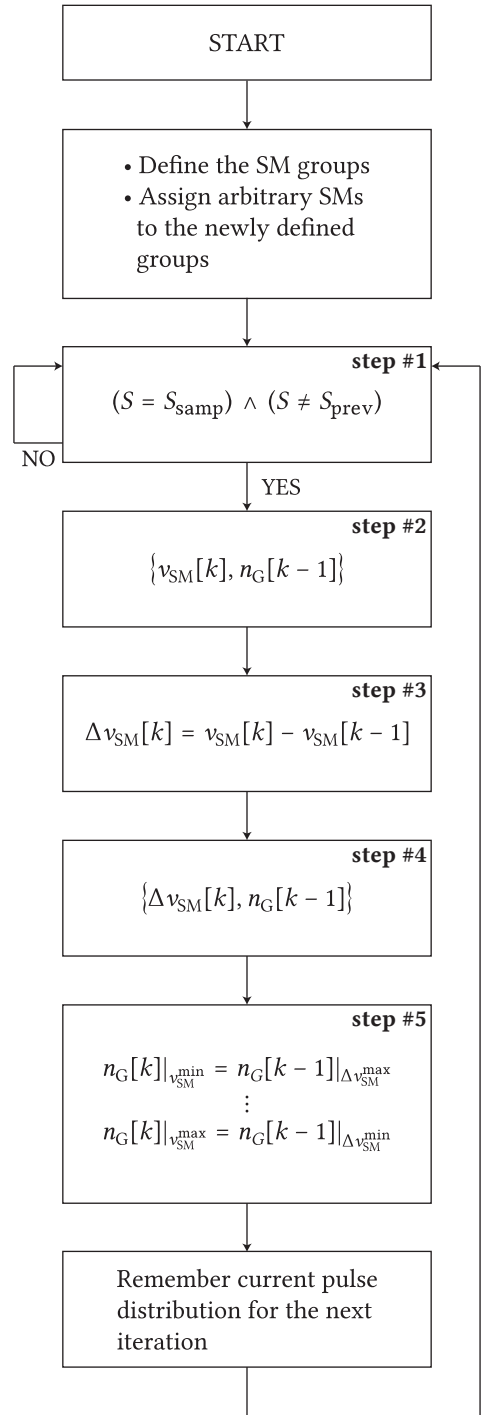


**Fig. 6.18** SM voltage balancing algorithm flow

The algorithm ends by remembering the pulse distribution being the result of the last sorting actions since these are going to be needed in the upcoming switching period (in other words, these will represent the terms  $n_G[k - 1]$  in **step # 2**).

**Tab. 6.3** Calculated values for all of the passive components considered in **Sec. 6.3**.

Number of MMC SMs	System operating frequency	MMC branch inductance	MMC SM capacitance	Output filter capacitance
12	1kHz	1mH	2.65mF	2.65mF

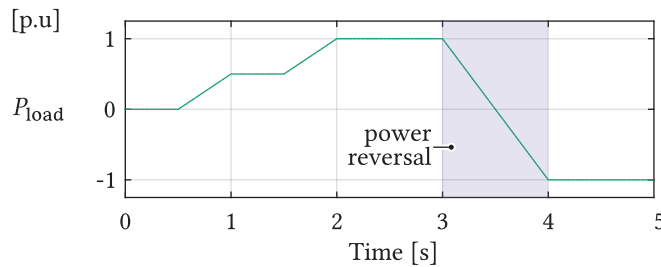
**Tab. 6.4** Tuning parameters of the control loops used within the model

Output voltage controller		Transformers' power balancing controller	
Parameter	Value	Parameter	Value
Proportional gain ( $k_{p1}$ )	6.67	Proportional gain ( $k_{p2}$ )	714.16
Integral gain ( $k_{i1}$ )	1.1	Integral gain ( $k_{i2}$ )	628.32
Sampling time ( $T_{s1}$ )	0.5ms	Sampling time ( $T_{s2}$ )	5ms

## 6.5 Simulation results under normal operating conditions

The proposed high-power DC-DC converter was modeled and simulated in PLECS. To test the converter operating performances, the load power profile depicted in **Fig. 6.19** was used. **Tab. 6.3** summarizes the values of all passive components chosen during the previous sections and used for simulation purposes. To demonstrate the robustness of the SM voltage balancing algorithm, capacitance deviations of  $\pm 20\%$  from the rated value were randomly distributed throughout the model. Additionally, **Tab. 6.4** provides the tuning parameters of the control loops used for simulation purposes. It is noteworthy that the presence of the MMC branch energy controllers can not be observed in **Tab. 6.4**. As explained in **Sec. 6.4.3**, different operating principles of the analyzed converter enable the SMs voltage/energy balancing by means of a suitable modulation scheme.

**Fig. 6.20** presents the converter operating waveforms during the time interval  $T_{sim} = 5s$ . The converter successfully responds to the power requirements imposed by the defined load profile, which can be concluded based on the shape of both MMCs input currents ( $i_{in1}$  and  $i_{in2}$ , respectively). These two currents differ only in terms of ripple originating from the oscillations of the MMC SMs' voltages. Thus, the neutral conductor current ( $i_n$ ) does not contain any average component. It is noteworthy that, even though the load power demand changes, abrupt phase angle changes must not be allowed within the DAB-based converters as it would cause the LV stage currents unbalance [136], [138]. At the time instant  $T = 3s$ , the converter successfully reverses its power over the interval  $\Delta T = 1s$ .

**Fig. 6.19** Load power profile normalized with respect to the rated power of the converter

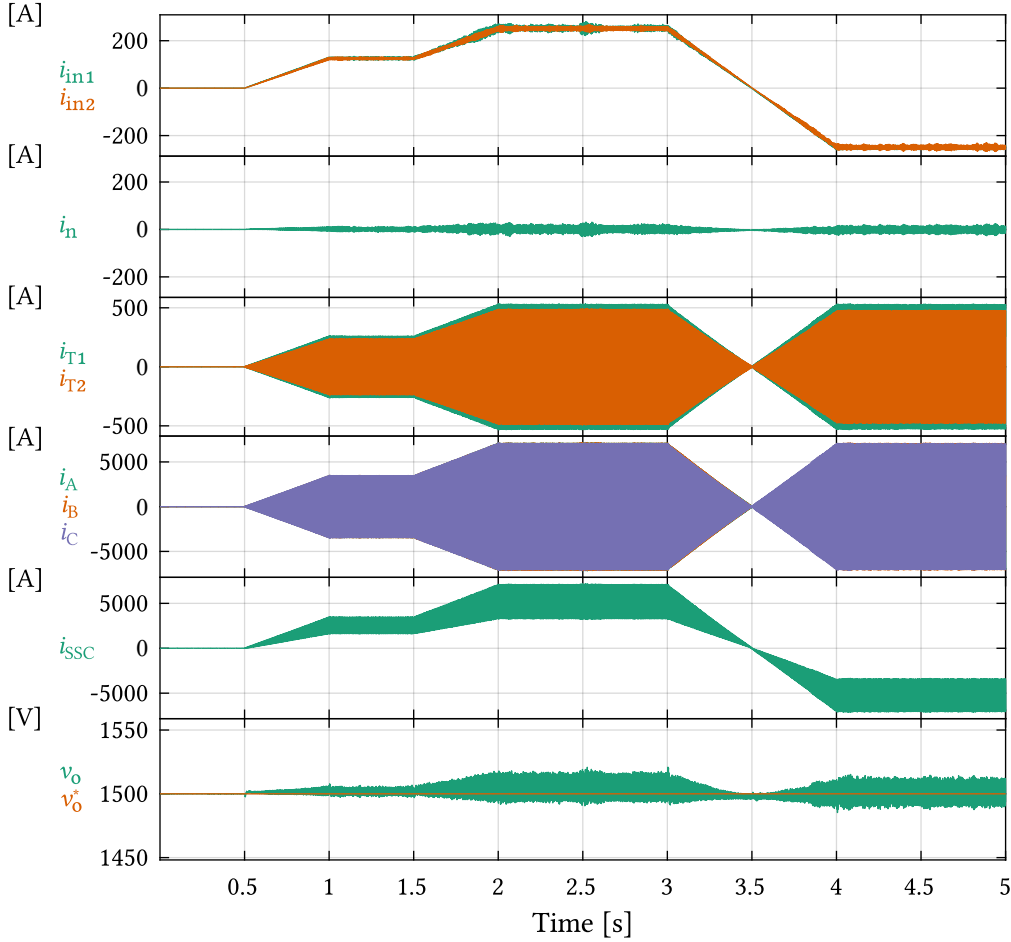


**Fig. 6.20** Operating waveforms of the proposed converter during the time interval  $T_{\text{sim}} = 5\text{s}$

To confirm the correspondence between the idealized waveforms, presented in **Fig. 6.6(b)**, and the ones obtained by means of simulations, **Fig. 6.21** presents both transformers' currents, the SSC output current along with the output voltage, during five operating cycles. Both  $T_1$  and  $T_2$  P-winding currents ( $i_{T1}$  and  $i_{T2}$ , respectively) correspond to the idealized waveforms presented in **Fig. 6.6(b)**. As expected, the SSC output current ( $i_{\text{SSC}}$ ) consists of the mean value along with the ripple occurring at six times the converter operating frequency, whereas the output voltage consists of the mean value along with the ripple originating from the SSC current oscillations. Also, the shape of the LV stage AC currents ( $i_A$ ,  $i_B$  and  $i_C$ ) corresponds to the one observed in the conventional 3PH DAB.

**Fig. 6.22** presents the output voltage spectrum with the frequency axis being normalized with respect to the converter operating frequency. Given that the output voltage mean value significantly exceeds the other harmonics being present in the output voltage, it is presented by the green bar. All the other harmonics can be read from the right-hand side axis, being colored in brown. It is easy to see that the dominant harmonic in the output voltage occurs at six times the operating frequency of the converter, which is expected owing to the correlation between the proposed topology and the 3PH DAB. Notwithstanding, a set of lower order harmonics can as well be observed. These can be considered a consequence of various factors such as SMs' voltage oscillations, which are not considered during the idealized waveforms derivation, non-ideal  $T_1$  and  $T_2$  turns ratio relation, etc.

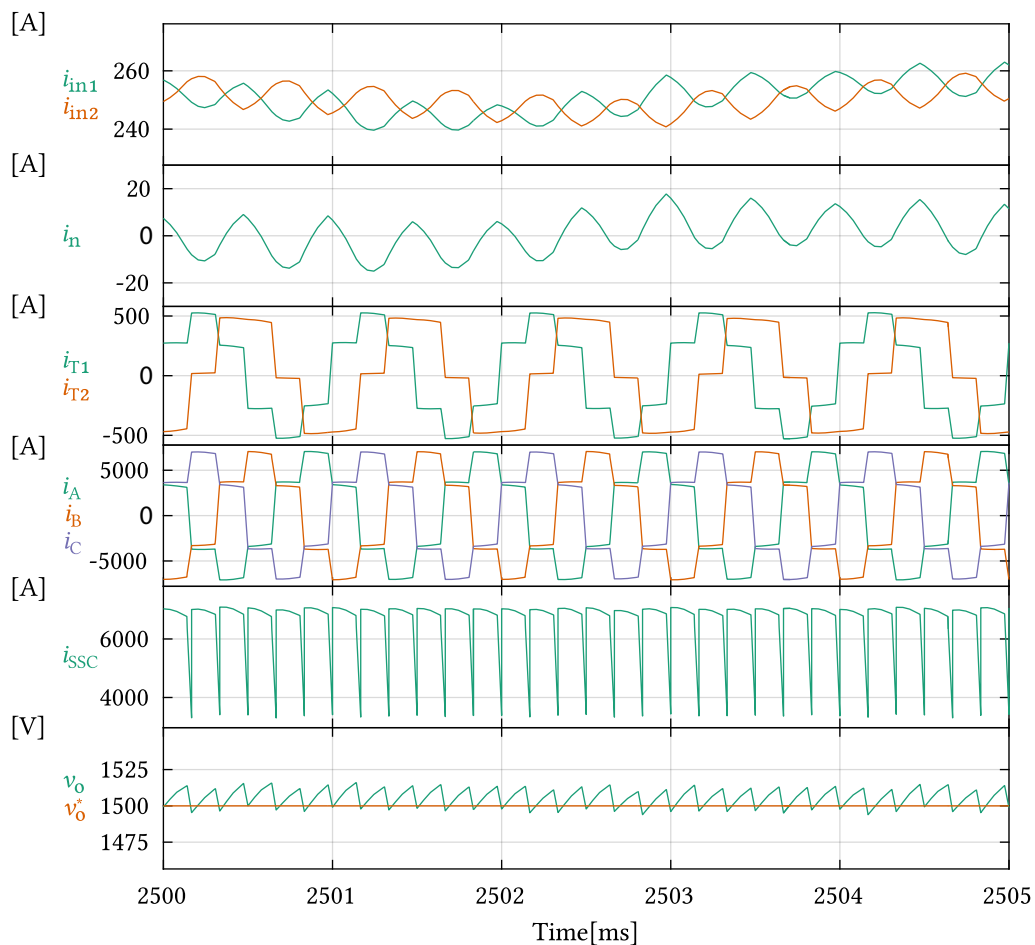


**Fig. 6.21** Converter operation during five fundamental cycles. Correspondence between the idealized waveforms presented in Fig. 6.6(b) and the ones obtained in simulations can be observed. The SSC output current consists of the mean value along with the ripple, occurring predominantly at six times the converter operating frequency, being superimposed.

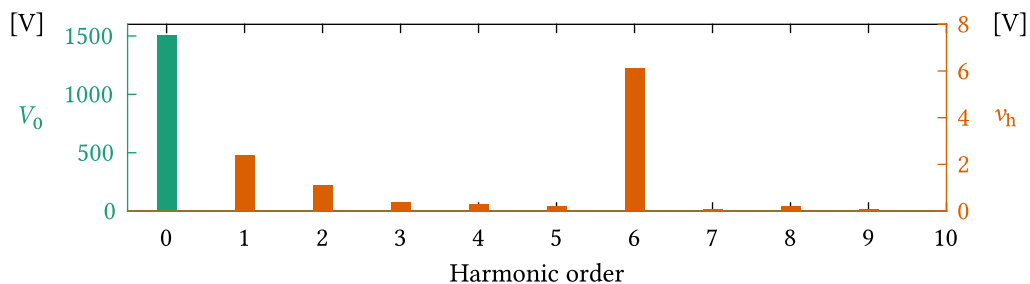


**Fig. 6.22** Output voltage spectrum. Owing to the presented sizing of the output capacitor, harmonics in the output voltage fall significantly below the mean value, which corresponds to the reference value. Therefore, the output voltage mean value was labeled with green, whereas the values of all the other harmonics should be observed on the right-hand side axis colored in brown.



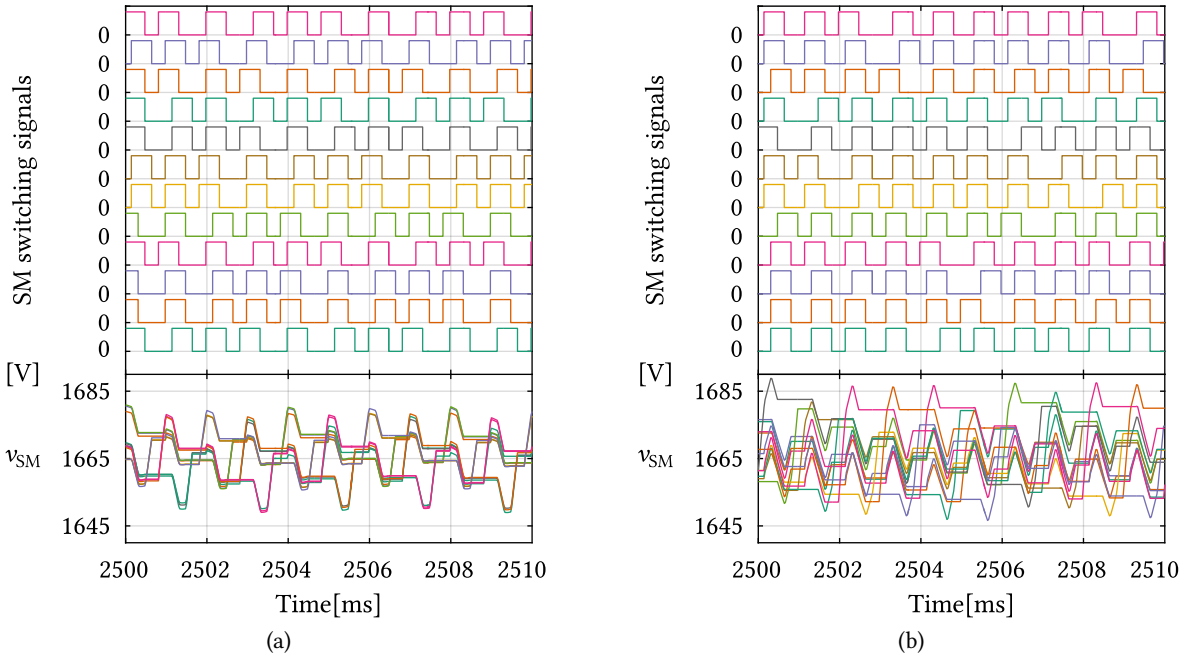


**Fig. 6.23** Both MMCs SM switching signals (the top-most plots) followed by the SMs' voltages (the bottom-most plots) over ten operating periods of the converter. It is noteworthy that every SM, irrespective of the power unit being observed, operates with the fundamental frequency switching. SMs' voltage ripples fall in the band chosen during the SM capacitance sizing, which confirms the validity of the provided sizing rule. (a) MMC<sub>1</sub> lower branch of phase A SM switching signals and voltages; (b) MMC<sub>2</sub> lower branch of phase A SM switching signals and voltages

**Figs. 6.23(a) and 6.23(b)** present MMC<sub>1</sub> and MMC<sub>2</sub> SM switching signals along with the SMs' voltages in the lower branch of phase A over ten operating periods. As can be seen from the bottom most plots, SMs' voltages mean value corresponds to the theoretical calculation  $\overline{v_{SM}} = V_{in}/2N = 1.67\text{kV}$ . As the SM capacitance deviations were randomly distributed throughout the model, SMs' voltages are not identical, nevertheless, they are balanced, which confirms the robustness of the proposed balancing algorithm. Peak-to-peak ripple of MMC<sub>2</sub> SMs equals  $\Delta v_{SM} \approx 40\text{V}$ , thus confirming the validity of the sizing method provided in **Sec. 6.3.4**. Last but not least, actions of the voltage balancing controller, observed through the switching signals reshuffling, can be observed. Each of the SMs within both MMCs switches at fundamental operating period, which is easy to verify by visual inspection of the top-most plots in the above figures.

## 6.6 System control under faulty operating conditions

The main convenience provided by a bipolar DC grid lies within its redundancy in case either of the DC poles happens to be lost. On these terms, the MMC being connected to the faulty DC pole gets safely isolated from the rest of the circuit, whereas the other one continues to supply the load with half the rated power. Consequently, such an operation mode can be referred to as the derated operating mode. Additionally, if either of the DC poles is lost, the 3PH voltage system can not be created on the LV side, therefore the converter operates as the 1PH-DAB, as will be shortly demonstrated.

### 6.6.1 Negative DC pole outage

**Fig. 6.24** depicts the way the converter operates in case the negative DC pole is lost. Under such a scenario, SMs of the lower MMC do not receive any switching signals, meaning that an SMs cluster can be modeled as presented in the figure bellow. In case a short circuit occurs across the negative DC pole and the neutral point (conductor), it can be supplied with energy by  $T_2$  S-winding (through the bypass diodes of MMC<sub>2</sub> SMs). As no voltage is generated by MMC<sub>2</sub>, its branch inductors block  $T_2$  primary voltage. Consequently, unreasonably high currents, threatening to destroy its SMs (more precisely, the bypass diodes), can be generated unless additional measures are taken. Therefore, ensuring zero voltage across  $T_2$  S- winding, while continuing to supply the load from the healthy DC pole, represents the main control objective for the analyzed case.

Since 1PH voltages need to be generated at both converter stages, there is a possibility to operate the SSC legs *B* and *C* in parallel. On these terms,  $T_1$  secondary current splits equally parts between these two legs. Consequently, no magnetic flux (field) is created through the  $T_2$  P-winding. Operation of two SSC legs, being a part of the 3PH DAB, in parallel has already been studied with the aim of performing the advanced triangular modulation schemes [140]. Nevertheless, in this case, the SSC supplies  $T_1$  P-winding with 50% duty cycle square-wave voltages despite the other modulation methods being feasible to implement. To control the power flow, phase shift control principles are retained meaning that the control block diagram presented in **Fig. 6.14** remains valid.

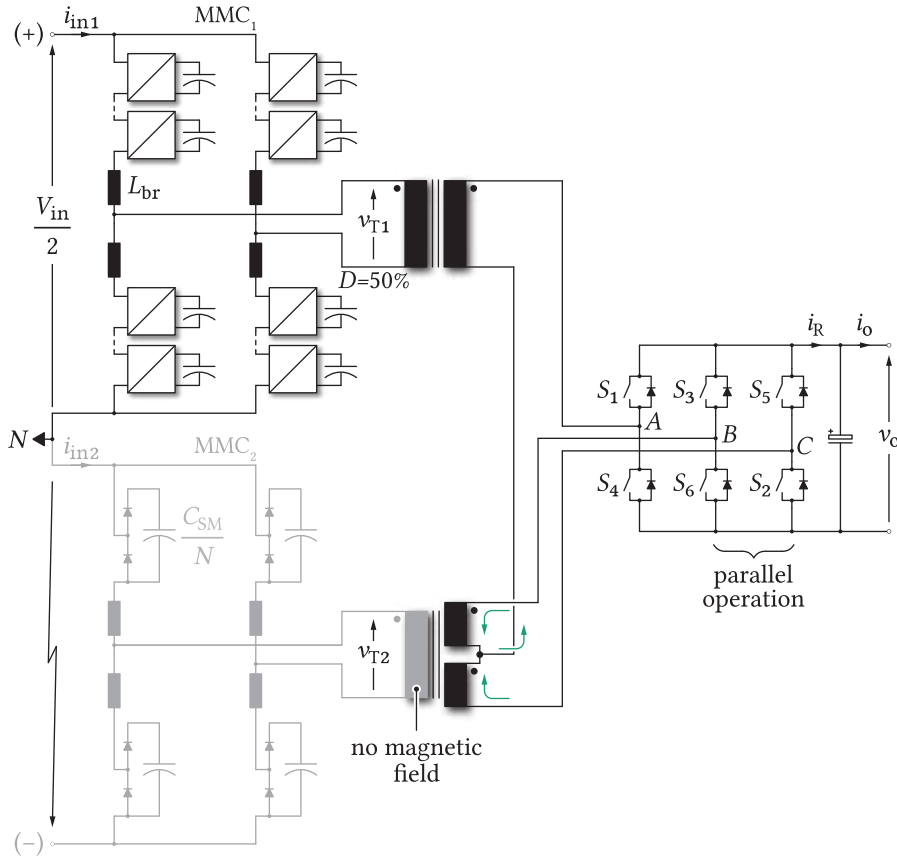


**Fig. 6.24** Converter operation in case the negative DC pole is lost

Further, operating principles of the 1PH DAB, with 50% duty cycle square voltages, allow for the energy transfer with the higher transformer voltage RMS when compared to the case analyzed in **Sec. 6.4** (i.e. normal operating conditions). Therefore, branch currents get reduced compared to the normal operating mode, meaning that SMs' voltage/current ratings are not to be exceeded, as will be displayed in the next section.

During the previous analysis, two assumptions were tacitly adopted so that equal current split between  $T_2$  S- windings could be claimed. Firstly, the SSC legs  $B$  and  $C$  must be switched on/off simultaneously. Secondly, the STC secondary impedances must be identical. It is noteworthy that the parallel operation of the SSC  $B$  and  $C$  legs represents a very idealized operating scenario since simultaneous switching of two separate legs tends to be practically unlikely. A mismatch in the legs' switching instants, denoted by  $T_\Delta$ , creates short term voltage pulses across  $T_2$  P- winding. Notwithstanding,  $MMC_2$  branch currents of significant amplitude can not be created during such short voltage pulses (e.g.  $1\mu s$ ). For that reason, delivering half the rated power to the LV side (or vice versa) can be maintained without jeopardizing the  $MMC_2$ .

Another subject relevant to the operation of the MMC-based circuits concerns the balancing of SMs' voltages. In case normal operating conditions of the converter are considered, a branch voltage reference assumes "low-to-high" change in a few steps. For instance, if a random branch of  $MMC_1$  is observed, its insertion sequence is  $\{0 \Rightarrow N/4 \Rightarrow 3N/4 \Rightarrow N \Rightarrow 3N/4 \Rightarrow N/4 \Rightarrow 0\}$ , as can be seen in **Fig. 6.7**. On the contrary, 50% duty cycle operation, relevant for the current analysis, requires sharp voltage changes of every branch, being potentially harmful to the insulation of magnetic components in the converter. To alleviate potential problems related to high  $dV/dt$ , Q2L operation, implying the sequential insertion of the SMs, was thoroughly analyzed in [139] for the case of 1PH MMC-based DAB. Apart from addressing potential insulation-related issues, Q2L operation enables a simple and straightforward balancing of the SMs. Similarly to the concept presented in **Sec. 6.4.3**, different switching pulses have different contributions to the voltage rise of an observed SM. Therefore, the algorithm identical to the one presented in **Fig. 6.18** can be used. As Q2L operation will be paid special attention to in **Chap. 8**, deeper analysis on this matter will be omitted for now.

### 6.6.2 Positive DC pole outage

In case a short circuit occurs across the positive DC pole and the neutral point (conductor), similar reasoning applied to the previous case can be applied. Namely, the main control objective on these terms can be defined as the prevention of the  $T_1$  P- winding feeding the fault with energy. For that matter,  $B$  and  $C$  legs of the SSC supply  $T_2$  S-winding with 50% duty cycle square voltages, whereas leg  $A$  remains inactive. Potential of the  $T_2$  S- winding center point ( $v_{cp}$ ), with respect to the negative rail of the SSC, equals  $v_{cp} = (v_B + v_C)/2$ . Given that  $B$  and  $C$  legs operate in a complementary manner,  $v_{cp} \approx v_o/2$ . Thus, it can be concluded that bypass diodes of the switches  $S_1$  and  $S_4$  remain reverse biased at all times. Consequently,  $T_1$  features no magnetic field changes guaranteeing the safe operation in this mode. Last but not least, the voltage balancing strategy of the SMs can be retained from the previously analyzed case.

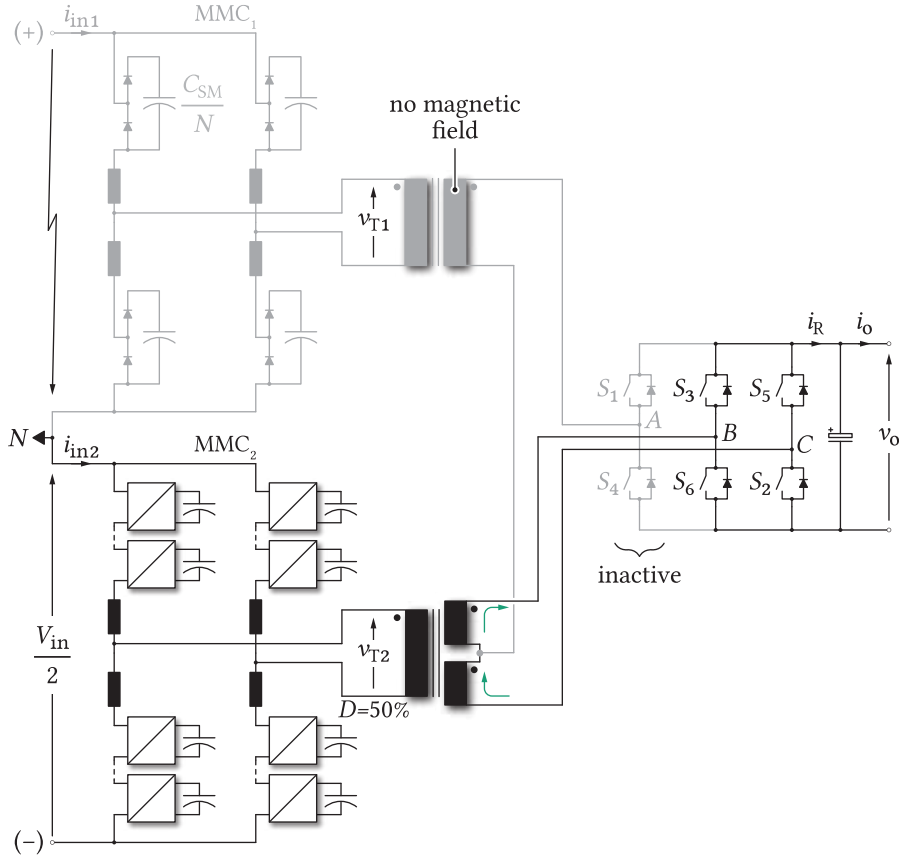


Fig. 6.25 Operation of the converter in case the positive DC pole is lost

## 6.7 Simulation results under faulty operating conditions

With the aim of providing a verification of the proposed control schemes, simulation results of the converter with parameters provided in **Tabs. 6.1** and **6.3** were performed in PLECS. To create the simulation environment which disfavors the ideal operating conditions, the STC with mismatched S-windings' impedances was used, as presented in **Fig. 6.26**. P- and S- side inductances were set as  $L_p = 105\mu\text{H}$  and  $L_s = 7.84\mu\text{H}$ , respectively. In case of the negative DC pole being lost, mismatch in the switching instants of the SSC legs B and C was set as  $T_\Delta = 1\mu\text{s}$ .

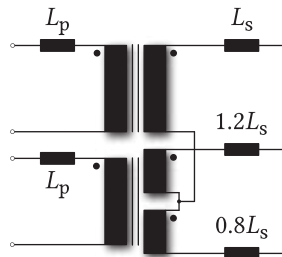
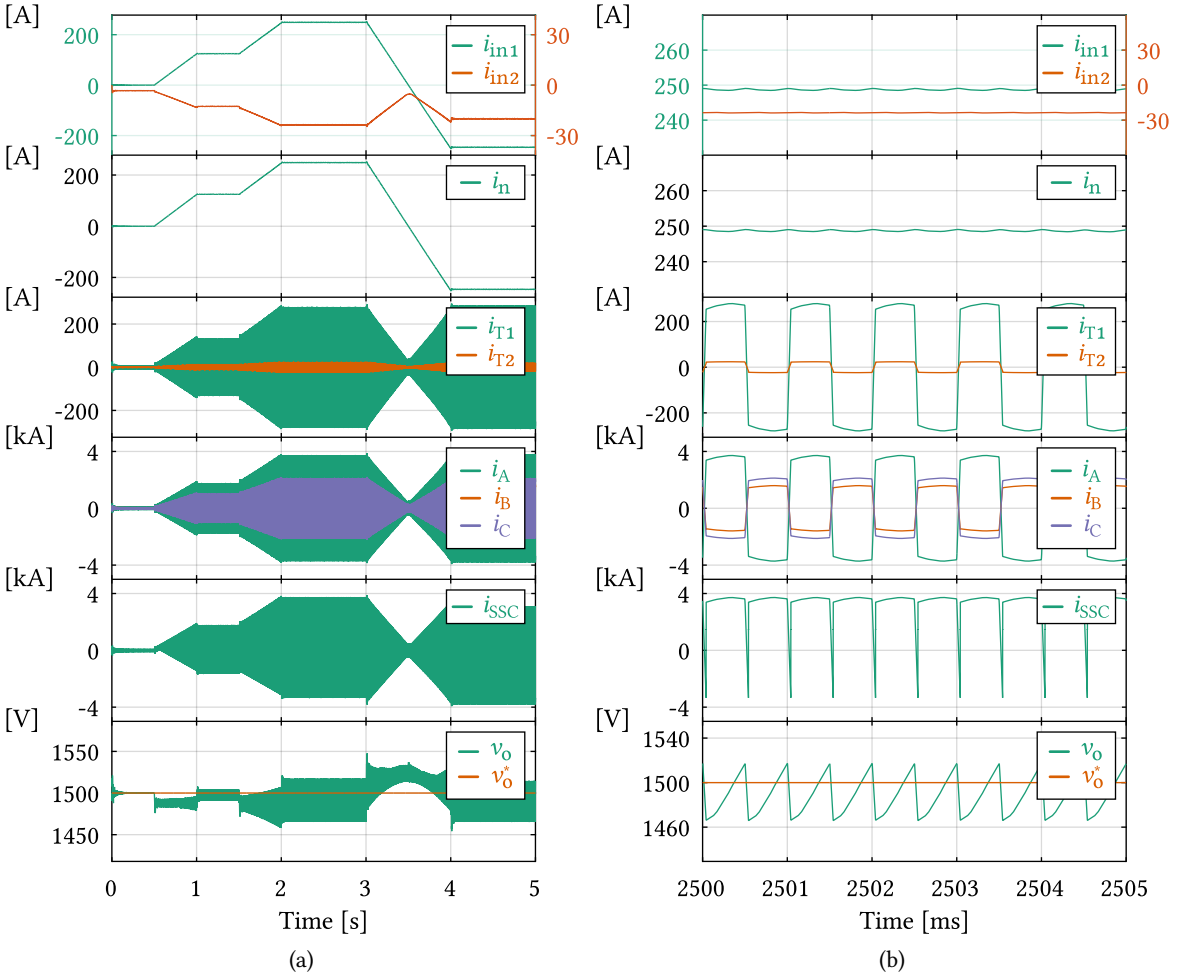


Fig. 6.26 Model of the STC used for simulation purposes

### 6.7.1 Negative DC pole outage

**Figs. 6.27(a)** and **6.27(b)** present relevant operating waveforms of the converter in case the negative DC pole is lost. To test the converter dynamic performance, the load power profile presented in **Fig. 6.19** was scaled by 1/2. As can be seen from **Fig. 6.27(a)**, the output voltage reference remains successfully tracked during the observed period, however, with half the rated power being delivered to the LV side and vice versa. **Fig. 6.27(b)** presents the converter operation during five fundamental cycles. Due to the STC S- windings' mismatches, followed by a mismatch in the switching instants of the STC B and C legs, low current can be observed in the P winding of  $T_2$ . Notwithstanding, its values fall in the range of 5% of the converter nominal current, which guarantees the safe operation under the analyzed scenario. As expected, the neutral conductor current corresponds to  $MMC_1$  input current. The SSC output current consists of the mean value along with the ripple occurring at two times the operating frequency of the converter, which is aligned with the basic operating principles of the 1PH DAB.



**Fig. 6.27** Operating waveforms relevant in case the negative DC pole is lost. (a) Operation of the converter over the time frame of 5s; (b) Operation of the converter during five fundamental cycles.

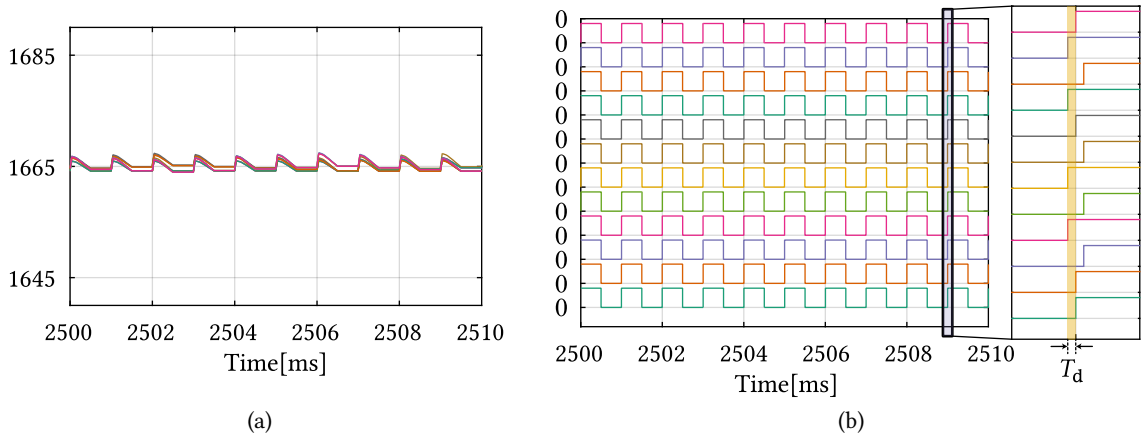


**Fig. 6.28** (a) MMC<sub>1</sub> SMs' voltages over ten fundamental cycles; (b) Switching signals passed to the lower branch of phase A of MMC<sub>1</sub>

By looking at the bottom-most plot from **Fig. 6.27(b)**, one can notice that the output voltage peak-to-peak ripple got increased when compared to the case assuming normal operating conditions. This is a consequence of the STC model used in the case analyzed at the moment. Namely, the STC leakage inductance was considered negligible during the analyses conducted in **Secs. 6.4** and **6.5**, whereas its inclusion into the analysis results in an increased STC currents for the same power transferred through any of its transformer units. Nevertheless, these differences do not corrupt the correctness of the results presented so far.

Given that the switching signals are withdrawn from the MMC<sub>2</sub>, **Fig. 6.28(a)** presents the SMs' voltages in the lower branch of MMC<sub>1</sub> phase A over ten fundamental cycles. As can be seen from **Fig. 6.28(a)**, SMs' voltages remain balanced around the mean value equal to  $\overline{v_{SM}} = V_{in}/2N$ , whereas the fundamental switching frequency of the SM remains achievable, as presented in **Fig. 6.28(b)**. As it has already been stated, SMs of the MMC-based DAB do not get inserted/bypassed simultaneously, implying the Q<sub>2</sub>L operation. From **Fig. 6.28(b)**, one can easily spot the shifts, labeled with  $T_d$ , in the time instants different SMs receive the insertion signals. In the presented case  $T_d = 2.5\mu s$ .

### 6.7.2 Positive DC pole outage

**Figs. 6.29(a)** and **6.29(b)** present relevant operating waveforms of the converter in case the positive DC pole is lost. As explained in **Sec. 6.6.2** MMC<sub>1</sub> remains isolated from the rest of the circuit, which can be concluded given that its input current equals zero during the whole simulation period. Consequently, the SSC B and C leg currents can be connected through the expression  $i_B = -i_C$ . As for the SSC output current along with the output voltage, conclusions identical to the ones drawn in **Sec. 6.7.1** can be made.

**Fig. 6.30(a)** presents MMC<sub>2</sub> voltages over ten fundamental cycles. As can be seen, the voltage balance is successfully maintained by the employed balancing algorithm, whereas SMs' voltage ripple remains within the boundaries defined in **Sec. 6.3**. **Fig. 6.30(b)** presents switching signals passed to the lower branch of MMC<sub>2</sub> phase A, from where fundamental switching frequency can easily be confirmed.

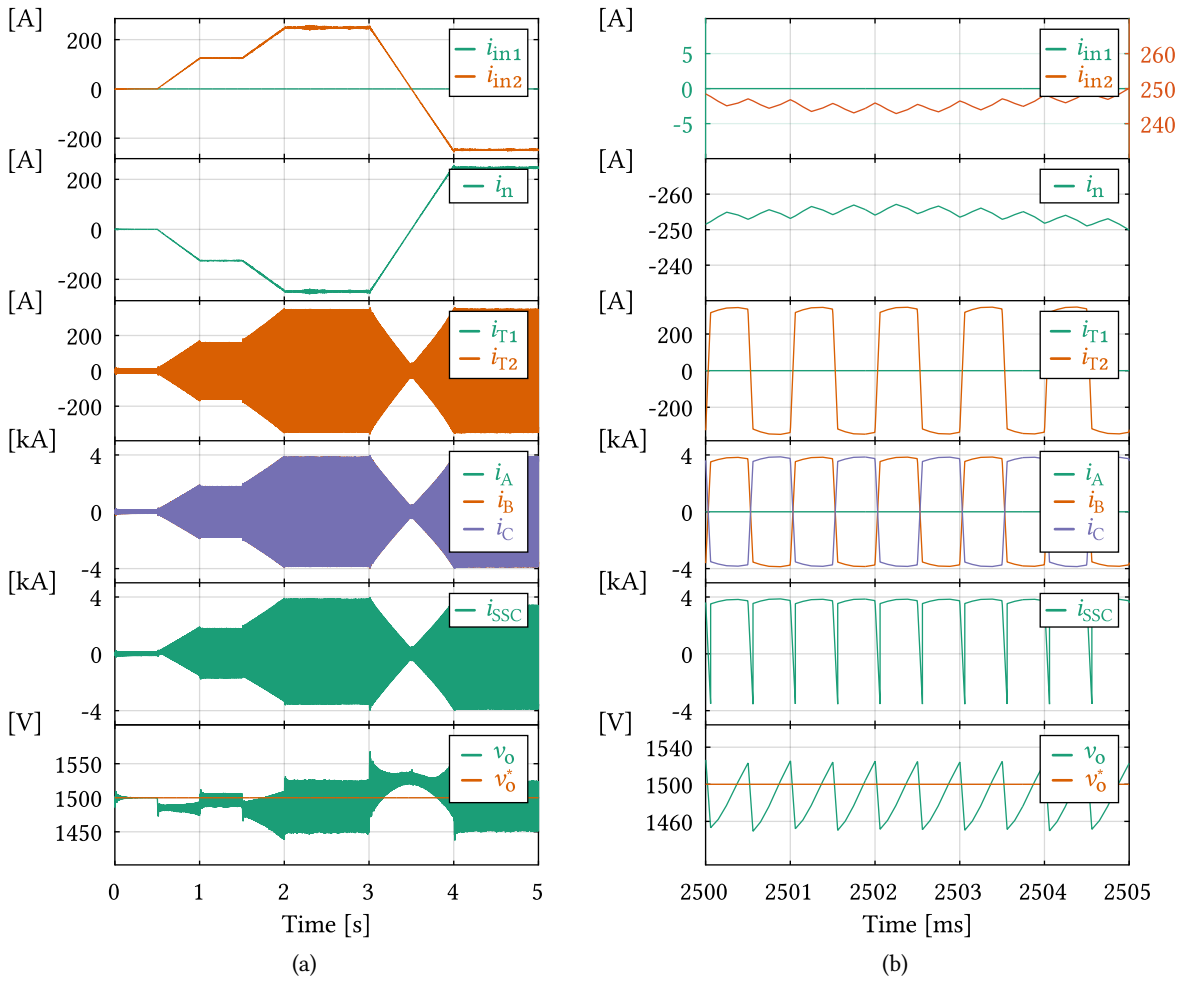


**Fig. 6.29** Operating waveforms relevant in case the positive DC pole is lost. (a) Operation of the converter over the time frame of 5s; (b) Operation of the converter during five fundamental cycles.

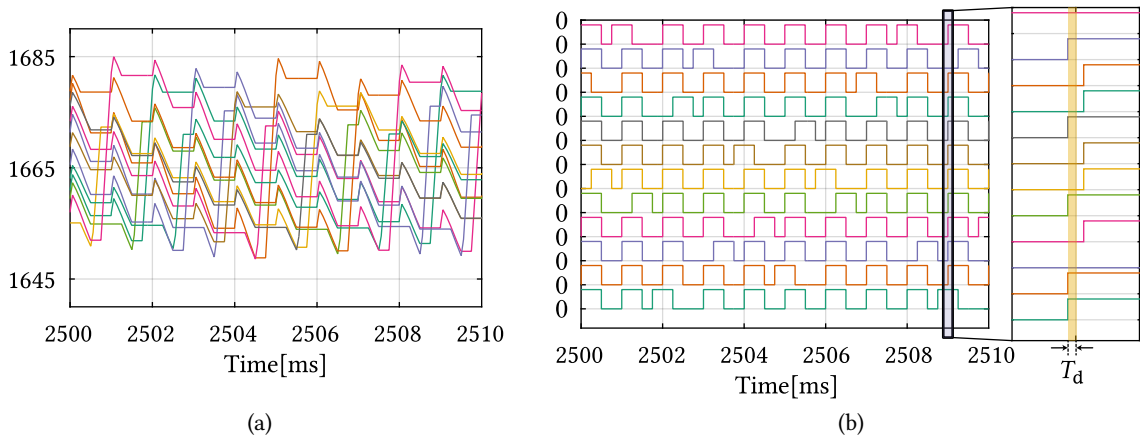


**Fig. 6.30** (a) MMC<sub>2</sub> SMs' voltages over ten fundamental cycles; (b) Switching signals passed to the lower branch of phase A of MMC<sub>2</sub>

## 6.8 Closing discussion

Throughout this chapter, a novel high power MMC-based DC-DC converter utilizing the STC was presented. As the use of the conventional SSC was proposed, routing of the energy in both directions is viable. Moreover, the use of two MMCs in the HV/MV stage allows for the redundancy, naturally offered in bipolar grids, to be exploited in case a suitable control scheme is applied under the faulty operating conditions. On these terms, a healthy part of the converter can continue to supply the load with half the rated power. Part of the converter being under fault (whether the DC pole of a bipolar grid is lost or one of the MMCs malfunctions) get isolated from the rest of the circuit by proper control tactics.

The key innovative step of the presented work refers to the unprecedented use of the STC in the domain of high power DC-DC conversion. So far, the STC has been used in the railway applications (line frequency operation), however, the operating frequency push towards the medium frequency range is proposed, following the modern power electronics trends.

Even though the energy can be routed in both directions, certain applications might not require such a feature. Therefore, modifications of the LV stage open the doors for new topologies requiring different analysis and control approach, which is exactly the topic of the next chapter. Moreover, removal of the LV stage allows a bipolar DC grid to be connected to an arbitrary 3PH load or even a conventional 3PH grid.



# 7

## High Power Unidirectional DC-DC Converter Utilizing Scott Transformer Connection

*The topic being discussed throughout this chapter concerns the high power, unidirectional, isolated, DC-DC converter intended to act as an interface between a high/medium voltage bipolar DC grid (or two separate DC grids) and another DC grid of an arbitrary voltage level. To achieve galvanic isolation, along with voltage matching, Scott transformer connection is employed. Furthermore, the medium frequency operation of the isolation stage is considered, leading to an increase in the converter's power density. The proposed converter combines two series connected single-phase modular multilevel converters on the high/medium voltage side and the conventional three-phase diode rectifier, on the low voltage side, through the Scott transformer connection operated in the medium frequency range.*

### 7.1 Topology derivation

Throughout the previous chapter, the high power bidirectional DC-DC converter utilizing the STC to provide galvanic isolation between two conversion stages was analyzed. As depicted in **Fig. 6.5**, handling the HV/MV across one of the converter ports can be ensured by employing two series connected 1PH MMCs, whereas the use of the conventional SSC was proposed on the LV side. Such a configuration enables bidirectional energy flow, which might not be required within a certain span of applications.

Consequently, modification of either of the converter stages becomes possible. In case the energy flow is assumed from the HV/MV towards the LV side, the conversion stage employed on the right-hand side of **Fig. 6.5** can be simplified. Namely, the SSC can be replaced by the conventional 3PH DR, which leads to the structure presented in **Fig. 7.1**. Such an adaptation of the LV stage discloses a new set of possibilities related to the converter operating principles, as will be discussed in the forthcoming sections.

With respect to the topology discussed in **Chap. 6**, two differences, apart from replacing the STC with the 3PH DR, can be observed. Firstly, instead of utilizing a capacitive filter on the LV side, second order *LC* filter is used. Secondly, the inductors belonging to two branches within the same MMC leg are coupled such that canceling of the AC fluxes is achieved. As a result, equivalent inductance seen from both transformers' P- windings gets reduced, the benefit of which will be clarified in the next section. Similarly to the topology illustrated in **Fig. 6.5**, HB SMs can be used in both MMCs. Also, the use of the STC combined with two 1PH MMCs preserves the possibility to continue the operation in case either of the DC poles or the MMCs is lost.

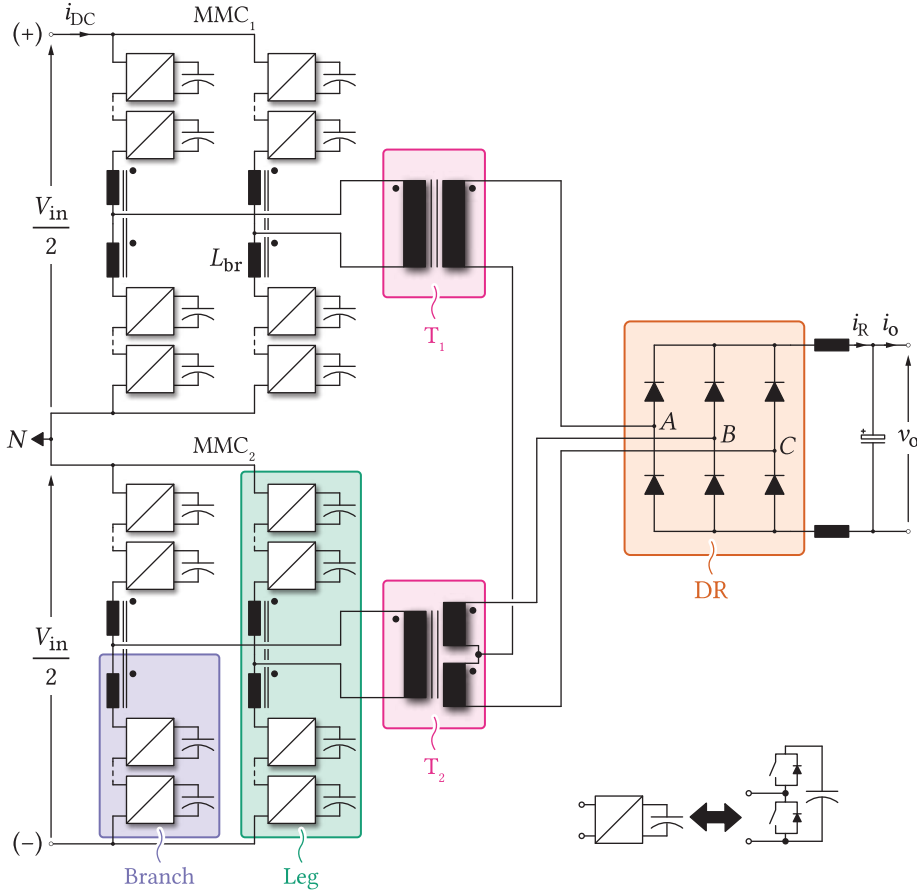


**Fig. 7.1** Modification of the topology analyzed in the previous chapter with the aim of providing the means for unidirectional power transfer. Two MMCs in the FB configuration are used in order to interface the HV/MV bipolar grid. By virtue of the STC, galvanic separation between two grids of the analyzed types is achieved. Considering that the converter is intended to provide the means for unidirectional power flow, 3PH DR is employed in the LV stage, which represents the key difference when compared to the converter depicted in Fig. 6.5.

Basic operating principles, supported by the elementary equations, of the STC were explained in **Chap. 6**. Therefore, the reader is encouraged to refer to **Sec. 6.2.2** in case any additional support on this matter is required.

## 7.2 Preliminary considerations

**Fig. 7.2** presents the equivalent circuit of the 1PH MMC where clusters of SMs were replaced with the ideal voltage sources, which is the modeling approach already adopted in **Chap. 2**. Additionally, the branch inductors belonging to the same leg are coupled, therefore, mutual inductance is denoted by  $L_m$ . Two loops according to the KVL, labeled with green and brown, can be formed, leading to (7.1) and (7.2), where subscripts "p" and "n" denote the upper and the lower branch quantities, respectively.

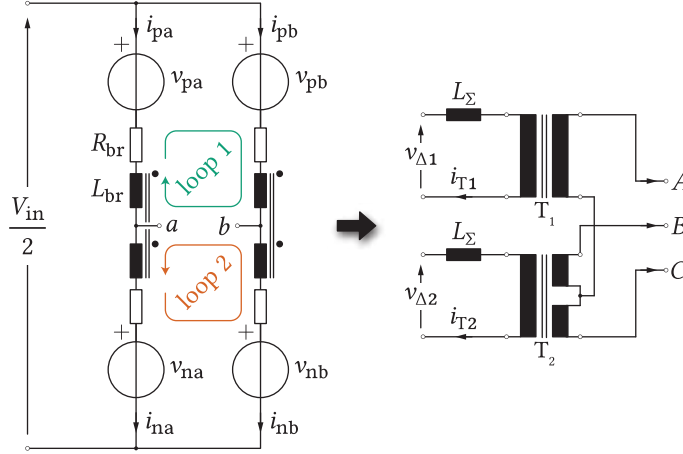


**Fig. 7.2** Equivalent circuit of the 1PH MMC (left); The STC with two 1PH MMCs being connected to its P-windings (right);

$$v_{ab} = v_{pb} - v_{pa} + L_{br} \frac{di_{pb}}{dt} + R_{br} i_{pb} - L_{br} \frac{di_{pa}}{dt} - R_{br} i_{pa} - L_m \frac{di_{na}}{dt} + L_m \frac{di_{nb}}{dt} \quad (7.1)$$

$$v_{ab} = v_{na} - v_{nb} + L_{br} \frac{di_{na}}{dt} + R_{br} i_{na} - L_{br} \frac{di_{nb}}{dt} - R_{br} i_{nb} + L_m \frac{di_{pa}}{dt} - L_m \frac{di_{pb}}{dt} \quad (7.2)$$

Summing (7.1) and (7.2), while keeping in mind that  $i_{ab} = i_{pa} - i_{na} = i_{nb} - i_{pb}$ , yields

$$v_{ab} = \frac{v_{na} - v_{pa}}{2} + \frac{v_{pb} - v_{nb}}{2} - \underbrace{(L_{br} - L_m)}_{L_{\sigma}} \frac{di_{ab}}{dt} - R_{br} i_{ab} \quad (7.3)$$

One can notice that (7.3) can be further reduced in case the adjacent MMC legs operate in a complementary manner. As highlighted in (7.1) and (7.2), leg "b" voltages can be set as  $v_{pb} = v_{na}$  and  $v_{nb} = v_{pa}$ , which finally provides

$$v_{ab} = \underbrace{v_{na} - v_{pa}}_{v_{\Delta}} - L_{\sigma} \frac{di_{ab}}{dt} - R_{br} i_{ab} \quad (7.4)$$

Consequently, seen from its AC terminals, a 1PH MMC can be represented with the serial connection of an ideal voltage source ( $v_{\Delta}$ ) and the equivalent MMC branch inductance  $L_{\sigma} = L_{br} - L_m$ , as presented on the right-hand side of **Fig. 7.2**. In case the inductors coupling factor is denoted by  $k$ , then  $L_{\sigma} = (1 - k)L_{br}$ . Sum of the STC leakage inductance and the equivalent MMC branch inductance was denoted by  $L_{\Sigma}$ . If the STC leakage inductance can be considered negligible with respect to the equivalent MMC branch inductance, then  $L_{\Sigma} \approx L_{\sigma}$ . However, such an assumption does not affect the generality of the results presented henceforward. In order to establish a basic structure underlying the upcoming system control-related discussions, the behavior of the STC S-side quantities needs to be investigated.

Ampere-turns balance equations can be set for both transformer units, leading to (7.5). This equation has already been derived in **Sec. 6.4.1**, nevertheless, it is repeat at this point for the sake of completeness.

$$\begin{bmatrix} i_A \\ i_B \\ i_C \end{bmatrix} = \begin{bmatrix} m_{T1} & 0 \\ -m_{T1}/2 & m_{T2} \\ -m_{T1}/2 & -m_{T2} \end{bmatrix} \begin{bmatrix} i_{T1} \\ i_{T2} \end{bmatrix} \quad (7.5)$$

Further, the STC S-side voltage balance equations can be derived as

$$\begin{aligned} v_{AB} &= \frac{v_{\Delta 1}}{m_{T1}} - \frac{v_{\Delta 2}}{2m_{T2}} - \frac{L_\sigma}{m_{T1}} \frac{di_{T1}}{dt} + \frac{L_\sigma}{2m_{T2}} \frac{di_{T2}}{dt} \\ v_{BC} &= \frac{v_{\Delta 2}}{m_{T2}} - \frac{L_\sigma}{m_{T2}} \frac{di_{T2}}{dt} \\ v_{CA} &= -\frac{v_{\Delta 1}}{m_{T1}} - \frac{v_{\Delta 2}}{2m_{T2}} + \frac{L_\sigma}{m_{T1}} \frac{di_{T1}}{dt} + \frac{L_\sigma}{2m_{T2}} \frac{di_{T2}}{dt} \end{aligned} \quad (7.6)$$

Substitution of (7.5) into (7.6) results in (7.7), from where one can notice that the equivalent MMC branch inductance becomes transferred to the STC S-side as  $L_y^* = L_\sigma/(2m_{T2}^2)$ . Dividing the equivalent MMC branch inductance by the square of  $T_2$  turns ratio points out that the STC is indeed analyzed from its S-side. Subsequent division by two suggests that two MMCs operate in parallel observed from the STC S-side. Additionally, three equivalent line voltages ( $v'_{AB}$ ,  $v'_{BC}$  and  $v'_{CA}$ ) can be identified.

$$\begin{aligned} v_{AB} &= \underbrace{\frac{v_{\Delta 1}}{m_{T1}} - \frac{v_{\Delta 2}}{2m_{T2}}}_{v'_{AB}} - \underbrace{\frac{L_\sigma}{2m_{T2}^2} \frac{di_A}{dt} + \frac{L_\sigma}{2m_{T2}^2} \frac{di_B}{dt}}_{L_y^*} \\ v_{BC} &= \underbrace{\frac{v_{\Delta 2}}{m_{T2}}}_{v'_{BC}} - \frac{L_\sigma}{2m_{T2}^2} \frac{di_B}{dt} + \frac{L_\sigma}{2m_{T2}^2} \frac{di_C}{dt} \\ v_{CA} &= -\underbrace{\frac{v_{\Delta 1}}{m_{T1}} - \frac{v_{\Delta 2}}{2m_{T2}}}_{v'_{CA}} - \frac{L_\sigma}{2m_{T2}^2} \frac{di_C}{dt} + \frac{L_\sigma}{2m_{T2}^2} \frac{di_A}{dt} \end{aligned} \quad (7.7)$$

In case sinusoidal voltages  $v_{\Delta 1}$  and  $v_{\Delta 2}$  are created by two MMCs interfacing the bipolar grid, their complex representatives can be chosen as  $\vec{v}_{\Delta 2} = \vec{v}$  and  $\vec{v}_{\Delta 1} = j\vec{v}$ . Consequently, the equivalent voltages seen from the STC S-side ( $v'_{AB}$ ,  $v'_{BC}$  and  $v'_{CA}$ ) can be described as (7.8). In case  $T_1$  and  $T_2$  turns ratios relation (6.1) holds, expression (7.8) describes a symmetrical system of line voltages. As depicted in **Fig. 7.3**, such a system can be represented by the equivalent star of phase voltages ( $v'_A$ ,  $v'_B$  and  $v'_C$ ).

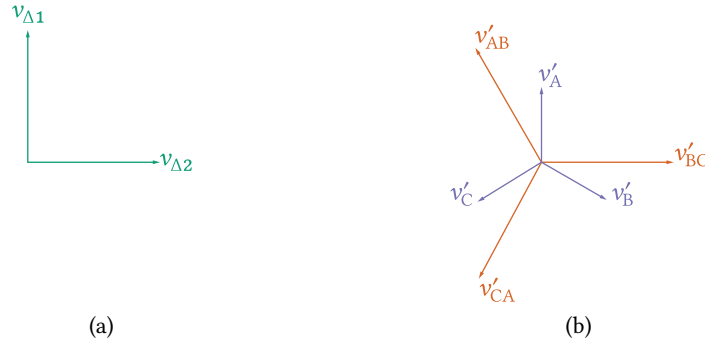


**Fig. 7.3** (a) Two AC voltages generated by the MMCs interfacing the bipolar grid; (b) Phasor diagram of an equivalent line voltage system seen from the STC S-side (brown) along with its equivalent star (purple)

$$\begin{aligned}
 \vec{v}'_{AB} &= \frac{\vec{v}}{m_{T2}} \left( -\frac{1}{2} + j\frac{m_{T2}}{m_{T1}} \right) \\
 \vec{v}'_{BC} &= \frac{\vec{v}}{m_{T2}} \\
 \vec{v}'_{CA} &= \frac{\vec{v}}{m_{T2}} \left( -\frac{1}{2} - j\frac{m_{T2}}{m_{T1}} \right)
 \end{aligned} \tag{7.8}$$

Consequently, the STC with two MMCs being connected to its P-windings can be perceived through the equivalent circuit from **Fig. 7.4**. It is straightforward to conclude that in case 3PH DR gets connected to the terminals A,B and C, no difference compared to the grid connected DR should be observed. Another remark relevant for such a case concerns the well known DR commutation process. Namely, the higher the inductance  $L_\gamma^*$ , the longer it takes for the rectifier output current to drift from one phase to another, causing the undesirable output voltage drop to get more emphasized. Consequently, the efforts should be made to reduce the equivalent inductance  $L_\gamma^*$ , which clarifies the need for coupling of the branch inductors in both MMCs.

Further, the above discussion refers to the normal operating conditions of the proposed converter. Should either of the DC poles be lost, the operation of the converter can not be analyzed by means of the equivalent circuit from **Fig. 7.4**. On these terms, the converter operates as the 1PH DR, therefore the new equivalent scheme is required, as will be discussed in **Sec. 7.3.2**.

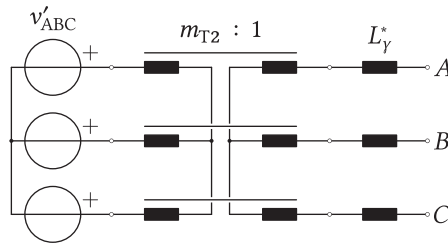


**Fig. 7.4** 3PH equivalent of the STC being connected to two 1PH MMCs acting as sinusoidal voltage sources

## 7.3 Operating principles

### 7.3.1 Normal operating conditions

Discussion on the converter operating principles will be conducted by means of the 3PH equivalent circuit from **Fig. 7.5(a)**. In other words, this section covers the converter operation with no faults, whereas the next section will address the operation with either of the DC poles or the MMCs being lost. According to **Fig. 7.3**, the presence of two 1PH sinusoidal, quadrature, voltages  $v_{\Delta 1}$  and  $v_{\Delta 2}$  across  $T_1$  and  $T_2$  P-windings, respectively, results in the symmetrical system of line voltages seen from the STC S-side ( $v'_{AB}$ ,  $v'_{BC}$  and  $v'_{CA}$ ). Further, according to (7.7) and (7.8), the magnitude of the equivalent line voltages can be calculated as (7.9), where  $m_{T2}$  and  $\hat{v}_p$  designate  $T_2$  turns ratio and voltage magnitude across both transformers' P-windings, respectively.

$$\hat{v}_s = \frac{\hat{v}_p}{m_{T2}} \quad (7.9)$$

Consequently, with the voltage drop caused by the DR commutation being temporarily neglected, the mean value of the DR output voltage equals

$$\bar{v}_R = \frac{3}{\pi} \hat{v}_s \quad (7.10)$$

Please notice that, by adjusting the magnitude of voltages generated by the MMCs, the mean value of the DR output voltage can be controlled. It is noteworthy that this represents the main difference with respect to the topology analyzed in **Chap. 6**. Namely, the converter depicted in **Fig. 6.5** relies on the **phase** modulation principles. On the contrary, the converter analyzed in this section represents an **amplitude** modulated structure.

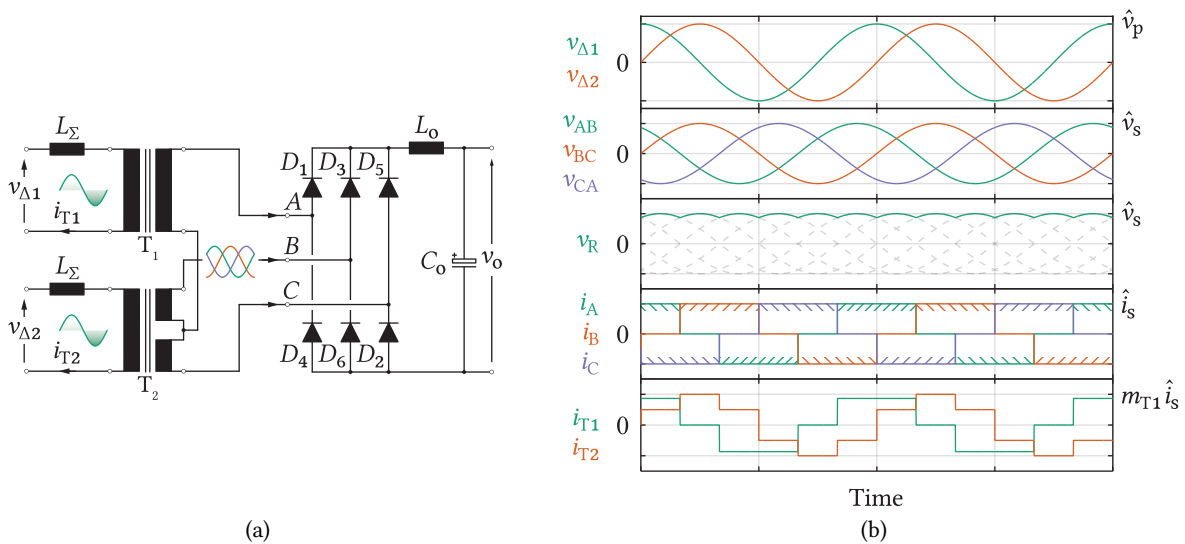


**Fig. 7.5** (a) Equivalent circuit of the analyzed converter; (b) Idealized operating waveforms

**Fig. 7.1** shows that the standard  $LC$  filter can be used to filter out the higher order harmonics from the DR output voltage. Therefore, the DR output current can be approximated by its DC component, which allows the idealized operating waveforms of the converter to be presented as in **Fig. 7.5(b)**.

To derive the complete expression for the converter output voltage mean value, 3PH DR commutation process must be taken into account. With the DR output current mean value being denoted by  $i_R$ , the output voltage of the converter can be calculated according to (7.11), where  $M$  denotes modulation index of both MMCs.

$$\bar{v}_o = \frac{3}{\pi m_{T2}} \underbrace{\left( M \frac{V_{in}}{2} \right)}_{\text{MMC AC voltage}} - \underbrace{\frac{3}{\pi} \omega L_Y^* i_R}_{\text{Commutation drop}} \quad (7.11)$$

Please notice that the higher the equivalent MMC branch inductance the higher the output voltage drop caused by the DR commutation process. However, it can be seen from (7.3) that the branch inductors coupling reduces the equivalent MMC branch inductance, thus diminishing the effect of the DR commutation process.

### 7.3.2 Operation under faults

As has been stated on a few occasions so far, malfunction of either of the DC poles (or the MMCs) causes the transition to a new, henceforth referred to as the derated, operating mode. In fact, the employment of a suitable operation scheme allows for the healthy part of the converter to continue delivering half the rated power to the LV side. Nevertheless, the transformer being connected to the faulty part of the converter must operate with no magnetic field, otherwise, bypass diodes of the faulty MMC become exposed to the risk of destruction.

Similarly to **Chap. 6**, two distinct cases, assuming the outage of the positive and the negative DC pole, respectively, will be analyzed. However, the nature of voltages generated by the MMCs in such an operating mode must be reconsidered for the reasons explained in the next few paragraphs. In case either of the MMCs gets isolated from the rest of the circuit, meaning that its switching signals are withdrawn, the symmetrical system of 3PH voltages can not be created on the STC S- side. Thus, the operation of the converter in the manner typical for the 1PH rectifier might seem logical at first glance. However, with the maximum amplitude of voltage obtained at the STC S- side being retained from the normal operating conditions, the output voltage of the 1PH rectifier equals

$$v_o^{(1ph)} = \frac{2}{\pi} \hat{v}_s \quad (7.12)$$

It is straightforward to notice, by comparing (7.12) with (7.10), that continuing the operation with sinusoidal voltage, under the faulty operating conditions, results in the output voltage drop by one third of the rated value. Despite seeming like an obstacle difficult to overcome, the above mentioned drawback can easily be addressed if the following considerations are made.

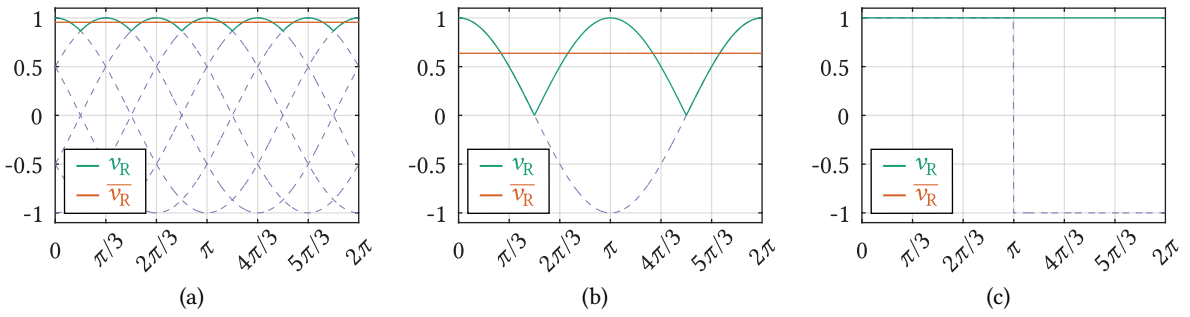


**Fig. 7.6** Voltage across the DC terminals of a DR ( $v_R$ ) along with its mean value ( $\overline{v_R}$ ); (a) 3PH DR operating with sinusoidal input voltages; (b) 1PH DR operating with sinusoidal input voltage; (c) 1PH DR operating with square input voltage

Even though the MMC was originally envisioned like a converter synthesizing sinusoidal voltages, its employment with square-alike voltages was proposed in the literature, as discussed in **Chap. 6**. As long as the energy balances are maintained throughout the MMC, an arbitrary voltage waveform can be synthesized by any of its legs. This feature can be utilized to boost the output voltage of the analyzed converter in case it operates with only one MMC being active.

In order to support the above discussion, **Figs. 7.6(a) to 7.6(c)** illustrate the voltage across the DC terminals of the 3PH DR and 1PH DRs operating with sinusoidal and square voltages, respectively. As can be seen from **Figs. 7.6(a) and 7.6(b)**, switching from 3PH to 1PH operation, while retaining the sinusoidal input voltage(s), leads to the output voltage mean value reduction by approximately 33%. However, theoretical value of the 1PH DR output voltage, obtained in case square wave input voltage is used, corresponds to the amplitude of the voltage pulse itself. Consequently, such a waveform represents a suitable choice for the derated operation mode. Please notice that the waveforms presented above do not consider the commutation process of the observed DRs.

### 7.3.2.1 Negative DC pole outage

**Fig. 7.7** presents operation of the converter from **Fig. 7.1** in case the negative DC pole is lost. On these terms, MMC<sub>1</sub> supplies its associated transformer with square-wave, 50% duty cycle, voltage. In case the STC S- side leakage inductances are equal,  $T_1$  S- winding current splits in two equal parts, meaning that legs *B* and *C* of the 3PH DR operate in parallel. Consequently, the analysis of this operating mode can be performed based on a simple circuit depicted in **Fig. 7.8(a)**, where general notation of currents, voltages and impedances was adopted given that the very same circuit will be reused. Namely, in the case relevant for the ongoing analysis,  $L_{p\Sigma}$  corresponds to the  $T_1$  P- winding inductance summed with the equivalent inductance seen from the AC terminals of MMC<sub>1</sub>. Further,  $L_{s\Sigma} = 3L_s/2$ , where  $L_s$  denotes the STC S- winding inductance.

In case the output filter is sized properly, while assuming the continuous conduction mode of the DR, it can be replaced with an ideal current source. Hence, the waveforms characterizing the circuit from **Fig. 7.8(a)** can be found in **Fig. 7.8(b)**. Superscripts "p" and "s" denote any of the quantities observed from either P- or S- side, respectively.



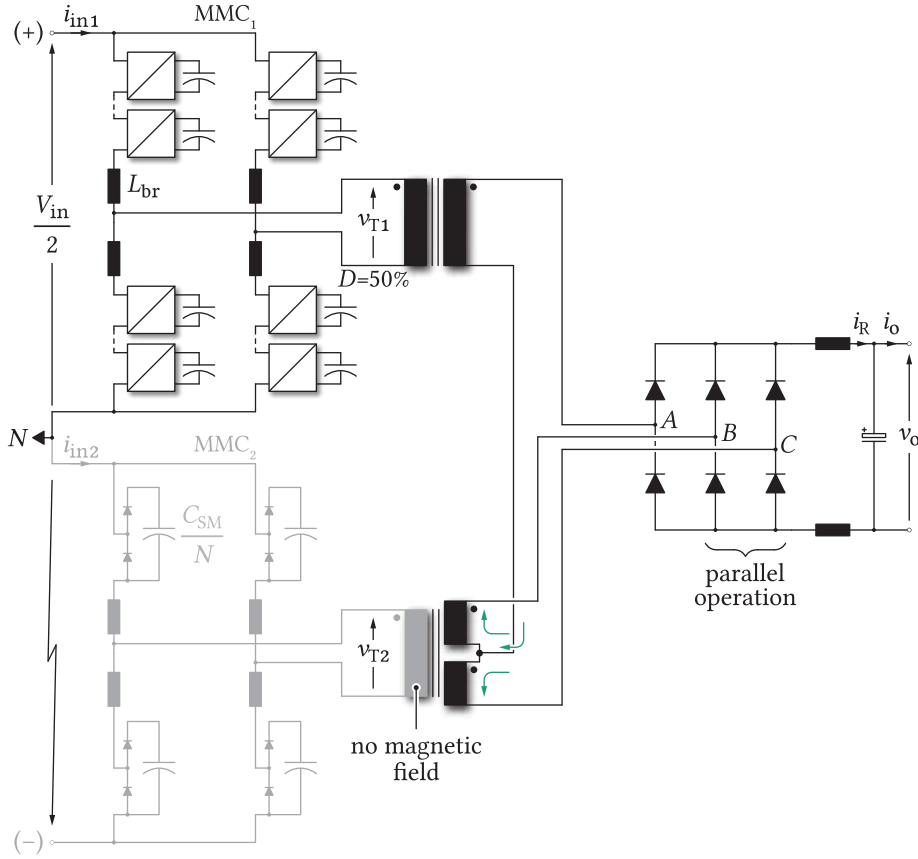


**Fig. 7.7** Operation of the analyzed converter in case the negative DC pole is lost

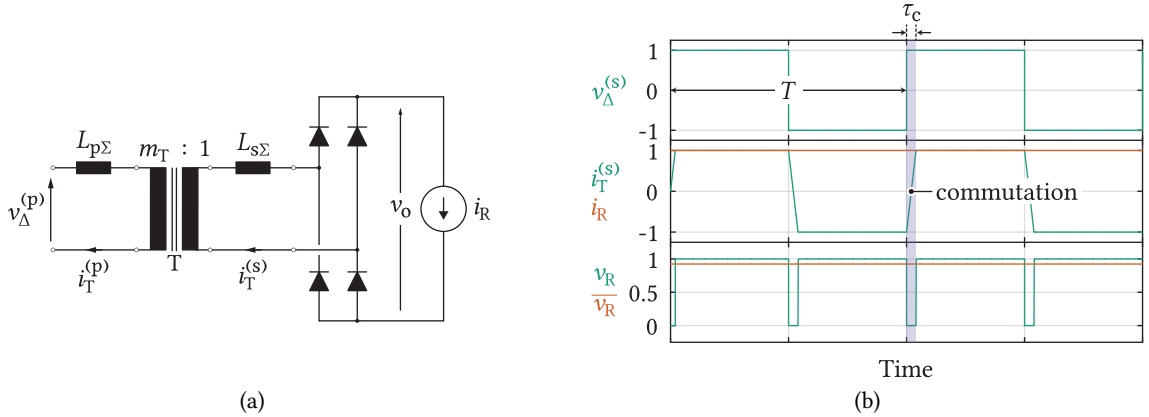


**Fig. 7.8** (a) Equivalent circuit describing the converter depicted in **Fig. 7.7**; (b) Idealized operating waveforms of the circuit on the left. Presented voltages and currents were normalized by adopting the base values as  $\max(v_{\Delta}^{(s)})$  and  $\max(i_R)$ , respectively.

From **Fig. 7.8(b)**, it can be seen that a fraction of the fundamental operating period, labeled with  $\tau_c$ , during which the transformer current changes its direction, requires all the diodes within the equivalent bridge to be turned on. Consequently, the rectifier output voltage drops to zero.

The above mentioned transition is well recognized as the 1PH DR commutation process. Duration of the commutation process affects the mean value of the load voltage, therefore, its minimization justifies the coupling of the MMC branch inductors, as mentioned in **Sec. 7.2**. Seen from the transformer's S-side, the commutation process can be described in a generalized form as

$$\frac{v_{\Delta}^{(p)}}{\overbrace{m_T}^{v_{\Delta}^{(s)}}} = \underbrace{\left( L_{s\Sigma} + \frac{L_{p\Sigma}}{m_T^2} \right)}_{L_c} \frac{di_T^{(s)}}{dt}, \quad (7.13)$$

from where (7.14) can be established

$$\tau_c v_{\Delta}^{(s)} = 2L_c i_R \quad (7.14)$$

Analysis of the bottom-most plot from **Fig. 7.8(b)** reveals that the term  $\tau_c v_{\Delta}^{(s)}$  from the above equation actually corresponds to the output voltage drop caused by the commutation process, which is easy to confirm from (7.15).

$$\begin{aligned} \overline{v_R} &= v_{\Delta}^{(s)} - \frac{2}{T} \tau_c v_{\Delta}^{(s)} \\ &= \frac{v_{\Delta}^{(p)}}{m_T} - \frac{2\omega L_c i_R}{\pi} \end{aligned} \quad (7.15)$$

In the above equation, the term  $v_{\Delta}^{(s)}$  represents MMC<sub>1</sub> AC voltage divided by T<sub>1</sub> turns ratio. As the maximum value of the AC voltage generated by a 1PH MMC corresponds to the voltage across its DC terminals (under the assumption of the MMC branches being charged to this voltage), (7.15) can be rewritten as (7.16), where  $P_o$  and  $v_o^*$  denote the output power and the reference value of the output voltage, respectively. Similarly to (7.11),  $M$  denotes the modulation index, however, in this case, it provides an information on the amplitude of the square-wave generated by the joint actions of two MMC legs.

$$\overline{v_R} = M \frac{V_{in}}{2m_{T1}} - \frac{2\omega L_c P_o}{\pi v_o^*} \quad (7.16)$$

From (7.16), one can easily conclude that as long as  $0 \leq M \leq 1$ , the DR output voltage can be adjusted with the aim of controlling the converter output voltage  $v_o$ . Therefore, the amplitude modulation principles are retained, nevertheless, with the MMC AC voltage reference being changed with respect to the case analyzed in **Sec. 7.3.1**.

### 7.3.2.2 Positive DC pole outage

**Fig. 7.9** present the case with a short circuit occurring between the positive DC pole and the neutral point (conductor). To prevent the SMs of MMC<sub>1</sub> from discharging through the fault impedance, its switching signals are withdrawn. On the other hand, MMC<sub>2</sub> supplies its transformer unit with the square-wave, 50% duty cycle, voltage, meaning the circuit continues to operate as the 1PH rectifier. Moreover, in case the STC S- side inductances are equal, no current flows through the DR phase A, leaving T<sub>1</sub> with no magnetic field. Consequently, MMC<sub>1</sub> is not jeopardized.

Analysis of the converter presented bellow can be performed based on the circuit presented in **Fig. 7.8(a)**, where  $L_{p\Sigma}$  corresponds to the sum of the equivalent inductance seen from the AC terminals of MMC<sub>2</sub> and T<sub>2</sub> P- winding inductance. Moreover,  $L_{s\Sigma} = 2L_s$  since effectively two windings of the STC operate in series on its S- side. Mean value of the DR output voltage can be derived similarly to (7.16). By replacing  $m_{T1}$  from (7.16) with  $m_{T2}$  along with keeping in mind that  $L_c = L_{\Sigma p}/m_{T2}^2 + 2L_s$ , yields

$$\overline{v_R} = M \frac{V_{in}}{2m_{T2}} - \frac{2\omega L_c P_o}{\pi v_o^*} \quad (7.17)$$

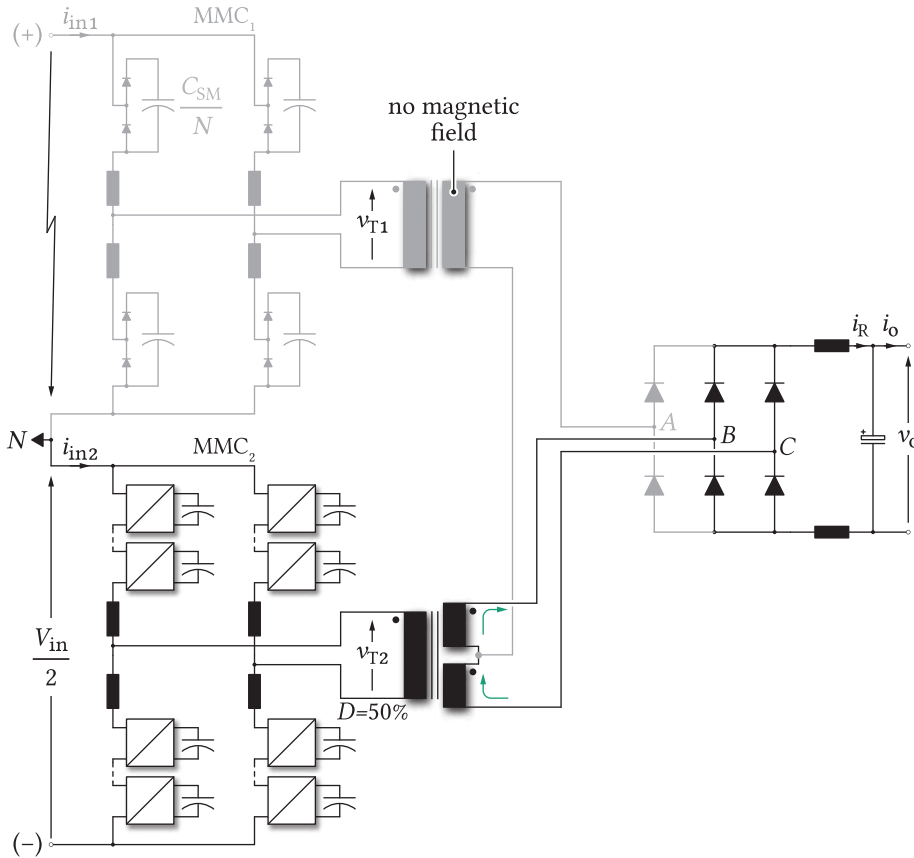


**Fig. 7.9** Operation of the analyzed converter in case the positive DC pole is lost

Expression (7.17) indicates that the structure presented **Fig. 7.9** relies on the amplitude modulation principles. By adjusting the modulation index  $M$ , which determines the amplitude of the square-wave generated by MMC<sub>2</sub>, the output voltage  $v_o$  can be controlled, as will be explained in one of the upcoming sections.

It is worthy of remark that both configurations presented in **Figs. 7.7** and **7.9** represent 1PH rectifiers by their essence. Consequently, the output voltage, and inherently current, oscillations occur at two times the operating frequency of the converter. For that matter, faulty operating modes can be thought of as the most critical when it comes to sizing of the  $LC$  filter employed in the LV stage.

### 7.3.3 Modulation considerations

In **Sec. 7.2**, a parallel between the converter being the subject of this chapter and the grid connected DR was drawn. Consequently, the highest priority task of the MMCs employed on the HV/MV side is to provide the STC S- windings with high fidelity sinusoidal voltages. As demonstrated in **Chap. 5**, the position of the branches' switching instants affects the quality of voltages seen from both AC and DC terminals of an MMC. To provide the reader with an insight into the modulation possibilities offered by the converter analyzed in this chapter, let one observe an MMC with  $N = 4$  SMs per branch. For the demonstration purposes, PSC modulation, with carrier frequency equal to  $f_c = 150\text{Hz}$  is used. Notwithstanding, the use of all the modulation methods, being available for the MMC, is not constrained by the following discussion.

In case a 1PH MMC is observed, its equivalent AC voltage, previously denoted by  $v_\Delta$ , results from the joint action of four converter branches. According to **Chap. 5**, misaligning the carrier sets modulating two adjacent branches, belonging to the same phase-leg, enables the improvement of the leg AC voltage quality at the price of amplifying the undesired harmonics observed in its DC voltage. In contrast to the case analyzed in **Chap. 5**, where paralleled SBRs were considered, any of the MMCs from **Fig. 7.1** operates with two phase legs in series seen from its AC terminal. Such a statement can also be confirmed from (7.4), which suggests that  $v_\Delta = v_{sA} - v_{sB}$ , where  $v_{si}$  denotes the AC voltage component of the leg  $i \in \{A, B\}$ . As a result, similar reasoning to the one derived in **Chap. 5** can be followed.

Let the analysis commence by denoting the shift between two carrier sets modulating two adjacent branches, belonging to the same leg, with  $\beta$ . The angle displacement between the carrier sets modulating two neighboring legs will be denoted by  $\delta$ . From a leg AC voltage standpoint, keeping the carrier sets, modulating two of its branches, aligned provides up to  $N + 1$  voltage levels, as presented in **Chap. 5**.

**Fig. 7.10(a)** illustrates such a case. For instance, the branches belonging to the leg  $A$  change their states at the same time. Due to the symmetry of references in the leg  $B$ , being a consequence of a complementary operation of the observed legs, all of the branches within an observed MMC change their state at the same time. Indeed  $N + 1$  voltage levels can be observed across the AC terminals of such a converter, as can be confirmed from the bottom-most plot of **Fig. 7.10(a)**. Further improvement in the AC voltage quality, presented in **Fig. 7.10(b)**, can be achieved through the proper setting of the displacement between the carrier sets on the leg level. In case the number of SMs per branch is even, choosing  $\beta = \pi/N$  causes two branches belonging to the same leg to switch at different time instants. Consequently, every leg of the analyzed converter creates up to  $2N + 1$  voltage levels.

Again, due to the symmetry of references, while retaining the identical setting of the lower and the upper carrier group, the other leg changes its state at the very same time instants. As a result, the number of voltage levels generated by a 1PH MMC equals  $2N + 1$ . Finally, the inclusion of an additional phase shift between the carriers sets modulating the legs  $A$  and  $B$  causes the legs to switch at different time instants. In case  $N$  is even, while  $\beta = \pi/N$  along with  $\delta = \pi/2N$ , the number of observed voltage levels increases to  $4N + 1$ , as can be seen from **Fig. 7.10(c)**.

It worth stressing that the case presented in **Figs. 7.10(a) to 7.10(c)** utilizes the number of SMs per branch which is very likely to be higher in the HV/MV applications. Thus, high fidelity voltage waveforms can be synthesized in case  $4N + 1$  modulation is used. Also, angular shifts discussed above remain valid in case the number of SMs per branch is even. In case  $N$  is odd, the methodology derived in **Chap. 5** can be recalled to derive proper values of these angles ( $\beta = 0$  and  $\delta = \pi/2N$ ). Last but not least, AC voltage improvement of an MMC occurs at the expense of hindering the quality of its DC voltage, labeled with  $v_c$  in the bellow figure. However, the coupling of the branch inductors, in the manner presented in **Fig. 7.1**, increases the equivalent inductance seen from the DC terminals of the MMC. Consequently, MMC input current ripple, potentially caused by the discussed modulation choice, can be successfully suppressed by the proper sizing of the leg inductances and their coupling factors.

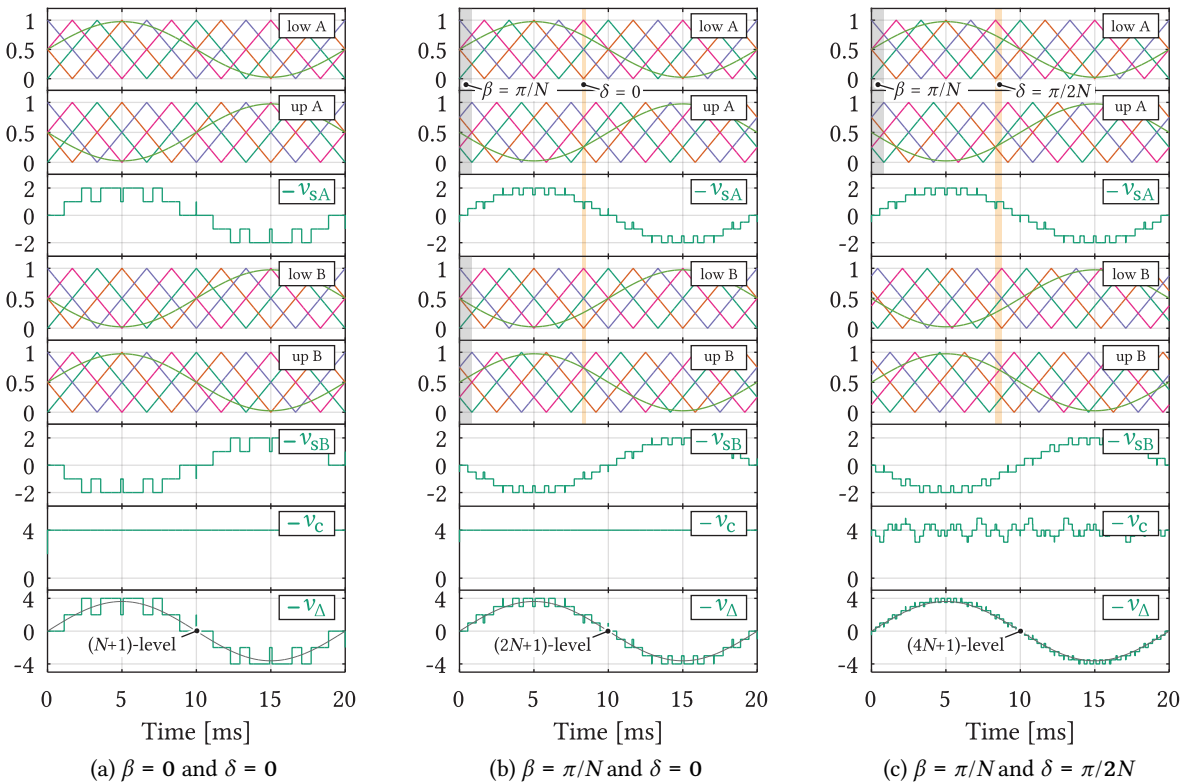


**Fig. 7.10** Variations in the number of voltage levels generated by an observed MMC depending upon the positions of the branches' switching instants. In the presented case, the number of SMs per branch was set as  $N = 4$ , combined with the use of PSC modulation. In all of the presented cases, the modulation signal was defined as  $m = 0.5 \times \{1 + 0.95 \sin(2\pi 50t)\}$ . As can be seen, improvements in the MMC AC voltage, observed by going from left to right, come at the price of hindering its DC voltage spectrum.

## 7.4 System design

### 7.4.1 Number of MMC SMs

Similarly to **Sec. 6.3.1**, the number of SMs per branch can be chosen depending on the available voltage across the DC terminals of either MMC as well as the voltage class of semiconductor devices to be used. In case the use of 1.7kV IGBTs is considered, while the input/output voltage ratings of the converter analyzed in the previous chapter will be reused here (i.e. 40kVdc/1.5kVdc), (6.8) provides one with  $N = 22$ , where no redundant SMs are taken into account.

### 7.4.2 Transformers' turns ratios

Proper choice of the transformers' turns ratios requires the critical case, from the STC S- side voltage amplitude standpoint, to be recognized. Namely, in case no faults occur within any of the converter parts, the STC S- side line voltage can be calculated as (7.11). With commutation losses being neglected for now, it is to be noticed that the MMC AC voltage gets divided by  $T_2$  turns ratio  $m_{T2}$ . On the other hand, in case the lower DC pole is lost (or the lower MMC malfunctions), the converter output voltage can be estimated as  $\overline{v_R} \approx MV_{in}/(2m_{T1})$ . In case  $M = 1$  in both cases, expression (7.18) can be derived under the assumption of transformers' turns ratios satisfying  $m_{T1}/m_{T2} = 2/\sqrt{3}$ .

$$\frac{\overline{v_R}|_{\text{fault}}}{\overline{v_R}|_{\text{norm.}}} \approx \frac{\pi}{2\sqrt{3}} = 0.9069 \quad (7.18)$$

It is straightforward to conclude that operating mode with the lower DC pole/MMC being lost represents the most critical case from the output voltage control standpoint. Once the steady state is reached, the mean value of the DR output voltage corresponds to the load voltage (in case resistance of the filter inductor is neglected), therefore  $T_1$  turns ratio can be calculated from (7.16). Substituting  $L_{p\Sigma} = (1 - k)L_{br}$  and  $L_{s\Sigma} = 3L_s/2$  into (7.16) and solving it for  $m_{T1}$ , yields

$$m_{T1} = \frac{\sqrt{\{M^2 V_{in}^2 \pi^2 - 8\pi\omega L_{br} P_{nom}(1 - k)\} v_o^{*2} - 6\omega^2 L_{br} L_s P_{nom}^2 (1 - k) + MV_{in} \pi v_o^*}}{4\pi v_o^{*2} + 3\omega L_s P_{nom}} \quad (7.19)$$

In the above equation,  $P_{nom}$  and  $k$  denote the converter rated power and the branch inductances coupling factor ( $L_m = kL_{br}$ ), respectively. Further, all the parameters apart from the modulation index  $M$  do not depend on the converter operating point. Therefore, to finalize the choice of  $m_{T1}$ , the modulation index  $M$  needs to be determined. In order to provide a certain voltage margin (e.g. 10% for the output voltage control purposes, steady state value of the modulation index can be set as  $M = 0.9$ . Subsequently,  $m_{T2}$  can be calculated according to (6.1).

What can also be noticed from (7.19) is that choosing the transformers' turns ratios requires the branch inductance to be known. As will be seen shortly, the branch inductor sizing relies on the knowledge of the transformers' turns ratio, therefore, these two are to be determined simultaneously.

### 7.4.3 MMC branch inductor design

In order to commence the analysis, one may firstly observe the conventional grid connected MMC, presented in **Fig. 2.1**. In case HB SMs are used, short circuit across the DC terminals of the converter causes the grid, the MMC is connected to, to supply the fault impedance with energy. In other words, the MMC behaves like the 3PH diode rectifier. On these terms, the only means of limiting the slope of the short circuit current, which provides sufficient time for all the SMs to get bypassed, are the branch inductors (in case the MMC is connected directly to the grid, otherwise, grid/transformer impedance needs to be included into the analysis).

In contrast to the conventional grid connected MMC, two MMCs begin interfaced with the 3PHs DR through the STC do not get exposed to the severe short circuit currents in case a fault occurs across either of the DC terminals, as explained in **Secs. 7.3.2.1** and **7.3.2.2**. Moreover, the branch inductors increase the commutation inductance, so far denoted by  $L_c$ , therefore, reduction of the AC side impedance represents one of the important goals in the converter design stage.

As presented in **Sec. 7.3.1**, normal operating conditions imply the generation of high fidelity sinusoidal voltages across the STC windings. For that purpose, additional measures from the modulation standpoint can be taken, allowing for the voltage seen from the AC terminals to contain up to  $4N + 1$  levels, as illustrated on a simple example from **Fig. 7.10(c)**. What can be noticed from the second last plot of this figure is undesirable voltage oscillation seen from the DC terminals of an observed power unit. These voltage oscillations cause the oscillations of the current drawn from the DC terminal and, consequently, the legs' common-mode currents. Since these oscillations are the cost at which the improvements in the AC voltage are made, no control measures can be taken to diminish their effect. Notwithstanding, the proper choice of the branch inductor ensures that the DC link current oscillations are constrained to the desired band. For that matter, however, voltage oscillations seen from the DC terminal of a 1PH MMC must be known.

In case PSC modulation is used, the left-hand side of **Fig. 7.11** presents a 1PH MMC with phase shifts between its branch and leg carrier sets being indicated. DC voltage spectrum of either leg can be calculated individually, however, slight modifications of the branch references and carrier sets allow for the results already presents in **Chap. 5** to be reused. As the analyzed converter consists of two legs, it can be claimed that, to a certain extent, such a structure resembles the leg of an MMC utilizing two parallel SBRs in each of its branches. The first step in the creation of an equivalent suitable for reutilization of expressions derived in **Chap. 5** implies the change in carrier sets' shifts indicated on the left side of **Fig. 7.11**. According to (5.24), the shift between two carrier sets modulating two adjacent SBRs equals  $2\pi/MN$ , while in the analyzed case  $M = 2$  (keep in mind that the equivalent model with two parallel SBRs is the goal to achieve). Also, as suggested by **Tab. 5.3**, the shift between the carrier sets of the upper and the lower branch should be set as  $\pi/2N$  in the analyzed case. As a result, the change of the phase-shifts, as presented on the right-hand side of **Fig. 7.11**, should be adopted. It is straightforward to notice that the phase-shifts orientation on the right represents the "direction" distribution from the left, however, rotated by  $90^\circ$ . The last step in creating the two SBRs equivalent implies the change in the branch voltage references. As can be seen from the circuit on the left side of the bellow figure, two neighboring branches (for instance the upper branches of phases *A* and *B*) receive the references containing sinusoidal waves being in counterphase. Conversely, sets of parallel SBRs receive the identical branch voltage references (in case balancing actions are neglected), meaning that leg *B* branch voltage references need to be swapped.

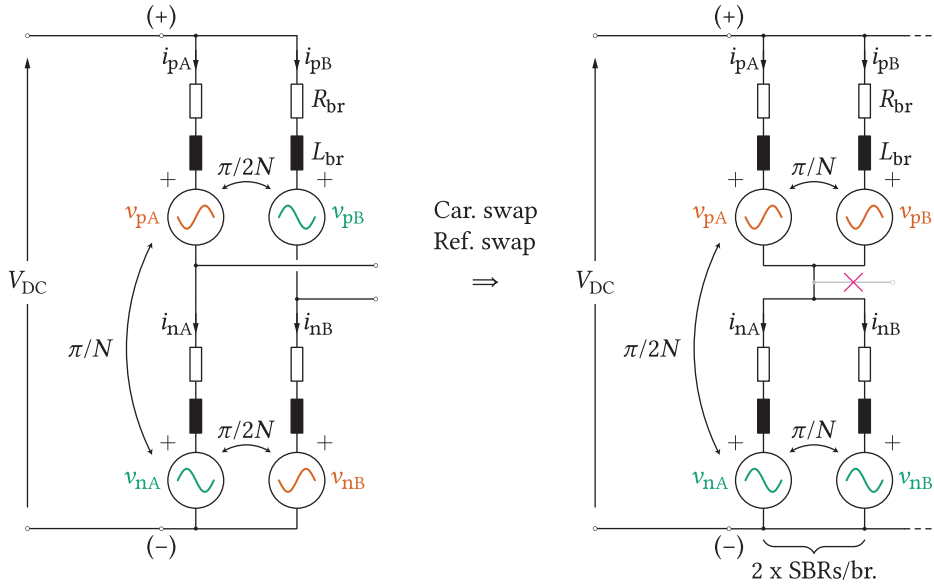


**Fig. 7.11** To reuse already derived expressions for the calculations of the leg voltage spectrum of an MMC comprising an arbitrary number of parallel SBRs, the equivalent circuit of a 1PH MMC can be transformed in the manner depicted above. Namely, by swapping the disposition of branch voltage references, as well as carrier sets, an equivalent circuit suitable for the analysis of the DC voltage component is created. Please notice that such a transformation can not be applied in case AC voltage is to be analyzed.

Consequently, by swapping the carriers, as well as the branch voltage references, of the original 1PH MMC circuit, two SBRs equivalent is created. It is noteworthy that the two SBRs equivalent created in this fashion can be used only in case voltage component seen from the DC terminals of the observed converter is to be analyzed further.

Once the spectral content of the converter's DC voltage is determined by means of the expressions derived in **Sec. 5.2.3**, DC terminal current can be estimated through the circuit presented in **Fig. 7.12**. It is straightforward to conclude that the equivalent inductance  $L_{DC} = (1 + k)L_{br}$ , seen from the DC terminals of an observed MMC, limits the ripple of the MMC input current  $i_{DC}$ .

Nevertheless, the expressions describing the MMC DC current ripple derived by means of the already existing results are quite cumbersome owing to the fact that its DC voltage contains numerous spectral components. As a result, such a determination method was found to be more suitable for the implementation in the form of an algorithm, which is presented in **Fig. 7.13**.

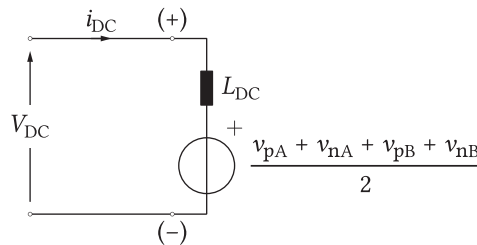


**Fig. 7.12** Equivalent circuit of a 1PH MMC seen from its DC terminals



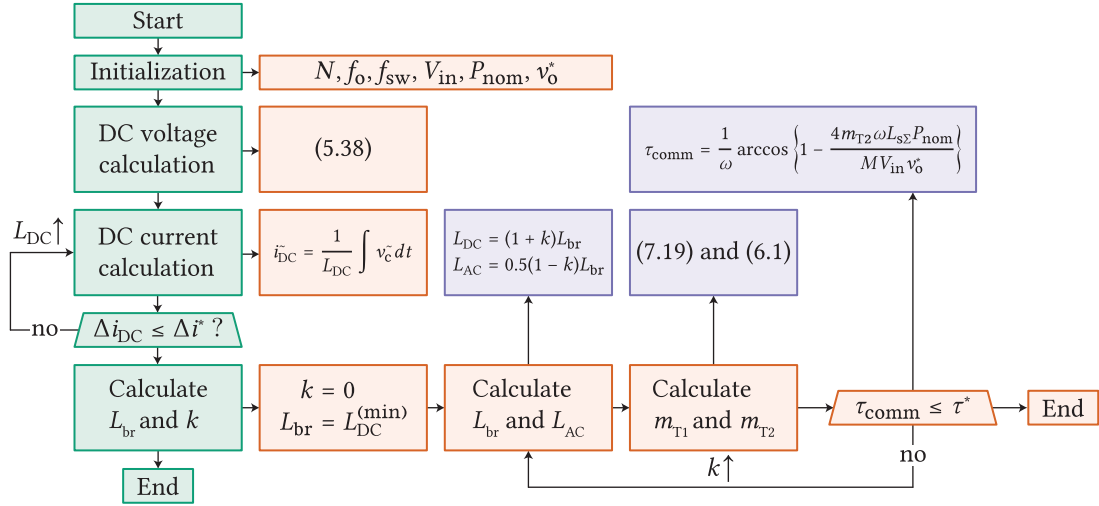


**Fig. 7.13** Algorithm flow with the main routine presented on the left (green) along with the subroutines expanded in the horizontal direction (brown and purple).

The algorithm starts by identifying the basic operating parameters of the converter, such as the number of SMs per branch, operating frequency, switching frequency, nominal power, etc. In order to proceed with the estimation of the DC voltage spectrum, the modulation type needs to be defined in advance. In this work, PSC modulation was considered. However, a similar procedure can be used for each of the modulation methods available for the MMC. Once the DC voltage spectral components are calculated, MMC input current ripple  $\tilde{i}_{DC}$  can be obtained by integrating the DC voltage ripple component  $\tilde{v}_c = v_c - V_{DC}$ . During the presented sizing procedure, it is assumed that the MMCs are connected to a stiff DC voltage source, i.e. no inductance of the power line the converter might be connected to exist. This represents the critical case from the input current limitation standpoint. Once the minimal inductance  $L_{DC}$ , providing satisfactory limitation of the DC current ripple amplitude is obtained, the algorithm proceeds towards determination of the branch inductance along with the coupling factor  $k$ .

Initially, the branch inductors coupling factor can be assumed as  $k = 0$ . However, the resulting AC side inductance could cause the DR commutation time to exceed a predefined limit. In order to calculate the DR commutation time,  $T_1$  and  $T_2$  turns ratios need to be calculated as (6.1) and (7.19), which confirms the statement, made in **Sec. 7.4.2**, regarding the simultaneous determination of the branch inductance and transformers' turns ratios. Thereafter, commutation time under the normal operating conditions, labeled with  $\tau_{comm}$  in **Fig. 7.13**, can easily be calculated based on the 3PH equivalent depicted in **Fig. 7.4**.

In order to provide an explanation on the reasons for prioritizing the normal operating mode commutation time over the ones observed during the faulty operating conditions, exemplary cases presented in **Figs. 7.14(a)** and **7.14(b)** can be analyzed. Since **Fig. 7.14(b)** represents the operating mode with the positive DC pole being lost, the DR output current equals half of the current typical for the normal operating conditions. **Fig. 7.14(a)** provides the normal operating mode equivalent circuit in case commutation between diodes  $D_6$  and  $D_2$  takes place. If the nominal power transfer is assumed, such a commutation process can be described with (7.20).

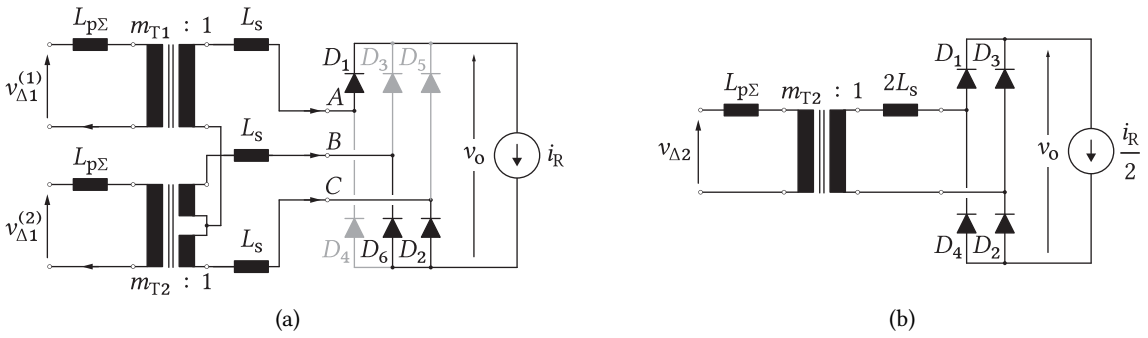


**Fig. 7.14** Exemplary circuits observed for the sake of comparing the commutation times in the normal and the faulty operating condition; (a) Commutation  $D_6 \rightarrow D_2$  occurs in the normal operating mode; (b) Commutation between the diode pairs  $\{D_3, D_4\} \rightarrow \{D_1, D_2\}$  occurring in the faulty operating mode.

$$2 \left( \frac{L_{p\Sigma}}{2m_{T2}^2} + L_s \right) i_R^{(\text{nom})} = \frac{\hat{v}_{\Delta 1}}{m_{T2}} \int_0^{\tau_{\text{comm},1}} \sin(\omega t) dt \quad (7.20)$$

On the other hand, the analysis of the commutation process presented in **Fig. 7.14(b)** gives

$$\left( \frac{L_{p\Sigma}}{m_{T2}^2} + 2L_s \right) i_R^{(\text{nom})} = \frac{\hat{v}_{\Delta 2}}{m_{T2}} \tau_{\text{comm},2} \quad (7.21)$$

At this point, let one assume the equality between the commutation intervals  $\tau_{\text{comm},1}$  and  $\tau_{\text{comm},2}$  from (7.20) and (7.21), respectively. Consequently, (7.22) can be derived by dividing (7.20) with (7.21).

$$\hat{v}_{\Delta 1} = \underbrace{\frac{\omega \tau_{\text{comm}}}{1 - \cos(\omega \tau_{\text{comm}})}}_{f_{\text{comm}}} \hat{v}_{\Delta 2} \quad (7.22)$$

**Fig. 7.15** provides a graphical representation of the term labeled with  $f_{\text{comm}}$  in the above equation. As the term  $\omega \tau_{\text{comm}}$  gives an image of the drop in the output voltage, irrespective of the observed case, seemingly reasonable span of angles was observed. As can be seen, establishing the equality in the commutation times, requires the peak of sinusoidal voltages generated under normal operating conditions to exceed the amplitude of the square wave generated under faulty operating conditions. If the output voltage in the circuit from **Fig. 7.14(b)** corresponds to the nominal value, supplying the STC P- windings with voltages satisfying any of the ratios indicated in **Fig. 7.15**, during normal operating conditions, causes the output voltage to exceed the nominal value. Therefore, establishing such a pair of P- side voltages, would not be reasonable from the practical standpoint.

According to the above discussion, one can conclude that the commutation takes more time during the normal operating mode compared to its faulty counterparts. Hence, every iteration of the algorithm in **Fig. 7.13** checks whether the commutation time in the normal operating mode complies with the limits set in advance.

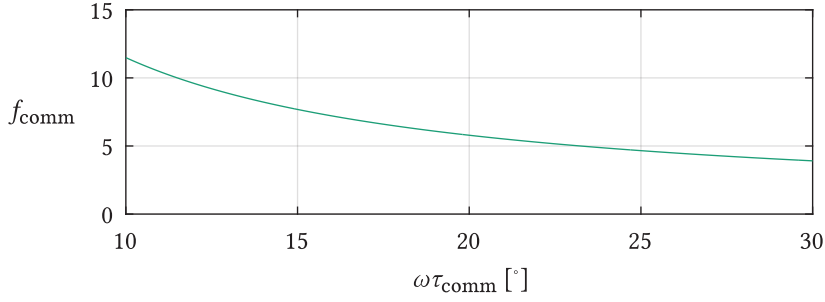


**Fig. 7.15** Ratio between the peak voltages in the normal and the faulty operating mode which would result in the equal commutation times for both of the cases observed in **Figs. 7.14(a)** and **7.14(b)**

As each of the diodes within the 3PH DR conducts during one sixth of the fundamental period, the required commutation time must not exceed this time span. However, the reference value  $\tau^*$  is normally set to the value lower than  $T/6$ . Unless the coupling factor/branch inductance pair does not satisfy the condition defined as  $\tau_{\text{comm}} \leq \tau^*$ , the coupling factor increases and the algorithm enters a new iteration. In **Fig. 7.13**, the equivalent inductance relevant for the calculation of the critical commutation time equals  $L_{s\Sigma} = (1 - k)L_{\text{br}}/(2m_{T2}^2) + L_s$ .

**Tab. 6.1** provides the parameters of the converter analyzed in **Chap. 6**. As the converter analyzed in this chapter represents the modification of the configuration analyzed in the previous one, the input/output voltage ratings are retained, as stated in **Sec. 7.4.1**. However, due to a difference in the operating principles, operating frequency of the isolation stage in the case being the subject of this chapter is selected as  $f_0 = 250\text{Hz}$ . Also, PSC modulation is used in order to synthesize the voltage references commanded by the output voltage controller, which will be covered shortly, thus,  $f_{\text{sw}} = 285\text{Hz}$ . Passing all these information to the algorithm depicted in **Fig. 7.13** results in the parameters given in **Tab. 7.1** in case  $L_s = 0.76\mu\text{H}$  (corresponding to roughly 1.5% of the transformers' base impedance). Commutation time limit was set as  $\tau_{\text{comm}}^* \leq 1/(24f_0)$ .

#### 7.4.4 SM capacitance design

In contrast to the previous chapter, where the fundamental switching frequency of the SMs was set as one of the important requirements to be met, the use of PSC modulation is considered in this work. Consequently, balancing of the SMs' voltages occurs naturally [114] in case the proper capacitor sizing is performed. Oscillation of SMs' voltages occurs as a consequence of the interaction among harmonic components in currents and voltages of an observed MMC branch. In the conventional MMC, operating with pure sinusoidal currents on the AC side, the sizing of the SM capacitances can be performed according to [48], [49]. As branch currents in the analyzed case are not purely sinusoidal, defining the SM capacitance requires spectral content of the branch currents to be known.

**Tab. 7.1** Parameters provided by the branch inductor/transformers' turns ratio sizing algorithm

$T_1$ turns ratio ( $m_{T1}$ )	$T_1$ turns ratio ( $m_{T2}$ )	Branch inductance ( $L_{\text{br}}$ )	Coupling factor ( $k$ )
11.82	10.23	5.4mH	0.91

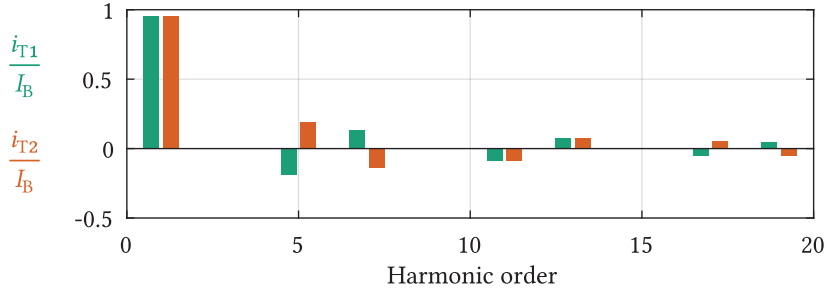


**Fig. 7.16** Harmonic content of the STC P- windings' currents

Through the observation of **Fig. 7.5(a)**, one can derive the expressions describing the currents flowing through the STC P- windings as

$$\frac{i_{T1}}{I_B} = \sqrt{3} \frac{\sin\left(\frac{n\pi}{3}\right) + \sin\left(\frac{2n\pi}{3}\right)}{n\pi} \quad (7.23)$$

$$\frac{i_{T2}}{I_B} = \frac{\sin\left(\frac{n\pi}{6}\right) + \sin\left(\frac{5n\pi}{6}\right) + 2\sin\left(\frac{n\pi}{2}\right)}{n\pi}, \quad (7.24)$$

where  $n$  and  $I_B$  denote the harmonic order and the base current, defined as  $I_B = P_{\text{nom}}/(m_{T2} v_0^*)$ , adopted for the normalization purposes, respectively.

**Fig. 7.16** provides a graphical representation of (7.23) and (7.24), from where one can see that the amplitudes of the first harmonics of  $T_1$  and  $T_2$  currents match each other. As the transformers' currents contain multiple harmonic components, the same can be claimed for the branch currents of both MMCs. Thereafter, the branch power oscillations can be calculated by summing the terms being the product of the branch voltage, consisting of the DC value and sinusoidal component at the fundamental frequency, and branch currents, whose spectral content is extended by the higher order harmonics (e.g.  $n = 5, 7, 11$ , etc.). Each of the branch power components causes the branch energy oscillations being directly proportional to the magnitude and inversely proportional to the frequency of an observed power component. Hence, only harmonics at the fundamental frequency will be taken into account in the process of determining the SM capacitance, which is the procedure adopted in the conventional MMC with no injection of additional harmonics in the leg common-mode current/voltage. However, some security factor (e.g. 1.1) can be adopted at the end of the calculation process in order to compensate for the errors committed by neglecting the higher order harmonics in the currents of both transformer units.

Of course, strict analytic/numeric calculations of the energy oscillations, observed in any of the converter branches, can be conducted by means of (7.23) and (7.24). Nonetheless, the method described above was used for simplicity purposes. For either of the MMCs, operating with  $N = 22$  SMs per branch and input voltage of 20kV, limiting the SM voltage ripple to  $\pm 5\%$  of the nominal value  $V_{\text{SM}} = 20\text{kV}/22 \approx 910\text{V}$ , results in the SM capacitance requirements of  $C_{\text{SM}} = 10\text{mF}$ .

### 7.4.5 Output filter design

Sizing of the output filter requires the most critical case from its operation viewpoint to be determined. From **Fig. 7.5(b)** one can see that normal operating conditions of the analyzed converter imply the DR output voltage containing the ripple at six times the operating frequency of the STC. On the other hand, continuing the operation in case any of the DC poles, or the MMCs, is lost, forces the operation mode change requiring 1PH rectification in the LV stage. For this reason, voltage across the DC terminals of the DR contains the harmonics occurring at even multiples of the STC operating frequency (e.g. 2, 4, 6, etc.). Hence, this operation mode will be considered critical from the output filter sizing standpoint.

Proceeding with the analysis requires further investigation of the filter inductor current ripple depending on which one of the MMCs remains active in case a fault occurs at the HV/MV side. According to **Fig. 7.8(b)**, which represents a generalized operating waveforms of the 1PH DR operating with square voltages, the filter inductor peak-to-peak current ripple can be calculated as (7.25), under the temporary assumption of the output voltage being ideally flat. Please notice that the DR supplied with square voltages at its AC terminals resembles a basic buck converter.

$$\Delta I_R = \frac{v_{\Delta}^{(s)} \tau_c}{L_o} \left( 1 - \frac{2\tau_c}{T} \right) \quad (7.25)$$

Substituting (7.14) and (7.15) into (7.25), yields

$$\Delta I_R L_o = 2L_c i_R \left( 1 - \frac{2\omega L_c i_R}{\pi v_o + 2\omega L_c i_R} \right) \quad (7.26)$$

For a certain choice of the filter inductor, the output current ripple in case the positive ( $\Delta I_{R1}$ ) and the negative ( $\Delta I_{R2}$ ) DC pole is lost relate to each other as

$$\frac{\Delta I_{R1}}{\Delta I_{R2}} = \frac{(12\omega L_s i_R + 4\pi v_o^*) m_{T1}^2 + 8\omega L_{p\Sigma} i_R}{\underbrace{(12\omega L_s i_R + 3\pi v_o^*) m_{T1}^2 + 8\omega L_{p\Sigma} i_R}_{>1}} \quad (7.27)$$

Since the above fraction has the value greater than one, irrespective of the output current value, outage of the positive DC pole represents the critical case from the output filter sizing standpoint. As the derivative of the function on the right-hand side of (7.25) is positive for all positive values of the output current  $i_R$ , the output inductor can be determined as

$$L_o \geq \frac{2\pi v_o^2 (2L_s m_{T2}^2 + L_{p\Sigma})}{\beta (\pi v_o^2 m_{T2}^2 + 2\omega L_s P_{nom} m_{T2}^2 + \omega L_{p\Sigma} P_{nom})}, \quad (7.28)$$

where  $\beta$  denotes the fraction of the DR output current  $P_{nom}/(2v_o^*)$ .

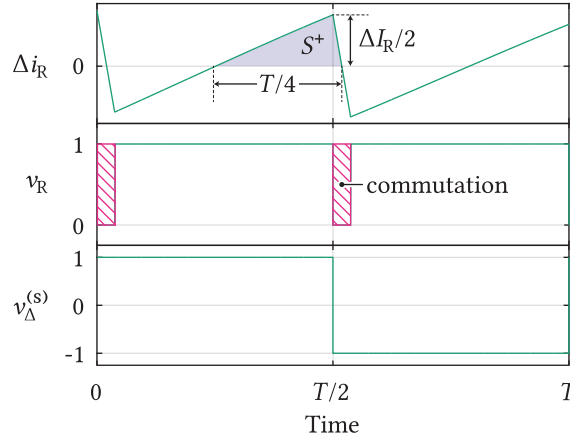


**Fig. 7.17** Output inductor current ripple ( $\Delta i_R$ ) with the DR output ( $v_R$ ) and STC the S- side ( $v_{\Delta}^{(s)}$ ) voltages, respectively, normalized with respect to  $\max(v_{\Delta}^{(s)})$

Furthermore, the output capacitor can be sized according to the desired voltage ripple requirement. Owing to similarity with the buck converter, it can be assumed that the filter inductor current ripple flows through the output capacitor, leading to

$$C_o \geq \frac{1}{\Delta V_o^*} \int_{S^+} \Delta i_R dt, \quad (7.29)$$

where  $\Delta V_o^* = \gamma v_o^*$  denotes the maximum value of the output voltage ripple under the terms defined above. Additionally, the integral labeled with  $S^+$  implies the integration of the output current ripple as long as it takes positive values. The top-most plot of **Fig. 7.17** presents the output current ripple along with the DR output/input voltages, respectively. According to the basic geometry laws, the area under the inductor current ripple, labeled with  $S^+$  can be calculated as  $S^+ = \Delta I_R T/16$ , which, when inserted into (7.29), provides one with (7.30), where  $\Delta I_R = \beta P_{\text{nom}}/(2v_o^*)$ .

$$C_o \geq \frac{T \Delta I_R}{16 \gamma v_o^*} = \frac{\beta P_{\text{nom}}}{16 f \gamma v_o^{*2}} \quad (7.30)$$

In case  $P_{\text{nom}} = 10\text{MW}$ ,  $v_o = 1.5\text{kV}$ ,  $f = 250\text{Hz}$ ,  $\beta = 0.1$ ,  $\gamma = 0.05$ , expressions (7.28) and (7.30) result in

$$L_o \geq 107 \mu\text{H} \quad (7.31)$$

$$C_o \geq 2.22 \text{mF} \quad (7.32)$$

According to the above requirements, the output filter parameters were chosen as  $L_o = 300 \mu\text{H}$  and  $C_o = 2.5 \text{mF}$ .

**Tab. 7.2** Parameters of the system used for simulation purposes

Input voltage ( $V_{in}$ )	Output voltage ( $v_o^*$ )	Rated Power ( $P_{nom}$ )	Operating frequency ( $f$ )	Carrier frequency ( $f_c$ )	No. of SMs per branch ( $N$ )	Branch self inductance ( $L_{br}$ )	Branch ind. coupling factor ( $k$ )	SM capacitance ( $C_{SM}$ )
$\pm 20\text{kV}$	$1.5\text{kV}$	$10\text{MW}$	$250\text{Hz}$	$285\text{Hz}$	$22$	$5.4\text{mH}$	$0.91$	$10\text{mF}$

## 7.5 System control

From the output voltage control standpoint, all of the operating modes analyzed in **Sec. 7.3** rely on identical principles, with minor differences existing among them. Therefore, the approach used to ensure that the output voltage tracks the reference value under normal operating conditions will be covered, whereas the details specific for the control under faulty operating conditions will be outlined. As for the balancing of the energies stored within the branches of the employed MMCs, conventional methods already described in **Chap. 3** are used, hence, this topic will be discussed just briefly. **Tab. 7.2** groups all the parameters of the system the control of which is the subject of the upcoming discussions.

According to (7.11), the mean value of the DR output voltage is adjusted with the aim of controlling the average voltage across the output capacitor ( $C_o$ ). Owing to the nature of the output filter, which consists of two reactive elements, two feedback loops, referred to as the outer voltage and the inner current loop, are formed, as presented in **Fig. 7.18**. Please notice that all of the denoted quantities represent the average values. The output voltage is measured, filtered (e.g. notch filter) to obtain its mean value and compared to the reference set by **Tab. 7.2**. Thereafter, voltage error is passed to the PI controller, whose output represents a desired mean value of the filter inductor current ( $i_R^*$ ). The converter load current ( $i_o$ ) can be used as a feed-forward in case its measurement is available. Such a step is rather logical given that the theoretical mean value of the inductor current equals the load current. The identical assumption was used in **Sec. 7.4.5** in order to select the output filter capacitance. The filter inductor current is measured, filtered and compared to the reference set by the output voltage controller. Subsequently, the current error is passed to the PI controller.

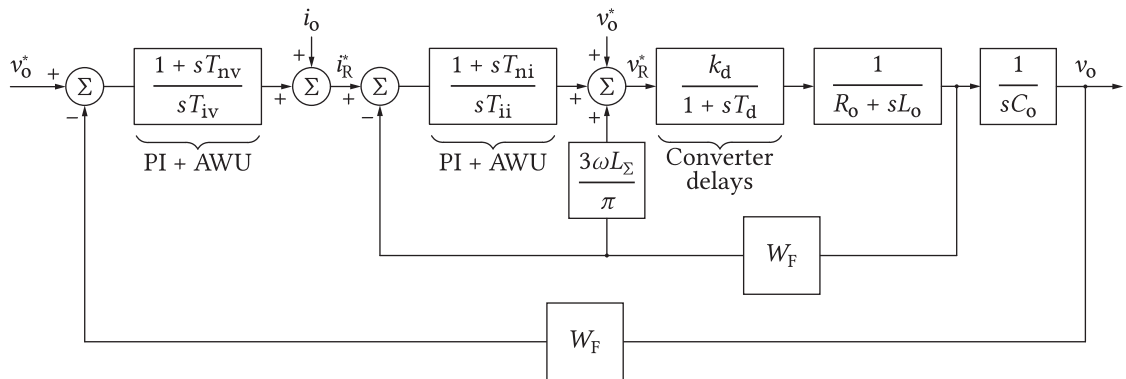


**Fig. 7.18** Output voltage control structure. As can be seen, two control loops are employed in order to control the output voltage. Parameter to be affected by the control algorithm is both MMCs' modulation index ( $M$ ), which can easily be extracted from the reference value of the DR output voltage ( $v_R^*$ ).

The DR commutation voltage drop can be compensated in advance by adding  $3\omega L_{\Sigma} i_R / \pi$ , where  $L_{\Sigma} = (1 - k)L_{br} / (2m_{T2}^2) + L_s$ , to the output of the current PI controller. Finally, the mean value of the DR output voltage ( $v_R^*$ ) is obtained. It is noteworthy that the steady state value of the DR output voltage equals the converter output voltage reference in case voltage drop across the filter inductor is neglected. Such an assumption is reasonable, otherwise, a significant amount of energy is lost inside the filter itself. Consequently, the output voltage reference can be used as a feed-forward, having a positive impact on the dynamic performance of the analyzed structure.

It is easy to conclude that a variable to be affected by the output voltage control is both MMCs' modulation index ( $M$ ), which can easily be obtained from the DR output voltage reference by solving (7.11). As already stated, to synthesize the desired AC voltage across both MMCs' terminals, PSC modulation is used, although the other modulation methods presented in the literature can as well be employed. It is noteworthy that, similarly to the conventional 3PH DR, dominant harmonics in the filter inductor current, as well as the output voltage occur at six times the frequency of sinusoidal voltage provided by the MMCs, as will be shown in the following section.

At this point, it is worth emphasizing that identical control structure is used under the faulty operating conditions. Nevertheless, the output voltage drop compensation is to be performed with different coefficient ( $3\omega L_{\Sigma} / \pi \rightarrow 2\omega L_c / \pi$ ), as suggested by (7.15). Also, modulation index of the MMC being operable represents the amplitude of the generated square wave in contrast to the normal operating conditions where two quadrature sinusoidal waves are synthesized. Therefore, (7.16) and (7.17) should be used, depending on which MMC continues the operation, instead of (7.11).

Control of the MMC internal quantities, such as the branch energies, can be performed as if the conventional grid connected MMC is analyzed. Namely, the STC P- winding currents can be expanded into Fourier series, as presented in **Fig. 7.16**. It can be seen that in either case, the transformer current does not contain any even harmonics, nor the ones being the multiples of three. Given that both MMCs supply their associated transformers with sinusoidal voltages (i.e. sine wave at the STC operating frequency), higher order harmonics in the STC P- winding currents do not contribute to the power transfer towards the MMC SMs. As a consequence, circulating currents at the fundamental frequency can be used with the aim of attaining the energy balance within the MMCs [113]. Another conclusion regarding the MMC SM switching frequency can be made based on **Fig. 7.16**. In case PSC modulation is employed, SM switching frequency should not be set as an integer multiple of the fundamental frequency, as suggested in [114], otherwise, the side band harmonics in an SM voltage spectrum coincide with the transformer current harmonics giving rise to divergence in the MMC branch energies. Hence, SM switching frequency was set as  $f_{SW} = 285\text{Hz}$ .

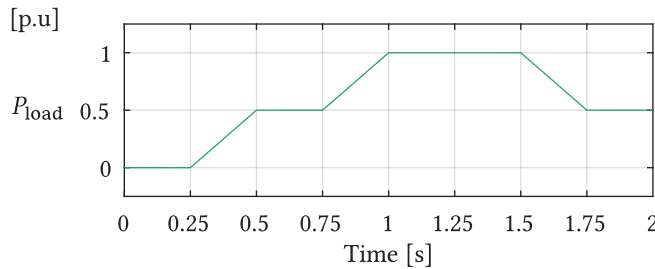


**Fig. 7.19** Load power profile normalized with respect to the rated power of the converter



## 7.6 Simulation results under normal operating conditions

The proposed high-power DC-DC converter was modeled and simulated in PLECS. In order to test the converter operating performances, load power profile depicted in **Fig. 7.19** was used. In order to demonstrate the operation robustness, SM capacitance deviations of  $\pm 20\%$  from the rated value, provided in **Tab. 7.2**, were randomly distributed throughout the model.

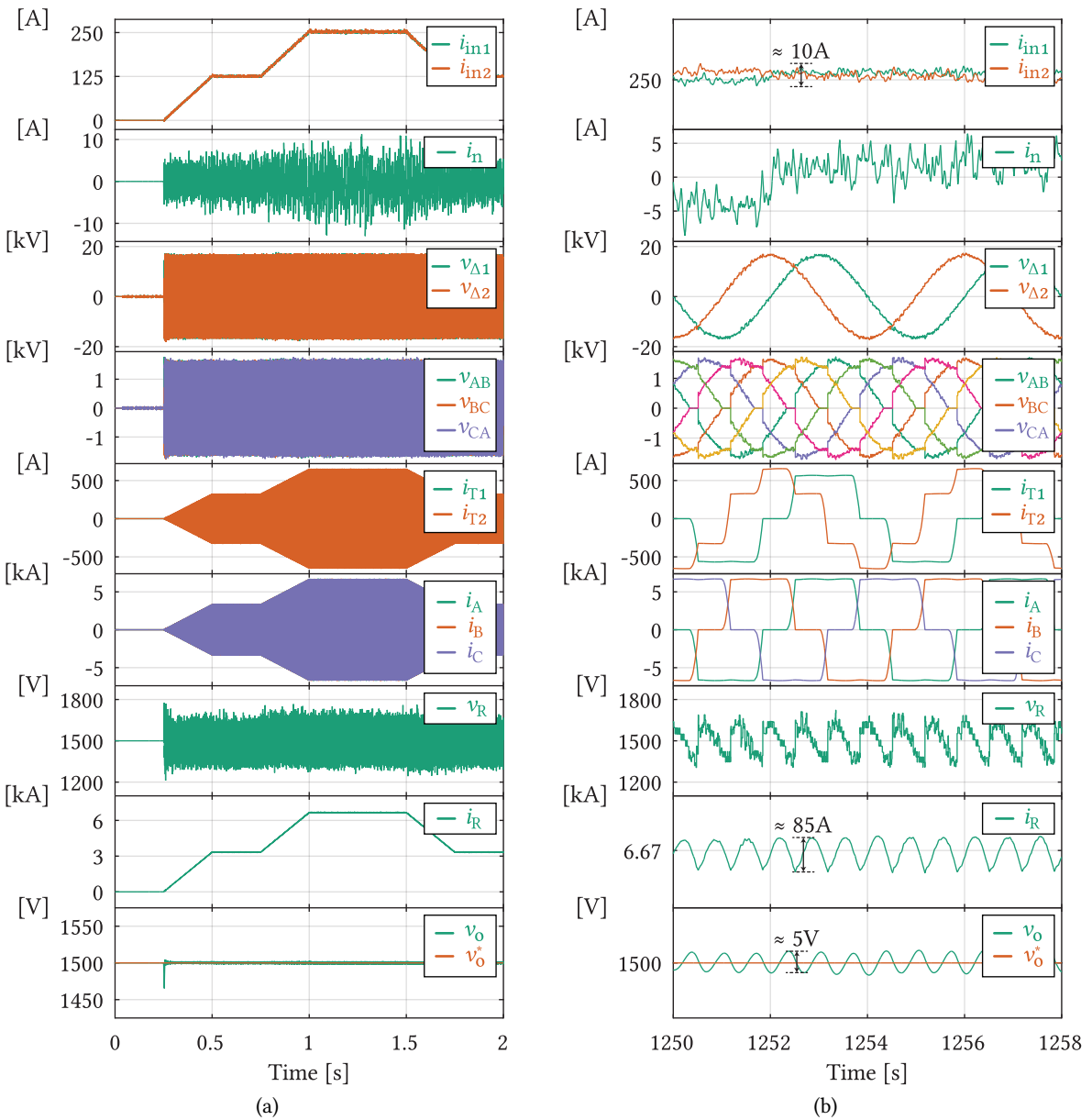


**Fig. 7.20** Operating waveforms of the analyzed converter (a) Operation of the converter during the period  $T_{sim} = 2s$ ; (b) Operation of the converter during two fundamental cycles.

**Fig. 7.20(a)** presents operation of the converter during the time interval  $T_{\text{sim}} = 2\text{s}$ . As can be concluded from the shape of the MMCs' input currents, labeled with  $i_{\text{in}1}$  and  $i_{\text{in}2}$ , respectively, the converter successfully responds to the load power requirements defined by the profile in **Fig. 7.19**. Moreover, these two currents differ only by the ripple components, which is obvious from the second plot presenting the neutral conductor current  $i_n$ .

To confirm the correspondence between the idealized operating waveforms presented in **Fig. 7.5(b)**, converter operation during two fundamental cycles is presented in **Fig. 7.20(b)**. The peak-to-peak current ripple of the MMCs' input currents, under the full load, falls in the range of approximately 5% of the mean value, which was the criteria used in the process of the branch inductors sizing. It is noteworthy that relaxation of this criteria results in the reduction in the branch inductances, as well as their coupling factors. Further, two MMCs generate high fidelity quadrature sinusoidal waves ( $v_{\Delta 1}$  and  $v_{\Delta 2}$ , respectively), which, by means of the STC get transformed into the symmetrical system of line voltages observed across the terminals of the 3PH DR. These voltages were labeled with  $v_{AB}$ ,  $v_{BC}$  and  $v_{CA}$  (the other three waveforms presented on the fourth plot from the top represent the inverses of these). The STC P- side currents, labeled with  $i_{T1}$  and  $i_{T2}$ , feature the expected shape, whereas the shape of the LV side currents  $i_A$ ,  $i_B$  and  $i_C$  corresponds to the one observed in the conventional grid connected 3PH DR. Output voltage of the DR, denoted by  $v_R$ , contains the mean value along with the dominant ripple component occurring at six times the operating frequency of the STC. It is noteworthy that the high frequency oscillations present in  $v_R$  are the consequence of the switching actions of two MMCs. Notwithstanding, spectral analysis, which will be presented in the upcoming paragraphs, indicates a negligible amount of energy carried by these. Similar conclusions made in case the DR output voltage is analyzed can be made should the filter inductor current ( $i_R$ ) is observed. Last but not least, the converter output voltage oscillates around the reference value, however, with a negligible oscillatory component being a consequence of the oscillations in the DR output voltage.

**Fig. 7.21(a)** provides the DR output voltage spectrum with the frequency axis being normalized with respect to the STC operating frequency. Due to the substantial difference between the mean value and the other harmonics, two different ordinates, colored in green (left) for the mean and brown (right) for the higher order harmonics, were used. As expected, the most dominant harmonics can be observed at multiples of six times the STC operating frequency. Nevertheless, although negligible, harmonics at frequencies differing from  $6nf$ , where  $n \in \mathbb{N}$ , appear as a consequence of non-ideal sinusoidal waves (which are created through the switching actions of two MMCs), oscillations of voltage across the SMs of both MMCs, etc. As the filter inductor current can be perceived as a consequence of the DR output voltage, identical conclusions can be made for the spectrum presented in **Fig. 7.21(b)**.

**Figs. 7.22(a)** and **7.22(b)** present SMs' voltages in the lower branch of phase A in both MMCs during ten fundamental periods. Given that the SM capacitance deviations of  $\pm 20\%$  were randomly distributed throughout the model, oscillations in the SMs' voltages are not identical. However, no divergence can be observed from the provided figures, which proves the stability of the operation under the normal operating conditions. The upper and the lower limit set for the SMs' voltages can be calculated as (7.33) and (7.34), respectively. Given that none of the SMs' voltages exceeds these limits, SM capacitance sizing method, discussed in **Sec. 7.4.4**, is validated.

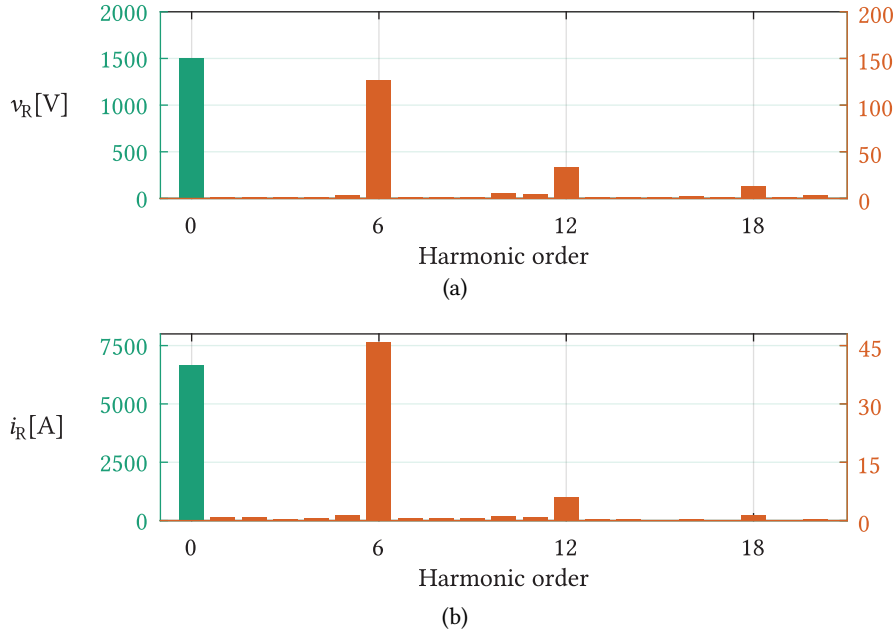


**Fig. 7.21** Spectral content of (a) DR output voltage; (b) Filter inductor current; As can be seen from both of the above plots, dominant harmonics in the DR output voltage/current are located at multiples of six times the operating frequency of the STC. Moreover, high frequency oscillations in the AC voltages generated by the MMCs do not contribute to the distortion of the filter inductor output current. Owing to the significant gap between the mean values and harmonics in both  $v_R$  and  $i_R$ , two different sets of axes are used - green (left) for the mean values and brown (right) for the harmonic components.

$$v_{SM}^{(max)} = 1.05 \frac{V_{in}}{2N} = 954.55V \quad (7.33)$$

$$v_{SM}^{(min)} = 0.95 \frac{V_{in}}{2N} = 863.64V \quad (7.34)$$

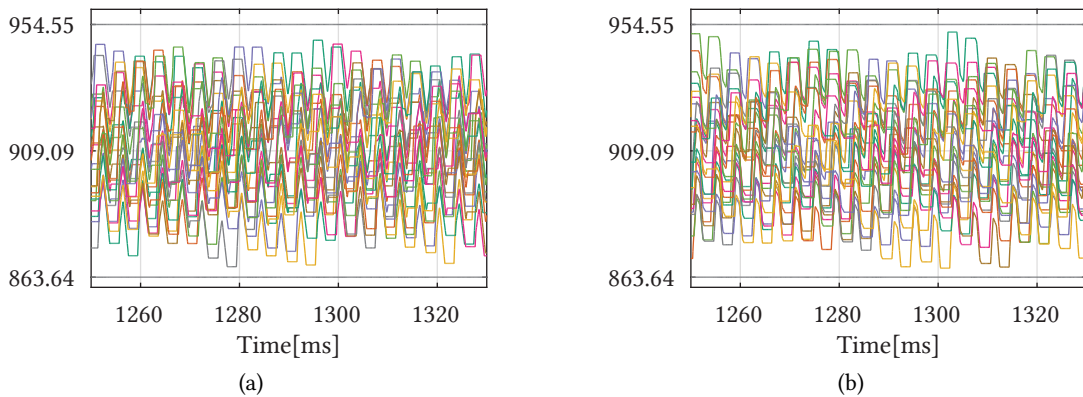


**Fig. 7.22** SMs' voltages in the lower branch of phase A in: (a) MMC<sub>1</sub>; (b) MMC<sub>2</sub>

## 7.7 Simulation results under faulty operating conditions

In order to demonstrate the ability of the proposed converter to maintain the operation, supplying half of the rated power to the load, in case either of the DC poles or the MMCs is lost, two distinct cases depicted in **Figs. 7.7** and **7.9** were simulated in PLECS. Power profile presented in **Fig. 7.19** was scaled by one half and used in order to test the dynamic operation of the analyzed structures.

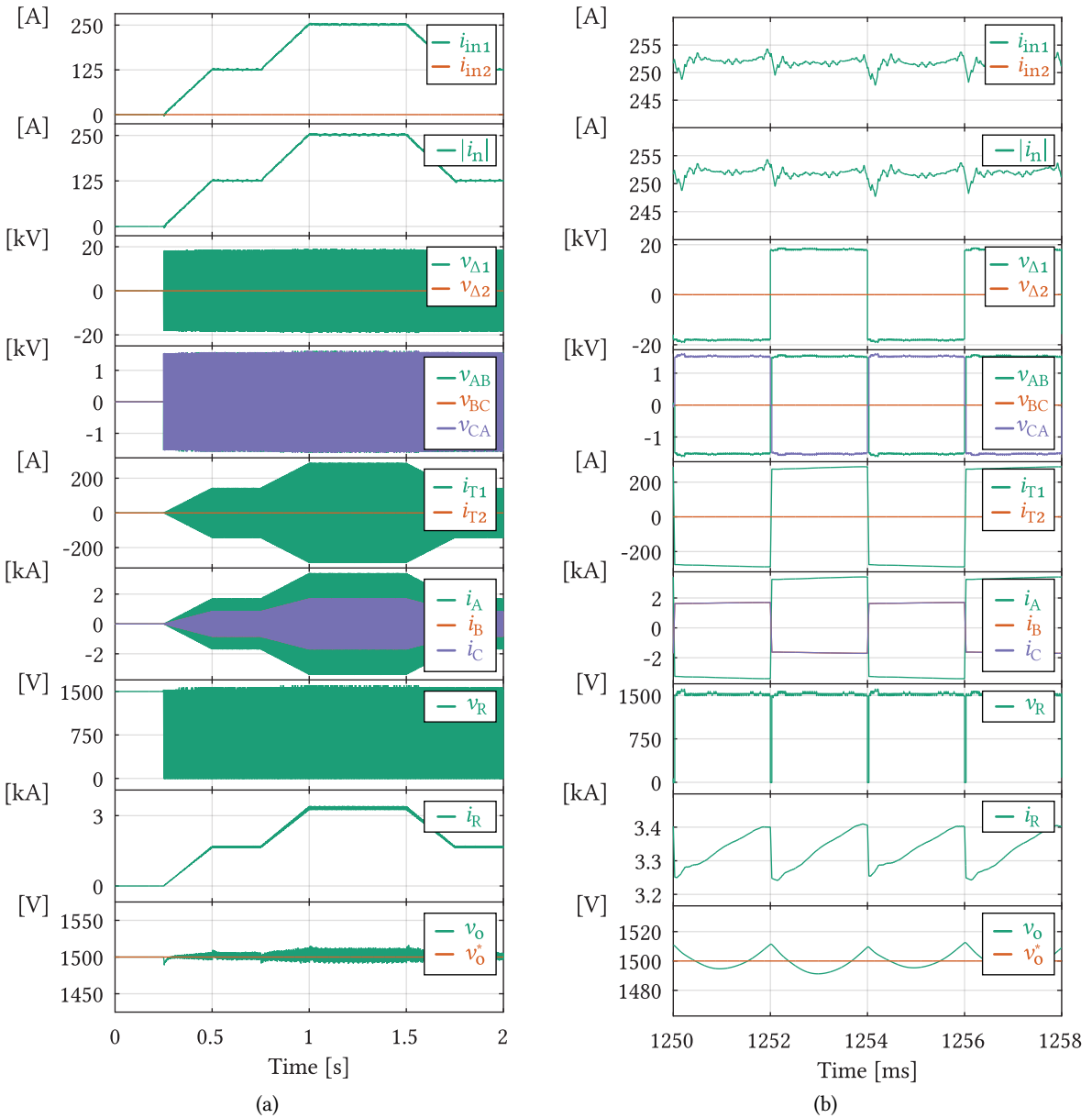


**Fig. 7.23** Operating waveforms of the analyzed converter in case negative DC pole is lost (a) Operation of the converter during the period  $T_{sim} = 2s$ ; (b) Operation of the converter during two fundamental cycles.

### 7.7.1 Negative DC pole outage

**Fig. 7.23(a)** provides operating waveforms of the converter in case a fault occurs across the negative DC pole and the neutral conductor (point). According to the profile of both MMCs' input currents, tracking of the reference power profile gets ensured, which inherently provides the successful tracking of the output voltage reference. As MMC<sub>2</sub> input current equals zero, it is straightforward to conclude that no contributions to the fault current are provided by the redundant operation of the analyzed topology. Moreover, the neutral conductor takes over the role of the faulty DC pole.

Further, **Fig. 7.23(b)** presents the operation of the converter during two fundamental cycles. As discussed in **Sec. 7.3.2**, the changeover from sinusoidal to square voltage waveforms, generated by the healthy side MMC, occurs. From the plot illustrating the STC S- side currents, labeled with  $i_A$ ,  $i_B$  and  $i_C$ , one can observe the equal sharing of current  $i_A$  by the  $T_2$  S- windings. Consequently, no flux changes take place in the P- winding, which results in  $v_{BC} = 0$ .

Through the comparison of **Figs. 7.20(b)** and **7.23(b)** one can notice that, on the terms defined in this section, 1PH rectification occurs in the LV stage. Namely, the DR output voltage and current consist of the mean value along with the ripple featuring oscillations at multiples of two times the fundamental frequency of the converter, which is confirmed in **Figs. 7.24(a)** and **7.24(b)**. Furthermore, insignificantly short DR output voltage drops to zero can be observed. These, in fact, characterize the commutation process and through a simple visual comparison with **Fig. 7.20(b)**, the correctness of the commutation processes analyses conducted in **Sec. 7.4.3** can be confirmed. In other words, the DR commutation process under normal operating conditions requires more time when compared to the cases analyzed in this section.

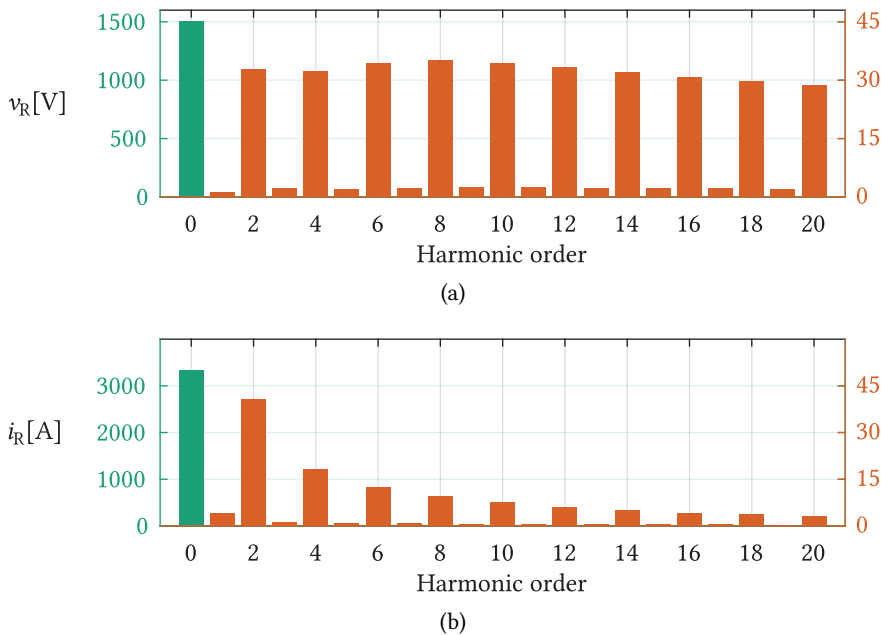


**Fig. 7.24** Spectral content of: (a) DR output voltage; (b) Filter inductor current; In both cases, dominant harmonics in the DR output voltage/current are located at multiples of two times the operating frequency of the STC. Owing to the significant gap between the mean values and harmonics in both  $v_R$  and  $i_R$ , two different sets of axes are used - green (left) for the mean values and brown (right) for the harmonic components.

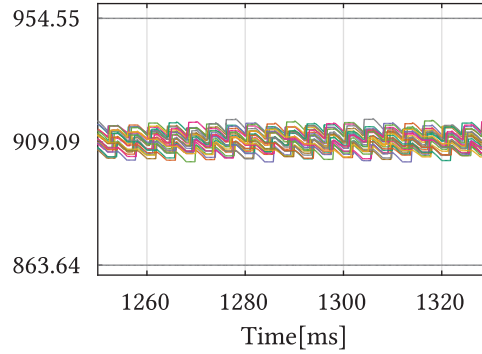


**Fig. 7.25** Voltages across the SMs of the phase leg A lower branch in MMC<sub>1</sub> in case negative DC pole is lost

Last but not least, **Fig. 7.25** presents the voltages across the SMs of MMC<sub>1</sub> during ten fundamental cycles. Despite the deviations of SMs' capacitances mentioned in **Sec. 7.6**, balancing of the SMs' voltages is achieved. Also, the observed oscillations fall significantly below the ones presented in **Figs. 7.22(a)** and **7.22(b)**. This is a consequence of the halved current in the LV stage (since only half the rated power is provided to the load), which results in the drop of the STC P- side currents, as can be seen by comparing **Figs. 7.20(b)** and **7.23(b)**

### 7.7.2 Positive DC pole outage

**Fig. 7.26(a)** presents the operation of the converter in case a fault occurs between the positive DC pole and the neutral conductor (point). Similarly to the previous case, the shape of the healthy side MMC input current indicates the successful tracking of the load power profile. Moreover, isolation of the faulty side MMC results in its input current being equal to zero, which leads to the neutral conductor taking over its role. Throughout the observed period, being set as  $T_{\text{sim}} = 2\text{s}$ , the output voltage tracking is provided. Additionally, **Fig. 7.26(b)** presents the converter operation during two fundamental cycles. As can be seen, MMC<sub>2</sub> provides its associated transformer unit with the square wave pulses, which results in the DR output voltage having the similar shape, however, with periodic drops to zero, which is a consequence of the inevitable commutation process. Nevertheless, these drops are almost negligible in duration when compared to half of the fundamental operating period.

Observation of the STC S- side currents discloses the relationship between the currents  $i_b$  and  $i_c$ . As a consequence of  $i_b = -i_c$ , the current flowing through the T<sub>1</sub> S- winding equals zero, which prevents it from feeding the fault with energy and exposing the bypass diodes of MMC<sub>1</sub> to the risk of getting destroyed. It is important to emphasize that the results presented in **Sec. 7.7** were obtained by the simulation model utilizing equal inductances on the LV side. However, the practical realization of the passive components being equal can be hardly achieved. Consequently, short voltage pulses can possibly be triggered through the T<sub>1</sub> S- winding due to the mismatches in the amplitudes of currents denoted by  $i_b$  and  $i_c$ . Nevertheless, duration of the voltage pulses induced on the P- side should not cause significant currents flowing through the branches of MMC<sub>1</sub>. Identical analysis can be conducted in case the negative DC pole is lost. Notwithstanding, additional measures, discussed in **Sec. 7.8** can be taken to completely suppress the above mentioned LV currents mismatch.

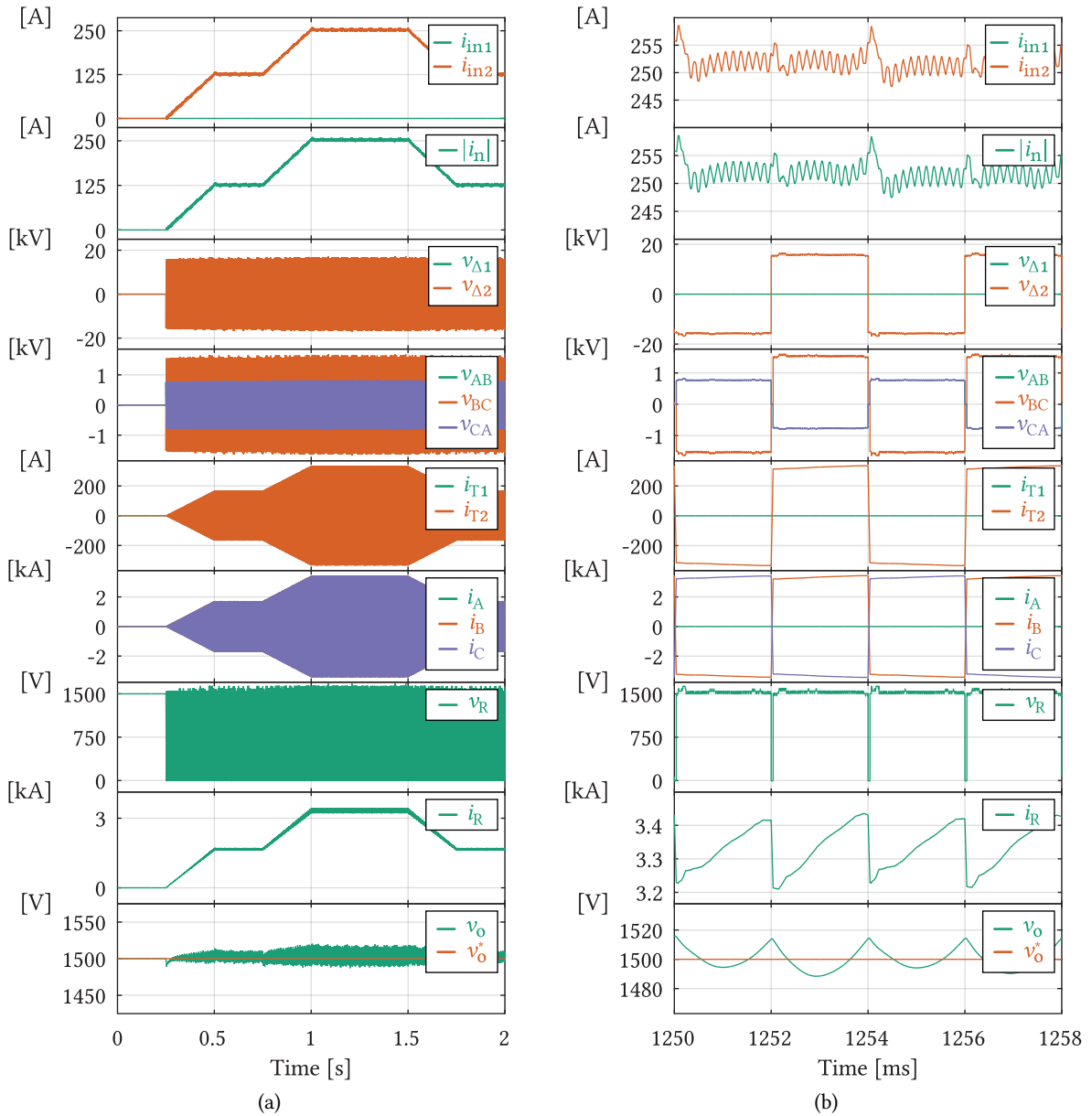


**Fig. 7.26** Operating waveforms of the analyzed converter in case the positive DC pole is lost (a) Operation of the converter during  $T_{sim} = 2s$ ; (b) Operation of the converter during two fundamental cycles.

Owing to the fact that 1PH rectification takes place in the LV stage, the DR output voltage and current consist of the mean value, followed by the oscillations occurring at multiples of two times the STC operating frequency. Such a statement can easily be confirmed from the spectral contents provided in **Figs. 7.27(a)** and **7.27(b)**. Lastly, voltages across the SMs of  $MMC_2$ , during ten fundamental cycles, can be seen in **Fig. 7.28**, leading to the identical conclusions made in the previously analyzed case.

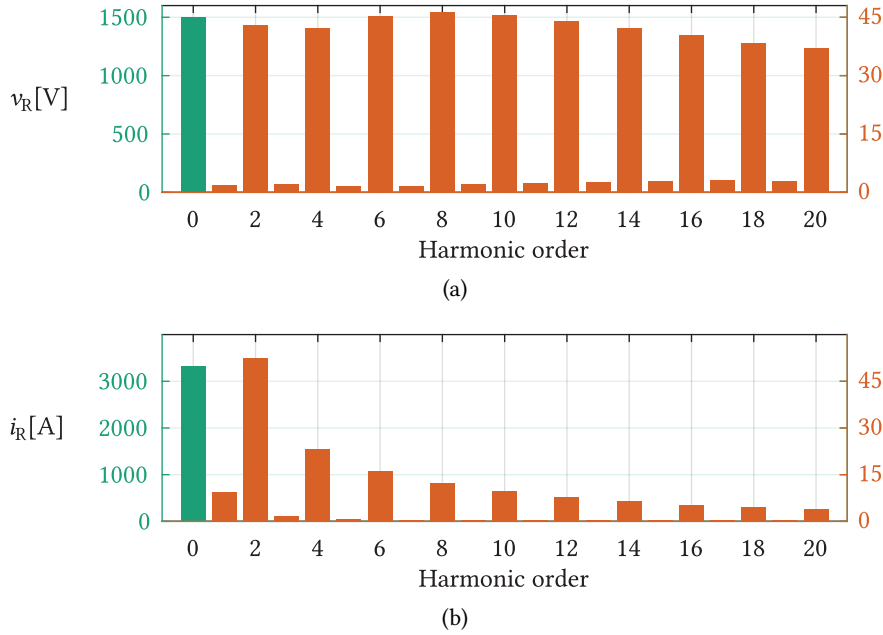


**Fig. 7.27** Spectral content of: (a) DR output voltage; (b) Filter inductor current; As can be seen from both of the above plots, dominant harmonics in the DR output voltage/current are located at multiples of two times the operating frequency of the STC. Owing to the significant gap between the mean values and harmonics in both  $v_R$  and  $i_R$ , two different sets of axes are used - green (left) for the mean values and brown (right) for the harmonic components.

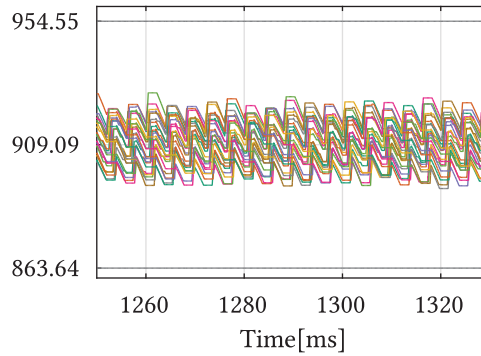


**Fig. 7.28** Voltages across the SMs of the phase leg A lower branch in  $MMC_2$  in case positive DC pole is lost

## 7.8 Concluding remarks

In this chapter, a detailed analysis of the operating principles, design and control of the unidirectional MMC-based high power DC-DC converter was conducted. As demonstrated, the analyzed configuration provides the possibility to exploit the redundancy principles offered by the existence of the neutral conductor in case an HV/MV bipolar DC grid is to be connected with another DC grid of an arbitrary voltage level. The uniqueness of the presented work lies in the unprecedented use of the STC with the aim of performing unidirectional high-power DC-DC conversion. Also, the operation in the medium frequency range was proposed.



However, the unparalleled exploration related to the use of the STC in the analyzed type of power conversion leaves the door open for discussions regarding various topics. For instance, under the faulty operating conditions, voltages and currents of either MMC differ from the ones observed in the normal operating mode. This creates a whole set of possibilities regarding the balancing of the MMCs' voltages. Implicitly, new challenges related to the MMCs' voltages generation are created.

Furthermore, during the discussions devoted to the branch inductance determination, the coupling of inductors belonging to the same MMC leg was the only option being considered. Nonetheless, coupling all of the inductors in an observed MMC, by wounding them on the same core, provides an increase in the equivalent inductance labeled with  $L_{DC}$  in **Fig. 7.12**. As a result, lower values of the branch self inductance can be considered for the identical value of  $L_{DC}$  to be obtained.

Inequality in the STC LV side inductances results in the short voltage pulses across the P- winding of the MMC being connected to the faulty DC pole. Similarly to the example provided in **Chap. 6**, these voltage pulses do not result in the significant currents flowing through the MMC being out of the operation. However, the possibility to suppress these currents to the full extent might be obtained through the use of the MMC branches employing the so-called mixed cells. Namely, in case a certain number of FB SMs were to be employed, blocking of voltage generated across the P- winding of an MMC connected to the faulty DC pole can be achieved.

Last but not least, normal operating mode implying sinusoidal voltages generation represents only one of the possibilities offered by the analyzed converter. In case square voltages, having the identical shape as the ones utilized in **Chap. 6**, were generated by the MMCs, better utilization of the converter DC link could be provided. The main motivation for such a statement originates from the analyses of the commutation processes in two operating modes provided in **Sec. 7.4.3**. Nonetheless, a change in the operating waveform introduces the need for new sizing procedures, as well as the modulation schemes.

Namely, generation of the square voltages allows for the Q2L operation principles to be considered. Although easy to comprehend from the ideological standpoint, an explanation of the transitions characterizing the Q2L operation of the MMC-alike structures requires deep mathematical analyses. It is exactly the following chapter which addresses this challenge, providing the reader with a thorough insight into the transition and sizing rules of the Q2L converter leg.



# Comprehensive Analysis and Design of a Quasi Two-Level Converter leg

*Quasi two-level operation of voltage source converters implies the sequential insertion/bypass of its switching structures, which are referred to as submodules. Consequently, a set of potential problems related to high voltage slopes gets alleviated. Moreover, the ease of stacking the submodules in series provides the means for satisfactory performance in terms of voltage scalability. Although resembling the modular multilevel converter, the quasi two-level converter features contrasting operating principles, leading to the completely different sizing rules. Moreover, the voltage transition process, typical for the quasi two-level converter, can be considered critical from the submodule capacitance sizing standpoint. Therefore, this chapter provides a thorough and generalized mathematical description of the converter leg dynamics during the so-called voltage transition. A comprehensive analysis method, providing the means for the submodule capacitance determination, is presented.*

## 8.1 Motivation

To operate in the HV/MV domain, 2LVL VSCs must satisfy the requirements of an application they are intended for, while withstanding substantial voltage stresses. Given the limited voltage blocking capabilities of commercially available IGBTs, reaching as high as 6.5kV, the series connection of switching devices/converter stages appears to be inevitable in case an HV/MV is to be handled across either of the converter ports. **Fig. 8.1(a)** presents a single leg of the conventional 2LVL VSC utilizing series connection, also referred to as the string, of power devices with the aim of realizing the switch of the desired voltage blocking capabilities. Within such a configuration, balancing of voltages across the employed power devices has been considered challenging given the high likelihood of a mismatch among individual power devices' parameters. On these terms, unequal voltage distribution, originating from the inevitable parameters mismatch, can lead to the destruction of a certain device within the string. Consequently, various methods of connecting the IGBTs in series have been proposed [30]–[33]. The proposed methods rely either on the employment of Balancing Circuits (BCs), being quite commonly referred to as snubbers, connected in parallel to every single device within a string or intelligent driver circuits ensuring satisfactory and safe operation of power devices or a hybrid combination of the two. Nevertheless, the employment of the presented 2LVL configuration within the grid connected applications results in quite high filtering requirements, even if the proper voltage balancing among the switching devices is ensured.

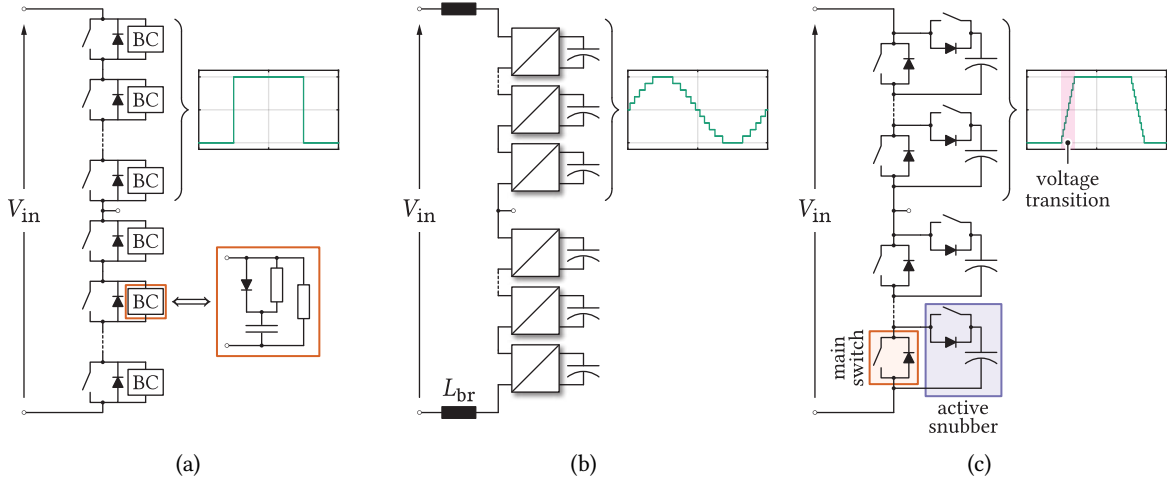


**Fig. 8.1** (a) Series connection of power switches with the aim of handling an HV/MV across the DC terminal of the conventional 2LVL VSC. In order to balance the voltages among the switches, RCD snubber circuits are connected in parallel to every single switching unit; (b) MMC consisting of the series connection of SMs, which can be either HB or FB. Compared to the Q2L converter, the MMC utilizes intentionally installed branch inductors ( $L_{br}$ ) in order to keep its relevant current components under control; (c) Q2L converter - instead of employing passive balancing circuits in order to equalize the voltages across the employed power switches, the active clamp consisting of series connection of a switch and capacitor is used;

Multilevel topologies, such as the NPC [41] and the Flying Capacitor (FC) converter [141], can be perceived as an improvement compared to the conventional 2LVL VSCs within the HV/MV domain owing to the better output voltage quality, reduced filtering requirements, etc. Notwithstanding the theoretical possibility of employing the NPC or the FC converter in this voltage range, the number of bypassing diodes or flying capacitors, respectively, increases quadratically with the number of voltage levels. Hence, these multilevel topologies can not be considered modular (in terms of voltage), given that a new design is required for different system voltages. On the other hand, as already discussed throughout the previous chapters, the MMC, presented in **Fig. 8.1(b)**, enables the straightforward increase of the converter's voltage handling capabilities. Namely, by stacking the SMs in series, the voltage handling capabilities of the converter increase. Further, in comparison to the standard VSCs, the MMC utilizes intentionally mounted branch inductors ( $L_{br}$ ) with the aim of controlling its relevant current components [85], [90], [113]. Normally, the series connection of SMs provides the opportunity to synthesize a high-quality stepwise sinusoidal voltages, therefore, requiring very little or no filtering at all. Nevertheless, in order to meet the requirements imposed upon the SM voltage ripple, high capacitance is usually needed. Consequently, the size and the cost of the converter are also increased.

The additional subject concerning the upcoming analysis refers to the DC systems, which have undoubtedly gained momentum due to the advantages they have shown over their AC counterparts. With the objective of obtaining a flexible and resilient DC grid, a reliable connection between two of its parts operating under different voltage levels needs to be guaranteed. Consequently, the DC-DC converter can be perceived as a part of vital importance with respect to the proper operation of a DC system. Additionally, even though a significant amount of research has been dedicated to the non-isolated DC-DC converters [119]–[124], the isolation stage can still be considered mandatory within the majority of applications owing to the various safety regulations.

In [60] the topology based on the 1PH DAB [127] was presented, however, it incorporated the MMC at both of its stages with the aim of obtaining an electronic tap changer. Moreover, MMC operation in the medium-frequency range was proposed, thus enabling the replacement of bulky LFT with a more compact MFT. According to [49], an increase in the MMC operating frequency results in the energy storage requirements reduction, which definitely results in the converter volume and cost cuts. However, reference [60] has not considered the adverse effects of sharp voltage transitions on the MFT insulation. Hence, Q2L operation, which was also referred to as trapezoidal operation, was proposed and analyzed in [58], [59] with the aim of realizing the 3PH DAB.

Q2L operation implies the sequential insertion of SMs (or a group of SMs) into the circuit over the equidistant time intervals  $T_d$  being referred to as the dwell time. Furthermore, the rail-to-rail operation was proposed, meaning that all the SMs belonging to a branch are either inserted or bypassed having gone through the transition, as shown in **Fig. 8.2**. It was stated that such an operation had proven to be beneficial from several points of view. Firstly, large MMC branch inductors can be removed providing a proper control algorithm, which maintains SMs' voltages balanced, is employed, leading to the disappearance of the MMC common-mode current. In other words, either of the converter branches conducts the output current only during half of the fundamental operating cycle, which perfectly corresponds to the conventional 2LVL VSC. Secondly, the SM capacitors serve as the energy buffers during, normally short, voltage transitions, meaning that once the transition is finished, current diverts to a branch being bypassed. The ultimate result of the aforementioned changes is a substantial reduction in the converter energy requirements. As a result, an increase in the power density along with the converter cost reductions can be expected. Consequently, the Q2L converter has the edge over the conventional MMC within a certain span of applications. Further, the MMC, with branch inductors being removed and operating in the Q2L mode, can also be depicted as in **Fig. 8.1(c)**. Since no branch inductors are present, MMC SMs can as well be perceived through the parallel connection of the main switch and its active snubber. Owing to the resemblance of the structures presented in **Figs. 8.1(b)** and **8.1(c)**, the terminology already adopted in the analysis of the MMC-alike circuits will be retained. Apart from utilizing very small capacitors for snubbing purposes, the Q2L structure presented in **Fig. 8.1(c)** reduces the voltage slope during the converter state change compared to the conventional 2LVL counterparts. Hence, its exploitation within carrier-based modulation schemes with the aim of synthesizing the low frequency output waveforms (low-speed drives as a possible application) was proposed in [56], [57].

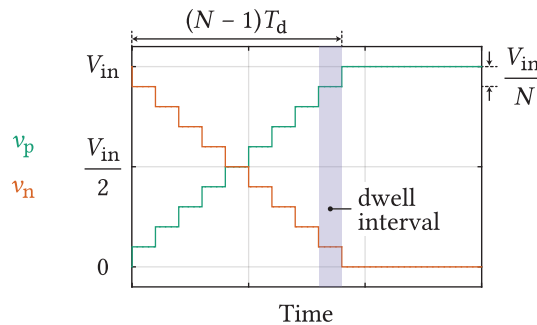


**Fig. 8.2** Sequential insertion of SMs into the circuit. The upper and lower branch voltages were denoted by  $v_p$  and  $v_n$ , respectively. The number of SM was denoted by  $N$ , whereas  $T_d$  designates the dwell time.

Despite the popularity the Q2L operation mode has enjoyed lately, the knowledge gap regarding the dynamics of the leg transition process existed. In fact, no publication has ever explained the converter phase current exchange between the strings of SMs, belonging to the same leg, over the voltage transition interval. Moreover, it was stated in [58] that, during the transition, a string of switches gets exposed to the converter output current which is a very strong statement given that the output current actually equals the difference between the upper and the lower branch current. Additionally, the influence of the branch stray inductance on the transition dynamics was neglected, even though it affects the transition itself along with the general converter operation, as will be seen in the upcoming sections. Throughout this chapter, it will be assumed that the transition period occurs according to the so-called Complementary Switching (CS) method despite the other methods being reported in [58]. Namely, the insertion of one SM in an observed branch implies bypassing of one SM in the adjacent branch within the same switching leg. Consequently, the new resonant circuit is formed at every new dwell interval. Therefore, this chapter presents a thorough mathematical description of the converter leg transition process dynamics. To conduct the desired analysis, the circuit consisting of a single leg is used. However, all the results are presented in a generalized form, hence, it is possible to apply them within a variety of configurations. The active snubber capacitance sizing method is presented, using the mathematical description of the transition process as the underlying basis.

## 8.2 Leg transient analysis

### 8.2.1 Problem statement

In order to provide the reader with a clearer insight into the main contributions of this chapter, **Fig. 8.3** presents the stages of the Q2L transition process. On the left-hand side, one can notice that all of the SMs in the upper branch are bypassed, therefore, it can be said that the leg AC terminal gets clamped to the positive DC rail under the assumption of the branch stray impedance being negligible. On the other hand, the cluster of SMs belonging to the lower branch must be charged to the full input voltage at a certain point, resulting in the current flowing through the equivalent capacitance, which equals  $C_{\Sigma} = C_{SM}/N$ , to drop to zero. As a result, the leg output current, denoted by  $i_o$ , flows through the upper branch. The right-hand side circuit presents an identical situation, however, with the lower branch being bypassed. As all the SMs in the upper branch get charged to the value approximately equal to  $V_{in}/N$ , under the assumption of SMs' voltage balancing controller successfully performing its task, the upper branch current drops to zero, meaning that the output current drifts to the lower branch, while the AC terminal of the observed leg gets clamped to the negative DC rail. Consequently, although it might seem strange at first glance, the output current flows through the branch being bypassed once the transition process is over.

This chapter focuses on what happens in between the operating modes depicted on the sides of **Fig. 8.3**. Nonetheless, there is one challenge to face in the analysis of the circuit depicted in the middle of **Fig. 8.3**. Once the transition commences, the output current becomes shared between the upper and the lower branch of the observed leg. However, what makes the analysis non-trivial is the fact that every new dwell interval implies the change in the capacitances denoted by  $C_p$  and  $C_n$ . As a result, the transition process as a whole can not be analyzed as if it occurred in the circuit with constant parameters. Hence, this chapter provides two methods allowing for such a challenge to be addressed.

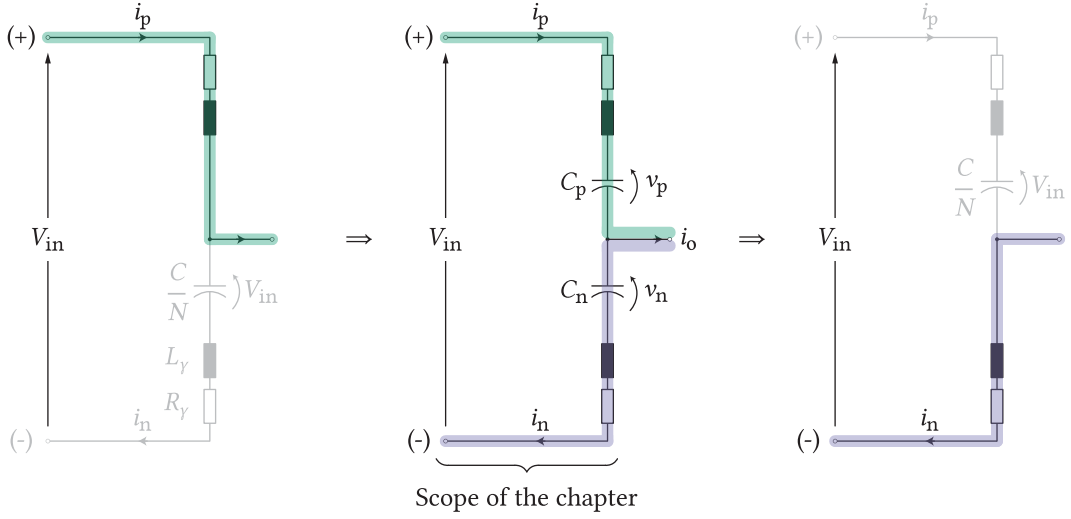


**Fig. 8.3** Q2L converter leg transition presented in different stages

With the aim of investigating the internal dynamics of the Q2L converter during its transition period, the switching leg presented in **Fig. 8.4(a)** will be observed. It is assumed that voltages  $v_{AN}$  and  $v_s$  have the same shape and amplitude, though being shifted by a certain angle denoted by  $\varphi$ . During the observed transition, voltage  $v_s$  remains unchanged. The converter input voltage  $V_{in}$  is assumed stiff, whereas the upper/lower branch stray inductance and resistance will be denoted by  $L_{Y\{p/n\}}$  and  $R_{Y\{p/n\}}$ , respectively. The number of SMs within a branch of the observed converter is denoted by  $N$ . It is noteworthy that despite conducting the analysis in the case of a single switching leg it is easy to expand it onto all the converters utilizing the Q2L operating principles.

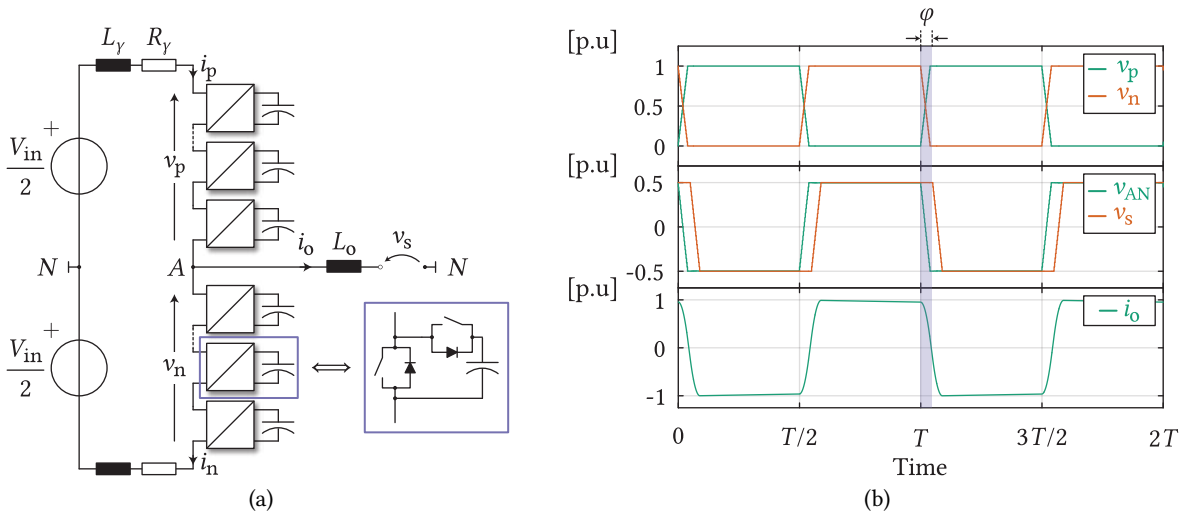


**Fig. 8.4** (a) The circuit used to analyze the Q2L converter leg transition process; (b) Idealized converter waveforms. The upper and the lower branch current ( $i_p$  and  $i_n$ , respectively) are not presented since they are yet to be calculated. All the quantities were normalized with respect to their amplitudes.

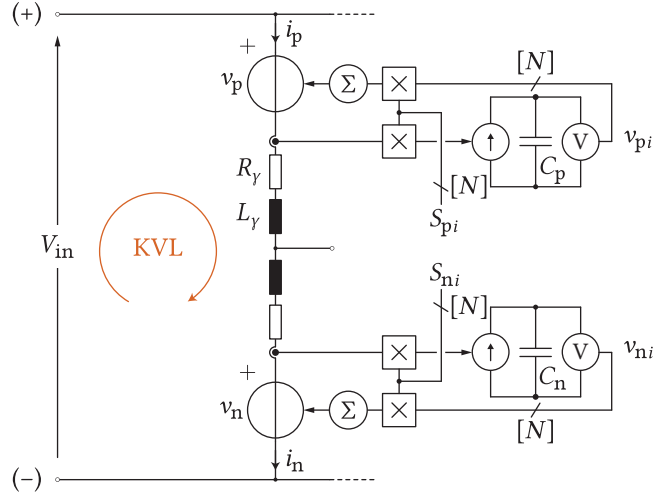


**Fig. 8.5** Equivalent circuit of the converter leg. Providing a proper balancing algorithm is employed, the upper and the lower string of SMs can be replaced with the controlled voltage source. Switching (insertion) signal passed to the  $i$ -th SM belonging to the upper/lower branch is denoted by  $S_{[p/n]i}$ .

Furthermore, the transition period during which the upper branch voltage  $v_p$  changes from zero to full input voltage  $V_{in}$ , whereas the lower branch voltage  $v_n$  changes in the opposite direction, according to **Fig. 8.4(b)**, will be observed. Similarly to the MMC, the leg voltage component, denoted by  $v_{AN}$ , driving the output current can be expressed as

$$v_{AN} = \frac{v_n - v_p}{2} \quad (8.1)$$

Providing there is a proper balancing algorithm employed, strings of the converter SMs can be replaced with the controlled voltage sources, therefore, the transition analysis can be conducted by observing the circuit presented in **Fig. 8.5**. It is noteworthy that unless a balancing algorithm is employed, voltages across the SMs' capacitors diverge, consequently making the converter operation unfeasible. Nevertheless, balancing algorithms differ depending on the application the Q2L converter is used for. Therefore, a thorough discussion covering this matter is omitted. Additionally, voltages across the SMs' capacitors are not identical, however, they all oscillate around the same mean value calculated as  $\overline{V_{SM}} = V_{in}/N$ .

Prior to proceeding with the analysis, an important remark needs to be made. As already stated, changing of the branch voltages, during the leg transition process, causes the equivalent capacitance of the branch to change depending on an observed dwell interval. However, irrespective of the number of SMs inserted in a branch, the number of semiconductor devices in the current conduction path equals  $N$  (in case FB SMs are used, this number needs to be doubled). As a result, what has been referred as the branch stray impedance so far can be considered constant despite the branch voltage, and inherently capacitance, being subject to changes. Additionally, the upper and the lower stray impedance can be considered equal and calculated as  $Z_Y = Z_{base} + NZ_{SM}$ , where  $Z_{SM}$  designates the impedance of a single SM, while the impedance of the branch being independent from the employed SMs is labeled with  $Z_{base}$ .



### 8.2.2 Piecewise analysis

Strict analysis of the Q2L converter leg transition process can be conducted through the individual observation of every dwell interval, which can be considered suitable should the calculations be performed by means of the computer. Namely, the start of a dwell interval is considered the time axis origin ( $t = 0$ ), whereas a branch current/voltage initial conditions are inherited from the previously analyzed one. Finally, acquired responses are grouped together in order to obtain the complete image of the transition. Considering that the number of SMs within a branch equals  $N$ , the total number of differential equations to be solved equals  $N_{eq} = N$ , providing the voltages within the observed converter leg are expressed according to

$$v_p = \sum_{k=1}^N V_0 h(t - [k - 1]T_d) \quad (8.2)$$

$$v_n = V_{in} - \sum_{k=1}^N V_0 h(t - [k - 1]T_d), \quad (8.3)$$

where  $V_0$  and  $h(x)$  denote the initial voltage of an inserted SM (which is assumed to be similar for all the SMs providing satisfactory operation of the balancing algorithm) and Heaviside step function (8.4), respectively. Index of an observed dwell interval was labeled with  $k$ .

$$h(x) = \begin{cases} 1, & \forall x \geq 0 \\ 0, & \text{otherwise} \end{cases} \quad (8.4)$$

One differential equation, describing an observed converter leg, can be written for every interval  $(k - 1)T_d < t \leq kT_d$ , such that  $k \in [1, N]$ . According to **Fig. 8.5**, KVL labeled with brown can be formed, from where (8.5) follows. Both  $v_p$  and  $v_n$  actually represent the series connection of SMs, however, with different number of switching stages being inserted into the loop.

$$V_{in} = L_\gamma \frac{d}{dt}(i_p + i_n) + R_\gamma(i_p + i_n) + v_p + v_n \quad (8.5)$$

Differentiating the above equation, while keeping the basic capacitor voltage equation  $\left(i_c = C \frac{dv_c}{dt}\right)$  in mind, leads to

$$0 = L_\gamma \frac{d^2}{dt^2}(i_p + i_n) + R_\gamma \frac{d}{dt}(i_p + i_n) + k \frac{i_p}{C} + (N - k) \frac{i_n}{C} \quad (8.6)$$

Further, by following the branch current directions defined in **Fig. 8.5**, expression (8.7) can be derived.

$$0 = 2L_\gamma \frac{d^2 i_p}{dt^2} + 2R_\gamma \frac{di_p}{dt} + \frac{N}{C} i_p - \left( L_\gamma \frac{d^2 i_o}{dt^2} + R_\gamma \frac{di_o}{dt} + \frac{N - k}{C} i_o \right) \quad (8.7)$$

From (8.7) one can see that the converter leg output current definitely affects its inner dynamics, hence it needs to be further investigated. **Figs. 8.4(a)** and **8.4(b)** depict the circuit to be analyzed, along with the idealized current and voltage waveforms which are to be used in the forthcoming analysis. Based on **Fig. 8.4(a)**, along with (8.1)-(8.3), one can easily derive (8.8), where it is assumed that every SM voltage remains balanced around the value  $V_{in}/N$ , which is in accordance with the basic operating principles of the MMC-alike circuits. Also, in the upcoming paragraphs, it will be shown that (8.8) can be generalized, therefore, allowing for the analysis of various topologies through the set equations differing with respect to each other only by a single coefficient.

$$\underbrace{\left(\frac{L_Y}{2} + L_O\right)}_{\approx L_O} \frac{di_o}{dt} + \underbrace{\frac{R_Y}{2} i_o}_{\text{negligible}} = V_{in} \frac{(N-k)-k}{2N} - \frac{V_{in}}{2} = -k \frac{V_{in}}{N} \quad (8.8)$$

Substitution of (8.8) into (8.7) yields

$$0 = 2L_Y \frac{d^2 i_p}{dt^2} + 2R_Y \frac{di_p}{dt} + \frac{N}{C} i_p - \left( \underbrace{L_Y \frac{d^2 i_o}{dt^2}}_{=0} + \underbrace{R_Y \frac{di_o}{dt}}_{=-k \frac{R_Y V_{in}}{N L_O}} + \frac{N-k}{C} i_o \right) \quad (8.9)$$

Transposing (8.9) into Laplace domain provides one with

$$0 = \underbrace{2L_Y \left( s^2 i_p(s) - s \cdot i_p|_{(k-1)T_d} - \frac{di_p}{dt}|_{(k-1)T_d} \right)}_{\text{Part 1}} + \underbrace{2R_Y \left( s i_p(s) - i_p|_{(k-1)T_d} \right) + \frac{N}{C} i_p(s) - \left( \frac{N-k}{sC} \left\{ i_o|_{(k-1)T_d} - k \frac{V_{in}}{s N L_O} \right\} - k \frac{R_Y V_{in}}{s N L_O} \right)}_{\text{Part 2} + \text{Part 3}} \quad (8.10)$$

Analyzing (8.10), one can notice that parts **1** and **2** depend upon the initial condition which is subject to changes every time a new dwell interval commences. However, these two parts combined represent the differential equation with constant parameters. Part 3 is actually the one introducing the effect of a variable capacitance into the circuit (more precisely, the term  $(N-k)C^{-1}$ ). Given that (8.10) represents the second order differential equation, it is clear that the step response of the circuit it describes implies the existence of oscillations. Nevertheless, every time a new transition interval commences, the natural frequency of the circuit changes.

Moreover, an arbitrary circuit, formed during the voltage transition interval, oscillates in its natural manner only during the dwell interval being associated with it. With the observed dwell interval being finished, a new circuit is formed, using new parameters, and new voltage/current initial conditions, as presented in **Fig. 8.6**. To get a better insight into the previous discussion, **Fig. 8.7** presents the upper branch current transition in the converter depicted in **Fig. 8.4(a)**. Additionally, the transition period during which the upper branch voltage changes from zero to full input voltage is observed. Converter parameters used for the purpose of conducting the presented calculations can be found in **Tab. 8.1**.

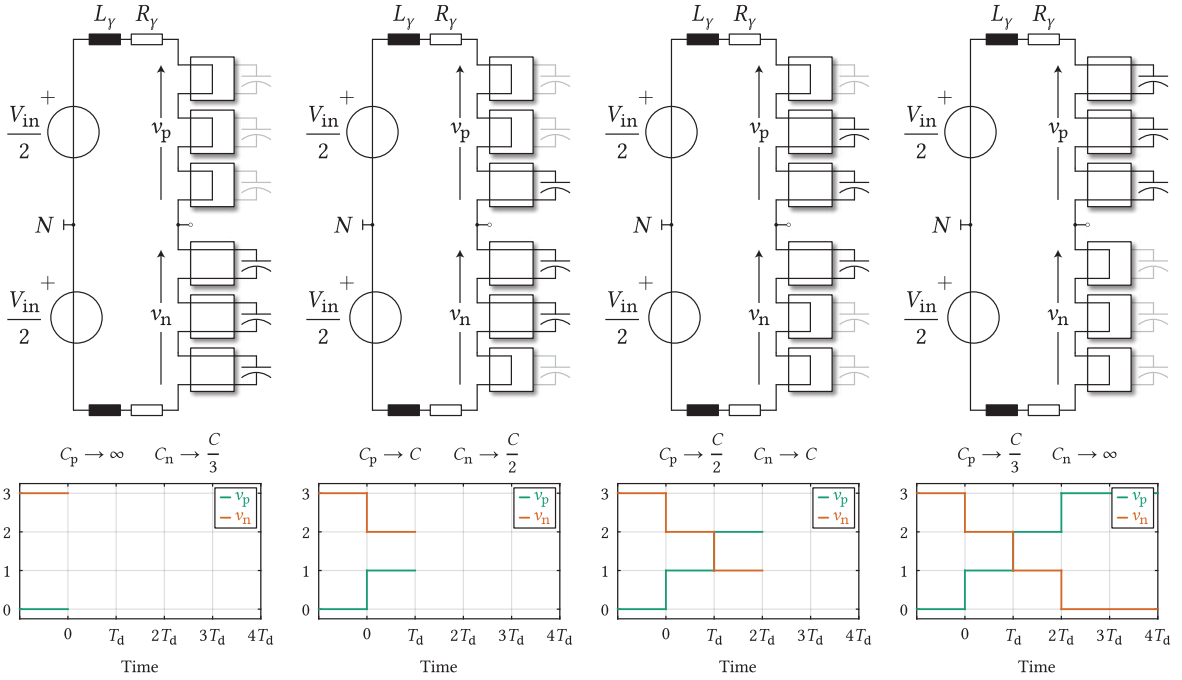


**Fig. 8.6** Q2L converter leg transition process in case  $N = 3$ . It can be seen that the branch equivalent capacitance changes depending on the leg switching stage, which introduces the resonances with different natural frequencies. Hence, every dwell interval can be analyzed individually, with new differential equations being taken into account. Please keep in mind that the exemplary cell insertion order, depicted above, was used for presentation purposes only.

**Fig. 8.7** contains several different plots, assuming the use of 1.7kV, 3.3kV and 6.5kV IGBT modules. Accordingly, dwell times were adjusted to match the approximate practical dead-times for a given voltage class. The number of SMs per branch was determined so that the average voltage across a SM capacitor equals approximately 55% of an employed semiconductor voltage class, as summarized in **Tab. 8.2**. Plots on the right-hand side of **Fig. 8.7** present the upper branch current behavior during the transition process assuming the stray inductance and the SM capacitance were increased by the factor of 100. Normalization was performed with respect to the maximum branch current. It is noteworthy that the converter with the increased passive components approaches the MMC behavior-wise, which can be concluded from the negligible branch current changes during the transition period. Even though the line between the Q2L converter and the MMC has not been distinctively drawn, it is clear from **Fig. 8.7** that the higher the branch inductance along with SM capacitance, the lower the resonant frequency of the converter leg, therefore, the lower the current changes originating from any transition processes. However, this contradicts the basic principles of Q2L operation mode.

**Tab. 8.1** Parameters of the converter used to showcase the behavior of its upper branch current during the voltage transition process

Input voltage ( $V_{in}$ )	Rated power ( $P_{nom}$ )	Operating frequency ( $f$ )	Branch stray inductance ( $L_\gamma$ )	Branch stray resistance ( $R_\gamma$ )	Output capacitance ( $L_o$ )
20kV	10MW	250Hz	1 $\mu$ H	40m $\Omega$	1.8mH

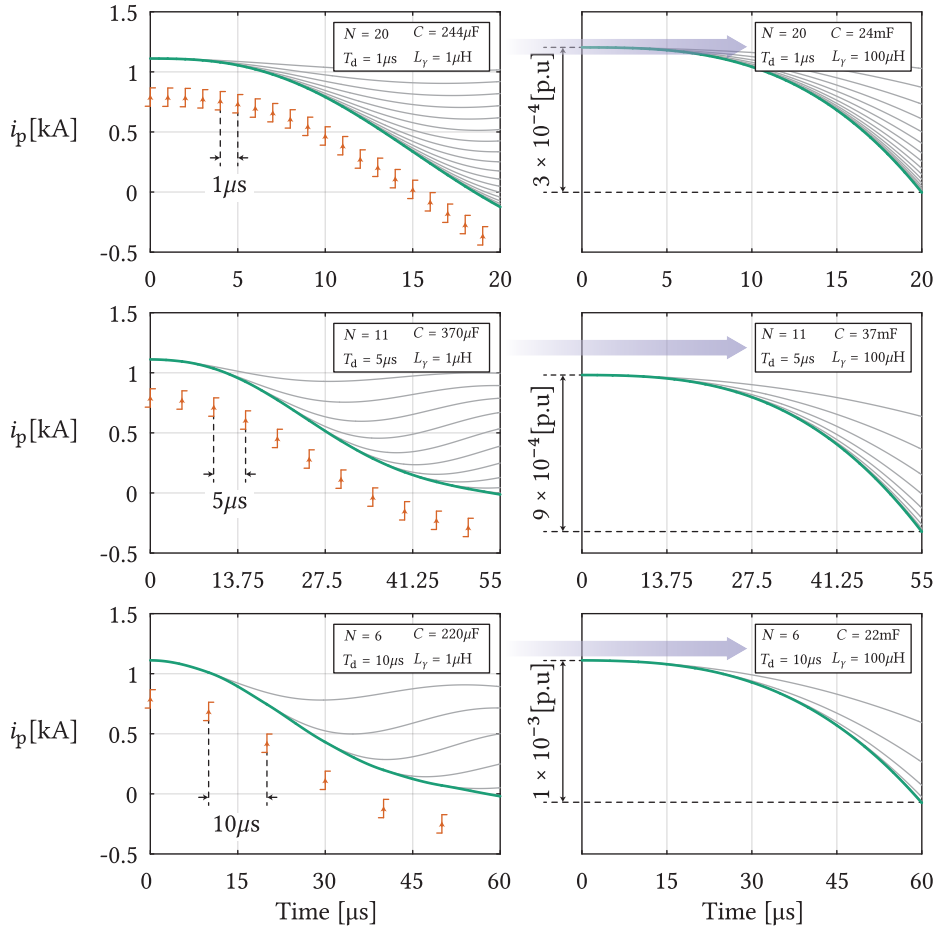


**Fig. 8.7** The upper branch current behavior during the transition process concerning different semiconductor voltage classes being employed (left). Level changes, indicated by brown steps, correspond to the insertion of one SM in the upper branch, followed by the bypassing of one SM in the lower branch. It can be seen that as long as the new level change is not triggered, the branch current oscillates along the so-called Non-Interrupted Response curve (gray). Insertion of a new SM into the circuit changes the branch resonant parameters, meaning that a new Non-Interrupted Response curve is established and followed until the next insertion takes place; The upper branch current behavior during the transition process providing the branch stray inductance and the SM capacitance were increased by the factor of 100 (right). The branch current was normalized with respect to its maximum value. Please notice that such an increase leads to the behavior recognized in the conventional MMC (considering that the branch current exhibits negligible change during the voltage transition period), which is in contrast to the basic principles of the Q2L operating mode. Therefore, if the Q2L operation is to be achieved without any additional common-mode current control, the branch stray inductance should be minimized. On these terms, however, the SM capacitance must be sized accordingly. Dwell times and the number of SMs were adjusted accordingly, depending on the voltage class of the employed switching devices.

Unless the conventional MMC operation is to be achieved, one should carefully design the converter circuit with the aim of minimizing the branch stray inductance, from which the SM capacitance can be determined. Otherwise, the leg output current drift from one branch to another takes too long and the Q2L operation becomes unfeasible. Please notice that the lower branch current can be easily calculated as  $i_n = i_p - i_o$ . Hence, the analysis of the upper branch can be considered sufficient.

**Tab. 8.2** Number of SMs per branch depending on the employed semiconductors voltage class

Voltage class	Number of SMs	Dwell time	SM capacitance
1.7kV	20	1 $\mu$ s	244 $\mu$ F
3.3kV	11	5 $\mu$ s	370 $\mu$ F
6.5kV	6	10 $\mu$ s	220 $\mu$ F

For a known branch stray inductance, piece-wise calculation of the branch current can be utilized with the aim of minimizing the SM capacitance meeting the requirements related to its voltage ripple under the most critical operating conditions. Namely, the critical operating conditions, at least from the converter design viewpoint, imply the operation with the maximal branch current, while providing the conditions to maintain the operation fulfilling the Q2L principles. An alternative to the piece-wise observations of the Q2L converter leg transition can be found in the analytic calculations, as presented in the following paragraphs.

### 8.2.3 Analytic analysis

It is worth restating that the assumption of the balancing algorithm, which keeps SMs' voltages within a predefined limits, existence holds. Hence, the average voltage across every SM capacitor can be assumed as  $\overline{V_{SM}} = V_{in}/N$ . In order to conduct the analysis of the Q2L converter branch current behavior, the transition at which the upper branch voltage exhibits the change from zero to full converter input voltage will be observed. Please note that, in accordance with **Fig. 8.4(b)**, the lower branch voltage changes in the opposite direction. To derive the upper branch current equation, it is necessary to know the shape of voltages labeled with  $v_p$  and  $v_n$  in **Fig. 8.4(a)**. The instant at which the transition commences will be adopted as the time axis origin ( $t = 0$ ), whereas the total transition time will henceforth be considered as  $T_T = NT_d$ .

#### 8.2.3.1 The upper branch voltage

Providing the SM insertion occurs sequentially, in equidistant time steps matching the dwell time  $T_d$ , as presented in **Fig. 8.2**, during an interval  $mT_d \leq t < (m+1)T_d$ , where  $m \in [0, N-1]$ , the instantaneous value of the upper branch voltage  $v_p$  can be calculated according to (8.11). With the aim of making the equations less cumbersome, floor  $\left\{\frac{t}{T_d}\right\}$  will temporarily be denoted by  $m$ .

$$v_p = V_{co}h(t) + \frac{1}{C} \int_0^t i_p dt + V_{co}h\left(t - T_d\right) + \frac{1}{C} \int_{T_d}^t i_p dt + \dots + V_{co}h\left(t - mT_d\right) + \int_{mT_d}^t i_p dt \quad (8.11)$$

Grouping the similar terms from (8.11), yields

$$v_p = \underbrace{\sum_{k=0}^m V_{c0} h(t - kT_d)}_{v_p^{(1)}} + \underbrace{\frac{1}{C} \sum_{k=0}^m \left( \int_{kT_d}^t i_p(\tau) d\tau \right)}_{v_p^{(2)}} \quad (8.12)$$

It can be seen from (8.12) that the upper branch voltage can be expressed through the sum of two terms which can be further inspected. Let one commence the analysis by observing the term labeled with  $v_p^{(1)}$ .

$$\begin{aligned} v_p^{(1)} &= \sum_{k=0}^m V_{c0} h(t - kT_d) \\ &= \frac{V_{in}}{NT_d} \sum_{k=0}^m h(t - kT_d) T_d \end{aligned} \quad (8.13)$$

According to **Tab. 8.2**, practical values of the dwell time  $T_d$  fall in the range of several microseconds. Therefore, with respect to the fundamental operating period of the converter (e.g. 4ms for 250Hz operation), the dwell time can, to a certain extent, be perceived as the time increment ( $T_d \rightarrow d\tau$ ), whereas the term  $kT_d$  can be considered almost continuous, therefore representing time ( $kT_d \rightarrow \tau$ ). Consequently, the sum can be replaced with the integral ( $\sum \rightarrow \int$ ), leading to

$$v_p^{(1)} = \frac{V_{in}}{T_T} \int_{\tau=0}^t h(t - \tau) d\tau \quad (8.14)$$

It is noteworthy that the shorter the dwell time the higher the precision of the results acquired using the above simplification. Additionally, using the basic property of Heaviside step function, provided in (8.4), equation (8.14) can be rearranged as (8.15). The above analysis can be illustrated as in **Fig. 8.8**.

$$v_p^{(1)} = \frac{V_{in}}{T_T} t \quad (8.15)$$

Applying the same reasoning to the second term in (8.12) provides

$$v_p^{(2)} = \frac{N}{CT_T} \int_0^t \left\{ \int_{\xi=\tau}^t i_p(\xi) d\xi \right\} d\tau \quad (8.16)$$

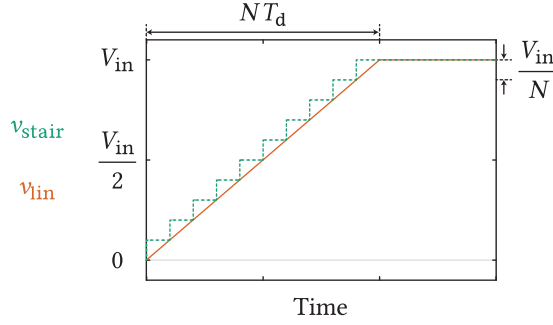


**Fig. 8.8** Graphical illustration of the linearization process

Finally, at any time instant fulfilling the condition  $0 < t < T_T$ , the upper branch voltage can be approximated as

$$v_p = \frac{V_{in}}{T_T} t + \frac{N}{CT_T} \int_0^t \left\{ \int_{\xi=\tau}^t i_p(\xi) d\xi \right\} d\tau \quad (8.17)$$

### 8.2.3.2 The lower branch voltage

By observing the idealized voltage waveforms provided in **Fig. 8.2**, instantaneous value of the lower branch voltage, during the interval  $mT_d \leq t < (m+1)T_d$ , where  $m \in [0, N-1]$ , can be expressed as

$$v_n = V_{co} \left\{ (N-1)h(t) - h(t-T_d) - \dots - h(t-mT_d) \right\} + \frac{N-1}{C} \int_0^{T_d} i_n(\tau) d\tau + \frac{N-2}{C} \int_{T_d}^{2T_d} i_n(\tau) d\tau + \dots + \frac{N-(m+1)}{C} \int_{mT_d}^t i_n(\tau) d\tau \quad (8.18)$$

Following the analysis already presented above, two terms  $v_n^{(1)}$  (the first line of the above expression) and  $v_n^{(2)}$  (second line of the above expression) can be identified. Further, the term labeled with  $v_n^{(1)}$  can be expressed as

$$v_n^{(1)} = V_{in} h(t) - \frac{V_{in}}{T_T} \sum_0^m h\left(t - kT_d\right) T_d \quad (8.19)$$

Approximation techniques applied within the paragraph devoted to the upper branch voltage determination can be reapplied here, leading to

$$v_n^{(1)} = V_{in} \left( 1 - \frac{t}{T_T} \right) \quad (8.20)$$

As for the other term from (8.18), one can easily notice from (8.21) that it can as well be presented with two separate terms  $v_n^{(2,1)}$  and  $v_n^{(2,2)}$ , respectively.

$$v_n^{(2)} = \underbrace{\frac{N}{C} \left\{ \int_0^{T_d} i_n d\tau + \int_{T_d}^{2T_d} i_n d\tau + \dots + \int_{mT_d}^t i_n d\tau \right\}}_{v_n^{(2,1)}} - \underbrace{\frac{1}{C} \left\{ \int_0^{T_d} i_n d\tau + 2 \int_{T_d}^{2T_d} i_n d\tau + \dots + (m+1) \int_{mT_d}^t i_n d\tau \right\}}_{v_n^{(2,2)}} \quad (8.21)$$

Sum of integrals in  $v_n^{(2,1)}$  actually represents the integral of the lower branch current over time (8.22).

$$v_n^{(2,1)} = \frac{N}{C} \int_0^t i_n(\tau) d\tau \quad (8.22)$$

The upper limit of the integral inside the sum in (8.23), should be paid the attention to. It can be seen that the last term of the integral sum from (8.21) considers the integral with the lower limit equal to  $mT_d$  and the upper one equal to the observed time instant  $t$ . However, if  $T_d$  is considered sufficiently small, it can be claimed that the error committed by extending the limit of the last integral within the sum in (8.23) to  $kT_d$  will not introduce large computational error into the calculations (the purpose of such a step being the simplification of mathematical operations to be performed).

$$v_n^{(2,2)} = \frac{N}{CT_T} \sum_{k=1}^{m+1} k \left\{ \int_{(k-1)T_d}^{kT_d} i_n dt \right\} T_d \quad (8.23)$$

Further, it can as well be claimed that the lower branch current will not significantly change during the dwell interval, providing  $T_d$  being considered infinitely small (in case  $T_d \rightarrow d\tau$ ). Hence, the integral from the above equation can be solved in a simplified manner, which yields

$$v_n^{(2,2)} = \frac{N}{CT_T} \sum_{k=0}^{m+1} \left( kT_d \right) i_n T_d \quad (8.24)$$

Once again,  $T_d$  can be translated into the time increment  $d\tau$ , leading to

$$v_n^{(2,2)} = \frac{N}{CT_T} \int_0^t \tau i(\tau) d\tau \quad (8.25)$$



Finally, combination of (8.20), (8.22) and (8.25) leads to the instantaneous value of the lower branch voltage during the observed transition period.

$$v_n = V_{in} \left( 1 - \frac{t}{T_T} \right) + \frac{N}{C} \int_0^t i_n(\tau) d\tau - \frac{N}{CT_T} \int_0^t \tau i(\tau) d\tau \quad (8.26)$$

Once the voltages across the Q2L converter branches are known, the upper/lower branch current can be evaluated as well. The motivation for expressing the branch instantaneous voltage equations by virtue of integral terms lies in the fact that Laplace transform can be applied and all the equations solved in the continuous domain even though voltage transition occurs in discretely defined time steps. In other words, no piecewise solutions are necessary once the analytic solutions defining the branch currents within the time frame defined as  $t \in [0, T_T]$  are derived.

### 8.2.3.3 Branch currents determination

To derive the expressions describing the branch currents during the Q2L converter transition process, derivatives of the upper and the lower branch voltage need to be calculated as

$$\frac{dv_p}{dt} = \frac{d}{dt} \left( \frac{V_{in}}{T_T} t + \frac{N}{CT_T} \int_0^t \left\{ \int_{\xi=\tau}^t i_p(\xi) d\xi \right\} d\tau \right) \quad (8.27)$$

$$\frac{dv_n}{dt} = \frac{d}{dt} \left( V_{in} \left( 1 - \frac{t}{T_T} \right) + \frac{N}{C} \int_0^t i_n(\tau) d\tau - \frac{N}{CT_T} \int_0^t \tau i(\tau) d\tau \right) \quad (8.28)$$

It can be seen from (8.27) that calculating the derivative of its second term is not that straightforward due to the existence of double integral. However, *Leibnitz integral rule* provided in (8.29) can be used for the purpose of conducting the desired differentiation.

$$\frac{d}{dt} \left( \int_{a(t)}^{b(t)} f(t, \tau) d\tau \right) = f(t, b(t)) \frac{db(t)}{dt} - f(t, a(t)) \frac{da(t)}{dt} + \int_{a(t)}^{b(t)} \frac{\partial f(t, \tau)}{\partial t} d\tau \quad (8.29)$$

Another mathematical relation defined by (8.30) will also be recalled to calculate the derivatives of the upper and the lower branch voltage.

$$\frac{d}{dt} \int_a^t f(\tau) d\tau = f(t) \quad (8.30)$$

By combining (8.29) and (8.30), the derivatives required for further analysis can be calculated as

$$\frac{dv_p}{dt} = \frac{V_{in}}{T_T} + \frac{N}{CT_T} ti_p \quad (8.31)$$

$$\frac{dv_n}{dt} = -\frac{V_{in}}{T_T} - \frac{N}{CT_T} ti_p + \frac{N}{C} i_p - \frac{N}{C} i_o + \frac{N}{CT_T} ti_o \quad (8.32)$$

Summation of (8.31) and (8.32) yields

$$\frac{d}{dt}(v_p + v_n) = \frac{N}{C} i_p - \frac{N}{C} i_o + \frac{N}{CT_T} ti_o \quad (8.33)$$

Equation (8.33) suggests that the upper/lower branch current dynamics also depends on the leg output current dynamics. It can be shown that voltage across the Q2L converter phase inductor  $L_o$  can be calculated according to (8.34). One can also notice that approximately linear change of voltage across the output inductor occurs due to the sequential change of upper and lower branch voltages within the observed converter leg.

$$v_{L_o} = -\rho \frac{V_{in}}{T_T} t \quad (8.34)$$

Hence, the output current dynamics during the Q2L leg voltage transition process can be described with

$$\frac{di_o}{dt} = -\rho \frac{V_{in}}{L_o T_T} t, \quad (8.35)$$

where

$$\rho = \begin{cases} 1, & \text{1PH-DAB HB config.} \\ 2, & \text{1PH-DAB FB config.} \\ 2/3, & \text{3PH-DAB} \end{cases}$$

In (8.35) coefficient  $\rho$  changes depending on the analyzed circuit configuration, which can be seen in **Fig. 8.9**. In case Q2L VSC intended for low output frequency operation is observed, coefficient  $\rho$ , from the equation above, can be considered equal to zero, providing fundamental switching period of the converter is sufficiently small compared to the output current frequency (for instance, 200Hz switching frequency employed to synthesize 1Hz output current). In order to solve the equation obtained by differentiating (8.5), it comes in handy to observe all of its quantities in the Laplace domain.

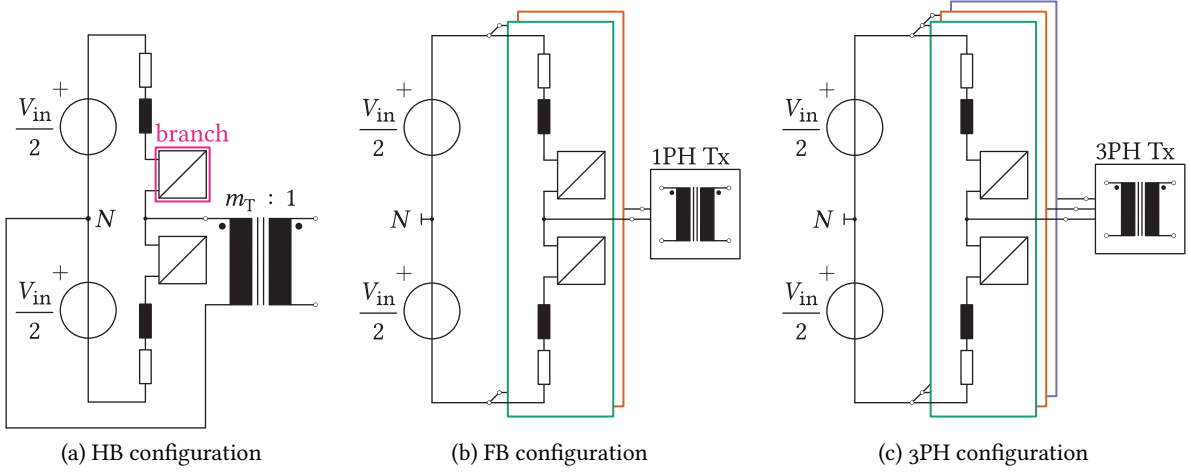


**Fig. 8.9** Circuit configurations used to investigate the Q2L converter branch current behavior. Depending on the application, each of the presented topologies can be employed either as the DAB or with the aim of synthesizing the low output frequency waveforms.

Therefore, the output current Laplace transform can be performed according to (8.36), assuming the converter phase current flows exclusively through the upper branch prior to entering the transition process.

$$I_o(s) = \frac{\hat{i}_o}{s} - \frac{\rho V_{in}}{s^3 L_o T_T} \quad (8.36)$$

In the above equation, the current flowing through the upper branch of the Q2L converter switching leg, at the beginning of the transition interval, was denoted by  $\hat{i}_o$ . Its value also depends on the analyzed configuration, according to (8.37), where  $\varphi$  denotes relevant voltage waveforms phase-shift in case DAB-alike topologies are analyzed. If, however, low output frequency applications were subject to the analysis, the output current amplitude is denoted by  $I_{max}$ .

$$\hat{i}_o = \begin{cases} V_{in}\varphi/(2\omega L_o), & \text{1PH-DAB HB config.} \\ V_{in}\varphi/(\omega L_o), & \text{1PH-DAB FB config.} \\ V_{in}\varphi/(3\omega L_o), & \text{3PH-DAB} \\ I_{max}, & \text{LF operation.} \end{cases} \quad (8.37)$$

The lower branch current  $i_n$  can be expressed as the difference between the upper branch current and the leg output current. Consequently, equation (8.38) can be established.

$$0 = \underbrace{2L_\gamma \frac{d^2 i_p}{dt^2} + 2R_\gamma \frac{di_p}{dt} + \frac{N}{C} i_p}_{\text{Part 1}} - \underbrace{\left( L_\gamma \frac{d^2 i_o}{dt^2} + R_\gamma \frac{di_o}{dt} + \frac{N}{C} i_o - \frac{N}{CT_T} t i_o \right)}_{\text{Part 2}} \quad (8.38)$$

With the aim of transposing (8.38) into the s-domain, the property provided in (8.39) is used.

$$\mathcal{L}\left\{tf(t)\right\} = -\frac{dF(s)}{ds} \quad (8.39)$$

As a result, the s-domain image of the upper branch current equals

$$I_p(s) = \frac{a_5 s^5 + a_4 s^4 + a_3 s^3 + a_2 s^2 + a_1 s + a_0}{b_6 s^6 + b_5 s^5 + b_4 s^4}, \quad (8.40)$$

where

$$\begin{aligned} a_5 &= 2C\hat{i}_0 L_\gamma L_o T_T^2 \\ a_4 &= 2C\hat{i}_0 R_\gamma L_o T_T^2 \\ a_3 &= \hat{i}_0 N L_o T_T^2 - C L_\gamma T_T V_{in} \rho \\ a_2 &= -\hat{i}_0 N L_o T_T - C R_\gamma T_T V_{in} \rho \\ a_1 &= -N T_T V_{in} \rho \\ a_0 &= 3N V_{in} \rho \\ b_6 &= 2C L_\gamma L_o T_T^2 \\ b_5 &= 2C L_o R_\gamma T_T^2 \\ b_4 &= L_o N T_T^2 \end{aligned}$$

Expression (8.40) can be split into two parts representing different time domain responses (8.41). The first part of (8.41) indicates that the upper branch current response to the voltage excitation defined by (8.33) represents a sum of cubic, square and linear function and a constant term. Second fraction in (8.41) represents a sinusoidal function.

$$\begin{aligned} i_p(s) &= \frac{a_5 s^5 + a_4 s^4 + a_3 s^3 + a_2 s^2 + a_1 s + a_0}{b_6 s^6 + b_5 s^5 + b_4 s^4} \\ &= \underbrace{\frac{p_3 s^3 + p_2 s^2 + p_1 s + p_0}{s^4}}_{\text{Cubic + Square + Linear + Constant Term}} + \underbrace{\frac{q_1 s + q_0}{b_6 s^2 + b_5 s + b_4}}_{\text{Sinusoidal Term}} \end{aligned} \quad (8.41)$$

Accordingly, the inverse Laplace transform of (8.41) can be represented in the form of (8.42), with all the coefficients being defined in (8.43) and (8.44)

$$\mathcal{L}^{-1}\left\{i_p(s)\right\} = Q_4(Q_3 t^3 + Q_2 t^2 + Q_1 t + Q_0) + e^{-\frac{R_\gamma}{2L_\gamma} t} S_3 \left[ S_1 \sin(\omega_r t) + S_2 \cos(\omega_r t) \right] \quad (8.42)$$

$$\begin{aligned}
Q_0 &= \rho V_{in} \left\{ (2CL_Y N^2 - 4C^2 N R_Y^2) T_T - 48C^3 R_Y^3 + 48C^2 L_Y N R_Y \right\} + 2\hat{i}_0 L_0 N^3 T_T^2 + 4C\hat{i}_0 L_0 N^2 R_Y T_T \\
Q_1 &= \rho V_{in} \left\{ 2CN^2 R_Y T_T + 24C^2 N R_Y^2 - 12CL_Y N^2 \right\} - 2\hat{i}_0 L_0 N^3 T_T \\
Q_2 &= -\rho V_{in} (N^3 T_T + 6CN^2 R_Y) \\
Q_3 &= \rho V_{in} N^3 \\
Q_4 &= \frac{1}{2L_0 N^3 T_T^2}
\end{aligned} \tag{8.43}$$

$$\begin{aligned}
S_1 &= \rho V_{in} \left\{ (2C^3 N R_Y^3 - 3C^2 L_Y N^2 R_Y) T_T + 24C^4 R_Y^4 - 48C^3 L_Y N R_Y^2 + 12C^2 L_Y^2 N^2 \right\} + \dots \\
&\dots + \left\{ 2C\hat{i}_0 L_Y L_0 N^3 - 2C^2 \hat{i}_0 L_0 N^2 R_Y^2 \right\} T_T \\
S_2 &= \left\{ \rho V_{in} \left( (2C^2 N R_Y^2 - CL_Y N^2) T_T + 24C^3 R_Y^3 - 24C^2 L_Y N R_Y \right) - 2C\hat{i}_0 L_0 N^2 R_Y T_T \right\} \sqrt{2CL_Y N - C^2 R_Y^2} \\
S_3 &= \frac{1}{L_0 N^3 T_T^2 \sqrt{2CL_Y N - C^2 R_Y^2}} \\
\omega_r &= \frac{\sqrt{2CL_Y N - C^2 R_Y^2}}{2CL_Y}
\end{aligned} \tag{8.44}$$

Since (8.43) and (8.44) are quite cumbersome, it would be useful to graphically examine the effect of certain factors on the upper/lower branch current shape during the voltage transition period. For that matter, the converter operating with parameters provided in **Tab. 8.1** is observed. However, three different branch stray inductance values were used with the aim of conducting the analysis of the desired response components, whereas the SM capacitance was fixed at  $C_{sm} = 370\mu F$  (this value was set according to the sizing algorithm, which is to be presented shortly). The number of SMs per branch was set as  $N = 11$ , whereas the results can be found in **Fig. 8.10**.

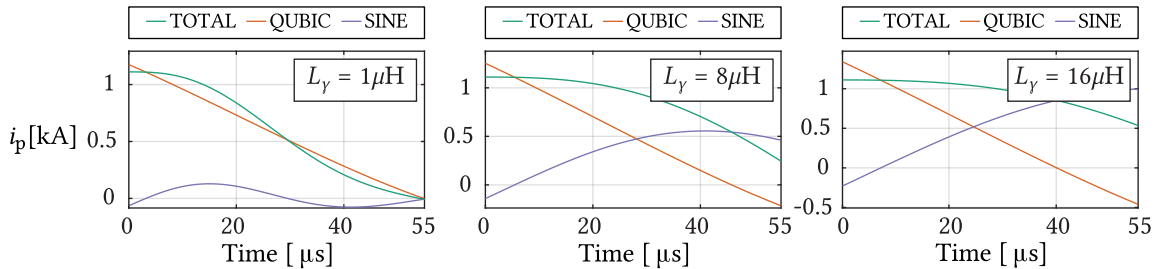


**Fig. 8.10** Effect of the branch stray inductance on the upper branch current components. The number of SMs per branch was set as  $N = 11$ , whereas the SM capacitance was set as  $C = 370\mu F$ . It can be seen that an increase in the branch stray inductance causes an increase in both the period and the amplitude of sinusoidal component. Moreover, the non-sinusoidal part of (8.42) tends to be less sensitive to the stray inductance changes.

As presented, the higher the stray inductance, the more emphasized the effect of the sinusoidal component in the branch current response. This is, to a certain extent, logical given that, for a fixed SM capacitance, higher inductance reduces the natural frequency of all the oscillations occurring within the observed circuit.

With the aim of getting an insight into the effect of the aforementioned stray inductance upon the branch currents over the complete fundamental operating period, the circuits utilizing the parameters defined in **Fig. 8.10** were simulated in PLECS. It can be seen from **Fig. 8.11** that with an increase in the branch stray inductance (moving from left to right) its current oscillations become more emphasized, both in terms of duration and the overshoot. Additionally, the higher the stray inductance the more time the leg output current needs to drift from one branch to another. Consequently, the need for a larger SM capacitance, with the aim of keeping its voltage within a predefined limits, gets increased. During the previously conducted analysis, it was assumed that the converter input voltage was stiff. Notwithstanding, a certain capacitive filter at the converter input stage would be inevitable in practice. Last but not least, if the branch stray inductance were unreasonably high, the output current drift would not manage to occur prior to the following voltage transition. Therefore, the basic principles of the Q2L operation mode would be violated and the converter operation approaches the MMC. Hence, during the converter design phase, efforts to keep the branch stray inductance as low as possible should be made.

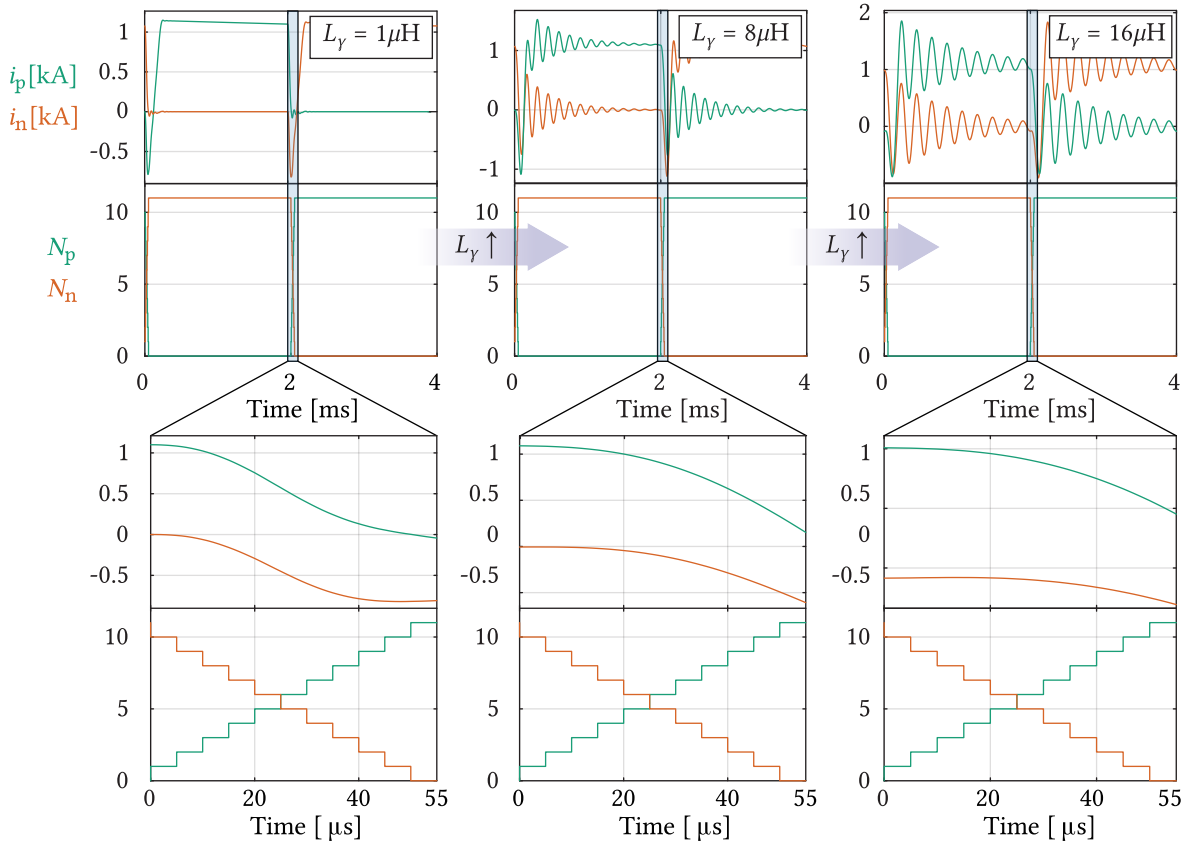


**Fig. 8.11** Effect of the branch stray inductance on general converter behavior.

### 8.3 Submodule capacitor sizing

**Figs. 8.10** and **8.11** demonstrated the adverse effect the branch stray inductance has on the Q2L converter operation. Consequently, for a known branch parameters, the SM capacitance needs to be determined such that a compromise between its desired voltage ripple and the Q2L operation can be made. **Fig. 8.12** presents the idealized upper branch current during the voltage transition period. At the beginning of the transition interval, one SM within the upper branch gets inserted into the circuit, meaning that the whole current flowing through the upper branch during the interval defined as  $0 < t \leq T_T$  flows through its capacitor, consequently changing its voltage.

It is indicated in **Fig. 8.12** that the area under the current curve represents the charge received by the capacitor of a firstly inserted SM during the observed process. Hence, the capacitor of every SM must be sized according to this area since the balancing algorithm selects one of the SMs to the beginning of the insertion sequence depending upon the voltage distribution over the branch. Furthermore, it would be highly beneficial if the upper branch current crossed zero within the observed interval considering that the charge acquired by the first SM being inserted into the circuit would be reduced compared to the case where no zero crossing occurs. However, if this comes out as unachievable, defining a certain band around zero described with  $|i| \leq \epsilon$  can be considered for the purpose of SM capacitance sizing. In other words, handling the transitions with no zero-crossings of the branch current is alleviated. It should be emphasized that determination of  $\epsilon$  depends on the circuit designer. However, one has to keep in mind that the higher the tolerance represented by this coefficient, the higher the possible capacitance being the output of the presented algorithm (the area denoted by  $Q^+$  increases). Moreover, the longer the transition the closer the converter approaches the MMC behavior-wise, therefore violating the basic Q2L principles.

**Fig. 8.13** presents the sizing algorithm flow chart. Firstly, all parameters related to the converter operation, such as input voltage, operating frequency, rated power, maximum branch current and passive components, apart from the SM capacitance, are defined. Additionally, a certain range of possible SM capacitances, over which the algorithm is going to perform the search, needs to be defined. Maximum capacitance  $C_{SM}^{\max}$  to be taken into account by the algorithm can be estimated assuming the constant output current flows through the branch during the transition (8.45).

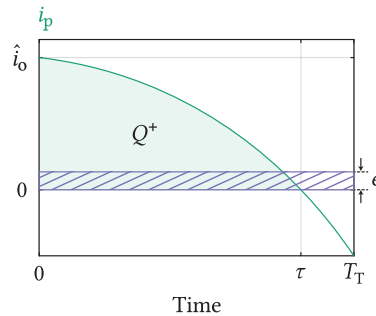


**Fig. 8.12** Q2L converter upper branch current shape during the transition process (idealized). It is noteworthy that once the transition period commences, the capacitor in an observed branch, being firstly inserted into the circuit, acquires all the charge denoted by  $Q^+$ . Therefore, the SM capacitor sizing needs to be conducted according to this charge given that some other SM will be assigned to this gate signal in the following transition interval.

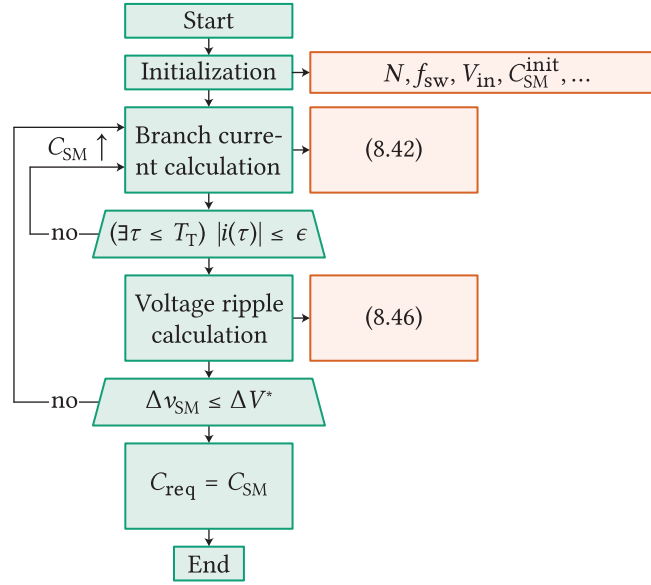


**Fig. 8.13** Flowchart of the algorithm used to determine SM capacitance value

$$C_{SM}^{\max} = \frac{\hat{i}_o T_T}{\Delta V^*} \quad (8.45)$$

In the above equation  $\Delta V^*$  refers to the desired SM voltage ripple under the nominal operating conditions, which implies the rated current flowing through the upper branch prior to commencing the transition. With the aim of calculating this current, (8.37) can be used, where the phase-angle resulting in the rated power flowing through the converter  $\varphi_{nom}$  should be used. Minimal capacitance  $C_{SM}^{init}$ , to be used with the aim of starting the algorithm, can be adopted as a fraction of the maximal one (for instance  $C_{SM}^{init} = C_{SM}^{\max}/4$ ). Thereafter, the upper branch current can be calculated according to (8.42)-(8.44), whereas the algorithm checks if the calculated current falls within the band defined by  $|i| \leq \epsilon$  for any time instant  $\tau \leq T_T$ . If so, the SM voltage ripple  $\Delta v_{SM}$  can be calculated according to (8.46), otherwise, the algorithm runs into a new iteration.

$$\Delta v_{SM}(k) = \frac{1}{C_{SM}(k)} \int_0^{\tau} i_p dt \quad (8.46)$$

If the capacitance taken into account in the observed iteration fulfills the desired voltage ripple criteria ( $\Delta v_{SM} < \Delta V^*$ ), the algorithm assigns its value to the required SM capacitance ( $C_{req}$ ). Moreover, once the first capacitance fulfilling the above mentioned criteria is found, the algorithm terminates the search given that the subsequent iterations would provide higher values of the SM capacitance. Of course, if needed, it is always possible to adopt a certain margin in the SM capacitance, as presented in the expression below.

$$C_{SM}^* = \gamma C_{req} \quad (8.47)$$



## 8.4 Simulation results

In order to validate the analysis conducted above, a set of simulations was performed using PLECS. Parameters of the simulated converter, which is presented in **Fig. 8.4(a)** can be found in **Tab. 8.1**. Moreover, the simulations were conducted utilizing various number of SMs depending upon the voltage class of semiconductors to be employed, as indicated in **Tab. 8.2**. Last but not least, simulation results during the transition are compared with both piece-wise calculations (8.10) and analytic equations (8.42)-(8.44).

**Fig. 8.14(a)** presents the converter operation over five fundamental cycles in case 6.5kV IGBTs are employed in every SM. It can be seen that SMs' voltages remain balanced during the observed interval. The SM capacitance was determined such that its voltage change during the transition interval remains less than 5% of the nominal value ( $V_{in}/N$ ). Please notice from the plot illustrating the upper and the lower branch current, that each of the branches conducts the output current only during half of the fundamental period. In other words, preservation of the Q2L operating principles is guaranteed. On the other hand, **Fig. 8.14(b)** presents operation of the converter during the leg voltage transition period. As indicated, maximal voltage change of a SM equals  $\Delta \hat{V}_{SM} = 130V$ , which is aligned with the voltage ripple criteria established above. **Figs. 8.15** and **8.16** present the same set of waveforms, however, in case 3.3kV and 1.7kV IGBTs are used in the SM building process. From both figures, one can notice that the SM capacitance sizing algorithm performs its role correctly. Namely, Q2L operation is guaranteed since both branches conduct the output current during half of the fundamental cycle (excluding the transition), while the SM voltage ripple remained within the predefined boundaries.

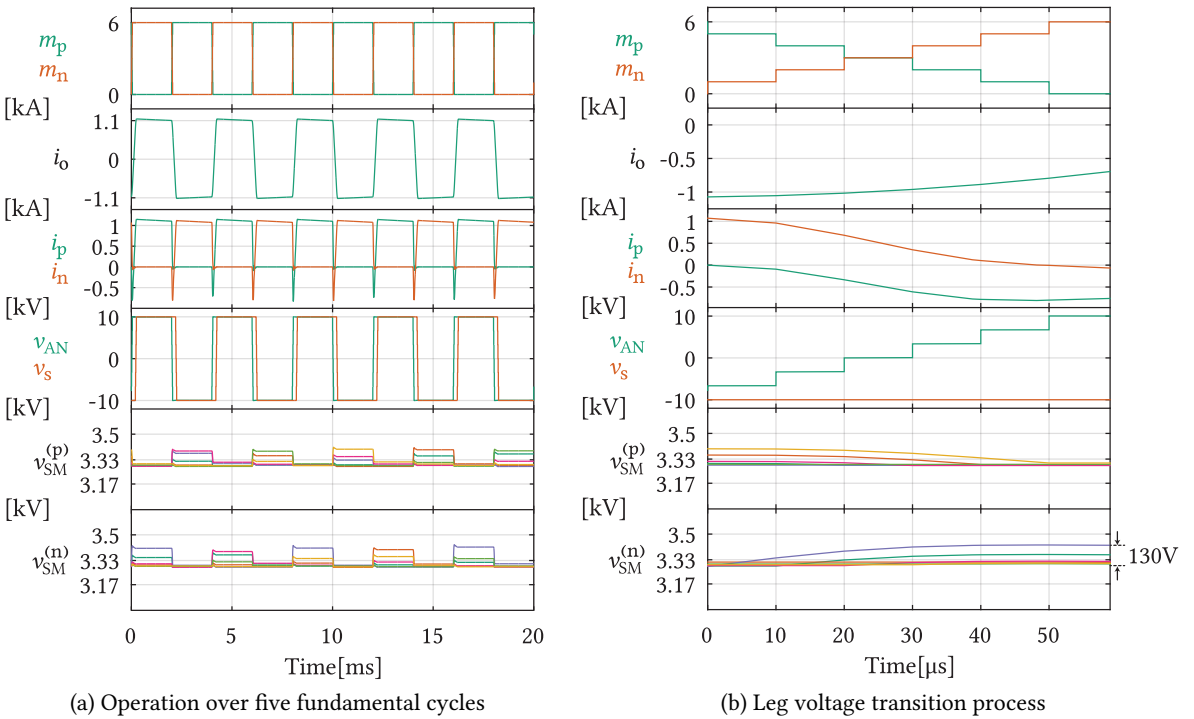
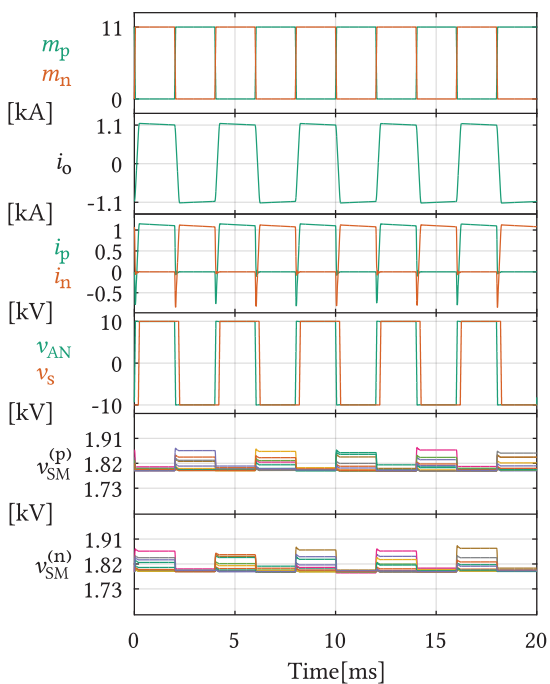
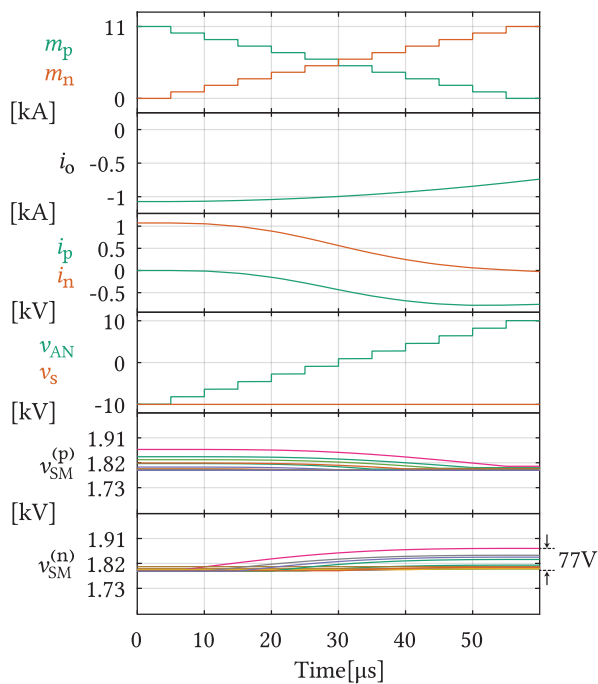


**Fig. 8.14** Simulation results in case 6.5kV IGBTs are used with the aim of realizing the SMs

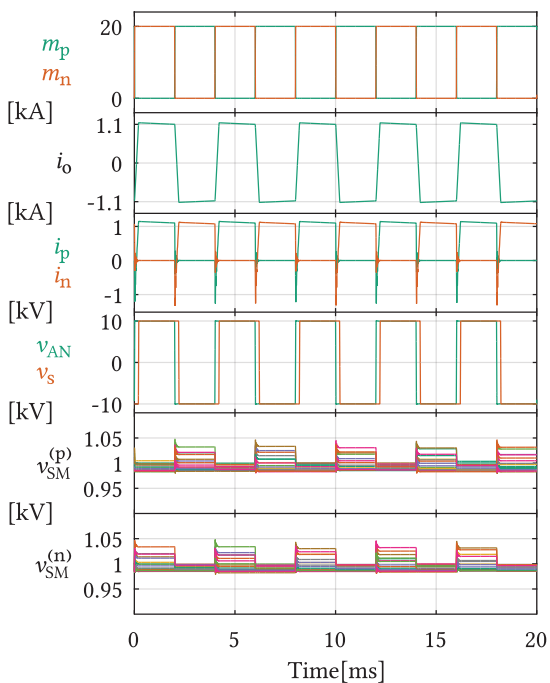


(a) Operation over five fundamental cycles

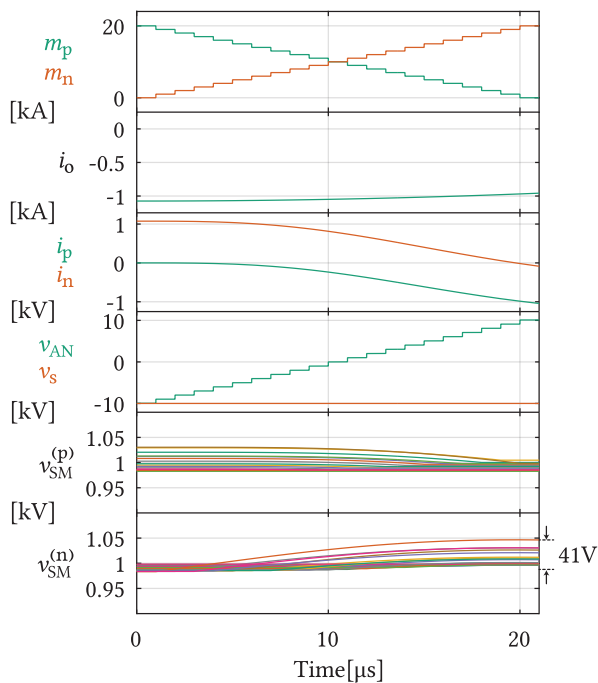


(b) Leg voltage transition process

**Fig. 8.15** Simulation results in case 3.3kV IGBTs are used with the aim of realizing the SMs



(a) Operation over five fundamental cycles



(b) Leg voltage transition process

**Fig. 8.16** Simulation results in case 1.7kV IGBTs are used with the aim of realizing the SMs

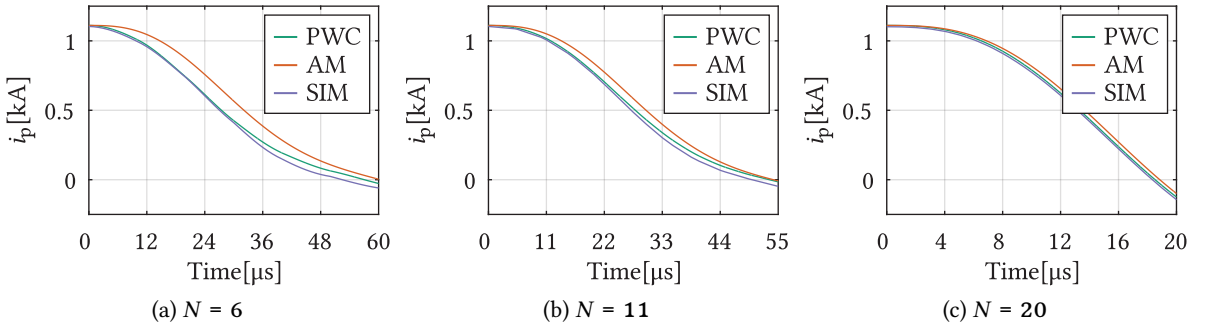


**Fig. 8.17** Comparison of the results obtained by means of the piece-wise calculations, analytic analysis and simulation tools. The analyses were conducted using different number of SMs, which confirmed that the higher the number of employed SMs, with reduced dwell time, the higher the precision of results obtained by means of expressions derived in **Sec. 8.2.3**.

With the aim of verifying the precision of expressions derived throughout **Sec. 8.2.3**, the comparison among the results obtained by means of the piece-wise calculations, analytic models and simulation tools, denoted in **Fig. 8.17** by PWC, AM and SIM, respectively, was made. As expected, an increase in the number of employed SMs, which allows for the reduction of the dwell time, ensures higher precision of the obtained results.

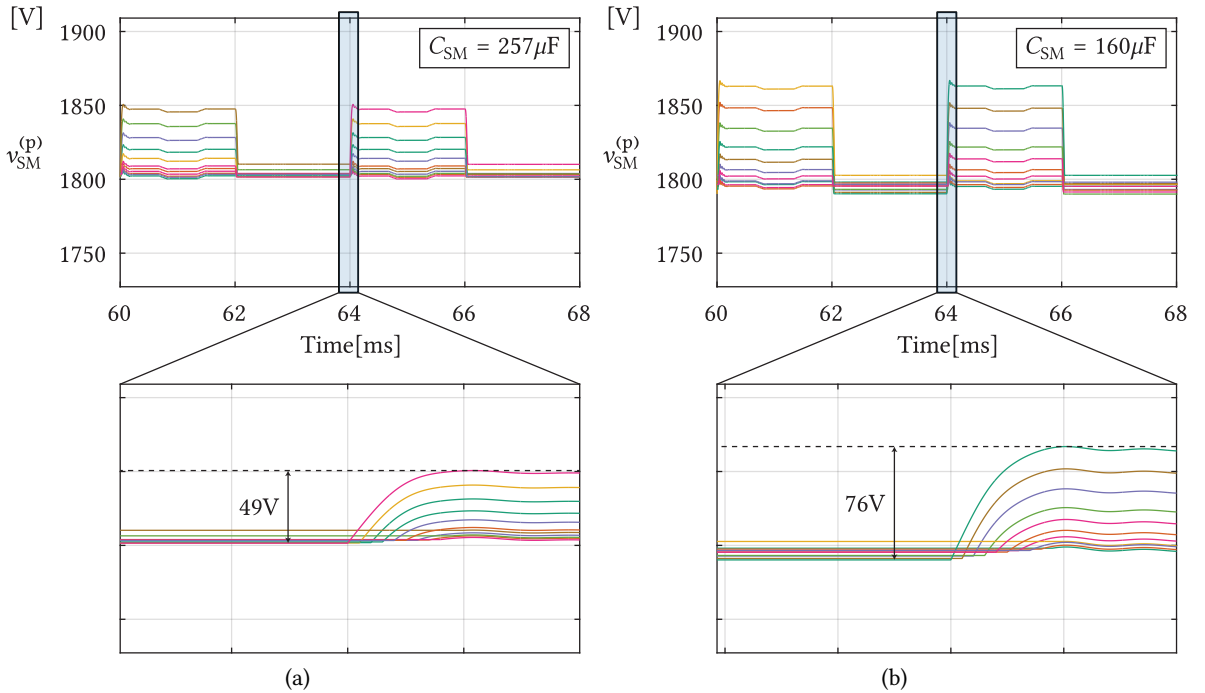


**Fig. 8.18** Voltage across the SM capacitors in case  $N = 11$  SMs per branch are employed. On the left-hand side, one can see that peak-to-peak voltage ripple, in case (8.48) is used for the sizing purposes, equals approximately 2.53% of the SM rated voltage. However, on the right-hand side, one can notice that even with almost 40% reduction in the SM capacitance, which is the result obtained based on the employment of the presented algorithm, the same voltage ripple criterion can be fulfilled.

The algorithm presented in **Sec. 8.3** was also employed with the aim of sizing the SM capacitance for the converter operating as the 3PH DAB. Reference [58] provided the SM capacitance sizing rule as

$$C_{SM} = \gamma \frac{N T_T}{3 \omega L_o \Delta V_{sm}(p.u)} \left( \varphi_{nom} - \frac{\omega T_T}{3} \right) \quad (8.48)$$

For the sake of comparison, 3PH DAB with parameters given in **Tab. 8.1** was observed. The number of SMs was set as  $N = 11$ . According to (8.48), the SM capacitance should be set as  $C_{SM} = 257 \mu F$  with the aim of constraining the SM voltage ripple to the values lower than 5% of its nominal mean value ( $\Delta V_{sm}(p.u) = 0.05$ ). The security factor  $\gamma$  was set as unity. On the other hand, by using the sizing algorithm presented in this chapter, the capacitance value of  $C_{SM} = 160 \mu F$  was chosen. **Fig. 8.18** presents voltages across the phase A upper branch in the 3PH DAB operating in the Q2L manner, while using the capacitances determined above. It can be seen that the use of the proposed algorithm provides the possibility to reduce the SMs capacitance by approximately 40%, while still fulfilling a desired voltage ripple constraints. Such a reduction in the SM capacitance originates from the high precision branch current calculation during the leg transition process.

## 8.5 Summary

This chapter presented a thorough mathematical analysis of the Q2L converter leg transition process. With the aim of alleviating mathematical determination of the SM capacitance, analytical formulas were derived. Instead of solving  $N$  differential equations (piece-wise solution) with the aim of determining converter's current shape over the transition interval, the approximation comprising the combination of sinusoidal, cubic, square, linear and constant term was provided. Given that presented approximation represents the linearization of transient waveforms, the smaller the dwell intervals, used to achieve desired transition, the better the approximation results. By virtue of the proposed equations, capacitor sizing algorithm was designed with the aim of finding the capacitance to meet the requirements of SM voltage ripple and Q2L operation. Furthermore, on the example of the 3PH DAB, it was shown that the proposed sizing algorithm reduces the need for SM capacitance compared to the sizing methods proposed in the literature. Simulation results obtained in PLECS were presented, from which it can be seen that the converter manages to operate in the Q2L mode while keeping the voltage ripple across SMs within desired limits.

# 9

## Summary and Future Works

*This chapter summarizes all the contributions this thesis has brought into the field of high power modular multilevel converter-based conversion. Moreover, a brief overview outlining the set of possible improvements to the work provided throughout this manuscript is presented.*

### 9.1 Summary and contributions

This thesis focused on various MMC-related topics, including the control and investigation of the possibilities provided by the MMC in the domain of both DC-AC and DC-DC high power conversion.

**Chap. 2** introduced the MMC as the device comprising the strings of series-connected SMs. Equation aggregation on the branch level was performed to provide the grounds for the modeling approach used throughout the subsequent discussions. Furthermore, based on the suitable system of equations describing the phase-leg of the conventional 3PH MMC, the decoupled nature of the AC and DC terminals was demonstrated. The presented reasoning has already been known and well mastered, nevertheless, it provided the framework for the discussions that followed in the next chapters.

**Chap. 3** commences with the identification of control loops relevant for the control of the terminal currents. It is worthy to note that DC and AC terminal currents of the MMC feature the possibility of being controlled decoupled from each other. Consequently, the total amount of energy stored inside the MMC can be affected. Further, to obtain equal energy distribution among the MMC branches, the concept of circulating currents was utilized. However, the proper control of circulating currents implies that they must remain invisible in the MMC DC link. Ensuring such a property requires the mapping of control references obtained in "per-phase" fashion and it is exactly where this thesis provided the reinforcement and the extension of methods already known in the literature.

A detailed explanation of the reference mapping method relying on the use of SVD was provided in **Chap. 3** and it served as the underlying basis for the derivations utilized to outline the differences between three horizontal and vertical balancing methods proposed in the literature. Although different at first glance, these energy balancing methods can be compared through an elegant control diagram to show that the only difference among them refers to a set of multiplication constants. As a result, a straightforward comparison among the dynamic responses of horizontal and vertical balancing controllers can be conducted analytically. It was shown that, regardless of the analyzed method, the identical performance in terms of the energy balancing in a horizontal direction is ensured. On the other hand, the benchmark of the very same control methods, however, concerning the vertical balancing, was conducted comprehensively for the first time.

One of the main amenities provided by the MMC relates to the theoretically unlimited possibility of stacking the SMs in series. Consequently, the voltage handling capabilities of the converter increase. In case the current rating of an application is preserved, stacking more SMs in series implies an increase in the converter power rating. However, the applications with a constrained selection of operating voltage exist (e.g. hydropower), meaning that the power extension of the MMC used to serve them can not be achieved through the stacking of additional SMs in series. In other words, boosting the current capabilities of the converter represents the main technical challenge on these terms.

In **Chap. 4** paralleling of the MMC branches was recognized as a method suitable to provide the effortless power extension without the need of undergoing any major hardware adaptations of the device. However, additional measures in the control domain must be taken, otherwise, stable operation of the converter can not be guaranteed owing to the discrepancies among the passive components representing a mandatory part of every MMC. Starting from the SVD-based expressions, provided in **Chap. 3**, the proper structure of the controller ensuring the energy balance within a set of parallel branches was derived. Moreover, the proposed controller operates being decoupled from the control layers used in the converter consisting of only two branches per leg (the conventional MMC), thus ensuring that control of terminal currents does not get hindered. Additionally, the control methods presented in **Chap. 4** do not depend on the parity of the number of branches paralleled within a leg. In other words, a universal and highly flexible solution was proposed.

Apart from providing the means for an effortless power extension, paralleling of the MMC branches, allows for an improvement in the quality of voltage seen from either of the converter terminals (DC or AC). In case PSC modulation is considered, suitable carrier sets displacements were proven to provide the number of voltage levels extension up to  $2MN + 1$  (where  $N$  and  $M$  denote the number of SMs per branch and the number of paralleled branches, respectively) when observed from the AC terminal of the leg. In **Chap. 5**, the results were derived analytically, in a comprehensive manner, whereas the demonstrated methodology can be applied in case any carrier-based modulation scheme is used. Even though the analysis considered the use of HB SMs, a straightforward extension to any other SM type can easily be performed.

Due to the outstanding scalability, the MMC found its place in literally all of the possible conversion schemes. As the first five chapters of this thesis focused on the inverter operation of the MMC, the focus of the last three chapters was laid on the use of the MMC in the high power DC-DC domain.

The high power MMC-based DC-DC converter utilizing the STC to interface an HV/MV bipolar DC grid with an LV DC grid was presented and thoroughly analyzed in **Chap. 6**. To interface the HV/MV DC grid, the proposed converter utilizes two series-connected MMCs while the conventional SSC, operating with the fundamental switching frequency, was used in the LV stage. It must be emphasized that the employment of the STC enables the exploitation of the redundancy principles naturally ensured by the presence of the neutral conductor in bipolar DC grids. In case any of the DC feeders is lost, the converter can continue to operate, delivering half the rated power to the LV stage. The same conclusion applies to the case with either of the MMCs malfunctioning. Taking into account the most common use of the STC (railway applications), the main original contribution of this chapter lies in the unprecedented proposal of the STC use in the high power DC-DC domain.

Moreover, the operating frequency shift towards the medium frequency range was considered, which is completely aligned with the trends of modern power electronics. To reduce the MMCs switching losses to the highest possible extent, the new modulator enabling the fundamental frequency switching of all the semiconductors within the converter was proposed. In order to control the converter power flow, DAB-alike control principles were adopted.

However, the topology presented in **Chap. 6** provides the possibility for bidirectional power flow, which might not be needed in certain cases. Therefore, replacing the SSC in the LV stage with a simple 3PH DR led to the structure described in **Chap. 7**. In contrast to the topology thoroughly explained in **Chap. 6**, the converter analyzed in **Chap. 7** represents the unidirectional converter. Moreover, as the LV stage employs the simple DR, amplitude modulation principles were adopted to establish the successful control of the converter power flow. Similarly to **Chap. 6**, the operating frequency push towards the medium frequency range was proposed.

Last but not least, **Chap. 8** provides a thorough and comprehensive analysis of the Q2L converter leg. Q2L operation of 2LVL VSCs assumes the insertion of SMs in the equidistant time steps, corresponding to what is referred to as the dwell time. As a results, a smooth transition of the Q2L converter AC voltage from one polarity to another occurs. However, the output current of an observed Q2L converter leg drifts from one branch to another during the above mentioned transition interval. It was exactly this current drift that had never been thoroughly explained, hence, **Chap. 8** dealt with this topic in detail, which needs to be outlined as one of its main contributions. It was demonstrated that knowing the Q2L converter branch currents, during the transition interval, provides the framework for the precise sizing of the SM capacitors. When compared to the methods originally proposed in the literature, reduction of the SM capacitance by almost 40% was achieved through the use of the analytic model derived in this chapter. Additionally, the results are presented in a generalized form, meaning that they can be applied to a variety of structures relying on the Q2L operating principles.

## 9.2 Future works

### 9.2.1 General control of the MMC-based converters

**Chap. 3**, supported by **App. A**, introduced the concept of the circulating currents mapping through SVD of the matrix describing the summation of leg common-mode currents in the MMC DC link. The null-space concept, however, can be used to define the converter circulating currents, irrespective of the observed converter topology. As a result, the analyses conducted in **Chap. 3** can be extended and generalized in order to provide the grounds for a step-by-step methodology concerning the general control of the MMC-based circuits.

### 9.2.2 Further considerations regarding the MMC operating with parallel branches

#### 9.2.2.1 Branch inductance optimization

**Fig. 9.1(a)** depicts the structure of the MMC branch, which comprises multiple parallel SBRs. As stated in **Chap. 4**, the presented control approach does not get affected by extending the structure

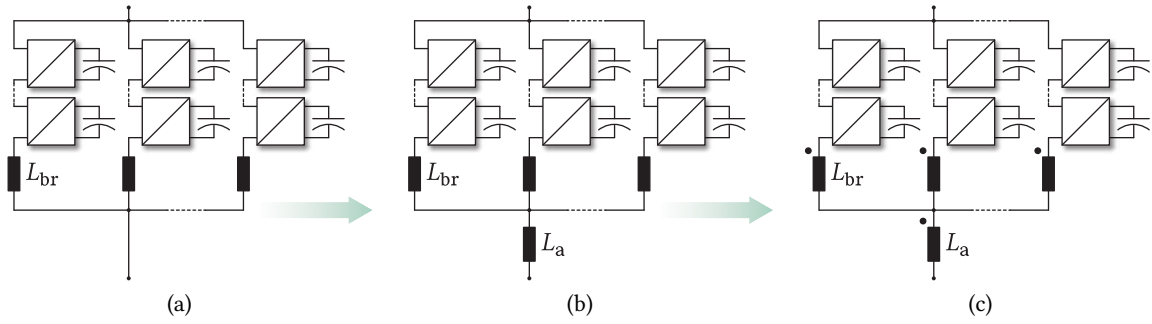


**Fig. 9.1** Different options regarding the realization of the equivalent branch inductance in case  $M$  parallel SBRs per branch are used to obtain the MMC of the desired power rating.

from **Fig. 9.1(a)** with an additional inductance  $L_a$ . In this way, equivalent inductance of the branch as a whole can be calculated as  $L_{br\Sigma} = L_a + L_{br}/M$ . As a result, the desired equivalent inductance can be realized with the reduction in the inductances labeled with  $L_{br}$ . A step further in the optimization of inductances mounted within an MMC branch comprising multiple parallel SBRs can be achieved through the coupling illustrated in **Fig. 9.1(c)**.

It is important to notice that the branch structure depicted in **Fig. 9.1(c)** requires additional considerations, from both the control and the hardware design standpoint, therefore it needs to be further investigated. Also, a thorough comparison among the cases presented in **Figs. 9.1(a)** to **9.1(c)** should be made.

#### 9.2.2.2 Application to different MMC-based topologies

The conventional 3PH MMC does not represent the only topology expressing the need for the power extension ensured through the branch paralleling. Hence, the possibility of exploiting the same power extension concept in case different topologies, such as the Matrix MMC or even the MMC-based DC-DC converters, needs to be examined.

#### 9.2.2.3 Improvement of the MMC leg voltage spectra with different modulation methods

In **Chap. 5** the possibility of improving the quality of voltage seen from either of the MMC terminals was presented. The considered modulation type was PSC modulation. However, various modulation schemes, considering the MMC, were reported in the literature. Thus, the question of providing a link between the concepts presented in **Chap. 5** and the other, non-carrier-based, modulation methods remains open.

#### 9.2.3 Improvements on the topologies employing the STC

During the analyses presented in **Chaps. 6** and **7**, the stiff DC link voltage was assumed. However, the variations of the converter input voltage (e.g.  $\pm 10\%$ ) might occur and their influence on the converter performance needs to be addressed.



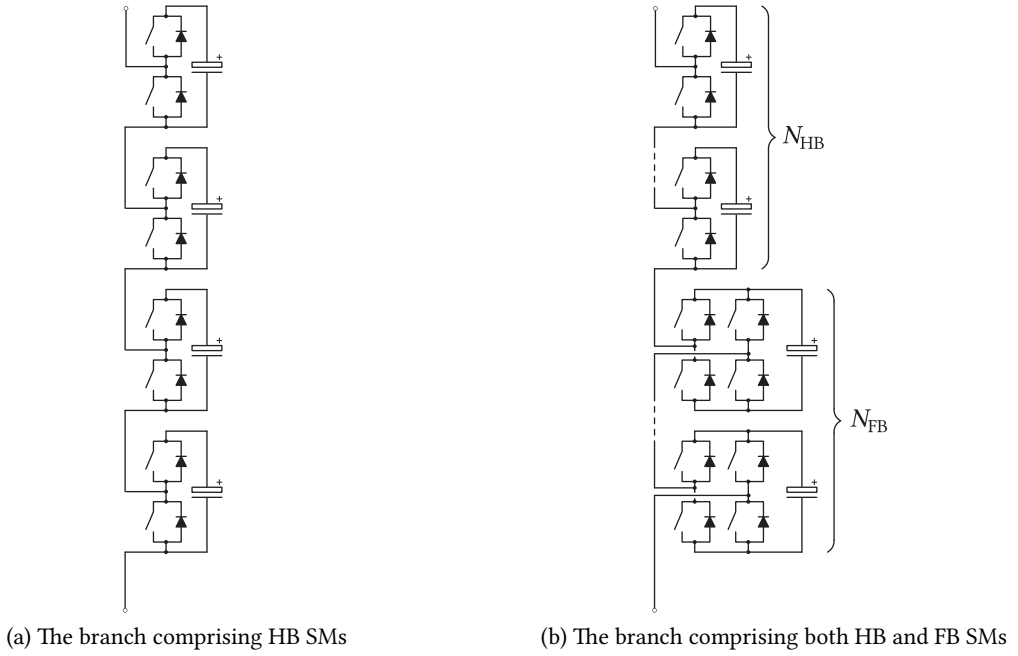


**Fig. 9.2** To achieve the blocking of fault currents, the MMC operating with mixed SMs can be used to interface an HV/MV DC grid. Namely, a certain number of HB SMs can be replaced with the FB counterparts, resulting in the branch structure presented on the right-hand side.

Furthermore, the transition from the normal operating mode, implying that no faults occurred in the system, to either of the faulty states analyzed in **Chaps. 6** and **7** needs to be covered. Another topic related to the faulty operating mode refers to the blocking of the STC fault currents. As demonstrated in **Chaps. 6** and **7**, in case HB SMs presented in **Fig. 9.2(a)** are used, asymmetries in the STC S-winding inductances gives rise to the currents flowing through the faulty MMC. Despite falling significantly below the converter rated currents, the fault currents can be blocked to the full extent in case the branches employing the so-called mixed SMs are used. Namely, a certain number of HB SMs can be replaced with the FB stages in order to form the structure presented in **Fig. 9.2(b)**. Notwithstanding, the determination of the number of FB SMs, along with the control/modulation methods used in case the branches illustrated in **Fig. 9.2(b)** are used, requires additional analysis.

Last but not least, the use of PSC modulation was analyzed in **Chap. 7** with the aim of realizing the sinusoidal voltage references passed to the MMC branches. A set of considerations regarding this topic refers to the choice of the modulation method. Namely, another modulation method might provide the improvements of the output voltage quality. However, an additional investigation on this matter is required. Furthermore, the operation with sinusoidal voltages can be reconsidered in the normal operating mode, however, such a decision introduces the need for a slightly modified converter design approach. Consequently, it is left as the topic to be addressed by the author in the future.



# Appendices



# A

## Notes on the Singular Value Decomposition

### A.1 Square matrix diagonalization

At this point, diagonalization of a square matrix might not seem pertinent. However, to bring the SVD closer to engineering applications, several relevant concepts from linear algebra are repeated here.

To provide the framework for the upcoming discussions, the concept of eigenvectors and eigenvalues needs to be elaborated. For that matter, let one consider a matrix  $A$ . If  $A$  is applied to a random vector  $\vec{x}$ , while

$$A\vec{x} = \lambda\vec{x}, \quad (\text{A.1})$$

$\vec{x}$  is referred to as the eigenvector of  $A$  with the eigenvalue  $\lambda$ . In other words, when matrix  $A$  is applied to any of its eigenvectors, each one of them retains the same direction, while being scaled with its associated eigenvalue. In [142], a definition of diagonalizable matrix was provided and it is repeated below for the sake of completeness.

**Lemma 1.** *Let  $A$  be a real (or complex)  $n \times n$  matrix, let  $\lambda_1, \lambda_2, \dots, \lambda_n$  be a set of  $n$  real (respectively, complex) scalars, and let  $\vec{v}_1, \vec{v}_2, \dots, \vec{v}_n$  be a set of  $n$  vectors in  $\mathbb{R}^n$  (respectively,  $\mathbb{C}^n$ ). Let  $C$  be the matrix formed by using  $\vec{v}_j$  for  $j^{\text{th}}$  column vector, and let  $D$  be the  $n \times n$  diagonal matrix whose diagonal entries are  $\lambda_1, \lambda_2, \dots, \lambda_n$ . Then*

$$AC = CD \quad (\text{A.2})$$

*if and only if  $\lambda_1, \lambda_2, \dots, \lambda_n$  are the eigenvalues of  $A$  and each  $\vec{v}_j$  is an eigenvector of  $A$  corresponding to the eigenvalue  $\lambda_j$ .*

To prove the above lemma, let one observe the product on the left-hand side of (A.2), where  $\begin{bmatrix} \vec{v}_1 & \vec{v}_2 & \dots & \vec{v}_n \end{bmatrix}$  represents the matrix with eigenvectors of  $A$ .

$$\begin{bmatrix} \vec{A}_1 & \vec{A}_2 & \dots & \vec{A}_n \end{bmatrix} \begin{bmatrix} \parallel & & & \parallel \\ \vec{v}_1 & \dots & \vec{v}_n & \\ \parallel & & & \parallel \end{bmatrix} = \begin{bmatrix} \vec{B}_1 & \vec{B}_2 & \dots & \vec{B}_n \end{bmatrix} \quad (\text{A.3})$$

According to the matrix multiplication rules, every vector  $\vec{B}_k$ , such that  $k \in [1, n]$ , can be obtained through the linear combination of columns (vectors) of  $A$ . Therefore, expression (A.4) can be established.

$$\vec{B}_k = \vec{A}_1 v_{k1} + \vec{A}_2 v_{k2} + \dots + \vec{A}_n v_{kn} = A \vec{v}_k = \lambda_k \vec{v}_k \quad (\text{A.4})$$

Substitution of (A.4) into (A.3) yields

$$\underbrace{\begin{bmatrix} \vec{A}_1 & \vec{A}_2 & \dots & \vec{A}_n \end{bmatrix}}_A \underbrace{\begin{bmatrix} \left| \vec{v}_1 \right\rangle & \dots & \left| \vec{v}_n \right\rangle \end{bmatrix}}_C = \underbrace{\begin{bmatrix} \left| \vec{v}_1 \right\rangle & \dots & \left| \vec{v}_n \right\rangle \end{bmatrix}}_C \underbrace{\begin{bmatrix} \lambda_1 & \dots & 0 \\ \vdots & \ddots & \vdots \\ 0 & \dots & \lambda_n \end{bmatrix}}_D, \quad (\text{A.5})$$

from where one can recognize the form provided in (A.2).

Now, suppose that the matrix  $C$  is invertible. Then, it can be written that  $D = C^{-1}AC$ , which leads to the definition and theorem given below.

**Definition 1.** An  $n \times n$  matrix  $A$  is diagonalizable if there is an invertible  $n \times n$  matrix  $C$ , such that  $C^{-1}AC$  is a diagonal matrix. The matrix  $C$  is then said to diagonalize  $A$ .

**Theorem 1.** An  $n \times n$  matrix  $A$  is diagonalizable if and only if it has  $n$  linearly independent eigenvectors.

Without providing a proof of the above theorem, which can be found in [142], one can observe an interesting property that matrix  $A$  must fulfill. Namely, all of its eigenvectors must be linearly independent. This is actually a property of symmetric matrices. Consequently, special attention will be devoted to their analysis.

## A.2 Symmetric matrices

In linear algebra, a symmetric matrix is a square matrix that is identical to its transpose, meaning that

$$A = A^T \quad (\text{A.6})$$

Symmetric matrices feature two interesting properties, which are found very useful in the upcoming analysis of the SVD.

- **The eigenvalues of symmetric matrices are real**

To prove the above statement, let  $A$  be a square matrix with real entries. Additionally, let one assume that  $A$  has a complex eigenvalue. Therefore, conjugate complex of (A.1), results in

$$A\vec{x}^* = \lambda^* \vec{x}^* \quad (\text{A.7})$$

Left multiplication of (A.1) with  $\vec{x}^{*T}$  and (A.7) with  $\vec{x}^T$  yields

$$\vec{x}^{*T} A \vec{x} = \vec{x}^{*T} \lambda \vec{x} \quad (\text{A.8})$$

$$\vec{x}^T A \vec{x}^* = \vec{x}^T \lambda^* \vec{x}^* \quad (\text{A.9})$$

Subtraction of the above equations provides

$$\underbrace{\vec{x}^{*T} A \vec{x} - \vec{x}^T A \vec{x}^*}_{=0} = (\lambda - \lambda^*) |\vec{x}|^2 \quad (\text{A.10})$$

The terms  $\vec{x}^{*T} A \vec{x}$  and  $\vec{x}^T A \vec{x}^*$  are actually scalars. Given that every scalar must be equal to its transpose, it is straightforward to show that the term on the left-hand side in (A.10) equals zero. Also, the existence of an eigenvector implies that its magnitude must be greater than zero, which leads to the conclusion that the condition  $\lambda = \lambda^*$  must be fulfilled in order to satisfy (A.10). Indeed, eigenvalues of symmetric matrices are real.

- **Eigenvectors corresponding to different eigenvalues are orthogonal**

For the purpose of providing a proof of the above property, assume that a symmetric matrix  $A$  has two eigenvectors  $\vec{x}_i$  and  $\vec{x}_j$ , with the corresponding eigenvalues  $\lambda_i$  and  $\lambda_j$ , respectively. Therefore, expressions (A.11) and (A.12) can be established.

$$A\vec{x}_i = \lambda_i \vec{x}_i \quad (\text{A.11})$$

$$A\vec{x}_j = \lambda_j \vec{x}_j \quad (\text{A.12})$$

Thereafter, (A.11) and (A.12) are multiplied with  $\vec{x}_j^T$  and  $\vec{x}_i^T$  from the left, respectively, yielding

$$\vec{x}_j^T A \vec{x}_i = \lambda_i \vec{x}_j^T \vec{x}_i \quad (\text{A.13})$$

$$\vec{x}_i^T A \vec{x}_j = \lambda_j \vec{x}_i^T \vec{x}_j \quad (\text{A.14})$$

Transposing the expression (A.14) and subtracting it from (A.13) gives

$$\underbrace{\vec{x}_j^T A \vec{x}_i - \vec{x}_j^T A^T \vec{x}_i}_{=0 \text{ since } A=A^T} = (\lambda_i - \lambda_j) \vec{x}_j^T \vec{x}_i \quad (\text{A.15})$$

In general  $\lambda_i \neq \lambda_j$  (since the eigenvalues are assumed to be distinct), which suggest that  $\vec{x}_j^T \vec{x}_i$  must be equal to zero, according to (A.15). Please notice that  $\vec{x}_j^T \vec{x}_i$  actually represents the scalar product of two eigenvectors. Since the scalar product of two orthogonal vectors equals zero, one can conclude that vectors  $\vec{x}_i$  and  $\vec{x}_j$  are indeed orthogonal.

What follows directly from the above properties is that the eigenvectors of a symmetric matrix with a set of distinct eigenvalues form an orthogonal matrix. For an orthogonal matrix, the relation  $A^T A = I$  holds. This is simple to prove by observing the product in (A.16), where  $X$  denotes the matrix whose columns are the unity length eigenvectors of the symmetric matrix  $A$ .

$$X^T X = \begin{bmatrix} \vec{x}_1^T \\ \vec{x}_2^T \\ \vdots \\ \vec{x}_n^T \end{bmatrix} \begin{bmatrix} \vec{x}_1 & \vec{x}_2 & \dots & \vec{x}_n \end{bmatrix} \quad (\text{A.16})$$

At the positions indexed with  $ii$ , the result of the above multiplication can be obtained as  $\vec{x}_i^T \vec{x}_i = 1$ . On the other hand, at the positions indexed with  $ij$ , in accordance with (A.15),  $\vec{x}_i^T \vec{x}_j = 0$ . Consequently,  $X^T X = I$ .

Although convenient, the eigenvalues of a symmetric matrix do not have to be distinct. In other words, different eigenvectors can have the same eigenvalue. To provide a thorougher analysis on this matter, assume there are multiple (for instance,  $M$ ) eigenvectors with one eigenvalue. Mathematically, such a situation can be formulated as

$$(\forall k \in [1, M]) \quad A \vec{x}_k = \lambda_M \vec{x}_k \quad (\text{A.17})$$

Since  $\lambda_M$  is the eigenvalue for  $M$  eigenvectors, it is said to have the multiplicity of  $M$ . Even though  $\lambda_M$  appears more than once, for each of its associated eigenvectors, it can be said that it is orthogonal to the eigenvectors corresponding to the eigenvalues different than  $\lambda_M$ . Consequently, eigenvectors  $\vec{x}_k$  from (A.17) belong to a subspace, denoted by  $S$ , which is orthogonal to all the eigenvectors whose eigenvalues differ from  $\lambda_M$ . Once this conclusion is made, vectors  $\vec{x}_k$  from (A.17) can be expressed through a set of basis vectors  $B = \begin{bmatrix} \vec{b}_1 & \vec{b}_2 & \dots & \vec{b}_M \end{bmatrix}$  forming the subspace  $S$ , which leads to



$$\begin{aligned}\vec{x}_1 &= C_{11}\vec{b}_1 + C_{12}\vec{b}_2 + \dots + C_{1M}\vec{b}_M \\ &\vdots \\ \vec{x}_M &= C_{M1}\vec{b}_1 + C_{M2}\vec{b}_2 + \dots + C_{MM}\vec{b}_M\end{aligned}\tag{A.18}$$

Since vectors  $\vec{b}_1, \dots, \vec{b}_M$  form the basis of the subspace  $S$ , they are, by definition, independent (a set of vectors  $B$  is said to represent a basis of a subspace  $S$  if all the vectors from  $B$  are linearly independent, while any of the vectors from  $S$  can be obtained through the linear combination of basis vectors from  $B$ ). Moreover, vectors from the set  $B$  can be selected to be orthogonal (keep in mind that two vectors can be linearly independent but not necessarily orthogonal). Substitution of any of the equations (e.g. the first one) from the system (A.18) into (A.1) gives

$$A(C_{11}\vec{b}_1 + C_{12}\vec{b}_2 + \dots + C_{1M}\vec{b}_M) = \lambda_M(C_{11}\vec{b}_1 + C_{12}\vec{b}_2 + \dots + C_{1M}\vec{b}_M)\tag{A.19}$$

Since the vectors from  $B$  are orthogonal it is easy to conclude that the previous expression is satisfied only if

$$\begin{aligned}A\vec{b}_1 &= \lambda_M\vec{b}_1 \\ A\vec{b}_2 &= \lambda_M\vec{b}_2 \\ &\vdots \\ A\vec{b}_M &= \lambda_M\vec{b}_M\end{aligned}\tag{A.20}$$

According to (A.1) and (A.20), all the basis vectors  $\vec{b}_1, \dots, \vec{b}_M$  represent the eigenvectors of  $A$  with the eigenvalue equal to  $\lambda_M$ . In conclusion, even if non-distinct (repeated) eigenvalues exist, an orthogonal set of eigenvectors corresponding to them can be selected. Consequently, if matrix  $A$  is symmetrical, the matrix whose columns represent the eigenvectors of  $A$  is always orthogonal. In order to support this claim even further, an example with the case relevant for this thesis scope will be provided in **Sec. A.5**.

Notwithstanding, it is important to notice that all of the discussion conducted so far referred to square matrices. However, not all the matrices are square (for instance, matrix  $T_1 = \begin{bmatrix} 1 & 1 & 1 \end{bmatrix}$  describing the sum of the 3PH MMC circulating currents), which discredits the concept of the eigenvectors and eigenvalues. Moreover, even if a random matrix is a square matrix, there is no guarantee that it is symmetric, therefore, its eigenvectors are not orthogonal. As a result, matrix diagonalization in the form presented in **Sec. A.1** can not be applied, which introduced the need for more general matrix decomposition methods.

### A.3 Derivation of the SVD

Let  $A$  be an  $m \times n$  matrix. As  $A$  is not necessarily a square matrix, the concept of eigenvectors and eigenvalues is not valid anymore. Consequently, diagonalization (decomposition) by means of the methods presented so far can not be applied. However, irrespective of the nature of  $A$ , it can be concluded that the product  $A^T A$  represents a symmetric matrix. As a result, the matrix of its eigenvectors  $V_n = \begin{bmatrix} \vec{v}_1 & \dots & \vec{v}_n \end{bmatrix}$  represents an orthogonal matrix. Moreover, diagonalization in the form of (A.2) can be performed, leading to (A.21).

$$(A^T A)V_n = V_n \Lambda_n \quad (\text{A.21})$$

Since all the vectors from  $V_n$  are linearly independent,  $V_n$  can be inverted (in other words,  $V_n$  is a full column rank matrix). Additionally,  $V_n$  is an orthogonal matrix, meaning that  $V_n^T = V_n^{-1}$ , which, when substituted into (A.21), yields

$$A^T A = V_n \Lambda_n V_n^T \quad (\text{A.22})$$

Also, the product  $AA^T$  represents a symmetric matrix. Thus, using the reasoning presented above leads to

$$AA^T = U_m \Lambda_m U_m^T \quad (\text{A.23})$$

At this point, one could ask whether there is a way to connect the eigenvectors from the matrices denoted by  $V_n$  and  $U_m$ . Basically, this represents the SVD problem statement. Prior to proceeding with the analysis, it is useful to show that expression (A.24) holds for any non-zero vector  $\vec{x}$ .

$$\vec{x}^T A^T A \vec{x} = (A\vec{x})^T (A\vec{x}) = (A\vec{x}) \cdot (A\vec{x}) \geq 0 \quad (\text{A.24})$$

Moreover, if  $A$  is a non-singular matrix (which means that its determinant is different from zero) then  $(A\vec{x}) \cdot (A\vec{x}) > 0$  and  $A^T A$  is said to be positive definite matrix. Identical proof can be made regarding the matrix  $AA^T$ .

The above conclusion reveals a very important feature - eigenvalues of a positive (semi)definite matrix are non-negative. If, in the above expression,  $\vec{x}$  were to be the eigenvector of  $A^T A$ , with the eigenvalue  $\lambda$ , then

$$\vec{x}^T A^T A \vec{x} = \lambda |\vec{x}|^2, \quad (\text{A.25})$$

from where it is straightforward to conclude that  $\lambda \geq 0$ .

According to (A.21), let  $\vec{v}$  be the eigenvector of  $A^T A$  with the eigenvalue  $\lambda$ , which is expressed in (A.26).

$$A^T A \vec{v} = \lambda \vec{v} \quad (\text{A.26})$$

Left multiplication of both sides of the above expression with  $A$  yields

$$A A^T \{A \vec{v}\} = \lambda \{A \vec{v}\} \quad (\text{A.27})$$

Through the observation of (A.26) and (A.27), one can conclude that matrices  $A^T A$  and  $A A^T$  have identical non-zero eigenvalues, though with different eigenvectors. From (A.27) it can also be seen that the eigenvectors of the matrix  $A A^T$  appear in the form of  $A \vec{v}$ . Furthermore, (A.23) suggests that diagonalization of the matrix  $A A^T$  can be performed by using the set of eigenvectors  $U_m = \begin{bmatrix} \vec{u}_1 & \dots & \vec{u}_m \end{bmatrix}$ . Based on the above discussion, the connection between the eigenvectors  $\vec{v}$  and  $\vec{u}$  from (A.22) and (A.23), respectively, can be anticipated in the form of (A.28), where  $\sigma \in \mathbb{R}$ .

$$A \vec{v} = \sigma \vec{u} \quad (\text{A.28})$$

Henceforth, the number of identical non-zero eigenvalues of  $A^T A$  and  $A A^T$  will be labeled with  $r \leq \min(m, n)$ . Therefore, the system of  $r$  equations (the other equations are trivial since the eigenvalues are equal to zero), written in the form of (A.28), can be established, leading to

$$\begin{aligned} A \vec{v}_1 &= \sigma_1 \vec{u}_1 \\ A \vec{v}_2 &= \sigma_2 \vec{u}_2 \\ &\vdots \\ A \vec{v}_r &= \sigma_r \vec{u}_r \end{aligned} \quad (\text{A.29})$$

Every equation from (A.29) resembles (A.1) to a certain extent. Nonetheless,  $\vec{v}$  and  $\vec{u}$  can not be referred to as the eigenvectors. Instead, these are referred to as the singular vectors, with the corresponding singular values  $\sigma$ .

Further, the system (A.29) can be rewritten in the matrix form as

$$\underbrace{A \begin{bmatrix} \vec{v}_1 & \vec{v}_2 & \dots & \vec{v}_r \end{bmatrix}}_V = \underbrace{\begin{bmatrix} \vec{u}_1 & \vec{u}_2 & \dots & \vec{u}_r \end{bmatrix}}_U \underbrace{\begin{bmatrix} \sigma_1 & \dots & 0 \\ 0 & \ddots & 0 \\ 0 & \dots & \sigma_r \end{bmatrix}}_\Sigma \quad (\text{A.30})$$

Since vectors  $\vec{v}_1, \dots, \vec{v}_r$  are orthogonal, right multiplication (A.31) with  $V$  results in (A.30). Consequently, the relationship defined in (A.31) holds and it is referred to as the SVD of matrix  $A$ .

$$A = U\Sigma V^T \quad (\text{A.31})$$

In order to identify the vectors from  $U$  and  $V$ , a connection with (A.22) should be made. For that purpose, let one look at  $A^T A$ , however, with  $A$  being expressed in its SVD form (A.31).

$$A^T A = V\Sigma^T \underbrace{U^T U}_I \Sigma V^T = V\Sigma^T \Sigma V^T \quad (\text{A.32})$$

Given that  $\Sigma$  represents a diagonal matrix with non-zero elements, one can conclude that the relation  $\Sigma^T \Sigma = \text{diag}(\sigma_1^2, \dots, \sigma_r^2)$  holds. Furthermore, the terms  $\sigma_i^2$  represent the non-zero, positive eigenvalues found in the matrix  $\Lambda_n$  from (A.22). Consequently,  $V$  contains all the vectors from  $V_n$ , which correspond to the non-zero eigenvalues.

In order to choose the vectors from  $U$ , one can use the relationships already established in (A.29), leading to

$$\begin{aligned} \vec{u}_1 &= \frac{1}{\sigma_1} A \vec{v}_1 \\ &\vdots \\ \vec{u}_r &= \frac{1}{\sigma_r} A \vec{v}_r \end{aligned} \quad (\text{A.33})$$

As already stated, all the vectors from  $V$  are orthogonal. The same applies to the vectors  $\vec{u}$  being chosen according to (A.33). In order to provide a proof of this statement, please observe the product  $\vec{u}_i^T \vec{u}_j$  from (A.34). As  $\vec{v}_j$  represents the eigenvector of  $A^T A$ , with the eigenvalue  $\sigma_j^2$ , it is straightforward to conclude that the product from below actually equals zero, owing to the orthogonality of the vectors from  $V$ .

$$\vec{u}_i^T \vec{u}_j = \frac{1}{\sigma_i \sigma_j} \vec{v}_i^T \underbrace{A^T A \vec{v}_j}_{\sigma_j^2 \vec{v}_j} = \frac{\sigma_j^2}{\sigma_i \sigma_j} \underbrace{\vec{v}_i^T \vec{v}_j}_{=0} \quad (\text{A.34})$$

Apart from being orthogonal, vectors from  $V$  and  $U$  can be selected to be orthonormal (orthogonal vectors with unity lengths). On these terms, matrices  $V$  and  $U$  are nothing but a rotation matrices, whereas  $\Sigma$  indicates the scaling (stretching). One can conclude, therefore, that every matrix performs the stretching and rotation of vectors, which can be graphically presented as in **Fig. A.1**.

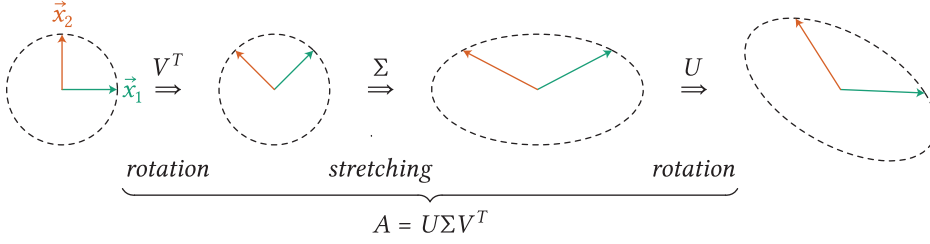


**Fig. A.1** Graphical representation of the effect that a  $2 \times 2$  matrix  $A$  has upon the vectors denoted by  $\vec{x}_1$  and  $\vec{x}_2$ . In other words, decomposition onto the steps in the multiplication  $A[\vec{x}_1 \ \vec{x}_2]$  is presented. Accordingly, every matrix can be perceived through two rotations and one scaling (stretching) action.

It is worthy to note that the SVD, being in the form derived so far, can be rewritten, as presented in (A.35)

$$\begin{aligned}
 A &= \begin{bmatrix} \vec{u}_1 & \dots & \vec{u}_r \end{bmatrix} \begin{bmatrix} \sigma_1 & & \\ & \ddots & \\ & & \sigma_r \end{bmatrix} \begin{bmatrix} \vec{v}_1^T \\ \vdots \\ \vec{v}_r^T \end{bmatrix} \\
 &= \begin{bmatrix} \vec{u}_1 & \dots & \vec{u}_r & | & \vec{u}_{r+1} & \dots & \vec{u}_m \end{bmatrix} \begin{bmatrix} \Sigma & 0 \\ 0 & 0 \end{bmatrix} \begin{bmatrix} \vec{v}_1^T \\ \vdots \\ \vec{v}_r^T \\ \vdots \\ \vec{v}_{r+1}^T \\ \vdots \\ \vec{v}_n^T \end{bmatrix} \\
 &= \underbrace{\begin{bmatrix} U_R & U_N \end{bmatrix}}_{U'} \underbrace{\begin{bmatrix} \Sigma & 0 \\ 0 & 0 \end{bmatrix}}_{\Sigma'} \underbrace{\begin{bmatrix} V_R^T \\ V_N^T \end{bmatrix}}_{V'^T}
 \end{aligned} \tag{A.35}$$

As will be presented shortly, SVD expressed in the above form provides the possibility for a straightforward identification of different subspaces of an arbitrary matrix  $A$ .

## A.4 SVD and its subspaces

This section aims at identifying the nature of the subspaces defined by the vector sets denoted by  $U_R$ ,  $U_N$ ,  $V_R$  and  $V_N$ . Let the analysis commence by restating that all the vectors from  $U_R$  and  $V_R$  are orthogonal. As demonstrated in (A.35), matrices  $U_N$  and  $V_N$  can be added to the structure derived in (A.30) in order to obtain the "large size" SVD (A.35). Anyhow, a simple matrix multiplication indicates that  $U_N$  and  $V_N$  are nullified, hence, their importance might seem to be negligible. Furthermore, the nullification of these matrices allows one to select them freely. As a result, it will be assumed henceforth that  $U_N$  is selected such that its vectors form an orthogonal set, being also orthogonal to the subspace spanned by the vectors from  $U_R$ . The identical claim holds for the matrices  $V_N$  and  $V_R$ .

If all the vectors from  $U'$  and  $V'$  are orthogonal, and selected as unit vectors (this is possible by the Gram-Schmidt orthonormalization [143] for instance), then  $U'$  and  $V'$  are unitary matrices. Since  $V'$  is an  $n \times n$  matrix, with all of its vectors being linearly independent, it can be said that  $V'$  represents the basis of the space  $\mathbb{R}^n$ . Consequently, any vector  $\vec{x} \in \mathbb{R}^n$  can be expressed through a linear combination of vectors from  $V'$  as

$$\vec{x} = \sum_{i=1}^n a_i \vec{v}_i \quad (\text{A.36})$$

In case  $\vec{x}$  is subject to mapping  $A$ , one can notice that

$$A\vec{x} = \sum_{i=1}^r a_i \sigma_i \vec{u}_i, \quad (\text{A.37})$$

which is easily derived in case (A.38) is considered.

$$A\vec{v}_i = \begin{cases} \sigma_i \vec{u}_i & , 1 \leq i \leq r \\ 0 & , \text{otherwise} \end{cases} \quad (\text{A.38})$$

The term  $A\vec{x}$  in (A.37) can be referred to as the column space of  $A$ , which will henceforth be labeled with  $C(A)$ . As can be seen, any vector in  $C(A)$  can be obtained through the linear combination of  $r$  linearly independent vectors  $\vec{u}_1, \dots, \vec{u}_r$ . As a result, matrix  $U_R$  represents the basis of  $C(A)$ . Moreover, the rank of a matrix corresponds to the number of independent vectors comprising the basis of its column space. Therefore,  $\text{rank}(A) = r$ .

In a similar fashion, one can conclude that vectors from  $U'$  comprise a basis of the space  $\mathbb{R}^m$ . Therefore, any vector  $\vec{x} \in \mathbb{R}^m$  can be expressed through a linear combination of vectors from  $U'$ , leading to

$$\vec{x} = \sum_{i=1}^m a_i \vec{u}_i \quad (\text{A.39})$$

In case one were to look for the product  $A^T \vec{x}$ , (A.40) can be derived as (A.41) holds.

$$A^T \vec{x} = \sum_{i=1}^r a_i \sigma_i \vec{v}_i \quad (\text{A.40})$$

$$A^T \vec{u}_i = \begin{cases} \sigma_i \vec{v}_i & , 1 \leq i \leq r \\ 0 & , \text{otherwise} \end{cases} \quad (\text{A.41})$$

Expression (A.40) suggests that  $r$  linearly independent vectors from  $V'$  represent a basis of the column space of  $A^T$ , which is actually the row space of  $A$ , denoted by  $R(A)$ . It is noteworthy that column rank and row rank of a matrix are always equal.

To determine the nature of the subspaces spanned by the vectors from  $U_N$  and  $V_N$ , one can start with the definition of a matrix null-space. If  $A : \mathbb{R}^n \mapsto \mathbb{R}^m$ , its right null-space (kernel) is defined as

$$N(A) = \left\{ \vec{z} \in \mathbb{R}^n : A\vec{z} = 0 \right\} \quad (\text{A.42})$$

Careful inspection of (A.35), (A.38) and (A.41) unveils a set of important conclusion. Namely, in case the vectors from  $V_N$  are orthogonal to the vectors from  $V_R$ , then (A.38) holds. Consequently, every vector from  $V_N$  belongs to the null-space of  $A$ . Furthermore, as all the vectors from  $V_N$  are orthogonal (meaning that they are linearly independent),  $V_N$  is said to represent the basis of the null-space of  $A$ . Given that  $V_N$  contains  $n - r$  vectors, one can write (A.43), which is also referred to as the rank-nullity theorem.

$$n = \text{rank}(A) + \dim(\ker(A)) \quad (\text{A.43})$$

Using the identical reasoning, it can be shown that the vectors from  $U_N$  form the basis of the left null-space of  $A$ , which is defined as

$$N(A^T) = \left\{ \vec{z} \in \mathbb{R}^m : A^T\vec{z} = 0 \right\} \quad (\text{A.44})$$

Finally, **Tab. A.1** summarizes the subspaces obtained through the SVD of an  $m \times n$  matrix  $A$ .

**Tab. A.1** Subspaces of the matrix  $A$  determined from its SVD

Matrix	Basis for a subspace
$U_R$	$C(A)$
$V_R$	$R(A)$
$U_N$	$\ker(A^T)$
$V_N$	$\ker(A)$

## A.5 Application of the SVD to a 3PH MMC

The main motivation of this appendix is to support the calculations presented in **Chap. 3**, which deals with the control of the conventional 3PH MMC. The matrix which describes the way the circulating (and simultaneously, the common-mode) currents sum up in the DC link of the analyzed converter is given in (A.45) and providing its SVD is considered the aim of this section.

$$T_i = \begin{bmatrix} 1 & 1 & 1 \end{bmatrix} \quad (\text{A.45})$$

Since  $T_i$  is a  $1 \times 3$  matrix, it can be concluded from (A.35) that the first matrix ( $U'$ ) in its SVD actually represents a  $1 \times 1$  matrix. As it was stated on a few occasions so far, all the vectors from  $U'$  and  $V'$  comprising (A.35) can be selected as unit length vectors. Hence, the first step in decomposing the matrix from (A.45) is

$$T_i = \begin{bmatrix} 1 \end{bmatrix} \Sigma' V' \quad (\text{A.46})$$

Further, it is easy to see that only one column (e.g. the first one) of  $T_i$  is independent. Therefore,  $r = \text{rank}(T_i) = 1$ . Given that  $\Sigma'$  has the same size as the matrix being decomposed ( $1 \times 3$  in this case), while comprising  $r$  non-zero elements, one can conclude that

$$T_i = \begin{bmatrix} 1 \end{bmatrix} \begin{bmatrix} \sigma & 0 & 0 \end{bmatrix} \begin{bmatrix} \vec{v}_{R1}^T \\ \vec{v}_{N1}^T \\ \vec{v}_{N2}^T \end{bmatrix} \quad (\text{A.47})$$

In general, if  $T_i$  were to be a  $1 \times M$  matrix, where  $M$  would correspond to the number of MMC phase-legs, there would be  $M - 1$  vectors comprising the basis of  $\ker(T_i)$ . As these vectors can be freely selected, with the only constraint that they must be orthogonal to the vector  $\vec{v}_{R1}$ , it is of the utmost importance to identify the vector  $\vec{v}_{R1}$ . For that matter, let one look at  $T_i^T T_i$ .

$$T_i^T T_i = V' \begin{bmatrix} \sigma^2 & 0 & 0 \\ 0 & 0 & 0 \\ 0 & 0 & 0 \end{bmatrix} V'^T \quad (\text{A.48})$$

Owing to the fact that  $T_i^T T_i$  is a symmetric matrix, the expression above represents its decomposition already presented in (A.2). Also, it can be seen from (A.48) that the matrix  $T_i^T T_i$  has only one distinct eigenvalue  $\lambda = \sigma^2$ , with the corresponding eigenvector being actually  $\vec{v}_{R1}$ , and two eigenvalues being equal to zero. Given that the eigenvalues of a symmetric matrix are non-negative, as proven in **Sec. A.2**,  $\sigma$  can be obtained as  $\sigma = \sqrt{\lambda}$ . Also, as stated in **Sec. A.2**, eigenvectors of symmetric matrices are orthogonal, whereas the eigenvectors belonging to a non-distinct eigenvalues, can be selected to be orthogonal to each other. The eigenvalue  $\lambda$  can be identified by solving the equation  $\det(T_i^T T_i - \lambda I) = 0$ , which yields (A.49), from where it is straightforward to conclude that  $\sigma = \sqrt{3}$ .

$$\lambda^2(3 - \lambda) = 0 \quad (\text{A.49})$$

Substituting  $\sigma = \sqrt{3}$  into (A.46) leads to

$$\vec{v}_{R1} = \frac{1}{\sqrt{3}} \begin{bmatrix} 1 \\ 1 \\ 1 \end{bmatrix} \quad (\text{A.50})$$



The choice of vectors  $\vec{v}_{N1}$  and  $\vec{v}_{N2}$  is, as stated above, constrained to the vectors being orthogonal to  $\vec{v}_{R1}$ , while their eigenvalue needs to correspond to zero. In other words, the sum of the column elements in  $\vec{v}_{N1}$  and  $\vec{v}_{N2}$ , respectively, must be zero. It is clear that there is an infinite number of vector pairs satisfying such a constraint, however, a solution being well known in the electrical engineering can be derived by looking at (A.50) more carefully. Namely,  $\alpha\beta 0$  transformation, implies the transformation of coordinates through the use of matrix

$$K = \sqrt{\frac{2}{3}} \begin{bmatrix} 1 & -\frac{1}{\sqrt{3}} & -\frac{1}{\sqrt{3}} \\ 0 & \frac{2}{\sqrt{3}} & -\frac{2}{\sqrt{3}} \\ \frac{1}{\sqrt{2}} & \frac{1}{\sqrt{2}} & \frac{1}{\sqrt{2}} \end{bmatrix} \quad (\text{A.51})$$

It can be seen that the third row of the above matrix, or the so-called zero vector, corresponds to  $\vec{v}_{R1}^T$ . Given that  $K$  is a full-rank matrix, meaning that all of its columns (rows) are independent, one can select the vectors  $\vec{v}_{N1}$  and  $\vec{v}_{N2}$  as

$$\begin{bmatrix} \vec{v}_{N1}^T \\ \vec{v}_{N2}^T \end{bmatrix} = \sqrt{\frac{2}{3}} \begin{bmatrix} 1 & -\frac{1}{\sqrt{3}} & -\frac{1}{\sqrt{3}} \\ 0 & \frac{2}{\sqrt{3}} & -\frac{2}{\sqrt{3}} \end{bmatrix} \quad (\text{A.52})$$

It is easy to check that  $\vec{v}_{N2}^T \vec{v}_{N1} = 0$ , meaning that these two vectors are indeed orthogonal. Moreover,  $\vec{v}_{N2}^T \vec{v}_{R1} = \vec{v}_{N1}^T \vec{v}_{R1} = 0$ , while  $T_i \vec{v}_{N1} = T_i \vec{v}_{N2} = 0$ , which confirms the validity of the choice presented in (A.52). As a result, SVD of the matrix  $T_i = \begin{bmatrix} 1 & 1 & 1 \end{bmatrix}$  is

$$T_i = \begin{bmatrix} 1 \end{bmatrix} \begin{bmatrix} \sqrt{3} & 0 & 0 \\ 0 & 0 & 0 \\ 0 & 0 & 0 \end{bmatrix} \sqrt{\frac{2}{3}} \begin{bmatrix} \frac{1}{\sqrt{2}} & \frac{1}{\sqrt{2}} & \frac{1}{\sqrt{2}} \\ 1 & -\frac{1}{\sqrt{3}} & -\frac{1}{\sqrt{3}} \\ 0 & \frac{2}{\sqrt{3}} & -\frac{2}{\sqrt{3}} \end{bmatrix} \quad (\text{A.53})$$



# B

## Expansion of the SM switching function obtained in the manner characterizing the MMC closed-loop control

In case HB SM is considered, according to [34], [35] it can be shown that expansion of a PWM waveform  $p(t)$ , obtained by comparing a complex reference signal  $m_o^*(t)$  (also referred to as the modulation index) with a triangular carrier, can be performed as (B.1), where  $\theta_1 = \omega_c t - \gamma_c - \pi m_o^* - \pi$  and  $\theta_2 = \omega_c t - \gamma_c + \pi m_o^* + \pi$ .

$$p(t) = m_o^*(t) + \frac{j}{2\pi} \sum_{\substack{k=-\infty \\ k \neq 0}}^{\infty} \frac{1}{k} e^{jk\theta_1} - \frac{j}{2\pi} \sum_{\substack{k=-\infty \\ k \neq 0}}^{\infty} \frac{1}{k} e^{jk\theta_2} \quad (\text{B.1})$$

In the above equation,  $\omega_c$  and  $\gamma_c$  denote the switching frequency and the phase-shift of an observed carrier. Substitution of  $\theta_1$  and  $\theta_2$  into (B.1) yields

$$p(t) = m_o^*(t) - \frac{j}{2\pi} \sum_{\substack{k=-\infty \\ k \neq 0}}^{\infty} \frac{(-1)^k}{k} e^{jk\omega_c t} e^{-jk\gamma_c} \left\{ e^{jk\pi m_o^*} - e^{-jk\pi m_o^*} \right\} \quad (\text{B.2})$$

Let one observe the term  $e^{jk\pi m_o^*}$  for the moment. Namely, in case  $m_o^*(t) = \frac{1}{2} + \hat{m} \frac{1}{2} \cos(\omega_o t)$ , this term can be effortlessly expanded by means of the Jacobi-Anger expansion (B.3), where  $J_n$  denotes the Bessel function of the first kind.

$$e^{jk\cos(\theta)} = \sum_{n=-\infty}^{\infty} j^n J_n(k) e^{jn\theta} \quad (\text{B.3})$$

Notwithstanding, in case of the MMC, modulation index can be synthesized in several different ways [84], [85], [117], [118], [144], which do not necessarily allow for a simple and straightforward expansion of the SM switching function. Also, it is noteworthy that, in case PSC modulation is used, all the SMs receive the same modulations index in case contributions of the local balancing controllers are neglected, which is anyhow an assumption established in **Chap. 5**.

At first instance, let one assume that  $m_o^*(t) = m_0 + \sum_{i=1}^{\infty} \hat{m}_i \cos(i\omega_0 t + \zeta_i)$ . As the modulation index becomes composed of an infinite sum of periodic signals, the expansion defined in (B.3) can not be used. However, it is straightforward to notice that

$$\begin{aligned} e^{jk\pi m_o^*(t)} &= e^{jk\pi m_0} e^{jk\pi \sum_{i=1}^{\infty} \hat{m}_i \cos(i\omega_0 t + \zeta_i)} \\ &= e^{jk\pi m_0} \prod_{i=1}^{\infty} e^{jk\pi \hat{m}_i \cos(i\omega_0 t + \zeta_i)} \end{aligned} \quad (B.4)$$

An important observation can be made from the above equation. Firstly, the function  $e^{jk\pi m_o^*(t)}$ , which is the crucial term of (B.2), can be represented by the product of terms being expandable in the form of (B.3). Secondly, it can already be noticed that analysis of the switching function  $p(t)$  can also be performed in the frequency domain, where an infinite product can be replaced with an infinite array of convolutions. As will be seen shortly, such a maneuver significantly alleviates the further derivations. Translating (B.2) into the frequency domain, while recalling that  $\mathcal{F}\{e^{jk\omega_c t} f(t)\} = F(\omega - k\omega_c)$ , provides one with

$$P(\omega) = M_o^*(\omega) - \frac{j}{2\pi} \sum_{\substack{k=-\infty \\ k \neq 0}}^{\infty} \frac{(-1)^k}{k} e^{-jk\gamma_c} \left\{ \mathcal{F}(e^{jk\pi m_o^*(t)})(\omega - \omega_c) - \mathcal{F}(e^{-jk\pi m_o^*(t)})(\omega - \omega_c) \right\} \quad (B.5)$$

Proceeding with the intended analyses obviously requires further investigation of the function  $\mathcal{F}(e^{jk\pi m_o^*(t)})(\omega)$ . According to the convolution theorem  $\mathcal{F}\{x(t)y(t)\} = \frac{1}{2\pi} X(\omega) * Y(\omega)$ , where  $X(\omega)$  and  $Y(\omega)$  denote frequency domain images of  $x(t)$  and  $y(t)$ , respectively. Consequently, expression (B.6) can be derived for the case considering representation of the modulation index with a finite number of components denoted by  $N$ .

$$\mathcal{F}(e^{jk\pi m_o^*})(\omega) = \frac{e^{jk\pi m_0}}{(2\pi)^{N-1}} \left\{ \mathcal{F}(e^{jk\pi \hat{m}_1 \cos(\omega_0 t + \zeta_1)}) * \mathcal{F}(e^{jk\pi \hat{m}_2 \cos(2\omega_0 t + \zeta_2)}) * \dots * \mathcal{F}(e^{jk\pi \hat{m}_N \cos(N\omega_0 t + \zeta_N)}) \right\} \quad (B.6)$$

Further, combining (B.3) with the fact that  $e^{j\omega_k t} \leftrightarrow 2\pi\delta(\omega - \omega_k)$ , results in (B.7).

$$\begin{aligned} \mathcal{F}(e^{jk\pi \hat{m}_i \cos(i\omega_0 t + \zeta_i)})(\omega) &= \sum_{n=-\infty}^{\infty} j^n J_n(k\pi \hat{m}_i) e^{jn\zeta_i} \mathcal{F}\{e^{jn i \omega_0 t}\} \\ &= \sum_{n=-\infty}^{\infty} j^n J_n(k\pi \hat{m}_i) e^{jn\zeta_i} 2\pi\delta(\omega - n i \omega_0) \end{aligned} \quad (B.7)$$

At this point, all the conditions for further expansion of (B.6) are fulfilled. As will be seen shortly, looking for the convolution of two signals provided in (B.8) comes in handy.

$$\begin{aligned}
& \left[ \mathcal{F} \left( e^{jk\pi\hat{m}_i \cos(i\omega_0 t + \zeta_i)} \right) * \mathcal{F} \left( e^{jk\pi\hat{m}_p \cos(p\omega_0 t + \zeta_p)} \right) \right] (\omega) = \\
& = \int_{-\infty}^{\infty} \left( \sum_{n=-\infty}^{\infty} j^n J_n(k\pi\hat{m}_i) e^{jn\zeta_i} 2\pi \delta(\lambda - ni\omega_0) \right) \cdot \left( \sum_{q=-\infty}^{\infty} j^q J_q(k\pi\hat{m}_p) e^{jq\zeta_p} 2\pi \delta(\omega - \lambda - qp\omega_0) \right) d\lambda \\
& = \sum_{n=-\infty}^{\infty} j^n J_n(k\pi\hat{m}_i) e^{jn\zeta_i} 2\pi \int_{-\infty}^{\infty} \delta(\lambda - ni\omega_0) \left( \sum_{q=-\infty}^{\infty} j^q J_q(k\pi\hat{m}_p) e^{jq\zeta_p} 2\pi \delta(\omega - \lambda - qp\omega_0) \right) d\lambda \\
& = \sum_{n=-\infty}^{\infty} \sum_{q=-\infty}^{\infty} (2\pi)^2 j^{(n+q)} J_n(k\pi\hat{m}_i) J_q(k\pi\hat{m}_p) e^{j(n\zeta_i + q\zeta_p)} \delta(\omega - (ni + qp)\omega_0)
\end{aligned} \tag{B.8}$$

In order to provide a general form of (B.6), mathematical induction method can be employed. Hence, convolution of three functions having the form of (B.7) needs to be derived. By utilizing the same logic demonstrated during the derivation of (B.8), it can be shown that

$$\begin{aligned}
& \left( \mathcal{F} \left( e^{jk\pi\hat{m}_i \cos(i\omega_0 t + \zeta_i)} \right) * \mathcal{F} \left( e^{jk\pi\hat{m}_p \cos(p\omega_0 t + \zeta_p)} \right) * \mathcal{F} \left( e^{jk\pi\hat{m}_r \cos(r\omega_0 t + \zeta_r)} \right) \right) (\omega) = \\
& = \sum_{z=-\infty}^{\infty} \sum_{n=-\infty}^{\infty} \sum_{q=-\infty}^{\infty} (2\pi)^3 j^{(z+n+q)} J_z(k\pi\hat{m}_r) J_n(k\pi\hat{m}_i) J_q(k\pi\hat{m}_p) e^{j(n\zeta_i + q\zeta_p + z\zeta_r)} \delta(\omega - (zr + ni + qp)\omega_0)
\end{aligned} \tag{B.9}$$

By observing (B.8) and (B.9) one can easily derive an expression describing the convolution of an infinite number of functions in the frequency domain. Nevertheless, such an approach would be rather impractical given that it would require an infinite number of sums to be incorporated into the calculations. On the other hand, achieving a satisfactory precision in the representation of modulation index can quite often be guaranteed with the use of only  $N$  terms in the product given within (B.4). As explained in **Sec. 5.1.2** in a thorough manner, modulation index can be represented with the satisfactory precision as

$$m_0^* \approx m_0 + \hat{m}_1 \cos(\omega_0 t + \zeta_1) + \hat{m}_2 \cos(2\omega_0 t + \zeta_2) + \hat{m}_3 \cos(3\omega_0 t + \zeta_3) \tag{B.10}$$

Replacing the coefficients from (B.10) into (B.9) gives

$$\begin{aligned}
& \left( \mathcal{F} \left( e^{jk\pi\hat{m}_1 \cos(\omega_0 t + \zeta_1)} \right) * \mathcal{F} \left( e^{jk\pi\hat{m}_2 \cos(2\omega_0 t + \zeta_2)} \right) * \mathcal{F} \left( e^{jk\pi\hat{m}_3 \cos(3\omega_0 t + \zeta_3)} \right) \right) (\omega) = \\
& = \sum_{z=-\infty}^{\infty} \sum_{q=-\infty}^{\infty} \sum_{n=-\infty}^{\infty} (2\pi)^3 j^{(z+n+q)} J_z(\underbrace{k\pi\hat{m}_3}_{c_k}) J_q(\underbrace{k\pi\hat{m}_2}_{b_k}) J_n(\underbrace{k\pi\hat{m}_1}_{a_k}) e^{j(\overbrace{n\zeta_1 + q\zeta_2 + z\zeta_3}^{\theta_{nqz}})} \delta(\omega - (3z + 2q + n)\omega_0)
\end{aligned} \tag{B.11}$$

Thereafter, substitution of (B.6) and (B.11) into (B.5) results in (B.12), from where two distinct sums denoted by  $S_1$  and  $S_2$  can be observed. Also, it is noteworthy that the sum  $S_2$  can be obtained by replacing the coefficients  $\hat{m}_i$ , such that  $i \in [0, 3]$ , into  $S_1$  with their negative counterparts. In other words,  $S_2 = S_1(-m_0, -\hat{m}_1, -\hat{m}_2, -\hat{m}_3)$ .

$$\begin{aligned}
 P(\omega) = M_0^*(\omega) - \frac{j}{2\pi} \bigg\{ & \underbrace{\sum_{\substack{k=-\infty \\ k \neq 0}}^{\infty} \sum_{z=-\infty}^{\infty} \sum_{q=-\infty}^{\infty} \sum_{n=-\infty}^{\infty} \frac{(-1)^k}{k} e^{-j[k(\gamma_c - \pi m_0) - \theta_{nqz}]} j^{(z+n+q)} J_z(c_k) J_q(b_k) J_n(a_k) 2\pi \delta(\omega - k\omega_c - (3z+2q+n)\omega_0)}_{S_1} - \\
 & \underbrace{\sum_{\substack{k=-\infty \\ k \neq 0}}^{\infty} \sum_{z=-\infty}^{\infty} \sum_{q=-\infty}^{\infty} \sum_{n=-\infty}^{\infty} \frac{(-1)^k}{k} e^{-j[k(\gamma_c + \pi m_0) - \theta_{nqz}]} j^{(z+n+q)} J_z(-c_k) J_q(-b_k) J_n(-a_k) 2\pi \delta(\omega - k\omega_c - (3z+2q+n)\omega_0)}_{S_2} \bigg\}
 \end{aligned} \tag{B.12}$$

Expression (B.12) appears to be quite cumbersome and non-intuitive. Therefore, it should be simplified to the highest possible extent. As sums  $S_1$  and  $S_2$  can be obtained from one another, it is sufficient to thoroughly analyze only one them. The first step in simplifying  $S_1$  can be perceived through expressing it as (B.13).

$$S_1 = \sum_{\substack{k=-\infty \\ k \neq 0}}^{\infty} S_{1,k} = \sum_{k=1}^{\infty} \underbrace{S_{1,k} + S_{1,-k}}_{S'_{1,k}} \tag{B.13}$$

In its expanded form, the term  $S'_{1,k}$  can be written as

$$\begin{aligned}
 S'_{1,k} = & \frac{(-1)^k}{k} \sum_{z=-\infty}^{\infty} \sum_{q=-\infty}^{\infty} \sum_{n=-\infty}^{\infty} J_z(c_k) J_q(b_k) J_n(a_k) e^{-j\left[k(\gamma_c - \pi m_0) - \theta_{nqz} - \frac{z+q+n}{2}\pi\right]} 2\pi \delta(\omega - k\omega_c - (3z+2q+n)\omega_0) \\
 & - \frac{(-1)^k}{k} \sum_{z=-\infty}^{\infty} \sum_{q=-\infty}^{\infty} \sum_{n=-\infty}^{\infty} J_z(-c_k) J_q(-b_k) J_n(-a_k) e^{j\left[k(\gamma_c - \pi m_0) + \theta_{nqz} + \frac{z+q+n}{2}\pi\right]} 2\pi \delta(\omega + k\omega_c - (3z+2q+n)\omega_0)
 \end{aligned} \tag{B.14}$$

Given that indices in the above sums span the complete set of round numbers (mathematically formulated,  $\{z, q, n\} \in (-\infty, \infty)$ ), any combination  $\{z, q, n\}$ , apart from  $\{0, 0, 0\}$ , is ultimately encountered by its negative counterpart. Therefore, the sum  $S_{pn,k} = S'_{1,k}(n, q, z) + S'_{1,k}(-n, -q, -z)$  can be expressed according to (B.15). Further simplification of (B.15) can be achieved in case terms multiplied by the same coefficients are grouped together. For this purpose, properties of Bessel functions defined in (B.16) to (B.18) can be used.

$$\begin{aligned}
S_{\text{pn},k}(\omega) = \frac{(-1)^k}{k} 2\pi \bigg\{ & J_z(c_k)J_q(b_k)J_n(a_k)e^{-j\left[k(\gamma_c - \pi m_0) - \theta_{nqz} - \frac{z+q+n}{2}\pi\right]} \delta(\omega - k\omega_c - (3z + 2q + n)\omega_0) - \\
& J_z(-c_k)J_q(-b_k)J_n(-a_k)e^{j\left[k(\gamma_c - \pi m_0) + \theta_{nqz} + \frac{z+q+n}{2}\pi\right]} \delta(\omega + k\omega_c - (3z + 2q + n)\omega_0) + \\
& J_{-z}(c_k)J_{-q}(b_k)J_{-n}(a_k)e^{-j\left[k(\gamma_c - \pi m_0) + \theta_{nqz} + \frac{z+q+n}{2}\pi\right]} \delta(\omega - k\omega_c + (3z + 2q + n)\omega_0) - \\
& J_{-z}(-c_k)J_{-q}(-b_k)J_{-n}(-a_k)e^{j\left[k(\gamma_c - \pi m_0) - \theta_{nqz} - \frac{z+q+n}{2}\pi\right]} \delta(\omega + k\omega_c + (3z + 2q + n)\omega_0) \bigg\} \quad (\text{B.15})
\end{aligned}$$

$$J_{-n}(x) = (-1)^n J_n(x) \quad (\text{B.16})$$

$$J_n(-x) = (-1)^n J_n(x) \quad (\text{B.17})$$

$$J_{-n}(-x) = J_n(x) \quad (\text{B.18})$$

Substitution of (B.16) to (B.18) into (B.15) results in

$$\begin{aligned}
S_{\text{pn},k}(\omega) = \frac{(-1)^k}{k} 2\pi \bigg\{ & J_z(c_k)J_q(b_k)J_n(a_k) \left( e^{-j\beta_1} \delta(\omega - \omega_1) - e^{j\beta_1} \delta(\omega + \omega_1) \right) + \\
& + J_{-z}(c_k)J_{-q}(b_k)J_{-n} \left( e^{-j\beta_2} \delta(\omega - \omega_2) - e^{j\beta_2} \delta(\omega + \omega_2) \right) \bigg\}, \quad (\text{B.19})
\end{aligned}$$

where

$$\begin{aligned}
\beta_1 &= k(\gamma_c - \pi m_0) - \theta_{nqz} - \frac{z + q + n}{2} \pi \\
\beta_2 &= k(\gamma_c - \pi m_0) + \theta_{nqz} + \frac{z + q + n}{2} \pi \\
\omega_1 &= k\omega_c + (3z + 2q + n)\omega_0 \\
\omega_2 &= k\omega_c - (3z + 2q + n)\omega_0
\end{aligned} \quad (\text{B.20})$$

The presence of Dirac functions shifted in the frequency domain indicates that converting the term  $S_{\text{pn},k}(\omega)$  back to time domain can possibly lead to identification of trigonometric functions. Accordingly, inverse Fourier transformation can be applied to (B.19), yielding

$$\begin{aligned}
S_{\text{pn},k}(t) = \frac{(-1)^k}{k} (j2) \times \\
\times \left\{ J_z(c_k)J_q(b_k)J_n(a_k) \frac{e^{j(\omega_1 t - \beta_1)} - e^{-j(\omega_1 t - \beta_1)}}{j2} + J_{-z}(c_k)J_{-q}(b_k)J_{-n} \frac{e^{j(\omega_2 t - \beta_2)} - e^{-j(\omega_2 t - \beta_2)}}{j2} \right\} \quad (\text{B.21})
\end{aligned}$$

Substituting (B.20) back to (B.21), while recalling that  $\sin(x) = \frac{e^{jx} - e^{-jx}}{j2}$ , gives

$$S_{pn,k}(t) = \frac{(-1)^k}{k}(j2) \times \left\{ \begin{aligned} &J_z(c_k)J_q(b_k)J_n(a_k) \sin \left( [k\omega_c + (3z + 2q + n)\omega_0]t - k(\gamma_c - \pi m_0) + \theta_{nqz} + \frac{z + q + n}{2}\pi \right) + \\ &+ J_{-z}(c_k)J_{-q}(b_k)J_{-n} \sin \left( [k\omega_c - (3z + 2q + n)\omega_0]t - k(\gamma_c - \pi m_0) - \theta_{nqz} - \frac{z + q + n}{2}\pi \right) \end{aligned} \right\} \quad (B.22)$$

As can be seen from (B.22) the terms belonging to the positive and negative set of indices  $z, q$  and  $n$  are distinct, which finally allows for the sum  $S_1$  to be expressed as

$$S_1(t) = \sum_{k=1}^{\infty} \sum_{z=-\infty}^{\infty} \sum_{q=-\infty}^{\infty} \sum_{n=-\infty}^{\infty} \frac{(-1)^k}{k}(j2)J_z(c_k)J_q(b_k)J_n(a_k) \times \underbrace{\sin \left( [k\omega_c + (3z + 2q + n)\omega_0]t - k\gamma_c + \theta_{nqz} + k\pi m_0 \right)}_{\chi_1} \underbrace{\sin \left( \frac{z + q + n}{2}\pi \right)}_{\chi_2} \quad (B.23)$$

It has been already stated that  $S_2 = S_1(-m_0, -\hat{m}_1, -\hat{m}_2, -\hat{m}_3)$ , therefore (B.24) can be written and subsequently rearranged as (B.25) by using the fact that  $(-1)^n \sin(x) = \sin(x - n\pi)$ .

$$S_2(t) = \sum_{k=1}^{\infty} \sum_{z=-\infty}^{\infty} \sum_{q=-\infty}^{\infty} \sum_{n=-\infty}^{\infty} \frac{(-1)^k}{k}(j2)J_z(-c_k)J_q(-b_k)J_n(-a_k) \times \sin \left( [k\omega_c + (3z + 2q + n)\omega_0]t - k\gamma_c + \theta_{nqz} - k\pi m_0 + \frac{z + q + n}{2}\pi \right) \quad (B.24)$$

$$S_2(t) = \sum_{k=1}^{\infty} \sum_{z=-\infty}^{\infty} \sum_{q=-\infty}^{\infty} \sum_{n=-\infty}^{\infty} \frac{(-1)^k}{k}(j2)J_z(c_k)J_q(b_k)J_n(a_k) \times \sin \left( \underbrace{[k\omega_c + (3z + 2q + n)\omega_0]t - k\gamma_c + \theta_{nqz}}_{\chi_1} - \underbrace{\left( k\pi m_0 + \frac{z + q + n}{2}\pi \right)}_{\chi_2} \right) \quad (B.25)$$

Finally, according to (B.5) and (B.12) it is of interest to find the difference of the sums given by (B.23) and (B.25), which leads to

$$S_1(t) - S_2(t) = \sum_{k=1}^{\infty} \sum_{z=-\infty}^{\infty} \sum_{q=-\infty}^{\infty} \sum_{n=-\infty}^{\infty} \frac{(-1)^k}{k}(j2)J_z(c_k)J_q(b_k)J_n(a_k) \left\{ \underbrace{\sin(\chi_1 + \chi_2) - \sin(\chi_1 - \chi_2)}_{2 \cos(\chi_1) \sin(\chi_2)} \right\} \quad (B.26)$$



Substitution of (B.26) into the time domain form of (B.5) results in

$$p(t) = m_0^*(t) + \frac{2}{\pi} \sum_{k=1}^{\infty} \sum_{z=-\infty}^{\infty} \sum_{q=-\infty}^{\infty} \sum_{n=-\infty}^{\infty} \frac{(-1)^k}{k} J_z(k\pi\hat{m}_3) J_q(k\pi\hat{m}_2) J_n(k\pi\hat{m}_1) \times \\ \times \sin\left(k\pi m_0 + \frac{z+q+n}{2}\pi\right) \cos([k\omega_c + (3z+2q+n)\omega_0]t - k\gamma_c + (z\zeta_3 + q\zeta_2 + n\zeta_1)) \quad (\text{B.27})$$

Prior to closing the discussion conducted throughout this section, a few remarks need to be made for the sake of completeness.

- It was stated that translating (B.4) into the frequency domain alleviates the derivation of the SM switching function in its final form (B.27). Although each of the terms under the product in (B.4) can be transformed using the Jacobi-Anger expression as

$$e^{jk\pi m_0^*} = e^{jk\pi m_0} \prod_{i=1}^{\infty} \left( \sum_{n=-\infty}^{\infty} J_n(k\pi\hat{m}_i) e^{jn\zeta_i} e^{jni\omega_0 t} \right),$$

an infinite product of sums appears, which makes the manipulation of mathematical expressions more difficult. Based on a simple example, one can conclude that  $(\sum_i a_i) \cdot (\sum_j b_j) \neq \sum_i \sum_j a_i b_j$ . Therefore, switching the summation places, which is needed in the process of simplifying the SM switching function is impossible under these terms. Conversely, it was seen from (B.8) and (B.9) that convolution of the frequency domain images of  $e^{jk\pi m_0^*}$  provides the result in the form of  $\sum_i \sum_j \dots \sum_q a_i b_j \dots k_q$ , which justifies the need to conduct a part of the analysis in the frequency domain.

- Derivation of all the expressions was conducted under the assumption of all the waveforms being naturally sampled, whereas modern system controllers rely on the use of digital technology. In the systems, alike the MMC, comprising multiple power electronics building blocks, the sampling of relevant voltages and currents is normally performed with the rate significantly exceeding the switching frequency of a single building block. Consequently, the system sampling influence upon the branch spectra can be neglected if PSC modulation is considered.

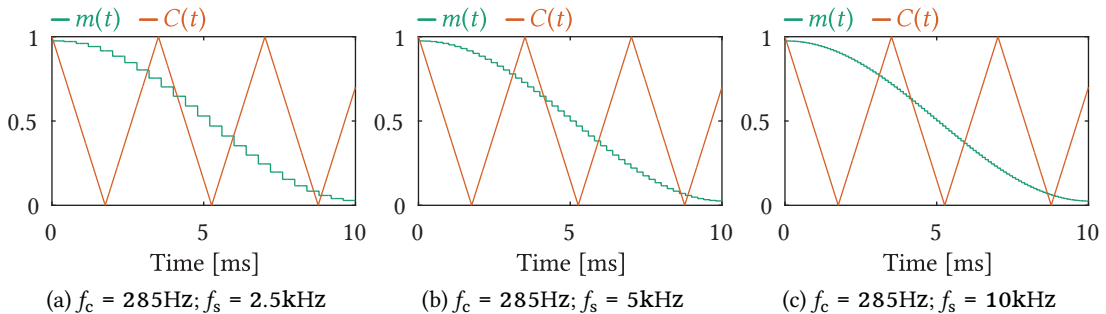


**Fig. B.1** Depending on the frequency at which the modulation index is sampled, it can be claimed that its changes are to be considered almost continuous. As can be seen, modulation index sampling frequencies of 5kHz and 10kHz result in almost invisible discontinuities if carrier frequency equals 285Hz. In general, the same can be claimed as long as  $f_s \gg f_c$ .

For example, in case switching frequency of a single MMC SM analyzed in **Chap. 5** equals  $f_c = 285\text{Hz}$ , sample intervals of the converter currents and voltage, which are shorter for at least an order or magnitude, cause the modulation indices to appear as almost continuous when observed from the perspective of a single SMs. **Fig. B.1** illustrates the above discussion for three different system sampling frequencies.

- The presented analysis refers to the use of HB SMs. Nevertheless, by utilizing the same logic, switching function of any type of the SM, modulated by an arbitrary type of carrier, can be obtained.

# Bibliography

- [1] A. R. Bergen, *Power systems analysis*. Pearson Education India, 2009.
- [2] P. Kundur, N. J. Balu, and M. G. Lauby, *Power system stability and control*. McGraw-hill New York, 1994, vol. 7.
- [3] N. Idir, Y. Weens, and J. Franchaud, "Skin effect and dielectric loss models of power cables," *IEEE Transactions on Dielectrics and Electrical Insulation*, vol. 16, no. 1, pp. 147–154, Feb. 2009.
- [4] D. Tiku, "Dc power transmission: Mercury-arc to thyristor hvdc valves [history]," *IEEE Power and Energy Magazine*, vol. 12, no. 2, pp. 76–96, Mar. 2014.
- [5] *Why HVDC - Technical Advantages*. [Online]. Available: <https://new.abb.com/systems/hvdc/why-hvdc> (visited on 06/24/2019).
- [6] J.-E. Skog, K. Koreman, B. Pääjärvi, T. Worzyk, and T. Andersröd, "The norned hvdc cable link—a power transmission highway between norway and the netherlands," *Proceedings of Energex 2006*, 2006.
- [7] *The 580 kilometer-long NorNed link is the longest subsea high-voltage cable in the world*. [Online]. Available: <https://new.abb.com/systems/hvdc/references/norned> (visited on 06/24/2019).
- [8] *Special Report - 60 years of HVDC*. [Online]. Available: <https://search-ext.abb.com/library/Download.aspx?DocumentID=9AKK106103A8195&LanguageCode=en&DocumentPartId=&Action=Launch> (visited on 06/24/2019).
- [9] B. Gemmell, J. Dorn, D. Retzmann, and D. Soerangr, "Prospects of multilevel vsc technologies for power transmission," in *2008 IEEE/PES Transmission and Distribution Conference and Exposition*, Apr. 2008, pp. 1–16.
- [10] A. S. Elansari, S. J. Finney, J. Burr, and M. F. Edrah, "Frequency control capability of vsc-hvdc transmission system," in *11th IET International Conference on AC and DC Power Transmission*, Feb. 2015, pp. 1–6.
- [11] M. Bahrman and P. Bjorklund, "The new black start: System restoration with help from voltage-sourced converters," *IEEE Power and Energy Magazine*, vol. 12, no. 1, pp. 44–53, Jan. 2014.
- [12] D. Van Hertem, O. Gomis-Bellmunt, and J. Liang, *HVDC grids*. Wiley Online Library, 2016.
- [13] C. Du and M. H. Bollen, "Power-frequency control for VSC-HVDC during island operation," in *The 8th IEE International Conference on AC and DC Power Transmission, ACDC 2006*, 2006, pp. 177–181.
- [14] *Why hvdc - economic and environmental advantages*. [Online]. Available: <https://new.abb.com/systems/hvdc/why-hvdc/economic-and-environmental-advantages> (visited on 06/24/2019).
- [15] A. Clerici, L. Paris, and P. Danfors, "HVDC conversion of HVAC lines to provide substantial power upgrading," *IEEE transactions on Power Delivery*, vol. 6, no. 1, pp. 324–333, 1991.
- [16] D. M. Larruskain, I. Zamora, O. Abarrategui, and Z. Aginako, "Conversion of AC distribution lines into DC lines to upgrade transmission capacity," *Electric Power Systems Research*, vol. 81, no. 7, pp. 1341–1348, 2011.
- [17] D. M. Larruskain, I. Zamora, O. Abarrategui, and A. Iturregi, "VSC-HVDC configurations for converting AC distribution lines into DC lines," *International Journal of Electrical Power & Energy Systems*, vol. 54, pp. 589–597, 2014.
- [18] M. Häusler, G. Schlayer, and G. Fitterer, "Converting AC power lines to DC for higher transmission ratings," *ABB review*, pp. 4–11, 1997.
- [19] *Boosting power with HVDC Light*. [Online]. Available: <https://search-ext.abb.com/library/Download.aspx?DocumentID=POW0077&LanguageCode=en&DocumentPartId=&Action=Launch>.
- [20] U. Javaid, D. Dujic, and W. van der Merwe, "Mvdc marine electrical distribution: Are we ready?" In *IECON 2015 - 41st Annual Conference of the IEEE Industrial Electronics Society*, Nov. 2015, pp. 000 823–000 828.
- [21] F. Agostini, U. Vemulapati, D. Torresin, M. Arnold, M. Rahimo, A. Antoniazzi, L. Raciti, D. Pessina, and H. Suryanarayana, "1mw bi-directional dc solid state circuit breaker based on air cooled reverse blocking-igbt," in *2015 IEEE Electric Ship Technologies Symposium (ESTS)*, Jun. 2015, pp. 287–292.
- [22] Z. J. Shen, Z. Miao, and A. M. Roshandeh, "Solid state circuit breakers for dc microgrids: Current status and future trends," in *2015 IEEE First International Conference on DC Microgrids (ICDCM)*, Jun. 2015, pp. 228–233.
- [23] E. Haugan, H. Rygg, A. Skjellnes, and L. Barstad, "Discrimination in offshore and marine dc distribution systems," in *2016 IEEE 17th Workshop on Control and Modeling for Power Electronics (COMPEL)*, Jun. 2016, pp. 1–7.
- [24] U. Javaid, F. D. Freijedo, D. Dujic, and W. van der Merwe, "Dynamic assessment of source–load interactions in marine mvdc distribution," *IEEE Transactions on Industrial Electronics*, vol. 64, no. 6, pp. 4372–4381, Jun. 2017.
- [25] V. G. Agelidis, G. D. Demetriades, and N. Flourentzou, "Recent advances in high-voltage direct-current power transmission systems," in *2006 IEEE International Conference on Industrial Technology*, Dec. 2006, pp. 206–213.
- [26] P. Lundberg, A. Gustafsson, and M. Jeroense, *Recent advancements in HVDC VSC systems - HVDC and Power Electronics technology and development*. [Online]. Available: <https://library.e.abb.com/public/e88c538bbd394c8baed8fe032573c082/Recent%20advancements%20in%20HVDC%20VSC%20systems.pdf>.

- [27] *Hvdc classic*. [Online]. Available: <https://new.siemens.com/global/en/products/energy/high-voltage/high-voltage-direct-current-transmission-solutions/hvdc-classic.html> (visited on 06/24/2019).
- [28] *Hvdc light®: Celebrating 20 years of innovation and writing the future*. [Online]. Available: [https://www.abb-conversations.com/2017/04/hvdc-light-celebrating-20-years-of-innovation-and-writing-the-future/?\\_ga=2.203929112.98968206.1561303042-2061379687.1548944480](https://www.abb-conversations.com/2017/04/hvdc-light-celebrating-20-years-of-innovation-and-writing-the-future/?_ga=2.203929112.98968206.1561303042-2061379687.1548944480) (visited on 06/24/2019).
- [29] T. Midtsund, A. Becker, J. Karlsson, and K. Egeland, *A Live Black-start Capability test of a Voltage Source HVDC Converter*. [Online]. Available: <https://library.e.abb.com/public/97ac6612486f42dcbe4e5342edd41a01/A%20Live%20Black%20Start%20Capability%20test%20of%20a%20Voltage%20Source%20HVDC%20Converter.pdf>.
- [30] J.-F. Chen, J.-N. Lin, and T.-H. Ai, "The techniques of the serial and paralleled igbts," in *Proceedings of the 1996 IEEE IECON. 22nd International Conference on Industrial Electronics, Control, and Instrumentation*, vol. 2, Aug. 1996, 999–1004 vol.2.
- [31] M. Bruckmann, R. Sommer, M. Fasching, and J. Sigg, "Series connection of high voltage igbt modules," in *Conference Record of 1998 IEEE Industry Applications Conference. Thirty-Third IAS Annual Meeting (Cat. No.98CH36242)*, vol. 2, Oct. 1998, 1067–1072 vol.2.
- [32] T. V. Nguyen, P. O. Jeannin, E. Vagnon, D. Frey, and J. C. Crebier, "Series connection of igbt," in *2010 Twenty-Fifth Annual IEEE Applied Power Electronics Conference and Exposition (APEC)*, Feb. 2010, pp. 2238–2244.
- [33] R. Withanage and N. Shmmas, "Series connection of insulated gate bipolar transistors (igbts)," *IEEE Transactions on Power Electronics*, vol. 27, no. 4, pp. 2204–2212, Apr. 2012.
- [34] H. Mouton and B. Putzeys, "Understanding the pwm nonlinearity: Single-sided modulation," *IEEE Transactions on Power Electronics*, vol. 27, no. 4, pp. 2116–2128, Apr. 2012.
- [35] H. d. T. Mouton, B. McGrath, D. G. Holmes, and R. H. Wilkinson, "One-dimensional spectral analysis of complex pwm waveforms using superposition," *IEEE Transactions on Power Electronics*, vol. 29, no. 12, pp. 6762–6778, Dec. 2014.
- [36] R. Simpson, A. Plumpton, M. Varley, C. Tonner, P. Taylor, and X. Dai, "Press-pack igbts for hvdc and facts," *CSEE Journal of Power and Energy Systems*, vol. 3, no. 3, pp. 302–310, Sep. 2017.
- [37] A. Lesnicar and R. Marquardt, "An innovative modular multilevel converter topology suitable for a wide power range," in *2003 IEEE Bologna Power Tech Conference Proceedings*, vol. 3, Jun. 2003, 6 pp. Vol.3-.
- [38] R. Marquardt, "Modular multilevel converter: An universal concept for hvdc-networks and extended dc-bus-applications," in *The 2010 International Power Electronics Conference - ECCE ASIA*, Jun. 2010, pp. 502–507.
- [39] J. V. M. Farias, A. F. Cupertino, H. A. Pereira, S. I. S. Junior, and R. Teodorescu, "On the redundancy strategies of modular multilevel converters," *IEEE Transactions on Power Delivery*, vol. 33, no. 2, pp. 851–860, Apr. 2018.
- [40] J. Gerdes, "Siemens debuts hvdc plus with san francisco's trans bay cable," *Living Energy*, vol. 5, pp. 28–31, 2011.
- [41] A. Nabae, I. Takahashi, and H. Akagi, "A new neutral-point-clamped pwm inverter," *IEEE Transactions on industry applications*, no. 5, pp. 518–523, 1981.
- [42] V. Guennegues, B. Gollentz, F. Meibody-Tabar, S. Rael, and L. Leclere, "A converter topology for high speed motor drive applications," in *2009 13th European Conference on Power Electronics and Applications*, Sep. 2009, pp. 1–8.
- [43] P. Barbosa, P. Steimer, J. Steinke, M. Winkelnkemper, and N. Celanovic, "Active-neutral-point-clamped (anpc) multilevel converter technology," in *2005 European Conference on Power Electronics and Applications*, IEEE, 2005, 10–pp.
- [44] P. W. Hammond, "A new approach to enhance power quality for medium voltage ac drives," *IEEE Transactions on Industry Applications*, vol. 33, no. 1, pp. 202–208, Jan. 1997.
- [45] M. Hiller, R. Sommer, and M. Beuermann, "Medium-voltage drives," *IEEE Industry Applications Magazine*, vol. 16, no. 2, pp. 22–30, Mar. 2010.
- [46] M. Hiller, D. Krug, R. Sommer, and S. Rohner, "A new highly modular medium voltage converter topology for industrial drive applications," in *2009 13th European Conference on Power Electronics and Applications*, Sep. 2009, pp. 1–10.
- [47] S. Rohner, S. Bernet, M. Hiller, and R. Sommer, "Modelling, simulation and analysis of a modular multilevel converter for medium voltage applications," in *2010 IEEE International Conference on Industrial Technology*, Mar. 2010, pp. 775–782.
- [48] M. Vasiladiotis, N. Cherix, and A. Rufer, "Accurate capacitor voltage ripple estimation and current control considerations for grid-connected modular multilevel converters," *IEEE Transactions on Power Electronics*, vol. 29, no. 9, pp. 4568–4579, Sep. 2014.
- [49] K. Ilves, S. Norrga, L. Harnefors, and H. Nee, "On energy storage requirements in modular multilevel converters," *IEEE Transactions on Power Electronics*, vol. 29, no. 1, pp. 77–88, Jan. 2014.
- [50] A. J. Korn, M. Winkelnkemper, and P. Steimer, "Low output frequency operation of the modular multi-level converter," in *2010 IEEE Energy Conversion Congress and Exposition*, Sep. 2010, pp. 3993–3997.

- [51] J. Kolb, F. Kammerer, and M. Braun, "A novel control scheme for low frequency operation of the modular multilevel converter," in *PCIM Europe*, vol. 2011, 2011, pp. 977–982.
- [52] J. Kolb, F. Kammerer, and M. Braun, "Straight forward vector control of the modular multilevel converter for feeding three-phase machines over their complete frequency range," in *IECON 2011 - 37th Annual Conference of the IEEE Industrial Electronics Society*, Nov. 2011, pp. 1596–1601.
- [53] M. Hagiwara, I. Hasegawa, and H. Akagi, "Start-up and low-speed operation of an electric motor driven by a modular multilevel cascade inverter," *IEEE Transactions on Industry Applications*, vol. 49, no. 4, pp. 1556–1565, Jul. 2013.
- [54] A. Antonopoulos, L. Ångquist, S. Norrga, K. Ilves, L. Harnefors, and H. Nee, "Modular multilevel converter ac motor drives with constant torque from zero to nominal speed," *IEEE Transactions on Industry Applications*, vol. 50, no. 3, pp. 1982–1993, May 2014.
- [55] M. Basic, P. C. de Oliveira e Silva, and D. Dujic, "High power electronics innovation perspectives for pumped storage power plants," *Tech. Rep.*, 2018.
- [56] A. Mertens and J. Kucka, "Quasi two-level pwm operation of an mmc phase leg with reduced module capacitance," *IEEE Transactions on Power Electronics*, vol. 31, no. 10, pp. 6765–6769, Oct. 2016.
- [57] J. Kucka and A. Mertens, "Control for quasi two-level pwm operation of modular multilevel converter," in *2016 IEEE 25th International Symposium on Industrial Electronics (ISIE)*, Jun. 2016, pp. 448–453.
- [58] I. A. Gowaid, G. P. Adam, S. Ahmed, D. Holliday, and B. W. Williams, "Analysis and design of a modular multilevel converter with trapezoidal modulation for medium and high voltage dc-dc transformers," *IEEE Transactions on Power Electronics*, vol. 30, no. 10, pp. 5439–5457, Oct. 2015.
- [59] I. A. Gowaid, G. P. Adam, A. M. Massoud, S. Ahmed, D. Holliday, and B. W. Williams, "Quasi two-level operation of modular multilevel converter for use in a high-power dc transformer with dc fault isolation capability," *IEEE Transactions on Power Electronics*, vol. 30, no. 1, pp. 108–123, Jan. 2015.
- [60] S. Kenzelmann, A. Rufer, D. Dujic, F. Canales, and Y. R. de Novaes, "Isolated dc/dc structure based on modular multilevel converter," *IEEE Transactions on Power Electronics*, vol. 30, no. 1, pp. 89–98, Jan. 2015.
- [61] X. She, A. Q. Huang, and R. Burgos, "Review of solid-state transformer technologies and their application in power distribution systems," *IEEE Journal of Emerging and Selected Topics in Power Electronics*, vol. 1, no. 3, pp. 186–198, Sep. 2013.
- [62] A. Q. Huang, "Medium-voltage solid-state transformer: Technology for a smarter and resilient grid," *IEEE Industrial Electronics Magazine*, vol. 10, no. 3, pp. 29–42, Sep. 2016.
- [63] J. E. Huber and J. W. Kolar, "Solid-state transformers: On the origins and evolution of key concepts," *IEEE Industrial Electronics Magazine*, vol. 10, no. 3, pp. 19–28, Sep. 2016.
- [64] H. Fan and H. Li, "High frequency high efficiency bidirectional dc-dc converter module design for 10 kva solid state transformer," in *2010 Twenty-Fifth Annual IEEE Applied Power Electronics Conference and Exposition (APEC)*, Feb. 2010, pp. 210–215.
- [65] Y. Tran and D. Dujic, "A multiport medium voltage isolated dc-dc converter," in *IECON 2016 - 42nd Annual Conference of the IEEE Industrial Electronics Society*, Oct. 2016, pp. 6983–6988.
- [66] B. Zhao, Q. Song, J. Li, W. Liu, G. Liu, and Y. Zhao, "High-frequency-link dc transformer based on switched capacitor for medium-voltage dc power distribution application," *IEEE Transactions on Power Electronics*, vol. 31, no. 7, pp. 4766–4777, Jul. 2016.
- [67] B. Zhao, Q. Song, J. Li, Y. Wang, and W. Liu, "Modular multilevel high-frequency-link dc transformer based on dual active phase-shift principle for medium-voltage dc power distribution application," *IEEE Transactions on Power Electronics*, vol. 32, no. 3, pp. 1779–1791, Mar. 2017.
- [68] S. Cui, N. Soltan, and R. W. De Doncker, "A high step-up ratio soft-switching DC–DC converter for interconnection of MVDC and HVDC grids," *IEEE Transactions on Power Electronics*, vol. 33, no. 4, pp. 2986–3001, 2018.
- [69] M. M. C. Merlin, T. C. Green, P. D. Mitcheson, D. R. Trainer, D. R. Critchley, and R. W. Crookes, "A new hybrid multi-level voltage-source converter with dc fault blocking capability," in *9th IET International Conference on AC and DC Power Transmission (ACDC 2010)*, Oct. 2010, pp. 1–5.
- [70] G. Ortiz, J. Biela, D. Bortis, and J. W. Kolar, "1 megawatt, 20 khz, isolated, bidirectional 12kv to 1.2kv dc-dc converter for renewable energy applications," in *The 2010 International Power Electronics Conference - ECCE ASIA*, Jun. 2010, pp. 3212–3219.
- [71] N. Soltan, H. Stagge, R. W. De Doncker, and O. Apeldoorn, "Development and demonstration of a medium-voltage high-power dc-dc converter for dc distribution systems," in *2014 IEEE 5th International Symposium on Power Electronics for Distributed Generation Systems (PEDG)*, Jun. 2014, pp. 1–8.
- [72] T. Lüth, M. M. C. Merlin, and T. C. Green, "Modular multilevel dc/dc converter architectures for hvdc taps," in *2014 16th European Conference on Power Electronics and Applications*, Aug. 2014, pp. 1–10.

- [73] C. Oates, K. Dyke, and D. Trainer, "The augmented modular multilevel converter," in *2014 16th European Conference on Power Electronics and Applications*, Aug. 2014, pp. 1–10.
- [74] C. Oates and K. Dyke, "The controlled transition bridge," in *2015 17th European Conference on Power Electronics and Applications (EPE'15 ECCE-Europe)*, Sep. 2015, pp. 1–10.
- [75] G. P. Adam, I. A. Gowaid, S. J. Finney, D. Holliday, and B. W. Williams, "Review of dc–dc converters for multi-terminal hvdc transmission networks," *IET Power Electronics*, vol. 9, no. 2, pp. 281–296, 2016.
- [76] M. Agamy, D. Dong, L. J. Garces, Y. Zhang, M. Dame, A. S. Atalla, and Y. Pan, "A high power medium voltage resonant dual active bridge for dc distribution networks," in *2016 IEEE Energy Conversion Congress and Exposition (ECCE)*, Sep. 2016, pp. 1–6.
- [77] A. J. Korn, M. Winkelnkemper, P. Steimer, and J. W. Kolar, "Capacitor voltage balancing in modular multilevel converters," in *6th IET International Conference on Power Electronics, Machines and Drives (PEMD 2012)*, Mar. 2012, pp. 1–5.
- [78] J. Rodriguez, Jih-Sheng Lai, and Fang Zheng Peng, "Multilevel inverters: A survey of topologies, controls, and applications," *IEEE Transactions on Industrial Electronics*, vol. 49, no. 4, pp. 724–738, Aug. 2002.
- [79] J. Rodriguez, S. Bernet, B. Wu, J. O. Pontt, and S. Kouro, "Multilevel voltage-source-converter topologies for industrial medium-voltage drives," *IEEE Transactions on Industrial Electronics*, vol. 54, no. 6, pp. 2930–2945, Dec. 2007.
- [80] S. Kouro, M. Malinowski, K. Gopakumar, J. Pou, L. G. Franquelo, B. Wu, J. Rodriguez, M. A. Perez, and J. I. Leon, "Recent advances and industrial applications of multilevel converters," *IEEE Transactions on Industrial Electronics*, vol. 57, no. 8, pp. 2553–2580, Aug. 2010.
- [81] A. Nami, J. Liang, F. Dijkhuizen, and G. D. Demetriades, "Modular multilevel converters for hvdc applications: Review on converter cells and functionalities," *IEEE Transactions on Power Electronics*, vol. 30, no. 1, pp. 18–36, Jan. 2015.
- [82] R. Teodorescu, M. Liserre, and P. Rodriguez, *Grid converters for photovoltaic and wind power systems*. John Wiley & Sons, 2011, vol. 29.
- [83] S. N. Vukosavic, *Grid-Side Converters Control and Design*. Springer, 2018.
- [84] A. Antonopoulos, L. Angquist, and H. Nee, "On dynamics and voltage control of the modular multilevel converter," in *2009 13th European Conference on Power Electronics and Applications*, Sep. 2009, pp. 1–10.
- [85] L. Harnefors, A. Antonopoulos, S. Norrga, L. Angquist, and H. Nee, "Dynamic analysis of modular multilevel converters," *IEEE Transactions on Industrial Electronics*, vol. 60, no. 7, pp. 2526–2537, Jul. 2013.
- [86] K. Sharifabadi, L. Harnefors, H.-P. Nee, S. Norrga, and R. Teodorescu, *Design, control, and application of modular multilevel converters for HVDC transmission systems*. John Wiley & Sons, 2016.
- [87] S. N. Vukosavic, *Electrical machines*. Springer Science & Business Media, 2012.
- [88] D. G. Holmes and T. A. Lipo, *Pulse width modulation for power converters: principles and practice*. John Wiley & Sons, 2003, vol. 18.
- [89] S. N. Vukosavic, *Digital control of electrical drives*. Springer Science & Business Media, 2007.
- [90] P. Münch, D. Görges, M. Izák, and S. Liu, "Integrated current control, energy control and energy balancing of modular multilevel converters," in *IECON 2010 - 36th Annual Conference on IEEE Industrial Electronics Society*, Nov. 2010, pp. 150–155.
- [91] J. Kolb, F. Kammerer, M. Gommeringer, and M. Braun, "Cascaded control system of the modular multilevel converter for feeding variable-speed drives," *IEEE Transactions on Power Electronics*, vol. 30, no. 1, pp. 349–357, Jan. 2015.
- [92] A. Rasic, U. Krebs, H. Leu, and G. Herold, "Optimization of the modular multilevel converters performance using the second harmonic of the module current," in *2009 13th European Conference on Power Electronics and Applications*, Sep. 2009, pp. 1–10.
- [93] K. Ilves, A. Antonopoulos, L. Harnefors, S. Norrga, L. Ångquist, and H. Nee, "Capacitor voltage ripple shaping in modular multilevel converters allowing for operating region extension," in *IECON 2011 - 37th Annual Conference of the IEEE Industrial Electronics Society*, Nov. 2011, pp. 4403–4408.
- [94] S. P. Engel and R. W. De Doncker, "Control of the modular multi-level converter for minimized cell capacitance," in *Proceedings of the 2011 14th European Conference on Power Electronics and Applications*, Aug. 2011, pp. 1–10.
- [95] "rank-nullity theorem." from mathworld—a wolfram web resource, created by eric w. weissstein. [Online]. Available: <http://mathworld.wolfram.com/Rank-NullityTheorem.html> (visited on 12/29/2019).
- [96] M. Basić, S. Milovanović, and D. Dujčić, "Comparison of the two modular multilevel converter internal energy balancing methods," in *20th International Symposium POWER ELECTRONICS (EE 2019)*, 2019, pp. 1–8.
- [97] G. Carrara, S. Gardella, M. Marchesoni, R. Salutati, and G. Sciotto, "A new multilevel pwm method: A theoretical analysis," *IEEE Transactions on Power Electronics*, vol. 7, no. 3, pp. 497–505, Jul. 1992.
- [98] J. Huber and A. Korn, "Optimized pulse pattern modulation for modular multilevel converter high-speed drive," Sep. 2012, LS1a–1.4.

- [99] G. Konstantinou, M. Ciobotaru, and V. Agelidis, "Selective harmonic elimination pulse-width modulation of modular multilevel converters," *IET Power Electronics*, vol. 6, no. 1, pp. 96–107, Jan. 2013.
- [100] K. Ilves, L. Harnefors, S. Norrga, and H. Nee, "Predictive sorting algorithm for modular multilevel converters minimizing the spread in the submodule capacitor voltages," *IEEE Transactions on Power Electronics*, vol. 30, no. 1, pp. 440–449, Jan. 2015.
- [101] A. Hassanpoor, L. Ångquist, S. Norrga, K. Ilves, and H. Nee, "Tolerance band modulation methods for modular multilevel converters," *IEEE Transactions on Power Electronics*, vol. 30, no. 1, pp. 311–326, Jan. 2015.
- [102] M. Lehmann, C. Hahn, and M. Luther, "A novel approach for energy balanced operation of submodules in multilevel vsc hvdc systems," in *2015 50th International Universities Power Engineering Conference (UPEC)*, Sep. 2015, pp. 1–6.
- [103] D. Wu and L. Peng, "Characteristics of nearest level modulation method with circulating current control for modular multilevel converter," *IET Power Electronics*, vol. 9, no. 2, pp. 155–164, 2016.
- [104] B. P. McGrath, C. A. Teixeira, and D. G. Holmes, "Optimized phase disposition (pd) modulation of a modular multilevel converter," *IEEE Transactions on Industry Applications*, vol. 53, no. 5, pp. 4624–4633, Sep. 2017.
- [105] M. Vasiladiotis, A. Christe, and T. Geyer, "Model predictive pulse pattern control for modular multilevel converters," *IEEE Transactions on Industrial Electronics*, vol. 66, no. 3, pp. 2423–2431, Mar. 2019.
- [106] F. Gao, D. Niu, H. Tian, C. Jia, N. Li, and Y. Zhao, "Control of parallel-connected modular multilevel converters," *IEEE Transactions on Power Electronics*, vol. 30, no. 1, pp. 372–386, Jan. 2015.
- [107] J. Pou, S. Ceballos, G. Konstantinou, G. J. Capella, and V. G. Agelidis, "Control strategy to balance operation of parallel connected legs of modular multilevel converters," in *2013 IEEE International Symposium on Industrial Electronics*, May 2013, pp. 1–7.
- [108] J. Pou, J. Zaragoza, G. Capella, I. Gabiola, S. Ceballos, and E. Robles, "Current balancing strategy for interleaved voltage source inverters," *EPE Journal*, vol. 21, no. 1, pp. 29–34, 2011. [Online]. Available: <https://doi.org/10.1080/09398368.2011.11463785>.
- [109] A. Volke, J. Wendt, and M. Hornkamp, *IGBT modules: technologies, driver and application*. Infineon, 2012.
- [110] R. Hermann, S. Bernet, Y. Suh, and P. K. Steimer, "Parallel connection of integrated gate commutated thyristors (igcts) and diodes," *IEEE Transactions on Power Electronics*, vol. 24, no. 9, pp. 2159–2170, Sep. 2009.
- [111] R. Grinberg, E. Bjornstad, P. Steimer, A. Korn, M. Winkelnkemper, D. Gerardi, O. Senturk, O. Apeldoorn, and J. Li, "Study of overcurrent protection for modular multilevel converter," in *2014 IEEE Energy Conversion Congress and Exposition (ECCE)*, Sep. 2014, pp. 3401–3407.
- [112] M. M. Steurer, K. Schoder, O. Faruque, D. Soto, M. Bosworth, M. Sloderbeck, F. Bogdan, J. Hauer, M. Winkelnkemper, L. Schwager, and P. Blaszczyk, "Multifunctional megawatt-scale medium voltage dc test bed based on modular multilevel converter technology," *IEEE Transactions on Transportation Electrification*, vol. 2, no. 4, pp. 597–606, Dec. 2016.
- [113] A. Antonopoulos, L. Ångquist, and H.-P. Nee, "On dynamics and voltage control of the modular multilevel converter," in *Power Electronics and Applications, 2009. EPE'09. 13th European Conference on*, IEEE, 2009, pp. 1–10.
- [114] K. Ilves, L. Harnefors, S. Norrga, and H. Nee, "Analysis and operation of modular multilevel converters with phase-shifted carrier pwm," *IEEE Transactions on Power Electronics*, vol. 30, no. 1, pp. 268–283, Jan. 2015.
- [115] A. Christe and D. Dujic, "Modular multilevel converter control methods performance benchmark for medium voltage applications," *IEEE Transactions on Power Electronics*, vol. 34, no. 5, pp. 4967–4980, May 2019.
- [116] A. Hassanpoor, S. Norrga, H. Nee, and L. Ångquist, "Evaluation of different carrier-based pwm methods for modular multilevel converters for hvdc application," in *IECON 2012 - 38th Annual Conference on IEEE Industrial Electronics Society*, Oct. 2012, pp. 388–393.
- [117] S. Cui, J. Jung, Y. Lee, and S. Sul, "Principles and dynamics of natural arm capacitor voltage balancing of a direct modulated modular multilevel converter," in *2015 9th International Conference on Power Electronics and ECCE Asia (ICPE-ECCE Asia)*, Jun. 2015, pp. 259–267.
- [118] L. Harnefors, A. Antonopoulos, K. Ilves, and H. Nee, "Global asymptotic stability of current-controlled modular multilevel converters," *IEEE Transactions on Power Electronics*, vol. 30, no. 1, pp. 249–258, Jan. 2015.
- [119] D. Jovcic, "Step-up dc-dc converter for megawatt size applications," *IET Power Electronics*, vol. 2, no. 6, pp. 675–685, Nov. 2009.
- [120] D. Jovcic, "Bidirectional, high-power dc transformer," *IEEE Transactions on Power Delivery*, vol. 24, no. 4, pp. 2276–2283, Oct. 2009.
- [121] J. A. Ferreira, "The multilevel modular dc converter," *IEEE Transactions on Power Electronics*, vol. 28, no. 10, pp. 4460–4465, Oct. 2013.
- [122] G. J. Kish and P. W. Lehn, "A modular bidirectional dc power flow controller with fault blocking capability for dc networks," in *2013 IEEE 14th Workshop on Control and Modeling for Power Electronics (COMPEL)*, Jun. 2013, pp. 1–7.

- [123] G. J. Kish, M. Ranjram, and P. W. Lehn, "A modular multilevel dc/dc converter with fault blocking capability for hvdc interconnects," *IEEE Transactions on Power Electronics*, vol. 30, no. 1, pp. 148–162, Jan. 2015.
- [124] A. Schön and M. M. Bakran, "A new hvdc-dc converter with inherent fault clearing capability," in *2013 15th European Conference on Power Electronics and Applications (EPE)*, Sep. 2013, pp. 1–10.
- [125] S. Cui, N. Soltan, and R. W. De Doncker, "Dynamic performance and fault-tolerant capability of a tlc-mmc hybrid dc-dc converter for interconnection of mvdc and hvdc grids," in *Energy Conversion Congress and Exposition (ECCE), 2017 IEEE*, IEEE, 2017, pp. 1622–1628.
- [126] S. Milovanović and D. Dujić, "Six-step MMC-based high power DC-DC converter," in *2018 International Power Electronics Conference (IPEC-Niigata 2018-ECCE Asia)*, IEEE, 2018, pp. 1484–1490.
- [127] R. W. A. A. De Doncker, D. M. Divan, and M. H. Kheraluwala, "A three-phase soft-switched high-power-density dc/dc converter for high-power applications," *IEEE Transactions on Industry Applications*, vol. 27, no. 1, pp. 63–73, Jan. 1991.
- [128] D. Weiss, M. Vasiladiotis, C. Banceanu, N. Drack, B. Odegard, and A. Grondona, "Igct based modular multilevel converter for an ac-ac rail power supply," in *PCIM Europe 2017; International Exhibition and Conference for Power Electronics, Intelligent Motion, Renewable Energy and Energy Management*, May 2017, pp. 1–8.
- [129] M. Glinka and R. Marquardt, "A new ac/ac-multilevel converter family applied to a single-phase converter," in *The Fifth International Conference on Power Electronics and Drive Systems, 2003. PEDS 2003*, vol. 1, Nov. 2003, pp. 16–23 Vol.1.
- [130] S. S. et. al., "A modular multilevel converter based railway power conditioner for power balance and harmonic compensation in scott railway traction system," in *2016 IEEE 8th International Power Electronics and Motion Control Conference (IPEMC-ECCE Asia)*, May 2016, pp. 2412–2416.
- [131] N. D. Yan Zhao and B. Wang, "Application of three-phase modular multilevel converter (mmc) in co-phase traction power supply system," in *2014 IEEE Conference and Expo Transportation Electrification Asia-Pacific (ITEC Asia-Pacific)*, Aug. 2014, pp. 1–6.
- [132] A. A. Badin and I. Barbi, "Simplified control technique for three-phase rectifier pfc based on the scott transformer," in *2006 IEEE International Symposium on Industrial Electronics*, vol. 2, Jul. 2006, pp. 931–936.
- [133] A. A. Badin and I. Barbi, "Unity power factor isolated three-phase rectifier with split dc-bus based on the scott transformer," *IEEE Transactions on Power Electronics*, vol. 23, no. 3, pp. 1278–1287, May 2008.
- [134] A. A. Badin and I. Barbi, "Unity power factor isolated three-phase rectifier with two single-phase buck rectifiers based on the scott transformer," *IEEE Transactions on Power Electronics*, vol. 26, no. 9, pp. 2688–2696, Sep. 2011.
- [135] J. Tukaram, S. Senthil Kumar, D. Ganesh, and V. Sravan Kumar, "Investigation of pwm current mode controllers for upf three phase - rectifier with split dc bus based on the scott transformer," in *2012 International Conference on Advances in Power Conversion and Energy Technologies (APCET)*, Aug. 2012, pp. 1–6.
- [136] S. P. Engel, N. Soltan, and R. W. De Doncker, "Instantaneous current control for the three-phase dual-active bridge DC-DC converter," in *Energy Conversion Congress and Exposition (ECCE)*, IEEE, 2012, pp. 3964–3969.
- [137] S. P. Engel, N. Soltan, H. Stagge, and R. W. De Doncker, "Improved instantaneous current control for the three-phase dual-active bridge DC-DC converter," in *ECCE Asia Downunder (ECCE Asia)*, IEEE, 2013, pp. 855–860.
- [138] S. P. Engel, N. Soltan, H. Stagge, and R. W. De Doncker, "Dynamic and balanced control of three-phase high-power dual-active bridge DC-DC converters in dc-grid applications," *IEEE Transactions on Power Electronics*, vol. 28, no. 4, pp. 1880–1889, 2013.
- [139] S. Shao, M. Jiang, J. Zhang, and X. Wu, "A capacitor voltage balancing method for a modular multilevel dc transformer for dc distribution system," *IEEE Transactions on Power Electronics*, vol. 33, no. 4, pp. 3002–3011, Apr. 2018.
- [140] H. van Hoek, M. Neubert, and R. W. D. Doncker, "Enhanced modulation strategy for a three-phase dual active bridge—boosting efficiency of an electric vehicle converter," *IEEE Transactions on Power Electronics*, vol. 28, no. 12, pp. 5499–5507, Dec. 2013.
- [141] T. A. Meynard and H. Foch, "Multi-level conversion: High voltage choppers and voltage-source inverters," in *Power Electronics Specialists Conference, 1992. PESC '92 Record., 23rd Annual IEEE*, Jun. 1992, pp. 397–403 vol.1.
- [142] *Diagonalization of Matrices*. [Online]. Available: <https://math.okstate.edu/people/binegar/3013-S99/3013-116.pdf> (visited on 12/27/2019).
- [143] *Gram-schmidt orthonormalization*. [Online]. Available: <http://mathworld.wolfram.com/Gram-SchmidtOrthonormalization.html> (visited on 12/27/2019).
- [144] L. Angquist, A. Antonopoulos, D. Siemaszko, K. Ilves, M. Vasiladiotis, and H. Nee, "Open-loop control of modular multilevel converters using estimation of stored energy," *IEEE Transactions on Industry Applications*, vol. 47, no. 6, pp. 2516–2524, Nov. 2011.



# Stefan Milovanović

*PhD candidate in Power Electronics*

✉ [stefan.milovanovic@alumni.epfl.ch](mailto:stefan.milovanovic@alumni.epfl.ch)  
born 08.07.1992  
Serbian

## EDUCATION

École Polytechnique Fédérale de Lausanne, Lausanne, Switzerland

2017-2020 PhD candidate, *EDEY Electrical Engineering Doctoral School*  
*MMC-based conversion for MVDC applications*

University of Belgrade, School of Electrical Engineering, Belgrade, Serbia

2015-2016 MSc, The Department of Power Converters and Drive Systems

University of Belgrade, School of Electrical Engineering, Belgrade, Serbia

2011-2015 BSc, The Department of Power Converters and Drive Systems

## TEACHING / SUPERVISION EXPERIENCE

2017-2018 Teaching Assistant on the course *Industrial Electronics I* (Modeling and control of grid-connected power electronics converters)

2019 Teaching Assistant on the course *Industrial Electronics II* (Modeling and control of power electronics converters and motor drives)

2019 MSc thesis supervision (*Modeling of the Modular Multilevel Converter in Hardware in the Loop Environment*, by Mr. Igor Lopušina)

## PROFESSIONAL EXPERIENCE

2016-2017 Teaching assistant, University of Belgrade, School of Electrical Engineering

2017- Doctoral assistant, École Polytechnique Fédérale de Lausanne, Lausanne, Switzerland

## LANGUAGES

English	Full working proficiency
French	A2 level
Serbian	native

## COMPUTER TOOLS AND CODING

Simulation	Matlab Simulink, PLECS, PSpice
PCB design	Altium
Coding	Matlab, C, Latex
OS	Windows, iOS

## REVIEW

Regular reviewer for IEEE Transactions on Power Electronics and IEEE Transactions on Industrial Electronics, plus various conferences